School of Electrical Engineering, Computing and Mathematical Sciences

Probing the Interstellar Medium Toward Timing Array Millisecond Pulsars with the Murchison Widefield Array

Dilpreet Kaur
0000-0003-4879-1019

This thesis is presented for the Degree of
Doctor of Philosophy
of
Curtin University

July 2021

To the best of my knowledge and belief this thesis contains no material previously published by any other person except where due acknowledgement has been made. This thesis contains no material which has been accepted for the award of any other degree or diploma in any university.

Dilpreet Kaur

"*You were born with wings. Don't crawl. Learn to use them to fly and fly.*"

— APJ Abdul Kalam

Acknowledgements

First and foremost, I would like to express my deepest thanks to my supervisor Dr. Ramesh Bhat for all the help, support and advice throughout this PhD journey. Thank you for all of those off-hour guidance whether it is for the uGMRT observations, conference preparations, or with scientific writing. Also, thank you for encouraging the artistic side of myself and giving it a shout-out multiple times, so that it can get some visibility. I would mention that without your excitement and support, my art piece would not have made to cover page/article of CIRA magazine, media release, SKA contact magazine, ICRAR outreach and of course in my thesis. Thank you for always cheering me up. I would also like to thank my co-supervisors Dr. Shi Dai, Dr. Ryan Shannon, and Dr. Steven Tremblay; your support and guidance throughout this journey means so much and helped me to become an independent researcher. I would like to thank S. McSweeney for providing the valuable feedback on refining the presentation of this thesis. Finally, to the whole pulsar group at CIRA, for all the urgent help whenever needed throughout the PhD and making this Journey extremely memorable.

I would like to thank my family who believed in me and always encouraged me to pursue my dream. Specially to my Mother, for giving me immense freedom to pursue my dream and showing trust with my decisions throughout. To my younger Sister for loving, caring and teasing me. To my Nanna who is more than excited to see the title "Dr" with my name and eagerly waiting for this proud moment. To my Grandmother for always being our backbone. You are an inspiration and role model to me. Thank you all for all your love, support and

encouragement. In the memory of my Dad who left us in a very early stage but he always believed that I will go far in academics and art. Thank you Dad, your reflection and blessings will always be there, whatever I do in my life.

Last but not the least, all my thanks goes to my husband, Rahul Joshi, for always being on my side and comforting me in this roller-coaster ride. Taking me to long drives in nature whenever I felt stuck or stressed with my PhD work, cooking tastiest food for me. Thank you for always encouraging me and listening to me when I felt enthusiastic or upset about my research. Undoubtedly, the completion of this thesis could not have been possible without your support.

In all sincerity, thank you everyone for these years of encouragement.

Abstract

Millisecond pulsars (MSPs) are among the most sought after targets for pulsar timing array (PTA) experiments. PTAs take advantage of the clock-like stability of MSPs spread across the celestial sphere, with the ultimate goal of making a direct detection of ultra-low frequency (nano-Hz) gravitational waves. However, in order to succeed in this goal, PTA experiments require very high timing precision (∼100-200 ns) for a large sample of MSPs over long time spans (∼10-20 years), and thus demand a thorough understanding of the emission and physical properties of pulsars that form PTAs, characteristics of the instruments used for observations, and the effects on pulsar signals as they pass through the ionised interstellar medium (ISM). The magnitudes of the ISM effects scale strongly with the inverse of observing frequency. Low-frequency radio telescopes such as the Murchison Widefield Array (MWA) operating at 80-300 MHz, which is also a precursor to the Square Kilometre Array (SKA), offer the strategic advantages for undertaking low-frequency studies of southern MSPs, many of which are the prime targets for both current and future PTAs.

The study of MSPs with the MWA requires phase-coherent de-dispersion in order to remove any dispersive smearing that occurs due to 10-kHz/100-μs resolutions of the MWA's voltage capture system (VCS). With the successful implementation of data reconstruction (via polyphase filter-bank inversion), it has become possible to attain microsecond level time resolution, which enabled high-fidelity detections of MSPs down to ∼80 MHz. The capability is demonstrated with the observations of PSR J2241−5236; a pulsar with a short period (2.18 ms), low dispersion measure (DM = 11.411 pc cm^{-3}), and a narrow pulse profile (width $\sim 130\,\mu$s at 1.4 GHz). Our studies revealed a dual-precursor type feature in the pulse profile that was either faint or absent in high-frequency observations from Parkes. The resultant high-fidelity detections also enabled DM determinations with very high precision, of the order of $(2-6)\times10^{-6}$ pc cm^{-3}, which is an order of magnitude better than those currently achievable at timing frequencies with

most other telescopes.

We also investigated a subtle ISM effect that arises as a consequence of multipath scattering, known as frequency-dependent or "chromatic" dispersion measure. This is due to the fact that the volume or path lengths sampled by the pulsar radiation is a strong function of the observing frequency. With the advent of wide-band pulsar instrumentation there are now good prospects of obtaining more precise DMs and thence improved timing precisions. However, this also necessitates making careful assessments of frequency-dependent DMs. We report the detection of such an effect from observations of PSR J2241−5236, conducted using the wide-band receivers and capabilities now available at the MWA, the upgraded Giant Metrewave Radio Telescope (uGMRT) and Parkes telescopes, thus providing a broadband coverage from 80 MHz to 4 GHz. Our analysis show the excess in DM scales with the observing frequency (ν) as $\delta\mathrm{DM} \sim \nu^{-3.8\pm0.5}$. Thus our analysis provides the first direct evidence of chromatic DM towards an important PTA pulsar.

MSP observations over a wide frequency range also necessitate the development of new analysis and timing techniques for attaining the best possible timing precision. Accounting for profile evolution is an integral part of these. Ignoring the frequency dependence of profile evolution can result in imperfect template matching, and hence biased arrival times, thereby reducing precision and sensitivity of timing data. As part of this thesis work, the multi-frequency PSR J2145−0750 data from joint MWA, uGMRT, and Parkes observations were exploited to test the applicability of a 2-dimensional template matching technique, as implemented in the software "PTIME", which models the profile evolution with frequency for timing analysis. Our analysis suggests that the application of PTIME across 80-4000 MHz can lead to improved DM precision over that obtainable using a single frequency template. A detailed comparison of the efficacy of multiple different techniques may help converge on most optimal methods that can be routinely used for the analysis of PTA data from wideband observations.

Statement of Contribution by Others

The content of Chapter 3 is my own work excepting the following. In this Chapter, we presented high time resolution studies of the millisecond pulsar J2241−5236 below 300 MHz with the MWA. The MWA data used for this project were reduced and calibrated by myself. The analysis and interpretation was carried out under the supervision of Dr R. Bhat, Dr S. Tremblay and Dr R. Shannon. I used the MWA flux calibration technique developed by B. Meyers for the analysis of spectral behavior at low frequencies. I wrote all the sections of the article. Dr R. Bhat, Dr S. Tremblay and Dr R. Shannon aided in the article writing process by providing guidance in terms of the structure and contextual discussion, both before and after referee comments were received. Rest of the co-authors are from the MWA's builders list included as a part of the MWA's publication policy.

The content of Chapter 4 is my own work excepting the following. The formulae for the aberration and retardation effects were derived by Dr S. McSweeney. Discussion with Dr W. van Straten helped us to understand the voids in the PSRCHIVE functioning to account for the binary parameters, which helped build some content of the paper. Dr D. Reardon also helped us to understand the orbital binary parameters. In this Chapter, we used contemporaneous data from three different telescopes; the MWA, uGMRT, and Parkes. I led the uGMRT proposal, as well as the MWA proposal to track the full binary orbit of the pulsar J2241−5236. S. Kudale and Dr R. Bhat helped with the uGMRT observations and provided feedback for its backend system. The remainder of the MWA data were obtained through the G0021 project (PI Bhat). The Parkes data were recorded as part of the ongoing PPTA project. I analysed all the data by myself. I prepared all the sections of the Chapter. Dr R. Bhat, Dr S. Dai and Dr R. Shannon aided in the writing process by providing guidance in terms of the structure and contextual discussion. Dr S. McSweeney also helped with improving the language and stylistic aspects of the presentation. The work presented in

this chapter is also being prepared for submission to a journal.

The content of Chapter 5 is my own work excepting the following. Dr S. Dai led the development of the PTIME software. I led the uGMRT proposal. The MWA data were obtained through the G0021 project (PI Bhat). The Parkes data were taken as part of the ongoing PPTA project (The P456 project; PI Hobbs). The Parkes observations were carried out by Dr R. Bhat. The uGMRT observations were strongly supported by S. Kudale and Dr R. Bhat. I analysed all the data under the supervision of Dr R. Bhat and Dr S. Dai. I prepared all the sections of the Chapter. Dr R. Bhat, Dr S. Dai and Dr R. Shannon aided in the writing process by providing guidance in terms of the structure and contextual discussion. Dr S. McSweeney helped with improving the language and stylistic aspects of the presentation.

(Signature of Candidate)

(Signature of Supervisor)

Contents

List of Figures

Chapter 1

Introduction

1.1 Discovery of Pulsars

Pulsars were discovered in 1967 by Jocelyn Bell and Antony Hewish at low frequencies (81.5 MHz). It was a serendipitous discovery by Jocelyn Bell who noticed a signal that appeared to be tracking with the sky and regularly pulsating every 1.3 s (Hewish et al., 1968). The prospective objects that emit these periodic signals were quickly identified as neutron stars (Gold, 1968). Neutron stars are the compact stellar remnants of core-collapse supernovae of massive stars. They were first theorised by Baade & Zwicky (1934). The progenitor star (mostly O and B type) undergoes a massive energy release through gravitational collapse. Neutron stars are the end points of the evolution of massive stars whose initial mass is $\sim$ 10 to 30 $M_\odot$. They are typically born with strong magnetic fields (B $\sim 10^8 - 10^{14}$ G), and a large angular momentum both related to the parent star. Pulsars are very small in diameter, typically having a radius of about $\sim$10 km and an approximate mass of $M_P \sim 1.4\ M_\odot$, which means they are extremely dense objects. The angular momentum gained during the explosion makes them spin very fast.

Even after more than 50 years from the discovery of these exotic objects, the emission mechanism responsible for electromagnetic radiation remains not

well understood. According to generally-adopted emission models, accelerating charged particles moving along the magnetic field emit electromagnetic radiation that is usually detected at radio frequencies, as a sequence of pulses. Because the magnetic axis is in general not aligned with the rotation axis, the signals from pulsars, just like a lighthouse (Figure 1.1), occur at extremely regular intervals of time, which is the pulsar's rotation period. If the magnetic axis and the rotation axis are almost orthogonal, the beam from both the magnetic poles can sweep past our line-of-sight, producing pulses separated by about 180 degrees in pulse longitude (in this case, the less intense pulse is called an 'interpulse').

1.2 Pulsar population and classification

The current population of pulsars is summarised in the "P-$\dot{P}$ diagram" which presents the pulse period (P) and its first derivative ($\dot{P}$) for all known pulsars. Figure 1.2 presents the current population of $\sim$2800 pulsars from the Australia Telescope National Facility (ATNF) pulsar catalogue (Manchester et al., 2005). The pulsars are generally classified as "normal pulsars" (also known as slow or long-period pulsars), and "recycled pulsars" (also known as millisecond pulsars). A clear distinction between these two populations can be seen in the P-$\dot{P}$ diagram. The normal pulsars occupy the top-right region of the diagram. The recycled pulsars occupy the bottom-left portion of the diagram. The parameters P and $\dot{P}$ play an important role in characterising some of the most basic properties of a pulsar. The slow down of the pulsar's rotation (i.e., spin down) is primarily due to the loss of rotational kinetic energy to magnetic dipole radiation. Assuming one hundred percent efficiency in this process i.e., the lost rotational kinetic energy is entirely radiated away in the form of magnetic dipole radiation, the surface magnetic field strength of pulsars can be written as

$$B = \sqrt{\frac{3c^3}{8\pi^2}\frac{I}{R^6 sin^2\alpha}P\dot{P}} \simeq 10^{12}\,G\Big(\frac{P}{s}\Big)^{1/2}\Big(\frac{\dot{P}}{10^{-15}}\Big)^{1/2}, \tag{1.1}$$

where c is the speed of light. The physical parameters, moment of inertia (I) and radius (R), are generally unknown, but usually $I = 10^{45}\,\mathrm{g\,cm^2}$, radius $R \approx 10\,\mathrm{km}$ are assumed as their values. As a simplification, the inclination angle α with respect to the rotation axis is assumed 90°, so $sin(\alpha)$=1. Under the formalism (i.e., the lost rotational kinetic energy = the magnetic dipole radiation), and under assumption that the initial period of the pulsar is much shorter than the observed one, the characteristic age (τ) of the pulsar can be estimated as

$$\tau = P/2\dot{P} \simeq 15.8\,\mathrm{Myr}\Big(\frac{P}{\mathrm{s}}\Big)\Big(\frac{\dot{P}}{10^{-15}}\Big)^{-1} \tag{1.2}$$

For normal (long-period) pulsars, $\tau \sim 10^{3-7}\,\mathrm{yr}$, and $\mathrm{B} \sim 10^{11-13}\,\mathrm{G}$. For millisecond pulsars, $\tau \sim 10^{8-10}\,\mathrm{yr}$, and $\mathrm{B} \sim 10^{8-9}\,\mathrm{G}$.

1.2.1 Millisecond pulsars

Millisecond pulsars (MSPs) have a completely different evolutionary history compared to those of long-period pulsars. As is well known, most stars are in binary systems. If the pulsar is born from a supernova explosion of the initially massive star, depending on the physical conditions at the time of explosion, it may receive a large kick velocity, e.g., if the lost mass is more than half the virial mass. But if not, the pulsar may be born in a binary system, with a main-sequence stellar companion (which is the secondary star). The companion star then evolves and becomes a red giant. If the expansion of red giant reaches the Roche lobe of the neutron star, the matter gets transferred to the neutron star through the Roche-lobe overflow. In this process, the in-falling plasma transfers the angular momentum to the neutron star, and the pulsar is spun up but in this process, as result of some complex physical mechanisms the magnetic field strength of the neutron star can be significantly reduced (Srinivasan et al., 1990). The binary generally remain in the accretion phase for a long time until the companion sheds off all its material and completely vanishes, or becomes a white dwarf (WD).

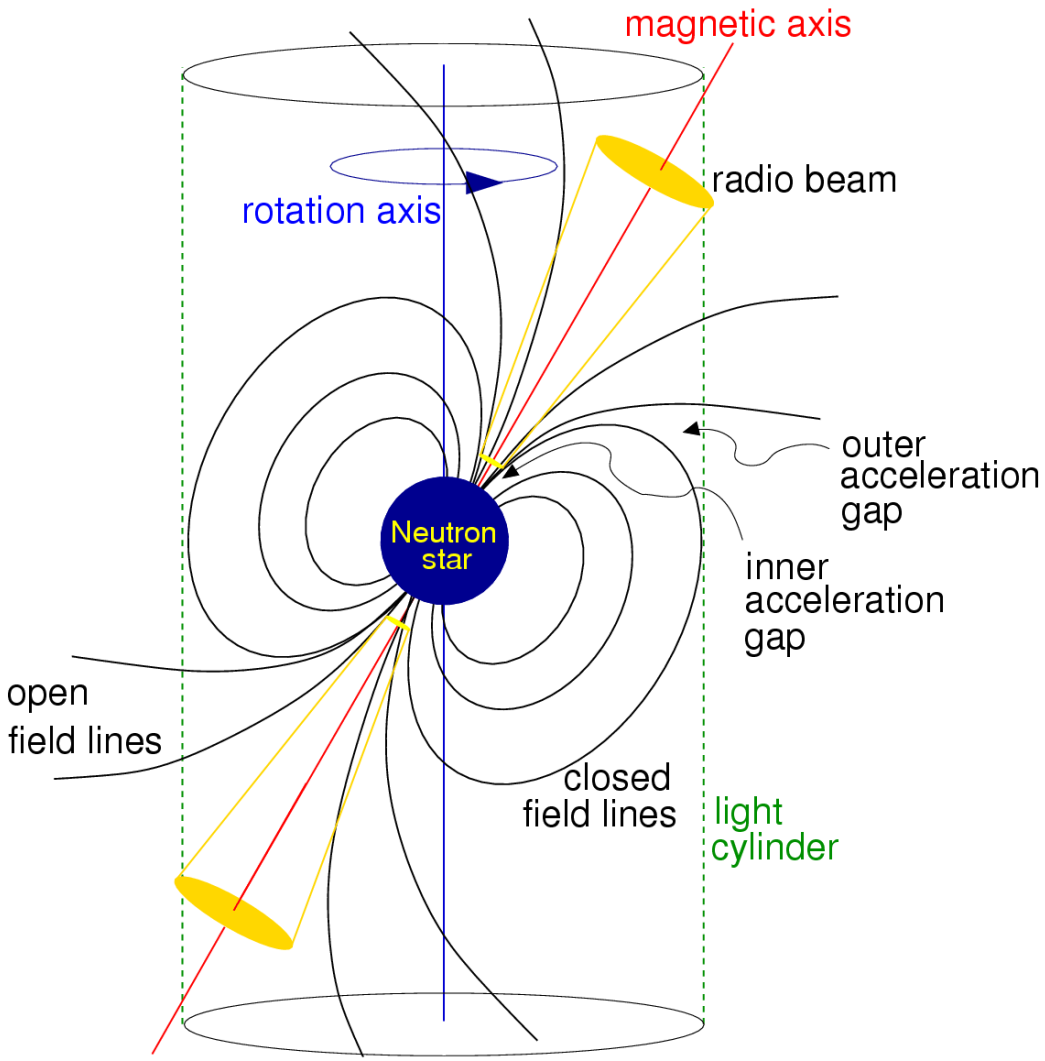

Figure 1.1: A schematic diagram of the emission geometry of a pulsar (Lorimer & Kramer 2005) showing a misalignment between the magnetic and spin axis, which is causing the pulsar radiation to sweep across the sky, producing the 'lighthouse' effect. The boundary within which the magnetospheric plasma is rotating at the speed of light is known as 'light cylinder'. The field lines beyond this radius are marked as open field lines.

These reborn pulsars are known as recycled pulsars. They have pulse periods of the order of a few milliseconds and have masses in the $1.2 \lesssim M_p \lesssim 2M_\odot$ range. Almost 80% of MSPs are found in binary systems as a result of their evolutionary

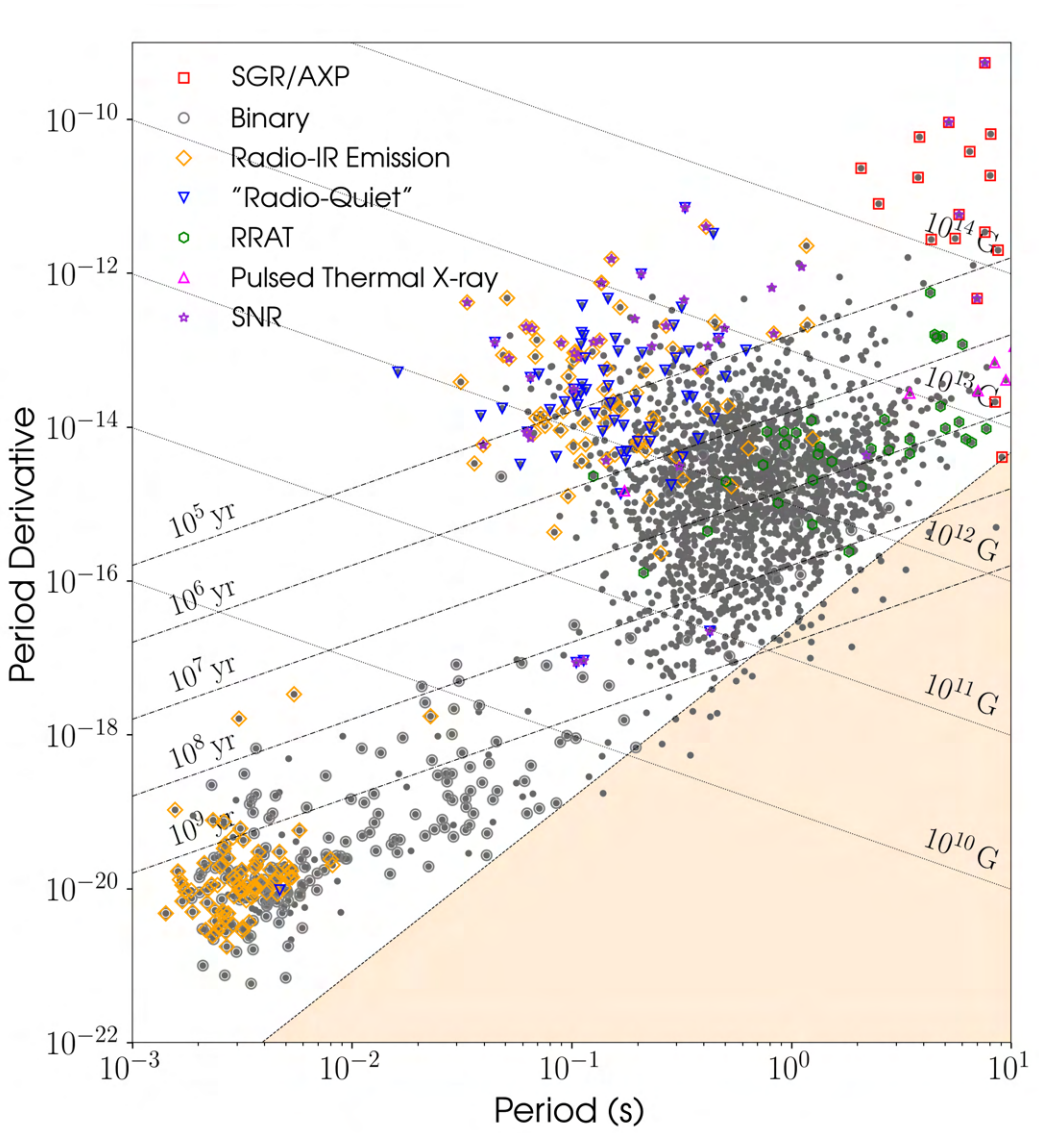

Figure 1.2: P-$\dot{P}$ diagram for radio pulsars with available period and period derivative measurements. The dashed lines present characteristic age and constant magnetic field strength. All radio pulsars are shown as grey dots and binary systems are surrounded by circles. Different types of pulsars, including rotating radio transients (RRAT), gamma-ray sources (GRS), anomalous X-ray pulsars (SGR/AXP) and associations with supernova remnants (SNR), are also represented symbolically as noted in the legend. The shaded region towards the bottom right represents a predicted 'death-line' beyond which neutron star pair production is thought to stop hence terminating the radio emission. Data retrieved from ATNF pulsar catalog (Manchester et al., 2005).

paths, with the majority of them having a WD companion star. In 1982, the first millisecond pulsar B1937+21, was discovered which has a spin frequency of 642 Hz (Backer et al., 1982). There are currently about more than 300 MSPs that are known. The fastest known spinning MSP is PSR J1748 − 2446ad which is in the globular cluster Terzan 5 and has a pulse period of $\sim$ 1.39 ms (Hessels et al., 2006). MSPs generally shows a remarkable stability in their spin periods and therefore can be used as accurate clocks of the universe (Hobbs et al., 2012). They are powerful tools to investigate a variety of astrophysics; e.g. probing the nuclear equation of state, and testing the theories of gravity.

1.3 Observable properties of pulsar signals

Radio pulsar emission has a number of notable characteristics that are very common across the whole pulsar population. Here we give a brief overview of these properties.

1.3.1 Pulse profiles and beam structure

Pulsars are generally weak radio sources. Their measured flux densities vary between $\sim$ 5 μJy and $\sim$ 1 Jy at 1400 MHz. Coherent addition of many hundred (or sometimes thousands) of pulses is required in order to produce a detectable "integrated profile". The properties of individual pulses change drastically from pulse to pulse. However, the integrated pulse profile, one of the defining characteristics of pulsars, sometimes referred to as "fingerprint" of a pulsar, is very stable over long time scales (at a given observing frequency). Figure 1.3 presents the integrated pulse profiles of a sample of pulsars from observations made with the Murchison Widefield Array (MWA). Some pulsars have relatively simple pulse profiles (e.g., PSR J0034−0721), while others have complex multi-component profile shapes (e.g., PSR J0437−4715, which is a MSP). The high diversity in pulse profiles is not fully understood, though is generally attributed to the structure

and size of emission beam, and the orientation of the beam centre relative to our line of sight. Several models of pulsar beam structure have been proposed in order to explain the observed diversity; e.g., the nested cone model (Mitra & Rankin, 2002; Gil & Krawczyk, 1997; Qiao et al., 2002), patchy emission; (e.g., Lyne & Manchester, 1988), and other empirical models (e.g., Karastergiou & Johnston, 2007).

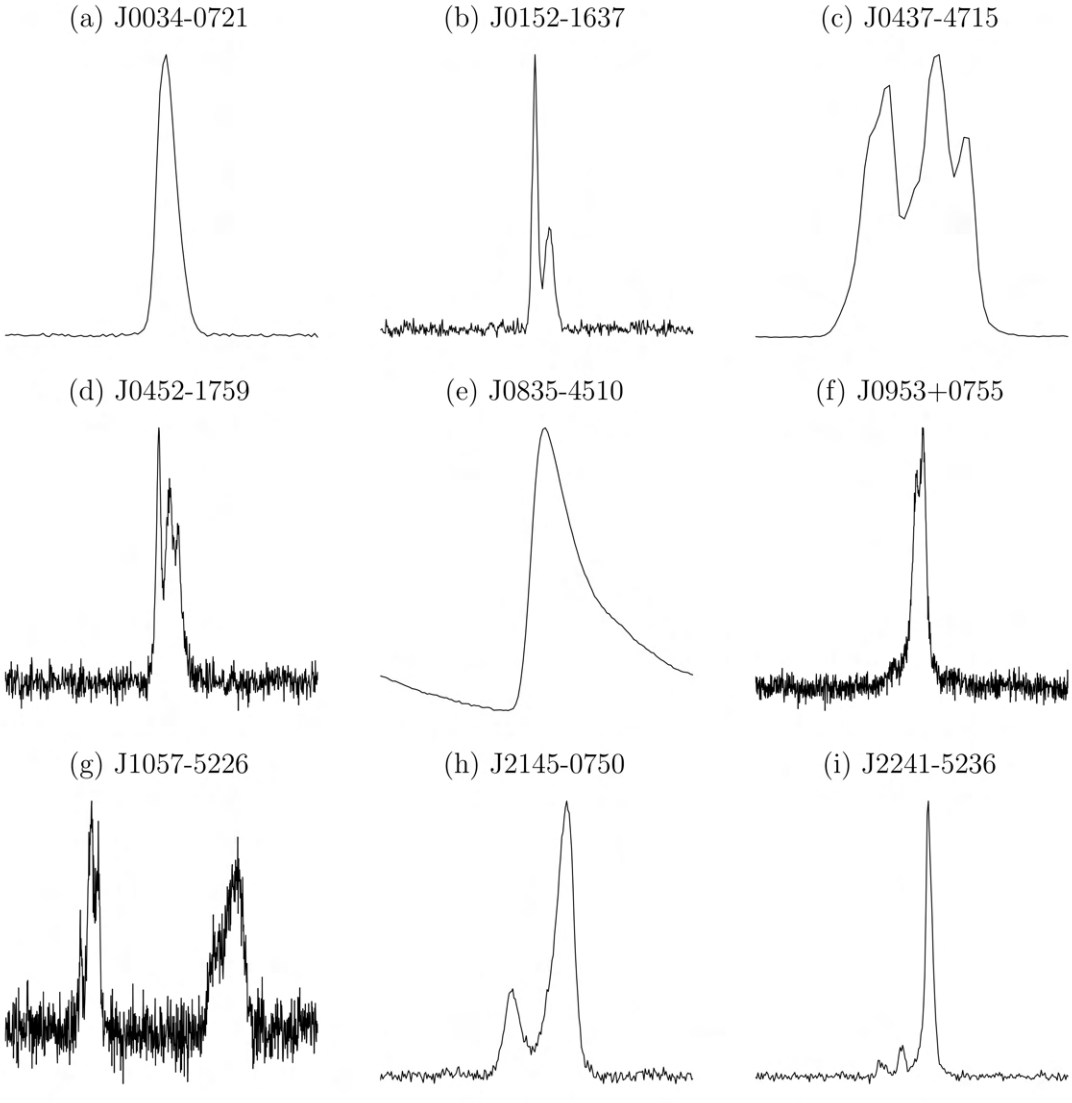

Figure 1.3: Integrated pulse profiles for a sample of pulsars observed with the MWA at a range of frequencies from 118 to 220 MHz.

1.3.2 Profile evolution with frequency

Pulsars generally show a significant evolution in their pulse profiles with the observing frequency. This is typically seen as a visible broadening of the pulse profiles or a change in relative separation between components with a progression from high to low observing frequencies. In some cases, more complex changes, e.g., appearance of new components, or even a complete disappearance of some components, is also seen. This is interpreted as a consequence of the emission at higher frequencies being emitted closer to the neutron star surface whereas re-emission at lower frequencies that originates from higher altitudes in pulsar magnetosphere. This can be explained by the well known radius-to-frequency mapping (RFM) model that was developed in the 70s (Cordes, 1978). In this RFM model, the emission frequency is related to local plasma conditions. Different altitudes have different plasma distributions, and different frequency observations sample different open field line regions. While the RFM model is generally in agreement with observations of a large number of long-period pulsars, it is not the case with most MSPs (Kramer et al., 1999). The size of the light cylinder ($r_{\rm L} = cP/(2\pi)$, where P is the pulse period and c is the speed of light) is much smaller for MSPs compared to those of long-period pulsars; hence, the emission originates from comparable heights at multiple different frequencies for MSPs. The profile evolution seen in MSPs is generally more complex (Figure 1.4, and 1.5), which makes the modelling of emission beam more challenging for MSPs (Gil & Krawczyk, 1997; Qiao et al., 2002; Bhat et al., 2014). In general, low frequency observations can probe much higher regions in the pulsar magnetosphere and can thus reveal new information relating to the emission mechanism and beam geometry.

1.3.3 Flux Density Spectra

The mean flux densities of pulsars have a strong inverse dependence on the observing frequency (e.g., Sieber, 1973; Maron et al., 2000; Jankowski et al., 2017).

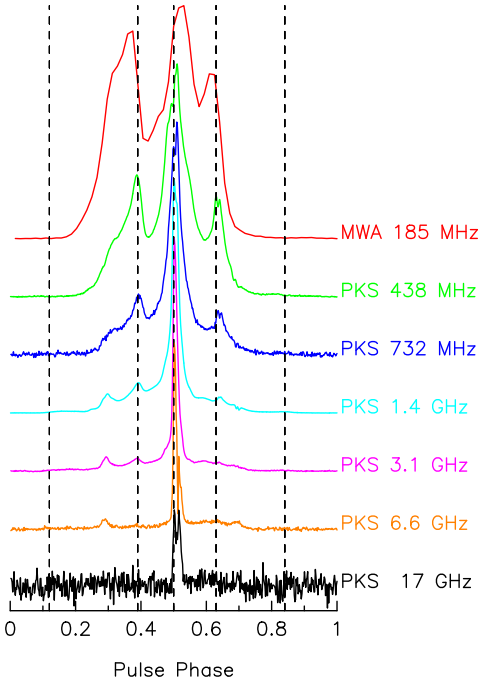

Figure 1.4: Profile evolution of pulsar PSR J0437−4715 from the MWA to Parkes frequency bands illustrating significant spectral evolution of profile components (Bhat et al., 2014).

The flux density spectra of the vast majority of pulsars can be well described by a simple power law $S \propto \nu^{\alpha}$ (Sieber, 1973; Jankowski et al., 2018), at least at frequencies above $\sim 300\,\mathrm{MHz}$, where ν is the observing frequency, and α is the spectral index. The spectral index of majority of the pulsars is less than zero with a mean value of -1.8 ± 0.2 (Maron et al., 2000). More recent work suggests somewhat different values; e.g., -1.4 ± 0.2 (Bates et al., 2013). In general, the pulse energies follow a power-law distribution with a turnover at low frequencies (for most normal pulsars). The mean spectral index of millisecond pulsars was generally reported to be steeper as compared with that of normal pulsars (Toscano et al., 1998). The spectrum of MSPs generally follow a single power law across a wide range of frequencies except in some cases, where spectra deviates from a single power law, with a spectral steepening or flattering seen at higher frequencies (e.g., Dai et al., 2015). However, the nature of spectra at frequencies below $\sim$ 300 MHz remains largely unknown for most MSPs, the knowledge of

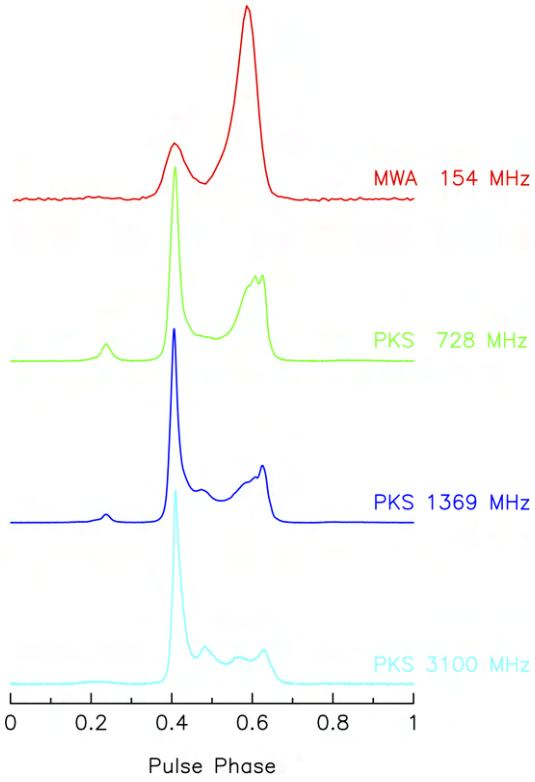

Figure 1.5: Pulse profile evolution of PSR J2145−0750 from the Parkes to the MWA frequency bands illustrating significant spectral evolution of profile components (Bhat et al., 2018).

which can be important for deriving the pulsar luminosity function, as well as for planning optimal frequency coverages of future low-frequency pulsar surveys.

1.4 Effects of the interstellar medium (ISM) on pulsar signals

Pulsars are very compact, spatially coherent sources, and as a result, their signals are subject to a wide range of effects that arise from propagation through the ionised ISM, which is essentially the magnetised plasma of the Milky Way galaxy. Typical electron densities are $n_e \sim 0.015\,\mathrm{cm}^{-3}$ in the mid-plane (Cordes & Lazio, 2002; Yao et al., 2017). Effects such as dispersion, scintillation, scattering and Faraday rotation strongly depend on the electron density distribution

and turbulence of the ISM plasma. The interaction of pulsar signals with the ISM provide powerful tools for studying and characterising the ISM in their line of sights, particularly at low observing frequencies, where they are much stronger and thus can be more readily characterised.

1.4.1 Dispersion

When pulsar signals travel through the ISM, they undergo a time delay due to the dispersive effects of interstellar plasma. This is observed as signals detected at lower frequencies arriving later than the signals at higher frequencies. This was first reported in the pulsar discovery paper by Hewish et al. (1968). This time lag is caused by perturbations in the ISM's free electrons, which oscillate at the 'plasma frequency' ($\nu_{\rm p}$) that depends on the equivalent mass of electrons $m_{\rm e}$ and electron number density $n_{\rm e}$, given as

$$\nu_{\rm p} = \sqrt{\frac{n_{\rm e}e^2}{\pi m_{\rm e}}} \simeq 8.5\,{\rm kHz}\sqrt{\frac{n_{\rm e}}{\rm cm^{-3}}} \tag{1.3}$$

Radio waves at a frequency $\nu > \nu_{\rm p}$ will thus experience a reduction in their group velocity, $v_{\rm g} = \mu c$ (Lorimer & Kramer, 2004), where c is the speed of light and the index of refraction μ is given by

$$\mu = \sqrt{1 - \left(\frac{\nu_{\rm p}}{\nu}\right)^2} \tag{1.4}$$

In comparison to an infinite frequency wave, this effect introduces a frequency-dependent time delay from pulsar to the Earth over a distance d, and can be expressed as

$$t = \left(\int_0^d \frac{dl}{v_{\rm g}}\right) - \frac{d}{c} \tag{1.5}$$

Substituting for $v_{\rm g}$,

$$t = \frac{e^2}{2\pi m_{\rm e} c} \frac{\int_0^d n_{\rm e}(l)dl}{\nu^2} \tag{1.6}$$

The integrated column density of free electrons along the line of sight of the pulsar is called the dispersion measure (DM), and is given by

$$\mathrm{DM} = \int_0^d n_\mathrm{e}(l) dl \tag{1.7}$$

and it is expressed in units of $\mathrm{pc\,cm^{-3}}$. Since the pulsar and the ISM have different relative velocities with respect to the observer, the DM of the pulsar will vary with time and these variations need to be tracked and corrected for in high-precision timing observations such as pulsar timing array experiments. One way to measure this delay is observing at two different frequencies. The time-delay in the arrival time between two pulses with frequencies ν_low and ν_high can be written as,

$$\triangle t = \frac{e^2}{2\pi m_\mathrm{e} c} \times \left(\frac{1}{\nu_\mathrm{low}^2} - \frac{1}{\nu_\mathrm{high}^2} \right) \times \mathrm{DM} \tag{1.8}$$

Substituting the values for e, m_e and c, equation 1.8 can be written as

$$\triangle t \simeq 4.15 \times 10^6 \times (\nu_\mathrm{low}^{-2} - \nu_\mathrm{high}^{-2}) \times \mathrm{DM} \tag{1.9}$$

Therefore, by measuring the pulse arrival times at two different frequencies, the DM can be inferred in the line of sight of the pulsar. The effectiveness of this however depends on the achievable frequency and timing resolutions of the radio telescope. An example of this effect is shown in Figure 1.6. By calculating the DM of a pulsar, one can estimate its distance using an ISM electron density model. Manchester & Taylor (1981) developed the first electron density model, which was later followed by other (Lyne et al., 1985) and TC93 (Taylor & Cordes, 1993) models. For nearly two decades, the NE2001 (Cordes & Lazio, 2002) model has been the standard model. More recently, Yao et al. (2017) developed a model entitled YMW16. The primary distinction is that the YWM16 is just an electron density model whereas NE2001 presents a model for both the electron density and spatial distribution of plasma turbulence. Indeed, discrepancies between the models and the general agreements continue to be actively debated.

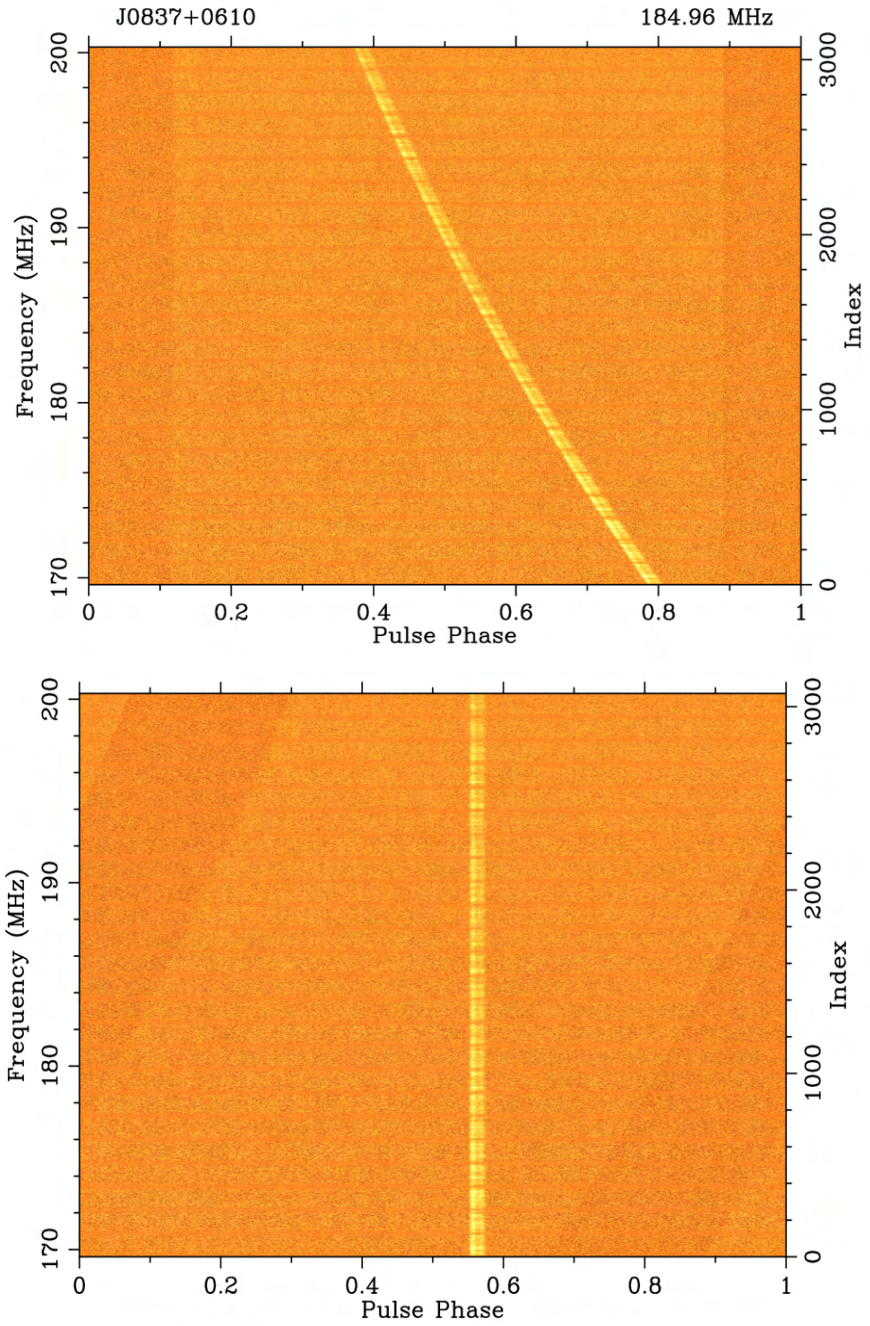

Figure 1.6: The dispersion effect from the interstellar medium on the radio signal from PSR J0837+0610 observed over 30.72 MHz bandwidth, centred at 185 MHz using the Murchison Widefield Array Voltage Capture System. The pulsar signal is plotted as a function of frequency and pulse phase. The dispersion measure of the pulsar is 12.86 pc cm^{-3}. This causes a dispersion delay time of $\sim$525 ms across the 30.72 MHz bandwidth. The bottom panel shows the coherently de-dispersed pulse.

1.4.2 Multi-path propagation: Scattering

The electron density distribution within the Galaxy is far from uniform, and typically characterised in the form of a power spectrum over spatial scales spanning across several orders of magnitude. This inhomogeneity induces multi-path propagation effects. The ISM's instantaneous refractive index changes continuously as a result of these electron density variations. The wavefronts are therefore deviated from their original path, i.e, they are scattered into a range of directions, and thus arriving with different time delays, resulting in an exponential pulse tail for an infinite thin screen model. For a scattering screen located somewhere in

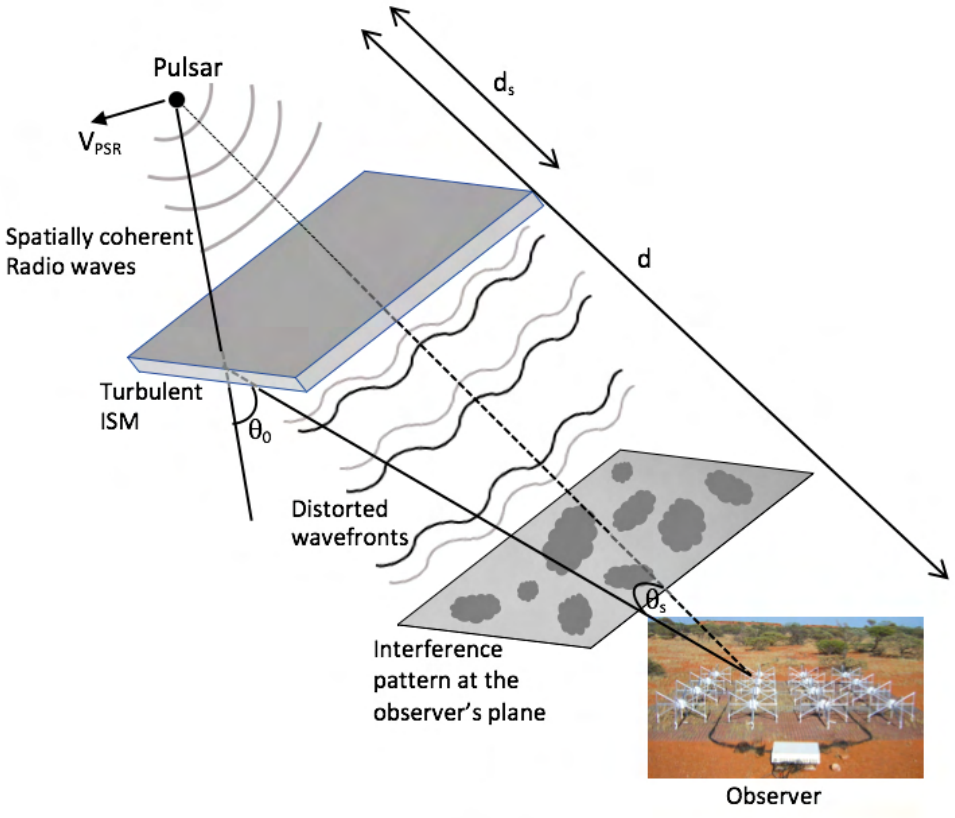

Figure 1.7: Schematic showing the interstellar medium effects on the pulsar emission which results in scattering and scintillation. The ISM is considered as a thin screen somewhere in between the pulsar and observer at distance d_s compared to the total distance between the pulsar and the observer d.

between the pulsar and the Earth, the electromagnetic waves with larger angles

of refraction arrive at later times compared to those that travelled undeflected, and this is observed as a broadening of the pulse shape. As represented in Figure 1.7, if d is the distance between the pulsar and the observer and $d_{\rm s}$ is the distance between the scattering screen and the pulsar, the radio signal received at an angle θ by an observer will have a time delay,

$$\triangle\, t(\theta) = \frac{\theta^2 d_{\rm s}}{c} \tag{1.10}$$

where c is the speed of light. The observed intensity (in the case of an impulse) as a function of time can be written as

$$I(t) \propto e^{-\Delta t/\tau_{\rm s}} \tag{1.11}$$

where $\tau_{\rm s}$ is the scattering timescale (Taylor & Cordes, 1993), and is commonly used to approximate the measured pulse broadening. It is given by

$$\tau_{\rm s} = \frac{\theta_{\rm s}^2 d_{\rm s}}{c} \tag{1.12}$$

where $\theta_{\rm s}$ corresponds to the size of the scattering disk, and it varies as the inverse square of the observing frequency (ν) as ν^{-2}. These scattering effects scale steeply with the observing frequency and distance (d) to the pulsar ($\tau_{\rm s} \propto \nu^{-4}\, d^2$; cf. Bhat et al., 2004). However, the scattering time scale also depends upon the type of the scattering disk. For a thin screen model, where the turbulence cascades from larger to smaller scales, resulting in a Kolmogorov spectrum, we will have $\alpha = 22/5 = 4.4$ and therefore, theoretically one can expect $\tau_{\rm s} \propto \nu^{-4}$ (Scheuer, 1968). Measurements show that the observed scattering times are compatible with a strictly Kolmogorov spectrum only in certain situations, and they tend to deviate significantly from the theoretical predictions, especially for high-DM pulsars, (e.g., Bhat et al., 2004; Lewandowski et al., 2015; Krishnakumar et al., 2017; Geyer et al., 2017; Meyers et al., 2017; Kirsten et al., 2019). Because the ISM

effects are stronger on pulsar radiation at low frequencies, studies of bright pulsars around frequencies below 300 MHz can prove ideal for distinguishing between various ISM theories. Besides physical characteristics of the medium that is giving rise to multipath scattering, this will also help to test different techniques to mitigate, such as those by using deconvolution techniques (Bhat et al., 2004) or by using other techniques like cyclic spectroscopy (Demorest, 2011), where the basic idea is to remove the scattering effect by coherently de-scattering the pulse.

1.4.3 Multi-path propagation: Scintillation

Shortly after pulsars were discovered, interstellar scintillation of pulsar signals was identified in the form of intensity modulation of pulsar signals both in time and frequency (Lyne & Rickett, 1968). It is identical to the well-known optical 'twinkling' of stars produced by the Earth's atmosphere. On the observer's plane, interference between scattered wavefronts traveling different path through the ISM produces a time and frequency dependent pattern as shown in Figure 1.7. These patterns are made up of bright emission "patches", often known as scintles as shown in Figure 1.8, which represent the two-dimensional image of pulse intensity as a function of observation time and frequency, referred to as the dynamic spectrum. The half width at half-maximum of the autocorrelation function of the dynamic spectrum is commonly characterized as the scintillation bandwidth $\triangle\nu_{\rm DISS}$, also referred to as the decorrelation bandwidth. Similarly, the scintillation timescale $\triangle t_{\rm DISS}$, or scintle size in time, can be estimated as the $1/e$ width along the time axis.

The scattering time scale, $\tau_{\rm s}$, and the decorrelation bandwidth, $\triangle\nu_{\rm DISS}$ are related to each other as,

$$2\pi\tau_{\rm s} \triangle \nu_{\rm DISS} = C_1 \tag{1.13}$$

where C_1 is a constant. For various turbulence wavenumber spectrum geometries and models, its value varies slightly. For a Kolmogorov spectrum, $C_1 = 1.16$ (Lambert & Rickett, 1999). As discussed in the previous section, the scattering

effects scale strongly with the observing frequency and distance to the pulsar, and therefore one can expect $\triangle\nu_{\rm DISS}$ to decrease accordingly (e.g., Cordes et al., 1985). For a Kolmogorov spectrum,

$$\triangle\,\nu_{\rm DISS} \propto \nu^{4.4} d^{-2.2} \tag{1.14}$$

and the diffractive time scale is given by

$$\triangle\,t_{\rm DISS} \propto \nu^{1.2} d^{-0.6} \tag{1.15}$$

Therefore, this effect become more prominent at high frequencies. It can be easily measured at frequencies (ν>1 GHz), where fractional bandwidth is not an issue with modern ultra-wideband receivers.

The potential of low frequency observations has already been demonstrated by Archibald et al. (2014); Bhat et al. (2014). Diffractive scintillation may also give rise to more subtle patterns in the dynamic spectrum, which may manifest as distinct arc-like features in the two-dimensional Fourier transform (Stinebring et al., 2001). In some circumstances, discerning them will require high signal-to-noise observations. The curvature can be utilized to determine the precise location of the effective scattering screen along the line-of-sight to the pulsar. Bhat et al. (2016) measured such properties for the MSP, PSR J0437−4715 which has a DM=2.645 pccm^{-3} using their MWA observations at 185 MHz. The predicted screen location turns out to be $\sim 115 \pm 3$ pc from the Earth. Their measured $\triangle\nu_{\rm DISS} = 1.7$ MHz and $\triangle t_{\rm DISS} = 4.5$ minutes.

Scintillation observations can also be used to estimate the space velocities of pulsars. The basic formalism is outlined below. The signals received over a time $\tau_{\rm s}$ have a phase variation of $\delta\Phi \sim 2\pi\nu\tau_{\rm s}$. Diffraction can only occur when the phases of electromagnetic waves do not differ by more than ∼1 radian, much like in optics. Consider a circular region on the scattering screen centered on the source with $\lesssim$1 radian phase deviations. The size of this region is known as the

field coherence scale, and is given by

$$s_0 = 1/(k\theta_s), \tag{1.16}$$

where the wavenumber $k = 2\pi/\lambda$ and θ_s is the size of the scattering disk.

As the line-of-sight to the source cuts through the interference pattern at the observer's plane with velocity V, it samples the spatial intensity distribution, leading to scintillations in time, with a characteristic scintillation timescale $\triangle t_{\rm DISS}$. We can therefore define a "scintillation velocity" from the spatial and temporal diffractive scales as,

$$V_{\rm ISS} = \frac{s_0}{\triangle t_{\rm DISS}} \tag{1.17}$$

By combining the equation 1.17 with the previous equations 1.16, 1.13 and 1.12, we can derive

$$V_{\rm ISS} = A\left(\frac{d_s}{\rm kpc}\right)^{1/2}\left(\frac{\triangle\nu_{\rm DISS}}{\rm MHz}\right)^{1/2}\left(\frac{\nu}{\rm GHz}\right)^{-1}\left(\frac{\triangle t_{\rm DISS}}{\rm s}\right)^{-1} \tag{1.18}$$

where the constant A depends on the relative geometry, location between the pulsar and the scattering screen and the form of the turbulence spectrum. Its value varies; e.g., $A = 3.85\times10^4\,{\rm km\,s^{-1}}$ (Gupta, 1995), and $A = 2.53\times10^4\,{\rm km\,s^{-1}}$ (Cordes & Rickett, 1998).

1.4.3.1 Refractive scintillation

Flux density variations found in pulsars on time scales of $\sim$ days to weeks (or even longer) were long thought to be an intrinsic characteristic of pulsars (Helfand et al., 1977). However, Sieber (1982) recognised that there is a strong correlation between the characteristic time scales of long-term intensity variations and the dispersion measure, and therefore the phenomenon could be attributed to the ISM instead of intrinsic variations in the pulsar emission as was previously thought.

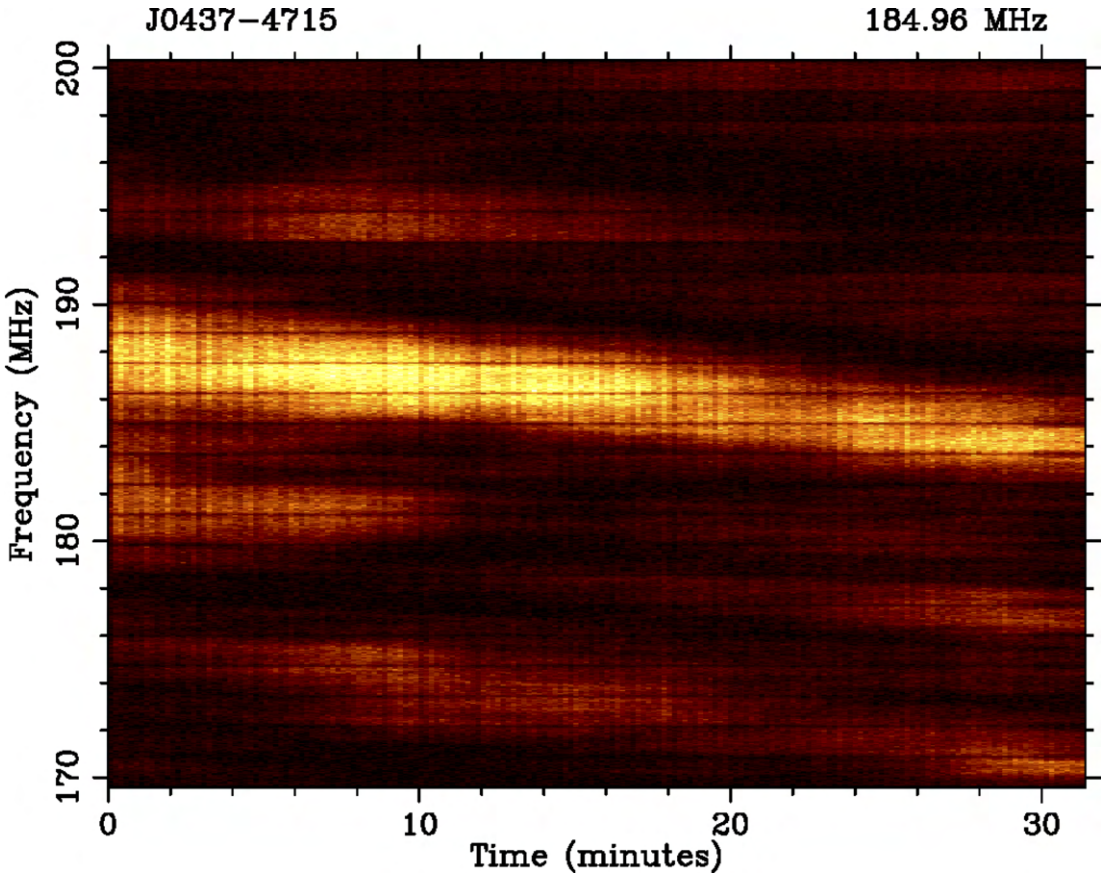

Figure 1.8: Dynamic spectra of PSR J0437−4715 showing patches of enhanced intensity ("scintles") detected by the MWA over 30 MHz bandwidth centred at $\sim$ 185 MHz (Bhat et al., 2018). This deep modulation of pulse intensity (in frequency) is caused by scintillation.

Rickett et al. (1984) proposed refractive interstellar scintillation as the cause of these long-term flux density variations arising from the focusing and defocusing of rays by the scattering screen. The time scales of refractive scintillation $\triangle t_{\rm RISS}$ are substantially longer than those of diffractive scintillation, and the effect increases with distance.

$$\triangle\, t_{\rm RISS} \propto \nu^{-2.2} d^{1.6} \tag{1.19}$$

As this effect also varies strongly with the inverse of observing frequency, the time scale is shorter at higher observing frequencies. For example, for PSR J0332+5434 (DM=26.764 pc cm^{-3}, distance $\sim$1 kpc), $\triangle t_{\rm RISS}$ $\sim$22 days, based on over 5 years of observations that were studied by Stinebring et al. (1996).

1.4.4 Extreme scattering events

Extreme scattering events (ESEs) originate when the scattering is dominated by a compact discrete scatterer present in the line-of-sight. It shows that there are deviations from the Kolmogorov power-law owing to significant over-density and turbulence (Kerr et al., 2018). ESEs were first discovered through the studies of a quasar, where the compact and dense area of plasma was modeled as a diverging lens, refracting the flux to its outer borders (Fiedler et al., 1987). Subsequently, such events were detected in the flux density, arrival times and DM studies of pulsars (Cognard et al., 1993; Maitia et al., 2003; Kerr et al., 2018). The origin and ISM role of ESEs are currently unknown (Bignall et al., 2015), however these are generally thought to be originate from density structures of approximately AU-scale (e.g., Walker, 2007). While the origin of ESEs is often attributed to the presence of high-density discrete clouds, scintillation arcs occurs when the scattering is dominated by a compact local high-density region that is localised somewhere in the line of sight. As they both are caused by compact scatterers, it is possible that these two phenomena are related (e.g. Coles et al., 2015; Kerr et al., 2018).

Such an event has been recently reported by Donner et al. (2019) along the line of sight towards PSR J2219+4754, where they reported the size of the scattering cloud to be approximately 20 AU with a density of a few tens of electrons per cm^3. ESEs have also been reported at multiple different epochs for many pulsars (Kerr et al., 2020). Understanding the occurrence, origin, and characteristics of ESEs is also important in the context of pulsar timing array observations before their influence on timing studies (and potential mitigation) can be fully investigated.

1.4.5 Faraday Rotation

Faraday rotation is an effect that causes rotation of the polarisation angle of the pulsar signals as they propagate through the ISM. The total amount of rotation

the signal experiences as it travels through the ISM is given as:

$$\Delta\Psi = (\lambda_1^2 - \lambda_2^2) \times \mathrm{RM} \tag{1.20}$$

where λ is the observing wavelength and RM is the rotation measure with units of $\mathrm{rad\,m^{-2}}$. The Galactic magnetic field strength (B) and the RM along the line of sight of the pulsar are related as:

$$\mathrm{RM} = \frac{e^3}{2\pi m_\mathrm{e}^2 c^4} \int_0^d n_\mathrm{e}(l) B_{||}(l)\, dl \tag{1.21}$$

Thus, the Galactic magnetic field parallel to the line of sight $B_{||}$ can be estimated by using both RM and DM:

$$B_{||} = 1.23\,\mu\mathrm{G}\Big(\frac{\mathrm{RM}}{\mathrm{rad\,m^{-2}}}\Big)\Big(\frac{\mathrm{DM}}{\mathrm{cm^{-3}pc}}\Big)^{-1} \tag{1.22}$$

This makes pulsars very efficient probes of the ionised component of the ISM and the Galactic magnetic field. Han et al. (2006) modeled the structure of the Galactic magnetic field using 223 RMs towards pulsars using this method. More recent similar work include Noutsos et al. (2008), Van Eck et al. (2011), and Sobey et al. (2019).

1.5 Pulsar timing

Millisecond pulsars make some of the highly stable clocks of the universe. Their rotation period can be measured with a high precision. Although individual pulses show variation in their amplitudes and shapes, the average pulse profile (i.e., the integrated pulse profile), which is the profile obtained by adding several thousands of individual pulses, is typically very stable. They can therefore be used to measure the pulse time of arrival (TOA). These TOAs are essentially the building blocks of pulsar timing. The difference between the observed and predicted arrival times is known as the timing "residual".

Figure 1.9 describes the propagation of the signals from the pulsar to the telescope, as well as the various processing steps that lead to the measurement of TOAs and timing residuals. The timing models are generated from the precise measurements of pulse arrival times, while taking into account the astrometry (position and motion), orbital dynamics (if in binary) of the pulsar, the effects due to the Earth and other Solar System bodies, as well as those caused by the ISM in the line of sight. The pulsar signals are frequency dispersed and scattered as they propagate through the ISM, before reaching the telescope. Once received by the radio telescope, thousands of pulses are averaged over to create a mean pulse profile. The signal-to-noise ratio of the detection depends upon several factors and can be understood in terms of the pulsar radiometer equation (e.g., Lorimer & Kramer, 2004):

$$S/N = \frac{S_{\rm mean} G \sqrt{n_{\rm p} t_{\rm int} \Delta\nu}}{T_{\rm sys}} \sqrt{\frac{P - W}{W}} \tag{1.23}$$

where $S_{\rm mean}$ is the pulsar's mean flux density (mJy) at an observing frequency ν, $G = A_{\rm e}/2k_{\rm B}$ is the telescope's gain (K Jy^{-1}) for an effective collecting area $A_{\rm e}$ and $k_{\rm B}$ is the Boltzmann constant. The quantity $t_{\rm int}$ is the observing integration time (s), $n_{\rm p}$ is the number of polarisations summed, $\Delta\nu$ is the observing bandwidth (MHz) around frequency ν, $T_{\rm sys}$ is the system temperature (in units of K; including sky noise); W and P are the pulse width and pulse period, respectively. In an ideal case, an observatory has a large collecting area (i.e., a large G) and a cooled receiver (i.e., a small $T_{\rm sys}$) with a wide bandwidth (i.e., large $\Delta\nu$).

Pulsars typically have steep flux density spectra, as a result of which their flux densities tend to increase towards lower frequencies; where the flux density S scales with frequency ν as $S \propto \nu^{-1.60\pm0.54}$ (Jankowski et al., 2018). However, at higher frequencies, ISM effects are suppressed and the pulse width tends to be typically narrower, giving a smaller $(P - W)/W$ owing to the emission originating from regions lower in the pulsar's magnetosphere. But building telescopes operating at higher frequencies is expensive as they require smooth and very ac-

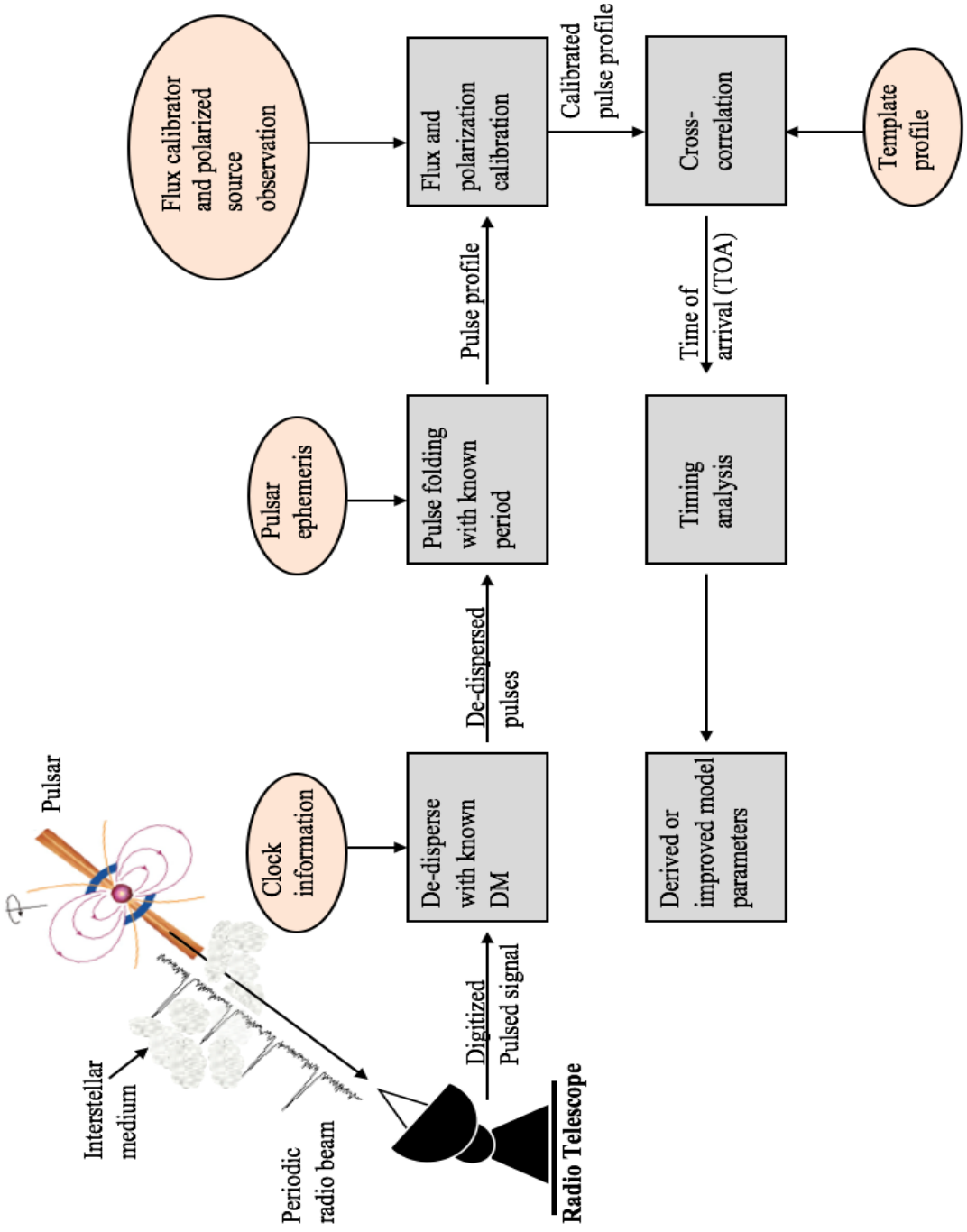

Figure 1.9: A schematic diagram outlining the major steps involved in the observing and data processing for pulsar timing. The various steps are summarized in details in Section 1.5.

curately shaped reflecting surfaces, whereas the ISM introduces significant pulse broadening at lower frequencies (see Section 1.4 for details). As a result of these, pulsar timing is typically performed at frequencies in the range of ~ 300 MHz to ~ 4 GHz.

The frequency-dispersed and scattered pulses, once received by the telescope's receiver (typically mounted at the focus, for single-dish telescopes), are in the form of a time series of voltages. This time series is first digitized and time-tagged by a local station clock, which provides the reference time for all electronics in the signal path. A hydrogen MASER or a Rubidium clock is typically used and synchronized to the Global Positioning System (GPS) time standard. The digitized time series is then de-dispersed to account for the frequency-dependent time delays due to the propagation of the pulsar signals through the ISM. This de-dispersed pulse train is then 'folded' (i.e., data samples with the same phase are averaged) at the expected pulse period using a 'timing model' (i.e., pulsar ephemeris). This results in a high S/N pulse profile, which is typically stable with time.

The process of digitizing, de-dispersing and folding is performed by the 'back-end' which usually provides folded archives or data written out in the `PSRFITS` standard format, which are readable by software packages such as PSRCHIVE (Hotan et al., 2004; van Straten et al., 2012). These archives can be typically thought of as a data cube of time-tagged, coherently de-dispersed, multi-channel folded profiles. Depending on the sophistication of the telescope and systems, they can be usually flux and polarization calibrated. Typically, for single-dish telescopes such as Parkes, the flux calibration solutions are obtained from observations of a quasar or a radio galaxy (e.g., HYDRA), while polarization calibration involves, conceptually, the inversion of the instrumental polarimetric response. This response can be determined by modelling the variations of the Stokes parameters as a function of the parallactic angle (van Straten, 2004; van Straten et al., 2012).

The pulse profile is then cross-correlated with a template profile to find the pulse TOA. The template profile is often an analytical model that is fitted to a particularly high signal-to-noise ratio profile that is formed by stacking together profiles obtained from many individual observations. The estimation of the TOAs can be performed from either the total intensity (Stokes I) data or from the full polarization data. A detailed timing model provides a prediction for the TOAs, and a regression analysis can be used to update parameters of the timing model and results in the form of timing residuals.

The measured TOAs need to be transferred to an inertial reference frame, such as the solar system barycenter (i.e., the center of mass of the solar system). This transformation takes the topocentric arrival times ($t_{\rm topo}$) and applies corrections for effects such as the light travel time, frequency-dispersion and relativistic effects, to obtain the barycentric-arrival-times ($t_{\rm SSB}$). This time transformation is defined as,

$$t_{\rm SSB} = t_{\rm topo} + t_{\rm corr} - \Delta D/\nu^2 + \Delta_{\rm R\odot} + \Delta_{\rm S\odot} + \Delta_{\rm E\odot} \tag{1.24}$$

where $\Delta t_{\rm corr}$ includes the clock corrections to the observatory. The co-ordinate transformations convert the locally measured topocentric time to the stationary reference frame of the solar system barycentre. The term $\Delta D/\nu^2$ accounts for correction in terms of dispersion measure; $\Delta_{\rm R\odot}$ is the Römer delay or the classical light travel time from the observatory to the Solar System Barycentre (SSB); $\Delta_{\rm S\odot}$ is the Shapiro delay, which is the relativistic correction to the light-travel time caused by the curvature of spacetime by massive bodies in the Solar System; and $\Delta_{\rm E\odot}$ is the Einstein delay that includes relativistic corrections for time dilation and gravitational redshift. The barycentric TOAs are then subtracted from the arrival times as predicted by a timing model of the pulsar. The differences between the predictions and the observations, called the 'timing residuals' are the fundamental quantities of pulsar timing.

All unmodelled physics is contained in these timing residuals, and it is the

analysis of these residuals that allow measurements of new parameters and extend our understanding of the pulsar system. It is with the precise modelling of these timing residuals that we aim to find evidence for the low-frequency stochastic gravitational wave background signals (Downs & Reichley, 1983). The timing model for a binary pulsar will require additional terms for the Römer, Einstein, and Shapiro delays to reference the emission to the barycentre of the pulsar's orbit. These pulsar binary corrections are computed using parameters within the pulsar ephemeris, which is determined by modelling the TOAs but, not known a priori (see Section 1.5.1).

1.5.1 Pulsar ephemeris

A pulsar ephemeris encapsulates the timing model of a pulsar. It contains parameters that describe the effect of the ISM along the line-of-sight (DM and RM measurements for example), as well as the motion of the pulsar relative to the SSB. It also contains a set of fundamental parameters that are measured upon the discovery of the pulsar, such as pulsar's period (P), its position in right ascension (α) and declination (δ) and its DM. Pulsar timing observations spanning over $\sim$1-2 year can provide an estimate of the period derivative ($\dot{P}$). These five parameters constitute a simple timing model. An erroneous measurement of P causes the predicted arrival times to become incrementally wrong with time resulting in a linear trend in the timing residuals. An error in the measurement of $\dot{P}$ causes a quadratic trend in the timing residuals. An incorrect position introduces a sine wave with a period of a year and similarly the pulsar's proper motion in α and δ also manifests as a sine wave, but with an amplitude that increases linearly with time.

1.5.1.1 Binary pulsars

Observations of pulsars in binary orbits will show a periodic variation in the measured pulse arrival times. The timing model therefore needs to be extended

to incorporate the additional motion of the pulsar as it orbits the common centre of mass of the binary system. The full transformation can be formulated as (e.g., Lorimer & Kramer, 2004),

$$t_{\rm SSB} = t_{\rm topo} + t_{\rm corr} - \Delta D/\nu^2 + \Delta_{\rm R\odot} + \Delta_{\rm S\odot} + \Delta_{\rm E\odot} + \Delta_{\rm RB} + \Delta_{\rm SB} + \Delta_{\rm EB} + \Delta_{\rm AB} \quad (1.25)$$

The last four terms in this equation describe an additional Römer delay due to the binary orbit, Shapiro and Einstein delays due to the gravitational field of the companion, and the effects due to changing aberration caused by the orbital motion.

For a non-relativistic binary system, the orbital parameters can be described by using Kepler's laws. In general, the orbital motion in the radial direction (which is most relevant to pulsar timing) of such a system is well modelled using these laws, and using just five parameters; the orbital period $P_{\rm b}$, the orbital eccentricity e, the projected semi-major axis $x = a\sin(i)$ (for semi-major axis a and orbital inclination angle i), the longitude of periastron ω (the angle between the pulsar's ascending passage through the plane of the sky that cuts the centre of mass of the orbit, and its closest approach to this centre of mass at periastron), and the epoch of periastron T_0. A sixth parameter, the longitude of the ascending node Ω, describes the orientation of the orbit in celestial coordinates (typically defined as the position angle East of North, of the ascending node relative to the centre of mass). Together, these six parameters are the "Keplerian parameters", and are shown schematically in Figure 1.10.

1.6 Applications of pulsar timing

Pulsar timing has a variety of astrophysical applications. For example, it can be used to determine the pulsar's spin down parameters (e.g. the spin period and its first derivative), as well as astrometric parameters (e.g., the pulsar's position, parallax, and proper motion). It can also be used to determine the orbital pa-

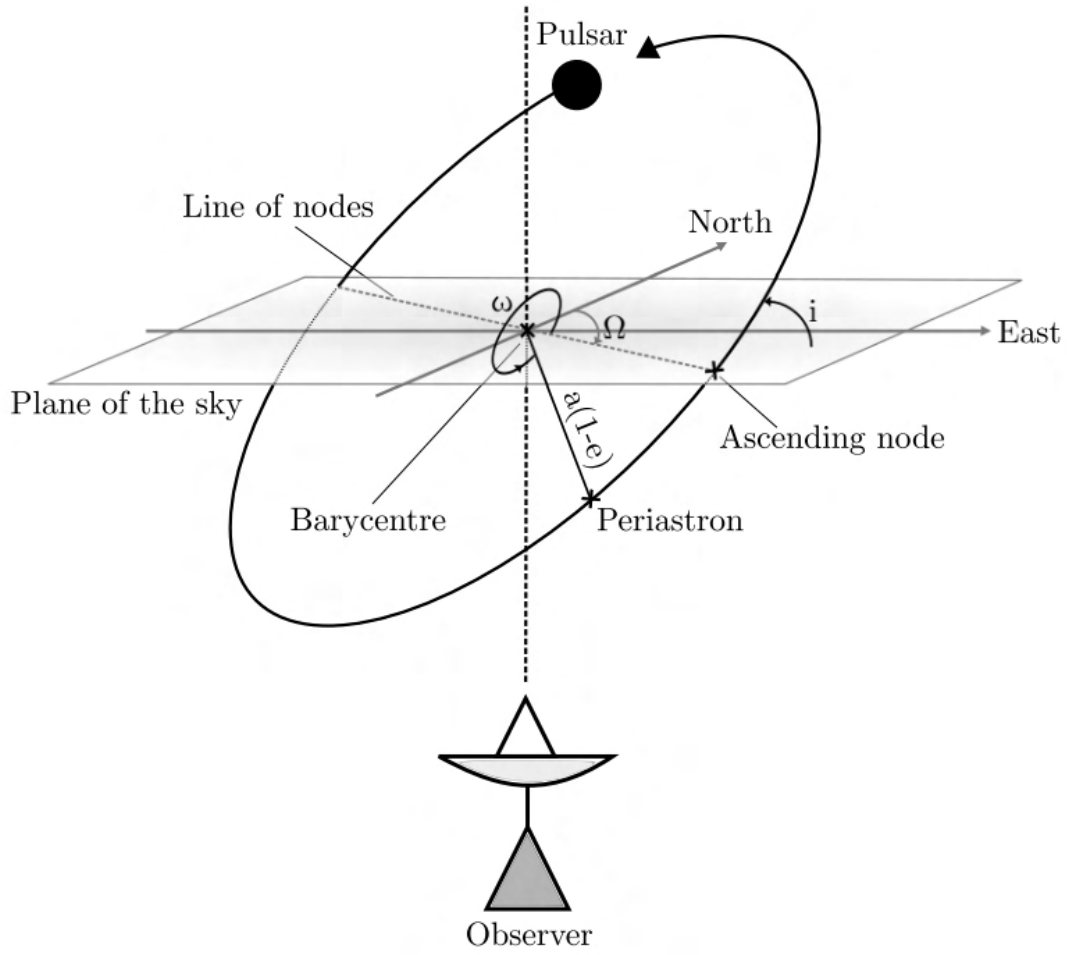

Figure 1.10: Schematic definition of angles in a Keplerian binary orbit. The orbit (black) is tilted from the plane (grey) by the inclination angle i. The intersection of these planes is called the line of nodes (grey dashed line). Periastron occurs at a distance of $a(1-e)$, for semi-major axis a and eccentricity e, and the longitude of periastron ω is defined from the line connecting the barycentre to the ascending node. The orientation of the orbit from the perspective of the observer is given by the longitude of the ascending node Ω in the plane of the sky (defined East of North). This figure was adapted from Figure 8.3 of Lorimer & Kramer (2004).

rameters and the component masses if the pulsar is in a binary system. High profile applications of pulsar timing includes testing general relativistic predictions (Kramer et al., 2006) and the use of pulsars for the detection of low-frequency (nHz) gravitational waves (Manchester, 2017).

The parameters such as pulsar's spin period and spin-down rate can be used

to deduce the magnetic field strength and characteristic age of the pulsar. Along with pulsar positions and velocities, these can enable us to address some broader questions about the neutron star population and their evolution (Kaspi, 2010). Some of the important topics that can be better investigated with improved timing precision include proper motions of pulsars, the mass measurements of neutron stars (e.g., using measurements like the Shapiro delay), a combination of which can then help understand the formation scenarios of MSPs. A large sample of pulsar proper motion measurements suggest that pulsars receive a large kick ($\sim 400\,\mathrm{km\,s^{-1}}$) during their formation (Hobbs et al., 2005). However, the precise physical processes responsible for this kick remains not well understood.

Precision measurements of TOAs of the binary pulsar B1913+16 (also known as the Hulse-Taylor binary; Taylor & Weisberg, 1989), enabled some of the first tests of general relativity (GR) using astrophysical systems such as binary pulsars. This was one of the significant achievements from early days of precision pulsar timing. The study of Keplerian orbital parameters can also lead to precise determination of the masses of neutron stars and their companions. Such studies will help rule out many equations of state for supranuclear matter (e.g., Demorest et al., 2010; Antoniadis et al., 2013; Fonseca et al., 2021; Riley et al., 2021). Discovery of more extreme systems, such as black-hole pulsar systems in future, can provide fundamentally stronger constraints on even alternative theories of gravity.

1.6.1 Search for low-frequency Gravitational waves

According to Einstein's general theory of relativity, accelerating massive bodies can create ripples in the fabric of space and time, which stretch and shrink anything in their path. These space-time ripples are gravitational waves (GWs).

Note – When the pulsar has been timed for many years and represents that how the pulsar TOA are behaving, it is referred to timing precision. Whereas, how precise are the TOAs on a given day represents TOA precision. Most of the data that is presented in this chapter is essentially dealing with smaller number of observations. We used these two terms interchangeably throughout the thesis.

With the direct detection of GWs from binary black-hole and neutron-star merger events (Abbott et al., 2016, 2017), the GW astronomy has became a major science frontier. The detection of low-frequency GWs at nHz frequencies is one of the main goals of pulsar timing array (PTA) experiments. PTA is an experiment that measures the TOAs of radio pulses from a sample of spatially distributed MSPs over many years in an attempt to make a direct detection of these gravitational waves (Hellings & Downs, 1983; Foster & Backer, 1990). These will be complementary to the detections that can be made by ground-based detectors which are sensitive to GWs in the high-frequency range as shown in Figure 1.11.

A PTA can also be thought of as a multi-arm Galactic-scale gravitational-wave detector, which measures the pulsar time of arrival delays induced by spacetime distortions caused by propagating GWs. A direct detection of GW signatures can be from individual super-massive black-hole binaries (SMBHBs) that give rise to continuous gravitational waves (Jenet et al., 2004; Sazhin, 1978); for example, SMBHB OJ287 (Sillanpaa et al., 1988; Valtonen et al., 2016). There are a variety of other GW sources that might provide observable tracers in pulsar data sets, including the superposition of several GWs from SMBHBs (Rajagopal & Romani, 1995; Jaffe & Backer, 2003), cosmic strings (Sanidas et al., 2013), and inflation (Grishchuk, 2005) from all across the sky, forming a stochastic gravitational wave background (GWB) signal. This signal will have approximate characteristic-strain spectrum of the form $h_c = A(f/1\,yr^{-1})^{\alpha}$ where A is the GW spectrum amplitude and α is spectral index.

In order to search for an isotropic stochastic background of low-frequency gravitational waves, it is necessary to observe a set of MSPs widely distributed in the sky and search for correlated timing variations among the sample. The functional form of timing residuals produced by gravitational waves travelling through the Earth depends on the pulsar-Earth-GW angle.

Telescopes around the world are observing large samples of MSPs for PTA experiments, with the ultimate goal of detecting this GW background at nHz

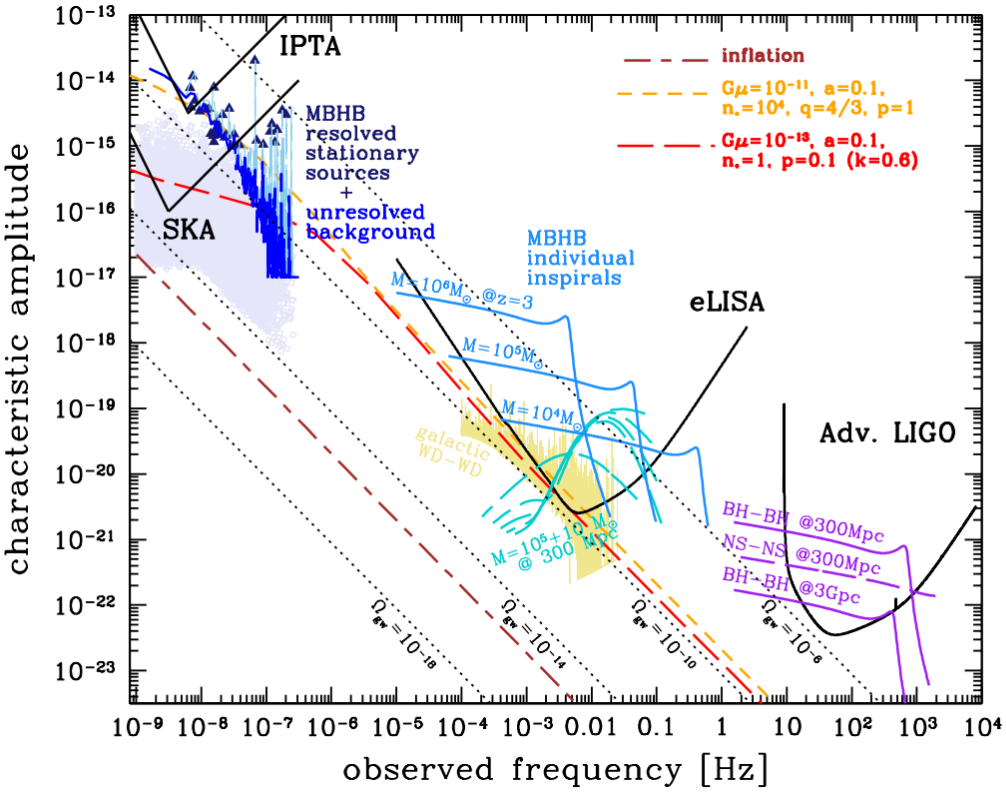

Figure 1.11: The gravitational wave spectrum showing the characteristic amplitude (h_c), as a function of observed frequency showing a nominal sensitivity level of different GW detectors (Janssen et al., 2015).

frequencies. There are three major established PTAs: the Parkes Pulsar Timing Array (PPTA; Manchester et al., 2013; Reardon et al., 2016; Kerr et al., 2020), the North American Nanohertz Observatory for Gravitational Waves (NANOGrav; Demorest et al., 2013; Arzoumanian et al., 2018, 2020), and the European Pulsar Timing Array (EPTA; van Haasteren et al., 2011; Desvignes et al., 2016), as well as some newly emerging groups: Indian PTA (InPTA; Joshi et al., 2018), China PTA (CPTA; Lee, 2016), and the MeerKAT PTA program (MPTA; Bailes et al., 2020). Over the past many years, PTAs have produced increasingly sensitive data sets, and provided increasingly stringent limits on the stochastic GWB (Shannon et al., 2015; Desvignes et al., 2016; Arzoumanian et al., 2018). Very recently, Arzoumanian et al. (2020) found a strong evidence of a stochastic process in the 12.5-year pulsar timing data set collected by the NANOGrav. A summary of

current PTA experiments is given in Table 1.1.

These PTAs together form the International Pulsar Timing Array (IPTA). IPTA has already had two public data releases (Verbiest et al., 2016; Perera et al., 2019), which combine data from all PTAs in order to reduce the time to the detection of GWs. The detection of low-frequency gravitational waves using PTAs will allow astronomers to gain an improved understanding of galaxy evolution and black hole growths (e.g. Taylor et al., 2017; Simon & Burke-Spolaor, 2016) and will aid in the investigation of the polarization states and confining the mass of the graviton (Lee et al., 2008; Chamberlin & Siemens, 2012; Gair et al., 2015; O'Beirne et al., 2019). This will also help to understand the intrinsic symmetry of the gravitational interaction and may provide inputs for quantizing gravity in the strong-field regime.

PTA	$N_{\rm p}$	Obs. Freq.	Telescopes	$N_{\rm pt}$	$h_{\rm c}$ *
PPTA	26	700 MHz - 4.0 GHz	Parkes 64m	3	$< 1.0 \times 10^{-15}$
NANOGrav	47	327 MHz - 2.3 GHz	Arecibo, GBT	5	$< 2.7 \times 10^{-15}$
EPTA	42	350 MHz - 2.64 GHz	Lovell, Efflesberg, Nancay, WSRT	1	$< 3.0 \times 10^{-15}$
InPTA	20	250 MHz - 1460 MHz	uGMRT, ORT	–	–
CPTA	42	600 MHz - 5.0 GHz	FAST, QTT	–	–
MPTA	40	580 MHz - 1650 MHz	MeerKAT	–	–

Table 1.1: Current state of established and newly emerged PTAs, $N_{\rm p}$: no. of pulsars being observed under timing array program, $N_{\rm pt}$: no. of pulsars with timing precision $\lesssim 200$ (ns), $h_{\rm c}$: the limits on the characteristic amplitude due to stochastic GW background

*PPTA; (Shannon et al., 2015), The North American Nanohertz Observatory for Gravitational Waves (NANOGrav; Arzoumanian et al., 2020), the European PTA (EPTA; Desvignes et al., 2016).

1.7 Motivation for this thesis

As is well known, the ISM effects have a strong frequency (ν) dependence (e.g. the dispersion delay $\propto \nu^{-2}$ and the scattering delay $\propto \nu^{-4}$), and consequently they are more prominent at lower observing frequencies. All PTA efforts currently focus at higher frequencies ($>300\,\mathrm{MHz}$) in order to reduce the impact of propagation effects on pulsar signals; particularly, dispersion and scattering. Yet, PTA projects have not been able to achieve the timing precision required to detect ultra-low frequency GWs (Verbiest et al., 2016; Lentati et al., 2016). As described in Table 1.1, the timing precision at the level of $\lesssim 200\,\mathrm{ns}$ has been achieved for only a handful of pulsars (N_{pt}). This may be partly due to our inaccurate modeling of the ISM in their lines of sight. However, the success of PTAs relies on our ability to achieve high timing precision for many more pulsars, and over long time spans. The achievable precision in pulsar timing, to first order, depends on the pulse profile width (W) and the signal-to-noise (S/N) of detection $\sigma_{\mathrm{TOA}} \propto W/(S/N)$ as demonstrated by Lorimer & Kramer (2004).

The interaction between pulsar radiation and free electrons in the interstellar medium (ISM) is considered to be one of the most important causes of TOA uncertainties in PTA data. Propagation through the ISM introduce delays, distortions and modulations in pulsar signals (e.g. Cordes & Shannon, 2010). As a result, all related observables can be expected to vary with time, due to the relative motion between the Earth, pulsar and the ISM. This is a source of noise in the measured TOAs because the pulsar radiation effectively samples different interstellar material over the course of time. The variations depend on the nature of the ISM in the line of sight. Typical DM variation seen in pulsars ranges from $\sim 10^{-3}$ to $\sim 10^{-5}\,\mathrm{pc\,cm^{-3}\,yr^{-1}}$ (e.g., Donner et al., 2020; Alam et al., 2020; Krishnakumar et al., 2021). If these variations are not accounted for, systematic errors of the order of 100s of nano seconds to a few tens of microseconds can arise at typical timing frequency of 1400 MHz in the timing data. Such unaccounted systematics have the potential to degrade the quality of PTA data to detect GWs.

Variations in DM can also arise due to other factors. For example, if the pulsar resides in a supernova remnant (e.g., the Vela and Crab pulsars; Hamilton et al., 1985; Lyne et al., 1988), the remnant material may substantially contribute to the observed DM. Solar wind can be another source of contribution (Madison et al., 2019; Tiburzi et al., 2020; Krishnakumar et al., 2021). And if the pulsar is in a binary system, a change in DM may also be seen during eclipses, or when the companion wind interacts with the pulsar signal (Polzin et al., 2018, 2019; Kudale et al., 2020). However, pulsars with high-density environments like supernovae or those showing high-DM variations caused by the binary eclipses are essentially not included for the PTA experiments.

PTA efforts over the past many years have focused extensively in measuring and correcting for DM variations. You et al. (2007) investigated DM variations in early years of PPTA data, their impact on pulsar timing measurements, and possible ways to correct for them. They carried out a statistically rigorous structure function analysis for each pulsar in their sample. They picked the 'best' wavelength pair from the ones available and calculated the DM for each batch of data. They concluded that their technique of correcting for DM variations, has significantly improved the timing residuals for some of the pulsars in their sample. Following this, Keith et al. (2013) modified the technique by using all the observed wavelengths to estimate DM(t), instead of using only a chosen best pair of wavelengths. An additional motivation to develop this technique was also to disentangle the timing noise that originates from the interstellar DM variations from other sources of noise e.g., spin down noise or noise due to pulsar's rotation irregularities. Keith et al. (2013) applied their algorithm on the PPTA data set and demonstrated that the modifications in the technique has made it unbiased from the wavelength-independent red noise.

Other PTA groups have also developed different techniques in order to measure and correct for DM variations in their data sets. The EPTA collaboration (Lee et al., 2014; Desvignes et al., 2016) developed a model-based algo-

rithm via a maximum likelihood estimator, designed to measure DM variations which can help to perform DM corrections even with non-uniform data sets. The NANOGrav collaboration makes use of the DMX method for DM corrections. It is performed for each pulsar by observing in (at least) two relatively large frequency windows, measuring multi-frequency TOAs in each, and fitting a piecewise constant DM model ("DMX") as part of the timing model. This method makes use of the DMX parameter as part of the TEMPO2 software package. In this procedure, the DM(t) function is treated as a piece-wise constant, and an independent DM value is fitted over a chosen time window, in a simultaneous fit with all other timing model parameters. Even though it is known that timing using the DMX method absorbs some of the other ISM effects in addition to the DM variation (Demorest et al., 2013), this method is widely used by the NANOGrav collaboration (Jones et al., 2017; Arzoumanian et al., 2015; Alam et al., 2020). In all these different techniques, it is very important to measure DM with a high precision to reach the required sensitivity for PTAs.

Much of the work described above has primarily focused on DM variations as a function of time. However, scattering effects can also be very important. For example, for NANOGrav pulsars, the scattering delays are of the order of 1-100 ns at 1500 MHz (Levin et al., 2016). These delays may seem smaller than the required timing precision, and are not measurable for most of the PTA frequencies as these delays are typically smaller than the highest time resolution acquired in pulsar observations of the PTAs which is of the order of a few microseconds. But over the course of several years these delays could potentially add noise to the timing data set (Lentati et al., 2017; Main et al., 2020). Interference between the scattered wavefronts give rise to the intensity modulations in time and frequency. Furthermore, depending on the paths they traverse, the radiation may also arrive over a range of delays, leading to a scatter-broadened pulse shape. This is again a strongly frequency-dependent effect. The width of the broadened pulse (τ_s) varies as ν^{-4} (e.g., Bhat et al., 2004). The same may be manifested as width in

frequency in scintillation pattern, since the observable scintillation bandwidth is inversely related to the pulse broadening time (see equation 1.13).

The angular distribution of the scattered wavefront, which we call the scattering angle, or the size of the scattering disk (θ_s), varies as the inverse square of the observing frequency, ν^{-2}. A consequence of this is the frequency dependence of the measured dispersion measure, especially when the observations are made over large bandwidths. This is because at the low frequencies the radiation traverses a larger volume, and therefore encounters a slightly different ISM. The theoretical treatment of this frequency-dependent ("chromatic") dispersion measure has been provided in great detail by Cordes et al. (2016). Figure 1.12 represents a cartoon from their work; a thin screen model, where the scattering is modeled in terms of a thin screen placed somewhere between the pulsar and the observer. A more realistic scenario is shown on the right hand side of the figure. The fluctuations in the ISM electron density are sufficient to produce a frequency dependence of DM, to the extent it may be important for precision timing. For example, $\delta\mathrm{DM} \sim 4 \times 10^{-5}\,\mathrm{pc\,cm^{-3}}$ for a pulsar at a distance of $\sim$1 kpc and DM of $\lesssim 30\,\mathrm{pc\,cm^{-3}}$ across an octave band around a frequency of 1.5 GHz, can induce TOA variations of few hundreds of nanoseconds. TOA variations can be of the order of few micro seconds for high DM pulsars and over wider observing bandwidths (Cordes et al., 2016).

To date, there has been only a limited observational work to investigate this effect. Donner et al. (2019) made an attempt to measure this towards PSR J2219+4754 using their high-cadence, low-frequency observations over a 3.5 year time span using three German stations of the International LOw-Frequency ARray (LOFAR) Telescope. They interpreted their observations as frequency-dependent DM and attributed it to the presence of ESEs caused by a dense cloud of size $\sim$20 AU along the line of sight of the pulsar. Their interpretation of results was later revisited by Lam et al. (2020) and they concluded that the DM variations seen in Donner et al. (2019) data were merely due to ISM variations

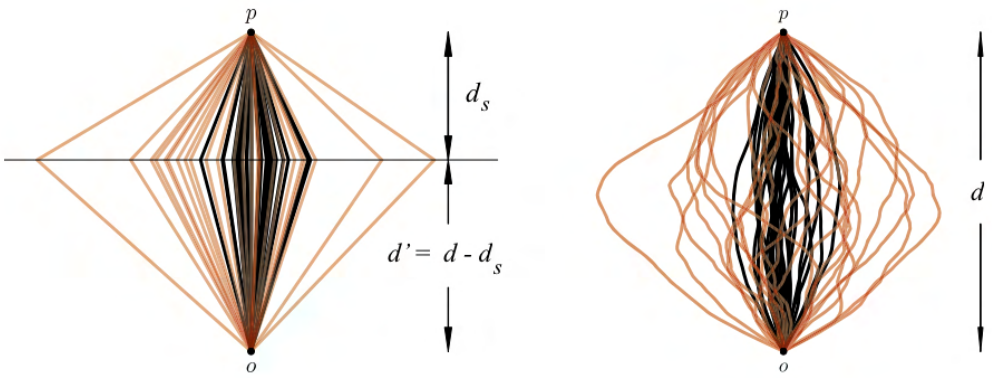

Figure 1.12: A diagrammatic representation of pulsar signal scattering from a thin screen (left) and a filled medium (right) somewhere in between the pulsar (p) and the observer (o) at a distance d_s from the pulsar. The simulated ray paths are presented by coloured lines, where the black lines are ray paths at frequency ν and red ones are at low frequencies ($\nu/2$). Figure adapted from Cordes et al. (2016).

and no ESE event occurred in the pulsar's line of sight.

Currently, there are no other reported studies of frequency-dependent DMs using low-frequency measurements. Donner et al. (2019) data spanned a frequency range from ∼100 to 200 MHz. The pulsar J2219+4754 used for their analysis is a long period pulsar (P=0.538 s), and is known for pulse profile variations with time. These variations could be due to intrinsic properties of the pulsar, or could be due to the ISM as suggested by Michilli et al. (2018). Although Donner et al. (2019) have accounted for the frequency-dependent profile shape variations in their DM analysis, over a period of 3.5 years, temporal pulse profile variations might bias their TOA estimates and thus DM analysis. In order to make more reliable detections, such analysis needs to be performed using MSPs, preferably over a wider range of frequencies. Investigations along these lines can be more instructive to understand the detailed nature of frequency-dependent DM.

Profile evolution with frequency is yet another important consideration while observing pulsars over a wide range in frequency. If not adequately modeled, this can result in inaccuracies in timing analysis, and may lead to incorrect estimation of arrival times, and hence a degradation in the detection sensitivity of PTAs

(e.g., Ahuja et al., 2007). One way to deal with this is to generate frequency-dependent templates for timing analysis. Modeling this has been a subject of active investigation in recent years. The only 2D-timing software package that is publicly available is "pulse portraiture" (Pennucci, 2019). This method make use of frequency-dependent templates that are composed of the smoothed mean profile, the smoothed basis eigenprofiles, and a function to describe the profile evolution curve in that basis. The TOAs are then measured simultaneously with an estimate of the instantaneous DM. Other efforts toward wide-band timing includes Liu et al. (2014), by using the Discrete Fourier Transform method on the channelised data. This method can mitigate the influence of ISM effects, such as diffractive scintillation, profile evolution with frequency, and DM variations, when measuring TOAs from broadband timing data. More recently, a 2D-timing software named "PTIME" has been developed by the members of the PPTA group. It is a software package that can be used to generate unbiased TOAs for each observation to account for the effects of interstellar scintillation, the pulse profile evolution with frequency, and DM variations. This software generates a template profile for every single sub-band across a large bandwidth. However, there have been limited efforts in testing the applicability of these software techniques on actual pulsar observations. The applicability of these various techniques over a wide range of frequencies to examine the improvements in DM measurements is another important investigation to progress towards PTA goals.

1.8 Thesis structure

The remainder of the thesis is organised as follows:

Chapter 2 describes the technical details of the three telescopes used for this thesis: the MWA telescope, the upgraded GMRT telescope, and the 64 m Parkes (Murriyang) radio telescope, as well as the descriptions of the backend systems used. This chapter also includes pulsar data analysis software and techniques used for the work presented in the thesis.

Chapter 3 presents high time resolution studies of the millisecond pulsar J2241−5236 at frequencies below 300 MHz. Parts of this work is already published (Kaur et al., 2019). The chapter also includes some additional work such as the low-frequency polarimetry and long-term DM variability.

Chapter 4 presents observations and analysis of data from contemporaneous observations made with the MWA, uGMRT and Parkes telescopes, to investigate frequency-dependent dispersion measures in the line of sight toward the millisecond pulsar J2241−5236.

Chapter 5 describes an application of two-dimensional timing technique on multi-frequency data of PSR J2145−0750 from observations made using the three telescopes as mentioned above, spanning a frequency range from ∼100 MHz to 4 GHz.

Chapter 6 presents a summary of the main results from this thesis, and discusses potential future directions that are relevant in the context of PTA efforts.

Chapter 2

Instruments, Methods and Data Reduction

2.1 The Murchison Widefield Array (MWA)

The increasing availability of low-frequency radio telescopes and improvements in signal processing techniques over the past decade have given a boost to pulsar studies at low frequencies. Telescopes like the Murchison Widefield Array (MWA; Tingay et al., 2013), the Low Frequency Array (LOFAR; van Haarlem et al., 2013), and the Long Wavelength Array (LWA; Taylor et al., 2012) and the Giant Meterwave Radio Telescope (GMRT; Swarup, 1991; Gupta et al., 2000) are undertaking pulsar observations at low frequencies. Such efforts, when coordinated with similar observations at higher frequencies, offer unique insights into the physics of the pulsar radio emission mechanism, as well as the physics of propagation through the ISM.

The MWA is the only telescope that provides a low frequency window for pulsar astronomy in the Southern hemisphere. Other Southern hemispheric radio telescopes (e.g. Parkes, MeerKAT, and UTMOST) operate at higher radio frequencies ($> 700\,\mathrm{MHz}$). Located at the remote and radio-quiet site of the Murchison Radio Astronomy Observatory (MRO) in Western Australia, the MWA op-

erates in the frequency range of 80-300 MHz.

Radio pulsar astronomy has been dominated by single-dish telescopes over the past few decades. Not only the MWA has the potential to emerge as a prominent facility for low-frequency pulsar astronomy in the southern hemisphere, it can also serve as an excellent pathfinder for transitioning from single dishes to multi-element interferometric arrays in preparation for the Square Kilometre Array (SKA) era. The MWA is also Australia's low-frequency precursor for the SKA, providing promising avenues for wide-ranging pulsar science including the ISM investigations of southern pulsars. Pulsar astronomy is also a headline science theme for the SKA (Janssen et al., 2015; Keane et al., 2015). The MWA consists of 128 tiles, where each tile comprises 16 dual-polarization dipole antennas arranged in the form of a 4×4 antenna grid. These tiles were distributed over a maximum area (baseline) of ~ 3 km for the Phase 1 configuration of the MWA (Tingay et al., 2013).

Since 2018 the MWA has been operating in "Phase 2" (upgraded in year 2016-2017), where 128 more tiles were added to extend the array to a maximum baseline of ~ 6 km (Wayth et al., 2018). As the current correlator (Ord et al., 2015) can only record signals from a maximum of 128 tiles (total of 256 dual polarizations), the array is periodically switched between the "compact" and "extended" configurations in order to cater to a wider range of science applications. The compact configuration includes 128 tiles in the inner "core" whereas the extended array (i.e., longer baseline) utilises predominantly outer tiles. Both array configurations are useful for a wide range of scientific investigations. However, the compact configuration is the preferred choice for pulsar observations due to the less adverse effects of the ionosphere at smaller spatial scales and thus the prospects of better convergence of the calibration solutions.

Unlike single-dish telescopes, multi-element array telescopes such as the MWA come with additional considerations. The MWA does not have any moving parts, therefore it beamforms by an electronic manipulation of the dipole sig-

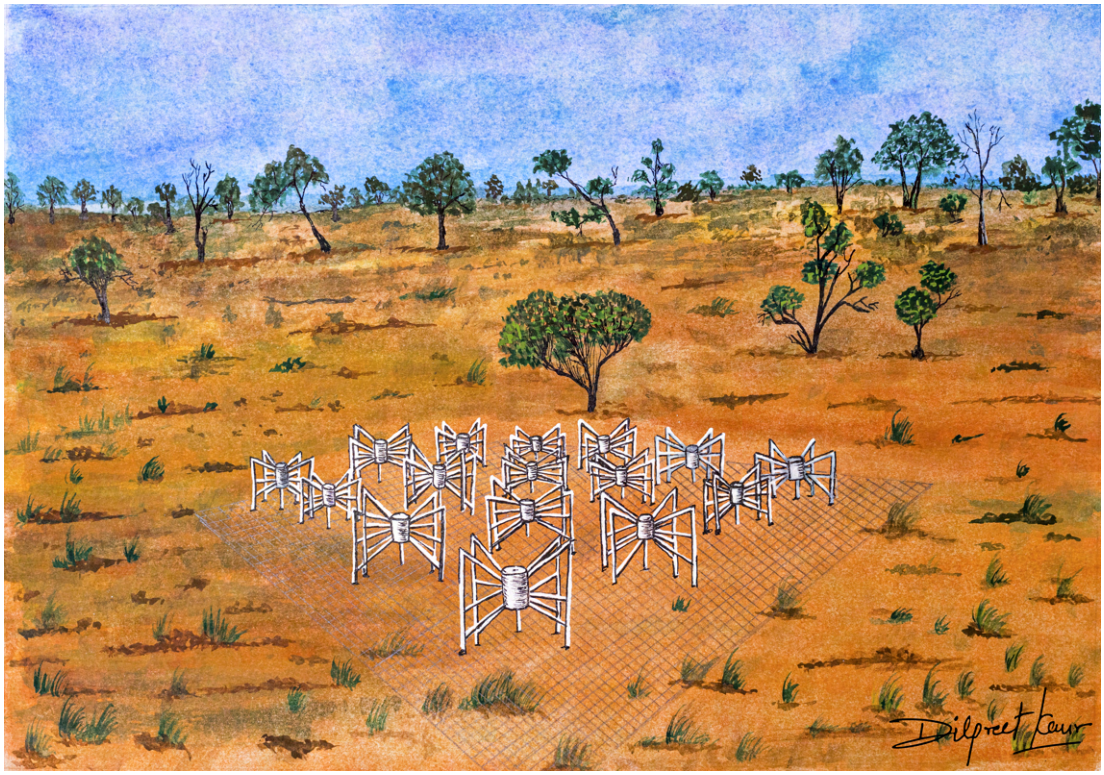

Figure 2.1: A watercolour painting of the MWA tile at the MRO site. A tile consists of 16 cross-dipole antennas, equally spaced by $\sim$1.1 m over the 5m$\times$5m metal mesh. Each tile is connected to an analog beamformer. A total of 256 such tiles are spread over an area of $\sim$6 km (i.e., Phase 2 MWA).

nals that are fed to an analog beamformer. This unit introduces pre-set delays to the signals to enable a coherent addition of the signals. After that the voltage signals are digitized and channelized in the receiver boxes. The channelization to 24$\times$128$\times$10 kHz coarse frequency channels is undertaken by a two-stage polyphase filterbank (PFB). The first PFB stage results in 256$\times$1.28 MHz wide "coarsely" channelised data from which 24 channels can be selected, either in a contiguous 30.72 MHz, or in a distributed channel mode (also known as "picket fence"), and then fed to the second stage ("fine PFB"), which outputs data at 10 kHz/100 μs resolutions. A majority of the data used in this thesis was taken in the picket fence mode.

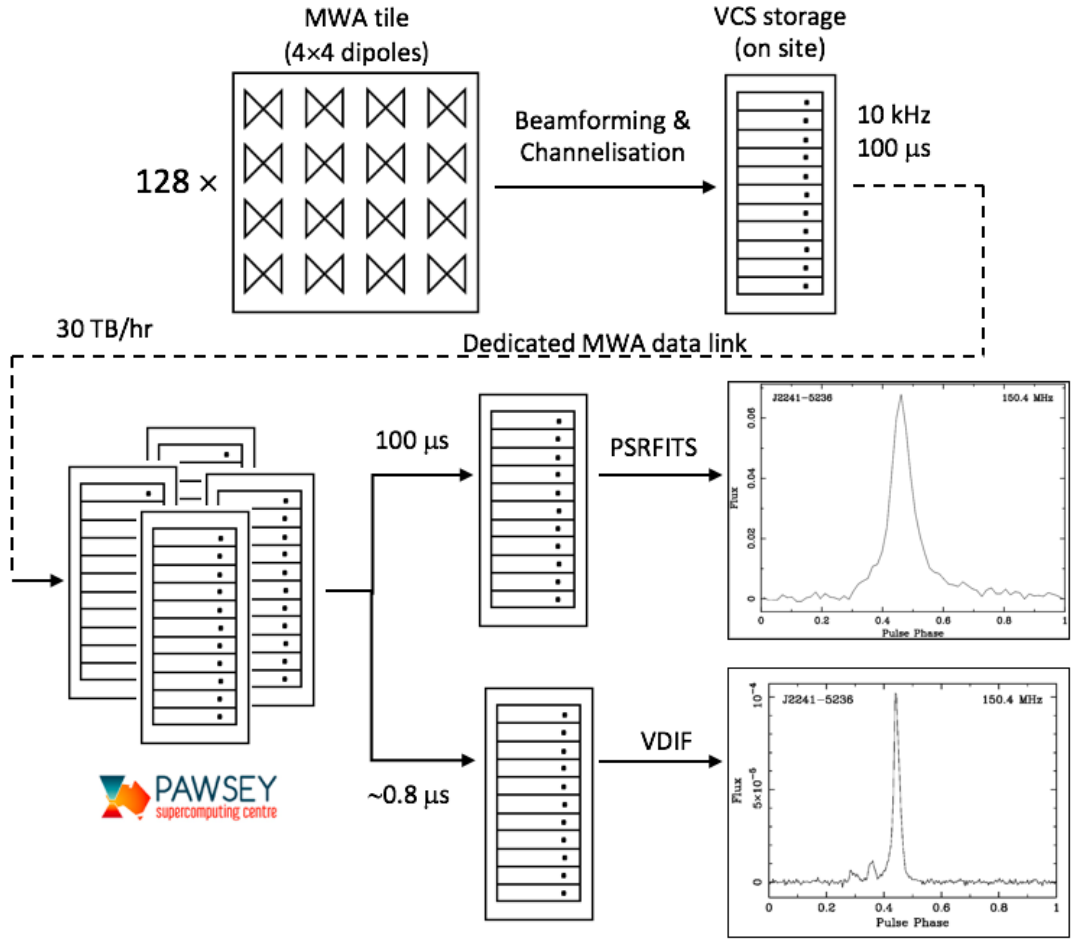

Figure 2.2: The flow diagram showing the MWA's pulsar signal path. Data recorded from 128 MWA tiles are recorded by the on-site VCS system with 10 kHz and 100 μs resolutions. The data are then transferred to the Pawsey supercomputing centre via a dedicated data transfer link, where further processing is performed on the Galaxy supercomputer. Data can be then coherently beamformed either at the original resolutions (in PSRFITS format), or in the VDIF format with a higher time resolution of $\sim 0.8\,\mu$s, which is obtained via re-synthesis back to 1.28 MHz coarse channel data. Latter enables coherent de-dispersion and is particularly important for MSP studies at the low frequencies of the MWA.

2.1.1 Pulsar astronomy with the MWA

The MWA was originally designed as an imaging interferometer, primarily for the detection of epoch of re-ionization (EoR) signals and conducting low-frequency galactic and extra-galactic surveys. Pulsar astronomy was not a key science driver for the MWA, but it was eventually made possible with the implementation of

a "voltage capture system" (VCS; Tremblay et al., 2015) functionality in the signal path. The MWA correlator produces visibilities at 40 kHz/0.5 second resolutions (Ord et al., 2015), whereas pulsar observations with the MWA require much higher time and frequency resolution than that possible with the correlator. However, it is possible to record voltage data from all 128 tiles of the array, at native 10-kHz/100-μs time and frequency resolutions. The VCS functionality captures the raw voltages streaming into the correlator from all the 128 tiles, with a frequency resolution of 10 kHz and a time resolution of 100 μs, over the bandwidth of 30.72 MHz. With these capabilities, a wide variety of pulsar science goals can be undertaken at the low frequencies of the MWA.

However, recording high time resolution data comes with additional challenges and limitations. The VCS records raw voltages and hence a high data rate of $\sim$30 TB per hour. Due to limited data storage facilities on-site, the system can record continuously for a maximum duration of $\sim$1.5 hour (90 minute) per observation. The data must then be transferred to the data archive server at the Pawsey supercomputing facility * before undertaking another observation. Unlike many other traditional radio telescopes, the MWA does not have a dedicated pulsar backend for beamforming and it is not equipped with a noise diode system for flux calibration. Thus, beamforming including the array calibration is performed offline at the Pawsey supercomputing centre.

The recorded voltages are first recombined (i.e., re-ordered) within the archive. Processing VCS observations can be very time consuming. The voltages from 128 tiles can be summed either incoherently, or coherently, or can even be correlated offline, depending on the science applications. More details on the MWA pulsar data analysis is present on the MWA wiki page†

*Pawsey Supercomputing Centre, which is supported by the Western Australian and Australian Governments and is situated in Perth, 800 km from the MRO site.

†https://wiki.mwatelescope.org/display/MP/Documentation/Documentation-CalibrationCombiningMethodCalCombine

2.1.2 Incoherent summation

The voltage data from the VCS can be summed incoherently by summing the power from each tile, to preserve the maximum field of view (FOV) ~ 450 deg^2 at 185 MHz. This produces a low-sensitivity output due to large system noise at low radio frequencies and the low intrinsic gain of the MWA tile (i.e., 16 dipoles). On the other hand, an advantage is that it is relatively quick and computationally inexpensive processing. Mathematically, incoherent summation can be written as

$$I(t,\nu) = \sum_{k=1}^{N} |v_{\rm k}(t,\nu)|^2 \tag{2.1}$$

where N is the number of tiles used in the summation and $v_{\rm k}(t,\nu)$ is the voltage sample from the $k^{\rm th}$ tile at time t, for the channel with a centre frequency ν.

The incoherent sum over both polarizations can be expressed as:

$$I(t,\nu) = \sum_{k=1}^{N} {v_{\rm k}}^{\dagger} v_{\rm k} \equiv \sum_{k=1}^{N} |v_{\rm k}(t,\nu)|^2 = \sum_{k=1}^{N} (|v_{\rm x,k}|^2 + |v_{\rm y,k}|^2) \tag{2.2}$$

where ${v_{\rm k}}^{\dagger}$ is the conjugate transpose of $v_{\rm k}$. This gives $\sqrt{2N}$ improvement in sensitivity over that of a single tile, assuming that two polarizations can be coherently summed (in the case of an unpolarized source). Unfortunately, this kind of data is also very susceptible to the radio frequency interference (RFI), thus requiring a careful analysis of the RFI and the use of RFI mitigation techniques (in time and frequency).

2.1.3 Coherent summation

Coherent summation retains the full theoretical sensitivity of the array. Forming a tied-array beam towards a given look direction involves applying tile-based phase corrections to the recorded complex voltages, so that the signals from each tile can be added coherently. This requires the knowledge of the exact locations of the tiles with respect to the centre of the array, as well as the cable lengths

(cf. Tingay et al., 2013; Wayth et al., 2018). This information is stored in the metadata file generated for each MWA observation.

Before beamforming, the data must first be calibrated, which is performed by the real time system (RTS) specifically designed for the MWA (Mitchell et al., 2008). This involves correlating the measured visibilities for each observation. It can be performed in two different ways: (1) using an in-beam calibration, where the visibilities are generated from the VCS pulsar observation itself, or (2) making a separate, dedicated observation of one or more known, bright calibrator sources, preferably within a few hours before or after the pulsar observation. In either case, a sky model containing the sources in the field is used to generate the phase and amplitude solutions for each MWA tile. Optionally, the RTS selects the brightest source (e.g., 3C444, PicA, HydraA etc.), and uses it to calibrate the tile amplitudes and gains.

A coherent voltage beam can be expressed mathematically as:

$$C(t,\nu) = \sum_{k=1}^{N} v_{\mathrm{k}}(t,\nu) e^{-i\phi_{\mathrm{k}}(t,\nu)} \tag{2.3}$$

where $\phi_{\mathrm{k}}(t,\nu)$ is the phase introduced to point the beam in the desired direction. For retaining both polarizations,

$$C_{\mathrm{k}} = {J_{\mathrm{k}}}^{-1}(\nu) W_{\mathrm{k}}(\tau,\nu) v_{\mathrm{k}} = \begin{bmatrix} C_{x,k} \\ C_{y,k} \end{bmatrix} \tag{2.4}$$

$$C = \sum_{k=1}^{N} C_{\mathrm{k}} = \begin{bmatrix} C_{x,k} \\ C_{y,k} \end{bmatrix} \tag{2.5}$$

where ${J_{\mathrm{k}}}^{-1}(\nu)$ = an appropriate inverse Jones matrix for the relevant frequency coarse channel, which presents the instrumental response for each MWA tile, and $W_{\mathrm{k}}(\tau,\nu)$ = complex weight matrix that is frequency dependent. This is recalculated every second to track the desired target.

The final steps are to remove the autocorrelations (which, for a sufficiently large number of tiles, may contain more correlated noise than signal), and then convert the desired astronomical signals to a voltage beam which is then converted to full Stokes parameters. The autocorrelated noise terms can be expressed as:

$$n_{\mathrm{C}} = \sum_{k=1}^{N} C_{\mathrm{k}} {C_{\mathrm{k}}}^{\dagger} = \begin{bmatrix} n_{xx} & n_{xy} \\ n_{yx} & n_{yy} \end{bmatrix} \tag{2.6}$$

where ${C_{\mathrm{k}}}^{\dagger}$ is the conjugate transpose of C_{k}. The Stokes parameters can be written as

$$I = \frac{1}{N}\Big[(|c_{\mathrm{x}}|^2 - n_{\mathrm{xx}}) + (|c_{\mathrm{y}}|^2 - n_{\mathrm{yy}})\Big],$$

$$Q = \frac{1}{N}\Big[(|c_{\mathrm{x}}|^2 - n_{\mathrm{xx}}) - (|c_{\mathrm{y}}|^2 - n_{\mathrm{yy}})\Big],$$

$$U = 2Re\left[\frac{1}{N}\Big(c_{\mathrm{x}}{c_{\mathrm{y}}}^{*} - n_{\mathrm{xy}}\Big)\right],$$

$$V = -2Im\left[\frac{1}{N}\Big(c_{\mathrm{x}}{c_{\mathrm{y}}}^{*} - n_{\mathrm{xy}}\Big)\right]$$

The final output is then written out in the PSRFITS format for further processing. Further details on coherent beamforming process can be found in Ord et al. (2019).

2.1.3.1 Microsecond time resolution with the MWA

As discussed earlier, the VCS output data has frequency and time resolutions of 10 kHz and 100 μs respectively (Prabu et al., 2015). The first PFB stage, also known as the 'coarse' PFB, results in 1.28 MHz frequency and $\sim$ 0.8 μs time resolutions. In the second stage, known as the 'fine' PFB, each coarse channel is further split into 128 $\times$ 10 kHz channels, but at the cost of decreasing the time resolution to 100 μs. These resolutions are sufficient for studying a vast majority of long-period pulsars but not for resolving temporal structures in short-period millisecond pulsars. However, it is possible to recover the higher time resolution of

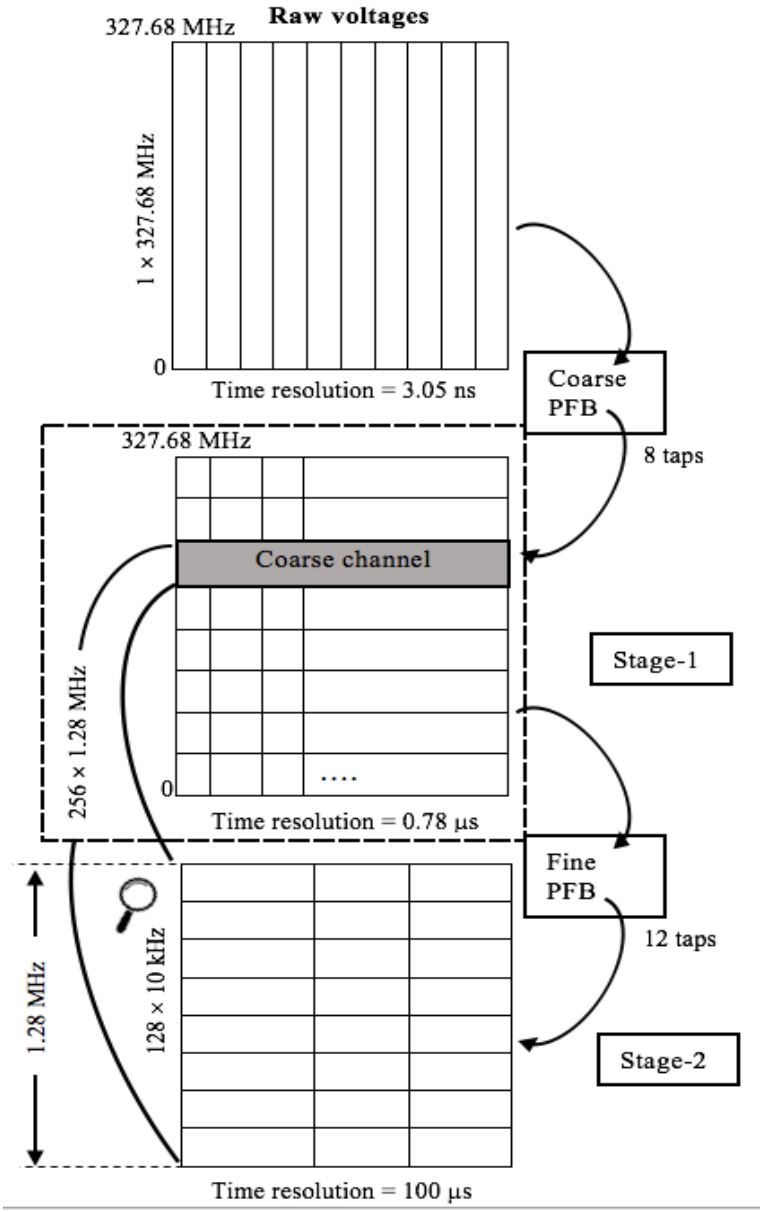

Figure 2.3: Block diagram representing the two stages of PFB in the MWA pulsar signal path.

the coarse PFB, by applying a synthesis filter that inverts (albeit imperfectly) the analysis filter implemented in the fine PFB (McSweeney et al., 2020). Figure 2.3 represents the path followed by raw voltages through different PFB stages. This algorithm enables the 1.28 MHz sample rate to be recovered, corresponding to a $\sim 0.78\,\mu$s time resolution (highlighted by the dashed box in Figure 2.3). The data are then written in the VDIF file format for further processing. Because the VDIF

file format supports complex voltages, the data can be subsequently de-dispersed coherently to eliminate any temporal dispersive smearing. This development thus opens up the possibility of studying MSPs at the MWA's frequencies. All MWA pulsar observations presented in this thesis were processed with this new beamformer.

2.1.3.2 Calibrating problematic data

Creating good calibration solutions for MWA pulsar (VCS) processing is an iterative process. This includes plotting and manually checking the bandpass amplitude and phase calibration solutions for each and every coarse channels (generated by the RTS) and identifying and flagging troublesome tiles and/or channels. The general practice has been to record multiple different calibration observations with a frequency setup that is identical to pulsar observation. Sometimes even after multiple iterations of flagging and cleaning, the calibrations may not necessarily converge to usable solutions. In this case, there are a few different options that can be considered. The first is to try a different calibration observation; second, to try in-beam calibration, where the pulsar (VCS) observation itself can be used to create visibilities and process them for calibration solutions. The RTS corrects for the bulk ionospheric positional shifts and small-scale variations are generally ignored. Sometimes, the ionospheric effects can be quite dramatic and calibration solutions are unobtainable even after trying out both these techniques. In such cases, nothing else can be done, and the pulsar observation is necessarily discarded.

In order to avoid discarding too many observations with no or poor calibration solutions, I have pioneered a new calibration technique in which a full calibration solution was constructed from parts of other calibration observations with similar but non-identical frequency setups (further details are presented in Chapter 4). This includes calibrating some selective nearby calibration observations even if they were taken with different frequency setups to that of the pulsar observa-

tion, but have at least some of the frequency channels common with the pulsar observation. Then calibrate all the selected calibration observations using the RTS. Identify/flag the troublesome tiles or channels and create the solutions. This needs to be carried out for each of the calibration observations. Once all the observations are calibrated, identify the corresponding Direction Independent (DI) Jones matrix representing each of the frequency coarse channel. The frequency of each of the 24 coarse channels (selected by the user) and be readily defined as the channel number multiplied by 1.28 MHz. The corresponding DI Jones matrices are numbered from 1 to 24 for a given set of observation. However, due to some complex settings of the GPU boxes, the numbering scheme flips to a reverse ordering if the frequency channels are above the channel number 128. So this can be a bit tricky and may require additional care. Pulsar observation can then be calibrated, using DI Jones matrices obtained from different calibration observations for all the coarse channels of the pulsar observation. In this manner, the calibration observations within a period of 24-48 hours of pulsar observation can be effectively used. The S/N of the pulsar depends on the stability of the ionosphere for that period of time. While this technique can be more laborious and time-consuming to converge to usable calibration solutions, it offers the prospects of salvaging observations that cannot be otherwise calibrated using standard practices. This procedure of calibration is only performed when it is absolutely warranted. The efficacy of this strategy is demonstrated through a specific observation made on MJD 58680, presented in Chapter 4. Despite all this, there were indeed some observations where the calibration proved difficult as presented in Chapter 3, Table 3.1.

2.1.3.3 Flux density calibration

Calibrating MWA-VCS data for absolute flux densities is non-trivial. A useful methodology was developed by Meyers et al. (2017). This involves a model of the instrument's beam response which is convolved with the Global Sky Model

(de Oliveira-Costa et al., 2008). The MWA beam patterns are simulated using the technique described by Sutinjo et al. (2015) and Sokolowski et al. (2017). The combination of these two is then used to estimate the system gain (G) and antenna temperature ($T_{\rm ant}$). The system temperature is then calculated by using $T_{\rm rec} = 40\,{\rm K}$ and by assuming a radiation efficiency (η) of 1.

$$T_{\rm sys} = T_{\rm ant} + T_{\rm rec}$$

As the MWA tile pattern is direction and frequency dependent, the process is conducted for each sub-band of observations across the MWA band. The system equivalent flux density (SEFD) can be expressed as

$$SEFD = f_{\rm c}\frac{T_{\rm sys}}{G}$$

As with other low-frequency interferometric arrays (e.g., LOFAR, the GMRT), the process of coherent beamforming is not always perfect. Hence, a scaling factor $f_{\rm c}$ is introduced to account for the difference between the expected and real improvements (over the sensitivity of a single tile):

$$f_{\rm c} = \sqrt{N_{\rm coh}}\left(\frac{(S/N)_{\rm coh}}{(S/N)_{\rm incoh}}\right)^{-1}$$

where $N_{\rm coh}$ is the number of tiles used in beamforming; $(S/N)_{\rm coh}$ and $(S/N)_{\rm incoh}$ are S/N of coherent and incoherent summed data. The conversion of arbitrary powers of raw voltage data to flux density units can be now performed by using:

$$S = S/N\left(\frac{f_{\rm c}T_{\rm sys}}{G\sqrt{n\Delta t\Delta\nu}}\right)$$

For the MWA, $n = 2$ (both polarizations used), Δt is the integration time and $\Delta\nu$ is the observing bandwidth. The uncertainty on the measured flux density

can be calculated as:

$$RMS = SEFD\sqrt{n \times \Delta\nu \times \Delta t} \times \sqrt{N_{bin}}$$

where N_{bin} is the number of bins in the on-pulse region.

2.2 The Giant Metrewave Radio Telescope

The Giant Metrewave Radio Telescope is the largest steerable radio telescope array in the world operating at metre wavelengths. Located at ~ 80 km north of Pune, India, it consists of 30 fully-steerable parabolic dishes of 45 m diameter, spread over a 25 km baseline. The entire telescope array forms a "Y-shape" with 14 dishes forming the central array and remaining 16 dishes are spread out to the three arms of Y. Operated by NCRA-TIFR [‡], it is a very versatile instrument for investigating a variety of radio astrophysical problems, ranging from the nearby Solar System to the edge of the observable Universe. Astronomers from all over the world have been using this telescope to produce many exciting new results since its commissioning in 2002. The legacy GMRT operated at five different radio bands from 150 to 1450 MHz with an instantaneous bandwidth of 33.33 MHz. Dual polarization signal from selected antennas can be incoherently or coherently summed (Roy et al., 2010; Gupta et al., 2000).

2.2.1 Upgraded Giant Metrewave Radio Telescope

By the end of year 2017, the GMRT was upgraded to uGMRT. The back-end systems underwent major changes to achieve improvements such as an increase in bandwidth (up to 400 MHz), direct processing of RF signals, a substantial increase in the dynamic range, a near seamless frequency coverage from 50 to 1500 MHz, and significantly improved channel resolution. The digital backend

[‡]The National Centre for Radio Astrophysics- Tata Institute of Fundamental Research

Figure 2.4: The GMRT telescope

part of this uGMRT is named the GMRT Wideband Backend (GWB). A high-level block diagram of the GWB is shown in Figure 2.5.

The upgraded system can provide four different beams with any arbitrary combination of antennas, at a given phase center, and the signals can be combined either in an incoherent or a phased-array mode. This feature can be exploited for simultaneous multi-frequency observations of pulsars. Unlike the legacy GMRT software backend (GSB), which used to perform real-time coherent de-dispersion of data for the entire bandwidth, this is difficult for the GWB due to the large bandwidth. However, coherent de-dispersion can still be performed on smaller sub-bands that make the full bandwidth. For the observations used in this work, we made use of BAND3, which offers 200 MHz of instantaneous bandwidth in the range 300 to 500 MHz, and BAND4, which offers 200 MHz of instantaneous bandwidth in the range 550 to 750 MHz. The 200 MHz bandwidth is processed as 512 sub-bands with 10.24 μs time resolution.

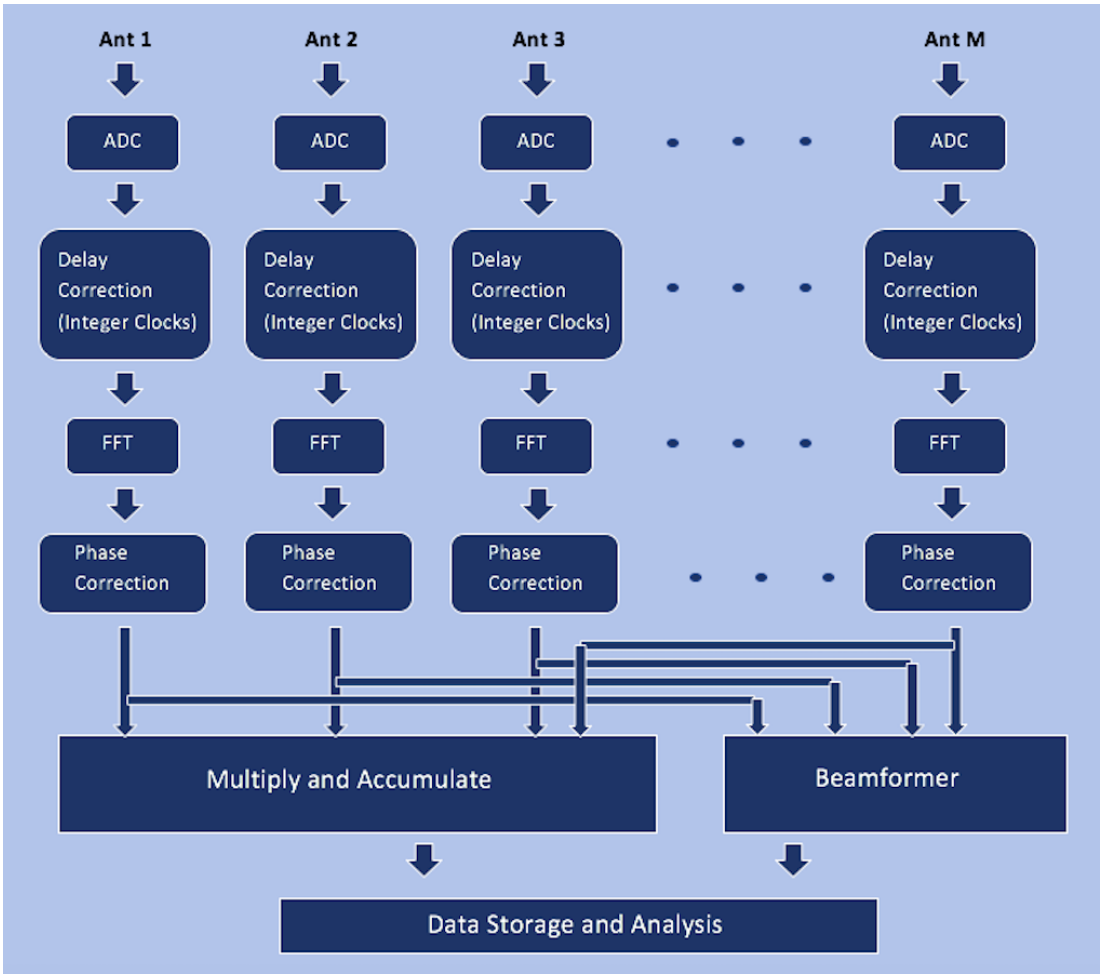

Figure 2.5: The digital backend GWB for the uGMRT. Diagram taken from www.gmrt.ncra.tifr.res.in

The calibration solutions for phasing up the antennas were made during each observation by selecting a nearby compact radio source (e.g., 3C48 or 3C286). Due to variable ionospheric conditions, the calibration solutions remain valid for only a limited time period, which depends on the frequency band being observed, and the number of antennas used for the phased-array (and their baselines). Different targets can easily be observed within a given observing set-up, but the receivers would remain the same. As the GMRT feed is mounted on a rotating turret, the turret takes time and once the receiver is chosen, certain routine procedures involving beam and calibration need to be performed. This entire process takes roughly about an hour.

2.3 The Parkes radio telescope

The Parkes telescope (recently given the indigenous Wiradjuri name *Murriyang*) is located in the central-west region of New South Wales. It is the largest single-dish (64 m), fully-steerable radio telescope in the southern hemisphere, operating since 1961. The legacy Parkes system hosted a large variety of receivers and back-ends, some providing wider fields of view and/or wider observing bandwidths to cater to specific astronomical requirements. Multibeam receivers, such as the 13-beam 20 cm receiver (Staveley-Smith et al., 1996) and the 7-beam "methanol" receiver (Green et al., 2009), have successfully carried out large-scale survey observations. These backend systems provide pulsar observations that allow recording of baseband data which can be coherently dedispersed in real time (for maximum time resolution and complete removal of dispersive effects); or to generate what is commonly called the "search mode" data, which is effectively a channelised filter bank data stream which can be then processed offline. In recent years, the Parkes receiver system has been upgraded to a new ultra-wide-bandwidth low-frequency receiver (UWL; Hobbs et al., 2020). For the work presented in this chapter, we have made use of the UWL receiver. The details of UWL are described in the next section.

2.3.1 The Ultra-wideband Low-frequency receiver

The UWL receiver at the Parkes 64 m telescope is an excellent addition to the wide band radio receivers that have been deployed around the world for pulsar timing (Hobbs et al., 2020). It provides the frequency coverage from 704 to 4032 MHz. The UWL range will form the low frequency part once the next-generation wideband receiver (ultra-wide band high-frequency receiver) is built and commissioned for Parkes, thereby providing a continuous frequency coverage from ∼700 MHz to ∼24 GHz. The UWL receiver can be used to perform all types of pulsar observations as well non-pulsar observations such as spectral line continuum, polarization, and even VLBI. The UWL covers the full ASKAP

Figure 2.6: The Parkes radio telescope (Murriyang).

band; thus, it can also be used for high time resolution, high-quality followups of ASKAP observations. Upgrading to this receiver will help improve the sensitivity for the PPTA and it is proving a very useful instrument for ISM studies and for studying other frequency-dependent phenomena. A general overview of the UWL observing setup and the signal chain is shown in Figure 2.7. Depending on the frequencies within the UWL band, the system temperature can vary from $\sim$20-40 K for 704-1344 MHz to $\sim$19-23 K for 1344-2368 MHz, and $\sim$20-27 K for 2368-4032 MHz.

2.4 Multi-telescope Observing Campaign

In order to study the frequency-dependent ISM effects in detail, we made use of all three telescopes described above contemporaneously. Given their completely different configurations, telescope operational strategies, data analysis and cali-

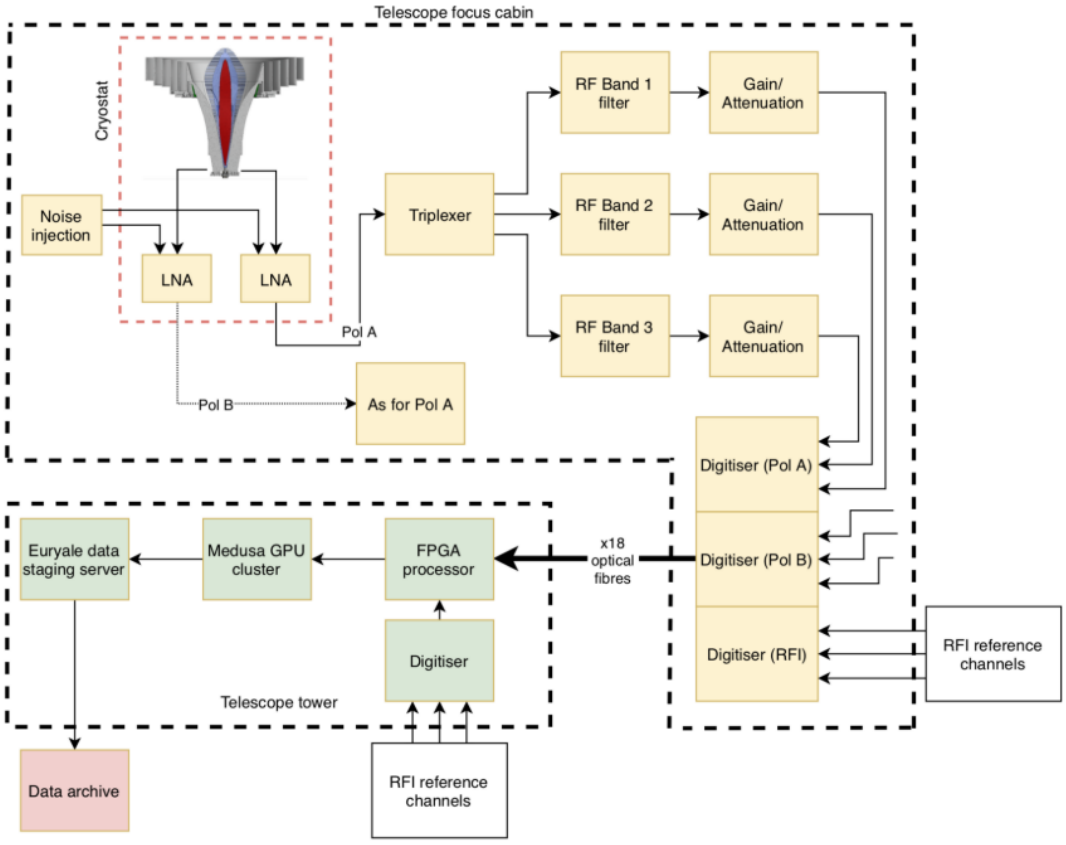

Figure 2.7: An overview of the primary components of the UWL system (Hobbs et al., 2020).

bration procedures, there were some significant challenges to process data from the multi-telescope campaign.

2.4.1 RFI environment at different observatories

All radio-astronomy receiver systems are affected by RFI, though at varying degrees. Ground-based, aircraft and satellite transmissions are especially problematic for radio observations at any frequencies. The RFI environment at the MWA is generally clean, owing to its radio-quiet location. For VCS data, we nominally flag a small number of edge channels in every coarse channel in order to avoid the non-trivial effects of aliasing, which can reduce the usable effective bandwidth by $\sim 30\%$ when employing a particularly brutal flagging scheme.

On the other hand, the uGMRT is located in a RFI hostile environment. This leads to substantial RFI contamination in most observations. For this thesis work, we made use of the BAND3 and BAND4 receivers. All the RFI excision analysis was performed offline, on the raw time series data before folding the profiles in time or frequency. The analysis was done by using the `paz` routine of `PSRCHIVE` by identifying and flagging the problematic channels. The GMRT BAND3 data were nominally $\sim 10\%$ more prone to RFI compared to BAND4 data.

As with the uGMRT, the Parkes UWL data are also quite significantly RFI contaminated. The UWL receiver is equipped with the adaptive RFI filtering. It is very carefully and well designed system to prevent saturation even in the presence of multiple strong satellite RFI as noted in Hobbs et al. (2020). To assist with the mitigation of RFI, the UWL band for each polarisation is split into three sub-octave RF bands using a triplexer (created using a power splitter and a diplexer) and band-limiting filters. These bands are separately amplified and digitised (i.e., three parallel signal paths, as shown in Figure 2.7). The three RF bands have a relatively flat response over the corresponding digital bands, which cover the frequency ranges 704-1344 MHz, 1344-2368 MHz and 2368-4032 MHz. The separate sub-octave RF bands provide adequate protection against inter-modulation products from strong RFI signals affecting other parts of the UWL band.

Despite the implementation of an RFI filtering scheme, the data from UWL are still affected by RFI. Because of its large frequency bandwidth and due to large data file size, it was hard to remove the RFI using the standard `pazi` routine, so a separate software tool called "Coastguard" is used to RFI clean and calibrate the UWL data. Coastguard is a data processing pipeline originally developed for the Effelsberg telescope (details can be found in (Lazarus et al., 2016). However, for the work presented in this thesis, we have used primarily the RFI zapping part.

2.5 Software

2.5.1 Data processing software

2.5.1.1 DSPSR

The Digital Signal Processing Software for Pulsar Astronomy (DSPSR) is an evolved software to fulfill the requirements of different telescopes including the uGMRT, Parkes, and the MWA. It is widely used as a pulsar processing software package, in both real-time as well as for offline processing. It can perform coherent dedispersion and data can be organized into a custom format ("pulsar archives") that contain frequency, sub-integration, polarization, and pulse phase information. These data can then be further processed using the `PSRCHIVE` software package.

2.5.1.2 PSRCHIVE

PSRCHIVE is a suite of software routines designed to perform pulsar data analysis (Hotan et al., 2004; van Straten et al., 2012). The package includes a range of algorithms useful for RFI mitigation, polarization analysis, pulsar timing and data visualization.

2.5.2 Pulsar timing

2.5.2.1 Generating analytic template

```
paas -i -d 1/xs file.ar
```

An analytical template is generated by fitting to a high signal-to-noise ratio copy of the profile that is formed by stacking together the profiles obtained from many individual observations. The profile should be frequency, time and polarization averaged. This can then be fed to the `paas` utility of the `PSRCHIVE`

package, to interactively select multiple components to fit the profile. Figure 2.8 presents a screenshot of an interactive window for the generation of an analytic template.

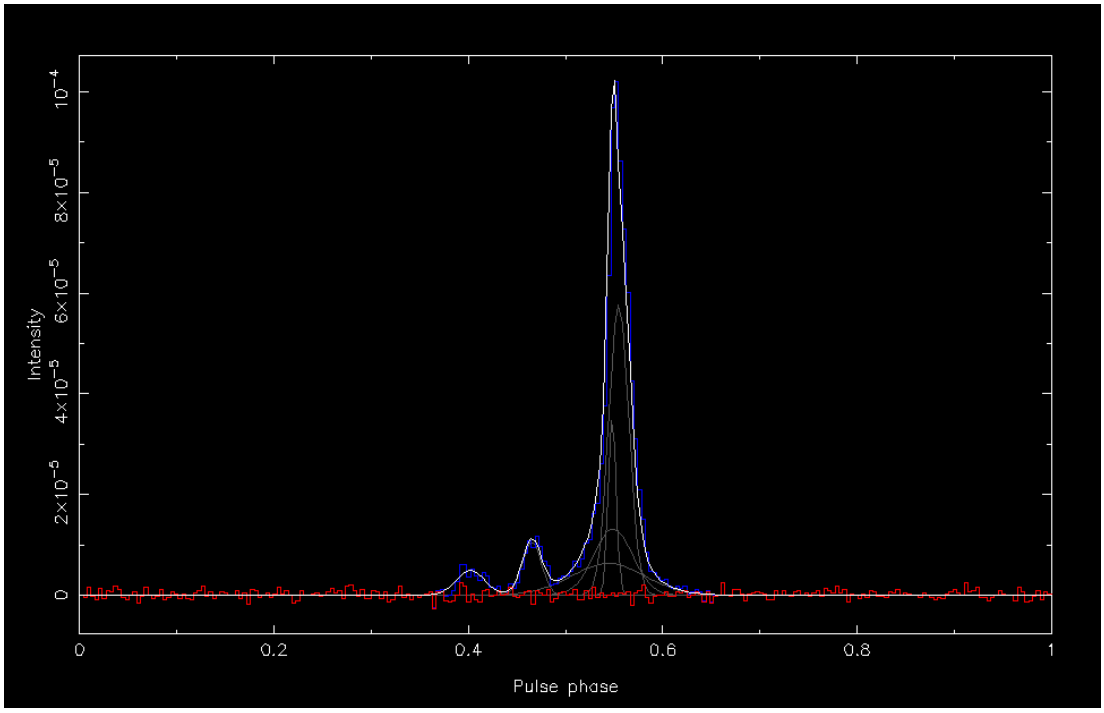

Figure 2.8: A screenshot showing an interactive window where manually selected profile components are fit to the measured profile of PSR J2241−5236 to generate an analytic template.

2.5.2.2 TEMPO2

TEMPO2 is the most widely used timing analysis package, which has been maintained and distributed by the Australia Telescope National Facility [§]. It is a software package for the analysis of pulsar pulse times of arrival (TOA). TEMPO2 is used to compare a model for a pulsar's rotation, position and orbital parameters with actual observations of pulse arrival times. The difference between the measured and predicted arrival times are known as the pulsar "timing residuals". After calculating these timing residuals, TEMPO2 carries out a linear least-squares-fit to improve the parameters in the model. For this thesis work,

[§]http://www.atnf.csiro.au/research/pulsar/tempo2

`pat` is used to obtain pulse times of arrival by cross-correlating the analytic standard template with the pulsar observation. The following command is used to create the timing file for which an initial timing model (ephemeris file) is required, which can be obtained from the ATNF Pulsar Catalogue [¶]. The `pat` utility determines the time of arrival (TOA) by calculating the phase shift between each profile and a standard template.

```
pat -s paas.std -f tempo2 data.FTp > file.tim
```

The timing file can be then be analysed with TEMPO2 to fit for different pulsar parameters, in order to measure and refine them. For the analysis presented in this chapter, we only fit for the dispersion measure for which, the below command is used. It gives an interactive window which allows a fit for various pulsar parameters providing the pre and post-fit residuals.

```
tempo2 -gr plk -f file.par file.tim -nofit
```

The output provides pre-fit and post-fit timing residuals. As we fit for the DM, output also presents the uncertainty of the fitted value and the magnitude of the change in the DM value, i.e., the change from its initial value.

[¶]http://www.atnf.csiro.au/research/pulsar/psrcat

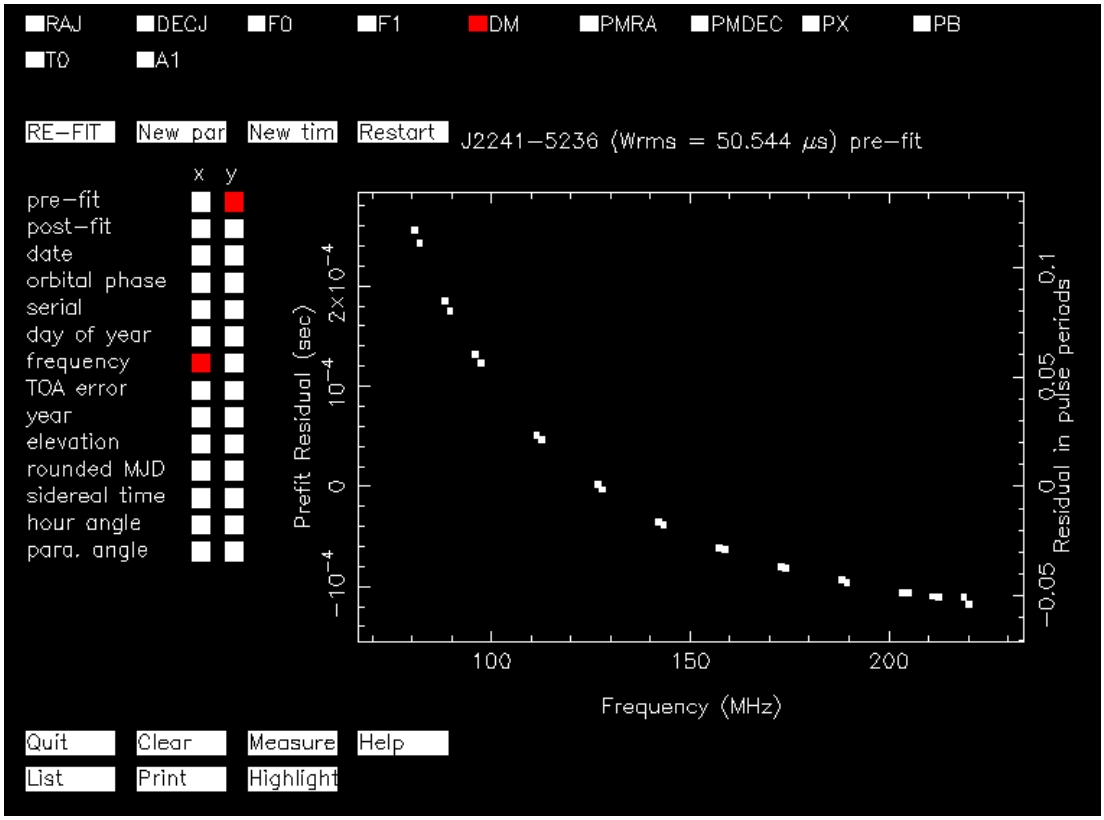

Figure 2.9: A screenshot showing pre-fit residuals from the TEMPO2 window for PSR J2241−5236 for which we measure the dispersion measure. The points represent the "timing residuals" as function of the observing frequency.

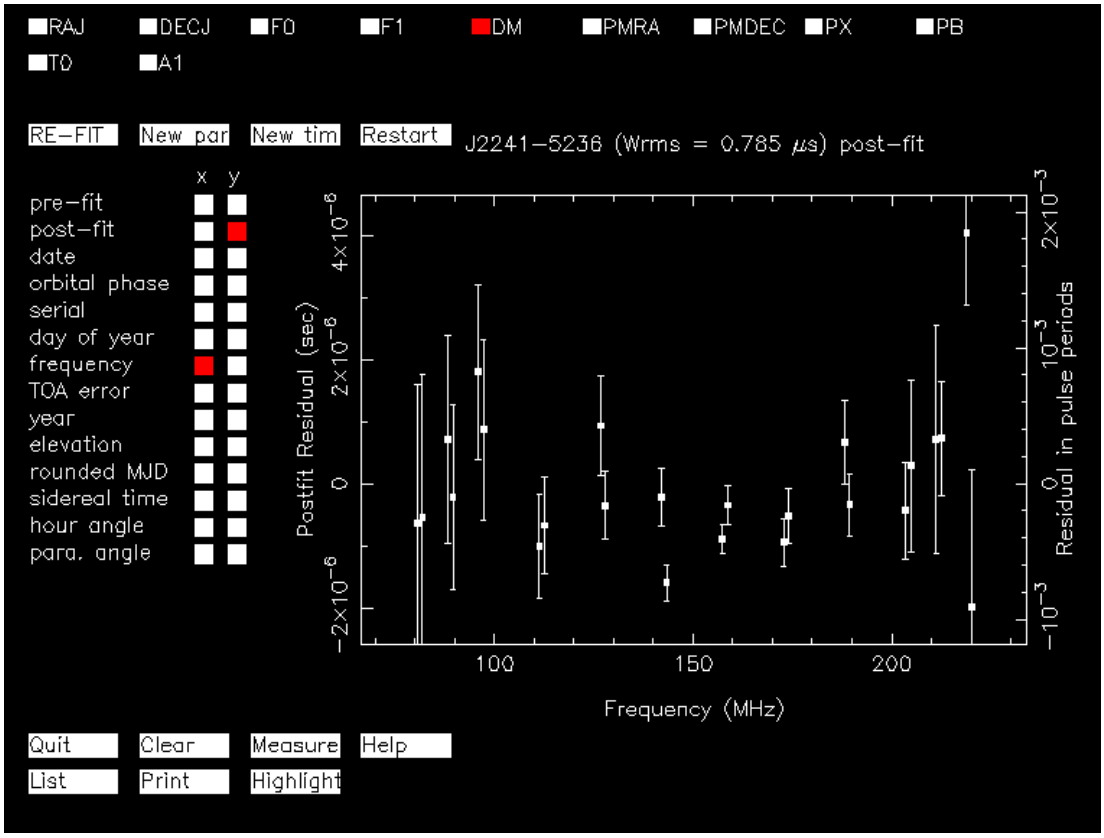

Figure 2.10: A screenshot showing post-fit residuals from the TEMPO2 window for PSR J2241−5236 after fitting for the dispersion measure.

```
Results for PSR J2241-5236


RMS pre-fit residual = 0.785 (us), RMS post-fit residual = 0.785 (us)
Fit Chisq = 47.17       Chisqr/nfree = 47.17/22 = 2.14399       pre/post = 0.999897
Number of fit parameters: 2
Number of points in fit = 24
Offset: -5.95714e-07 4.41639e-07 offset_e*sqrt(n) = 2.16358e-06 n = 24

PARAMETER       Pre-fit                 Post-fit                Uncertainty   Difference   Fit
-------------------------------------------------------------------------------------------------
RAJ (rad)       5.94153833508256        5.94153833508256        0             0            N
RAJ (hms)       22:41:42.0168997        22:41:42.0168997        0             0
DECJ (rad)      -0.918218751254693      -0.918218751254693      0             0            N
DECJ (dms)      -52:36:36.21282         -52:36:36.21282         0             0
F0 (s^-1)       457.310149756662        457.310149756662        0             0            N
F1 (s^-2)       -1.44225812954062e-15   -1.44225812954062e-15   0             0            N
PEPOCH (MJD)    55044.15587             55044.15587             0             0            N
POSEPOCH (MJD)  55044.15587             55044.15587             0             0            N
DMEPOCH (MJD)   55044.15587             55044.15587             0             0            N
DM (cm^-3 pc)   11.4115230998551        11.4115231081111        2.2301e-06    8.256e-09    Y
PMRA (mas/yr)   18.8642845640328        18.8642845640328        0             0            N
PMDEC (mas/yr)  -5.28891369987509       -5.28891369987509       0             0            N
PX (mas)        0.862364171800457       0.862364171800457       0             0            N
PB (d)          0.145672239773858       0.145672239773858       0             0            N
T0 (MJD)        55044.1580902993        55044.1580902993        0             0            N
A1 (lt-s)       0.0257952598333572      0.0257952598333572      0             0            N
START (MJD)     57977.7346172255        57977.7336172255        0             -0.001       Y
FINISH (MJD)    57979.7347478987        57979.7357478987        0             0.001        Y
TZRMJD          57978.7292823089        57978.7292823089        0             0            N
TZRFRQ (MHz)    218.880005              218.880005              0             0            N
TZRSITE         mwa
TRES            0.78537770721144        0.78545870606227        0             8.0999e-05   N
EPHVER          TEMPO2                  TEMPO2                  0             0            N
-------------------------------------------------------------------------------------------------
[textOutput.C:273] Notice: Parameter uncertainties multiplied by sqrt(red. chisq)
```

Figure 2.11: A terminal output showing the pre and post-fit timing residuals, a weighted fit, and the reduced-χ^2 of the fit. For each parameter in the timing model, the output contains its name, pre and post-fit parameter values, the uncertainty of the fitted value and the magnitude of the change in the parameter. This example shows the pre and post-fit timing residuals after fitting for the DM.

Chapter 3

A high time resolution study of the millisecond pulsar J2241−5236 at frequencies below 300 MHz

A substantial part of this chapter is based on the publication: D. Kaur, N. D. R. Bhat, S. E. Tremblay, R. M. Shannon, S. J. McSweeney, S. M. Ord, A. P.Beardsley, B. Crosse, D. Emrich, T. M. O. Franzen, L. Horsley, M. Johnston-Hollitt, D. L. Kaplan, D.Kenney, M. F. Morales, D. Pallot, K. Steele, S. J. Tingay, C. M. Trott, M. Walker, R. B. Wayth, A. Williams, and C. Wu, "A high time resolution study of the millisecond pulsar J2241−5236 at frequencies below 300 MHz", 2019, The Astrophysical Journal, 882, 2. The additional material in this chapter relates to the temporal variations in DM towards this pulsar over a period of five years (2015-2019) and the analysis of polarimetric profiles below 300 MHz. A summary of the published work is reproduced below.

3.1 Summary

One of the major challenges for pulsar timing array (PTA) experiments is the mitigation of the effects of the turbulent interstellar medium (ISM) from timing data. These can potentially lead to measurable delays and/or distortions in the pulse profiles and scale strongly with the inverse of the radio frequency. Low-frequency observations are therefore highly appealing for characterizing them. However, in order to achieve the necessary time resolution to resolve profile features of short-period millisecond pulsars, phase-coherent de-dispersion is essential, especially at frequencies below 300 MHz.

This chapter presents low-frequency (80-220 MHz), detection of one of the most promising pulsars for current and future PTAs, PSR J2241−5236. Using our new beamformer software for the MWA's voltage capture system (VCS), we reconstructed the time series at a much higher time resolution of $\sim 1\,\mu$s by re-synthesizing the coarse-channelised voltage data. We detected a dual-precursor type feature in the pulse profile that is either faint or absent in high-frequency observations from Parkes. Thanks to the microsecond level timing achievable for this pulsar at the MWA's low frequencies, we were able to measure dispersion measure (DM) to a precision of the order of (2-6)$\times 10^{-6}$ pc cm^{-3}.

3.2 Introduction

Millisecond pulsars (MSPs) are important targets for high-precision pulsar timing array (PTA) experiments, which involve regular monitoring of pulse arrival times from a celestial distribution of pulsars to search for ultra-low frequency (nHz) gravitational waves (e.g., Manchester et al., 2013; Demorest et al., 2013; van Haasteren et al., 2011; Janssen et al., 2015; Bailes et al., 2018). To achieve the required ∼100-200 ns timing precision, it is important to ascertain various factors contributing to the timing noise budget (e.g., Cordes & Shannon, 2010). PTA efforts over the past few years suggest that the interstellar medium (ISM)

propagation effects on pulsar signals are one of the major contributing factors and may ultimately limit the detection sensitivity of PTAs if they are not accurately measured and corrected for in timing measurements (Shannon & Cordes, 2017; Jones et al., 2017; Levin et al., 2016; Cordes et al., 2016).

The magnitudes of ISM effects scale strongly with the inverse of observing frequency. Therefore, PTAs generally observe pulsars at higher frequencies ($\sim$ 1-2 GHz) to reduce the effects of the ISM. Two dominant effects are: 1) dispersion, which arises from propagation through intervening ionized gas, quantified as the integrated electron density along the line of sight of the pulsar, and is called the dispersion measure (DM), and 2) pulse broadening, which arises from multi-path propagation in the turbulent ISM. The dispersion delay scales as ν^{-2}, and pulse broadening time as $\sim \nu^{-4}$ (e.g., Bhat et al., 2004), where ν is the observing frequency. Low-frequency observations of pulsars can therefore allow a robust characterization of ISM effects, unlike those at higher frequencies where their impact on timing measurements are not easily discernible. Low-frequency observations can also be used to investigate the recently proposed effects such as chromatic (frequency-dependent) DM, arising due to different path lengths traversed, or volumes sampled, at different frequencies, again owing to multipath propagation (Cordes et al., 2016). This may also have important implications for timing-array applications, as that would imply that correcting for ISM effects using low-frequency data is not straightforward. Thus, detailed observational investigations over a wide range of frequencies will be very instructive.

Developments in low-frequency radio instrumentation and advances in computing over the past decade have revitalized pulsar astronomy at low frequencies. Instruments such as the Murchison Widefield Array (MWA; Tingay et al., 2013), the Low Frequency Array (LOFAR; van Haarlem et al., 2013), and the Long Wavelength Array (LWA; Taylor et al., 2012) have been built, and operational, and are opening up new opportunities for observing pulsars at frequencies below 300 MHz. The MWA is also a low frequency (80-300 MHz) precursor to the

Square Kilometer Array (SKA). It has been recently upgraded, with a doubling of the number of tiles and maximum baseline, i.e. a 256-tile array extending out to ~ 6 km (Wayth et al., 2018). With its voltage capture system (VCS; Tremblay et al., 2015), which records data at 10-kHz/100-μs resolutions, the MWA has been producing a wide variety of pulsar science (e.g., McSweeney et al., 2017; Meyers et al., 2017; Xue et al., 2017), including characterization of the ISM towards important southern-sky PTA targets (e.g., Bhat et al., 2014, 2016, 2018).

For MSPs with short rotation periods ($P \lesssim 5$ ms; where P is the period) and narrow pulse profiles, the 10-kHz channelization of VCS limits their detection, especially at the lower frequencies of the MWA. For example, a pulsar with a DM of 10 pc cm^{-3} will be smeared to 1.62 ms at 80 MHz. Fundamentally, this hampers the ability to resolve fine temporal features in the pulse profiles of MSPs. Thus, we require the ability for higher time resolution and phase-coherent de-dispersion to remove temporal smearing at the low frequencies of the MWA.

Here we presented early science results from our new and improved beamformer software, which allows re-synthesis of 1.28-MHz/0.78-μs voltage samples from 10-kHz/100-μs native resolutions of the VCS, by performing an inversion of the polyphase filterbank (PFB) operation prior to VCS recording. This is demonstrated using our observations of PSR J2241−5236, an important PTA target. The pulsar was discovered in targeted searches toward unassociated Fermi-LAT candidates, and has a period of 2.18 ms and a DM of 11.41 pc cm^{-3} (Keith et al., 2011). The new beamformer has enabled the pulsar detections down to ~ 80 MHz, thereby allowing us to study the ISM and spectral properties of the pulsar. The published work is described in Section 3.3, 3.4, and 3.5. The polarimetric and temporal DM variations are summarised in Sections 3.6.2, and 3.7. Results and conclusion are summarised in Section 3.6, and 3.8.

Figure 3.1: A sketch of the MWA telescope, showing some of the tiles on site, receiving signal from pulsar PSR J2241−5236, which is in a binary system with a low-mass, black-widow type companion.

3.3 Observations

The MWA observations are typically made with a monthly cadence for MSPs. However, additional constraints due to pulsar data calibration (generally only possible during night-time hours) reduced the number of possible observations to only a handful per year. All the observations collected from calendar year 2015 to 2019 on this particular pulsar are detailed in Table 3.1. In the table, the number of tiles used to calibrate the data are only presented for those observations which were successfully calibrated and in which the pulsar was detected. For observations either with bad calibration or non-detections of pulsar are marked with a cross. For the published work, three observations were used, each separated by nearly $\sim$1 year during 2015-2017. All the observations were made with the MWA's VCS, which records 24 coarse channels, each of which has been finely channelized to 10 kHz using a 12-tap PFB. It records both polarizations from a maximum of 128 tiles, and has an aggregate data rate of $\sim 28\,\mathrm{TB\,hr^{-1}}$. The 30.72 MHz observing bandwidth currently feasible with the MWA can flexibly be recorded in either a contiguous band or can be split into 24×1.28 MHz coarse channels, which can be placed anywhere across the nominal operating frequency range (80-300 MHz). This distributed channel mode is particularly suitable for exploring frequency-dependent effects such as pulse profile evolution, scintillation and scattering (Bhat et al., 2018; Kirsten et al., 2019). The VCS data were transported to the Pawsey supercomputing facility, where all further processing, including calibration and beamforming, were carried out.

3.4 Data processing

The VCS data can be processed to form a coherent beam by applying suitable phase rotations to each voltage stream and then summing them to generate a phased array signal (Ord et al., 2019). It involves accounting for the polarimetric response for each tile and frequency channel by applying appropriate cable and

Table 3.1: Observational details of PSR J2241−5236

MJD	Frequency range (MHz)	Channel setup	Observing duration (s)	N_{tile} [a]
57287.58	170-200	1×30.72	4800	114
57707.45	80-220	12×2.56 [b]	1800	126
57978.70	80-220	12×2.56 [b]	3600	121
58069.95	80-220	12×2.56 [b]	3600	×
58084.40	80-220	12×2.56 [b]	3600	×
58086.32	80-220	12×2.56 [b]	3600	×
58795.53	80-220	12×2.56 [b]	2692	125
58816.55	80-220	12×2.56 [b]	2692	119

[a]No. of tiles used while producing calibration solutions

[b]2 × 2.18 MHz channels spraed over 80-220 MHz

× No-detection of the pulsar

geometric delays and complex gains (i.e. amplitudes and phases). Data are then calibrated using standard calibrators (e.g., Hydra A and 3C444), recorded in pointed observations prior to pulsar observations. The calibration solutions are generated for each tile and frequency channel using the Real Time System (RTS; Mitchell et al., 2008), and tiles that produced poor calibration solutions are flagged. The full processing pipeline is implemented on the Galaxy cluster at the Pawsey Supercomputing Centre. These data are then processed using the standard pulsar data analysis packages `DSPSR` (van Straten & Bailes, 2011) and `PSRCHIVE` (Hotan et al., 2004; van Straten et al., 2012) to generate multi-channel pulse profiles for further analysis.

3.4.1 Re-constructing the high-time resolution time series

High-quality MSP detections require coherent de-dispersion, in which the received voltage signal is deconvolved using the transfer function of the ISM (Hankins & Rickett, 1975). While this technique has been routinely implemented in pulsar instrumentation around the world (e.g., van Straten & Bailes, 2011), it was not possible earlier with the MWA due to our fine 10-kHz channelization and the filterbank format of beamformed data (written in full-Stokes PSRFITS). With

the new beamformer software, which reconstructs the data at a much higher time resolution by re-synthesizing the coarse-channel voltage samples (by effectively inverting the fine PFB operation that produced the fine channels), it has become possible to generate data that are amenable for coherent de-dispersion.

The MWA fine channelization is implemented via a PFB with a 12-tap Kaiser window function, which is one of a class of window functions that allows theoretically perfect inversion of the PFB channelization process (Crochiere & Rabiner, 1983; Oppenheim et al., 1999)*. The synthesis filterbank is achieved by first up-sampling the output of each 10-kHz fine channel to the initial time resolution (a factor of 128) and then passing them through a synthesis filter, which we choose to be the same filter used in the forward PFB stage, with an appropriately chosen phase ramp applied to each fine channel. Then each channel is low-pass filtered to remove the 127 images of the spectrum created by the up-sampling. The re-synthesized coarse channels have a time resolution of $\sim 0.78\,\mu$s and can be coherently de-dispersed to produce high-quality detections of MSPs at the MWA's frequencies. Further details of this are described in McSweeney et al. (2020).

3.5 Analysis

3.5.1 DM determination

Figure 3.2 presents MWA detections of PSR J2241−5236 across the 80-220 MHz range. As evident from the figure, the pulsar is visibly bright across the $\sim$ 100-200 MHz frequency range. Using the best detection (signal-to-noise ratio; S/N $\sim$ 70), we created an analytic template, which is a noise-free profile model, composed of von Mises functions, generated using the `paas` utility of `PSRCHIVE`. The analytic template is then cross-correlated with the observed profiles to obtain the times of arrival (TOAs) using the `PSRCHIVE` package. The TOAs are then analyzed using

*In practise, integer quantization in the analysis and/or synthesis process means the reconstruction will not be perfect.

the pulsar timing package TEMPO2 (Hobbs et al., 2006) to determine the DM. We adopted the latest available timing solution of the pulsar and only fit for DM in this analysis. As our observing system is configured as 24 individual frequency sub-bands, we derived the DM using a set 24 TOAs for every single observation.

As seen in Figure 3.2, the pulse width is relatively unchanged throughout the observed frequency range[†], and therefore for the purpose of the DM analysis, we assume that there is no significant pulse profile evolution within our observing band. Ideally, the profile evolution needs to be considered (cf. Pennucci, 2019), however, our data quality is not adequate for a detailed analysis. The data are subsequently re-processed using the refined DM to obtain better quality pulse profiles. The related analysis is illustrated in Figure 3.3, which shows pulsar signal across 80-220 MHz, with 12×2.56 MHz channels joined together. This detection is from MJD 57979 and corresponds to the brightest among all our observations. As seen from the Figure 3.3, our observations do not reveal any visible scatter broadening even at lowest observed frequency (80 MHz). These profiles at 80-220 MHz are then averaged in frequency to generate a standard profile centered at 150 MHz, as shown in Figure 3.4, which is then used as a final template for all observations to obtain the TOAs and DM measurements.

3.5.2 Flux density calibration

The flux density calibration for our data is carried out using the approach described by Meyers et al. (2017). This involves estimating the system gain (G) by simulating the tied-array beam pattern and integrating the response across the visible sky for the phased-array configuration used for observing. The tied-array beam pattern is then combined with the Global Sky Model of de Oliveira-Costa et al. (2008) to calculate the antenna temperature ($T_{\rm ant}$). Assuming a radiation efficiency (η) of unity, the system temperature ($T_{\rm sys}$) is then $T_{\rm sys} = T_{\rm ant} + T_{\rm rec}$, where $T_{\rm rec}$ is the measured receiver temperature. This process is conducted sep-

[†]The measured 10% pulse widths $\sim 150\,\mu$s across our 80-220 MHz range.

arately for each sub-band, as all of these quantities are strongly frequency dependent. While doing this, we also account for a "coherency factor" (cf. Meyers et al., 2017), for any loss in sensitivity in the coherent beamforming process. This information is then used to estimate the flux density for all the observed frequency bands using the radiometer equation (Lorimer & Kramer, 2004) and also by factoring in the duty cycle of the pulsar, which is equivalent pulse width (W) divided by the pulse period (W/P), where W is measured as integrated flux over the "on" pulse divided by the peak amplitude of the pulse.

3.6 Results and Discussion

PSR J2241−5236 has so far been primarily studied at frequencies above 700 MHz, with the Parkes telescope (Dai et al., 2015; Keith et al., 2011). Aside from a low S/N detection that was reported by Xue et al. (2017), there are no other low-frequency observation of this pulsar in the published literature. Unlike other bright southern MSPs such as PSRs J0437−4715 and J2145−0750 (e.g., Bhat et al., 2018), PSR J2241−5236 has a narrow pulse profile and shows little profile evolution within the MWA's band. Figure 3.4 presents the frequency-averaged profile centered at 150 MHz, and we measure a 10% pulse width (W_{10}) of $\sim 150\,\mu$s at 158 MHz, which is comparable to $\sim$130 μs measured at Parkes frequencies ($\sim$ 1-3 GHz).

In general, MSPs tend to show quite complex and rapid profile evolution with frequency (e.g., Dai et al., 2015; Bhat et al., 2018). In the case of J2241−5236, while the main pulse shows little evolution with frequency, MWA observations reveal an interesting dual precursor type feature, which is less prominent at Parkes frequencies (see Fig 3.4). On a closer examination of Figures 3.2 and 3.3, it is evident that the precursor emission is persistent over a large fraction of the observed MWA band, where it is nominally seen at 10-15% of the pulse peak. However, its relative phase appears to be slightly offset (leftward) compared to that seen at Parkes frequencies. This could possibly be due to the spectral evolution of the

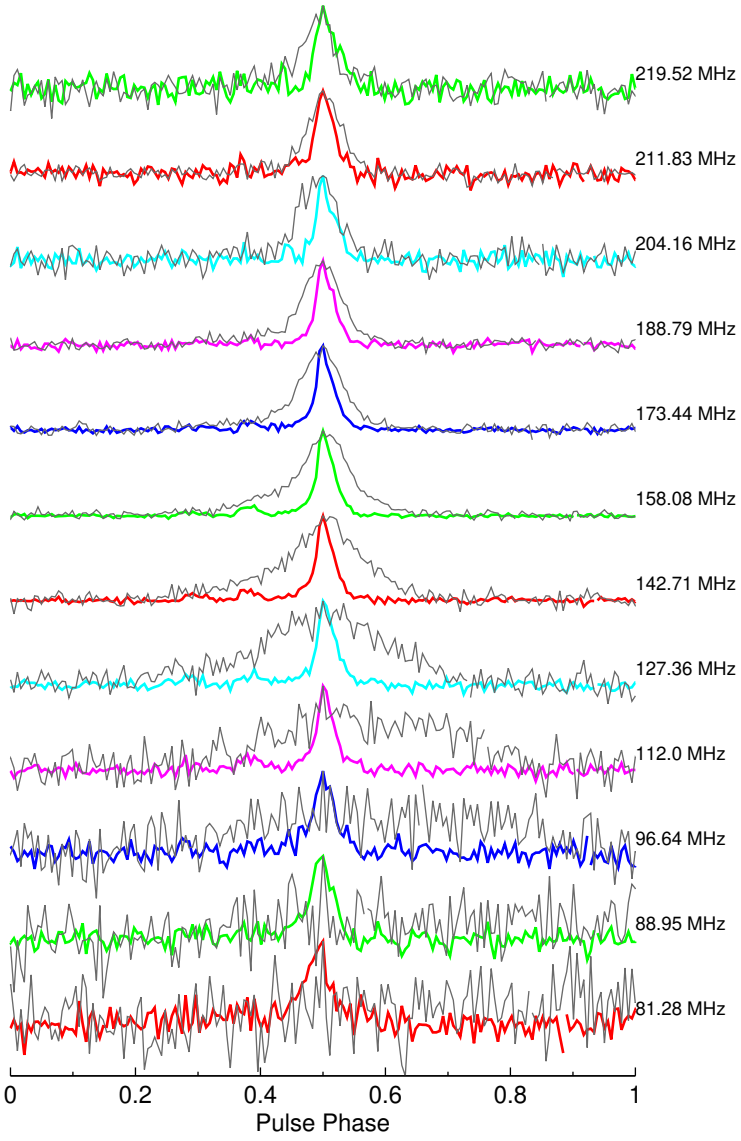

Figure 3.2: MWA detections of PSR J2241−5236 from observations made at MJD 57979. Data were coherently de-dispersed at each of the 12×2.56 MHz bands. The pulsar is detected throughout the 80-220 MHz range; the resultant profiles (in colour) are overlaid with the detections using the previous system, at 10 kHz resolution (in grey), where the pulse profile is significantly broadened due to residual dispersive smearing within 10 kHz channels (4% to ∼80% of the pulse period).

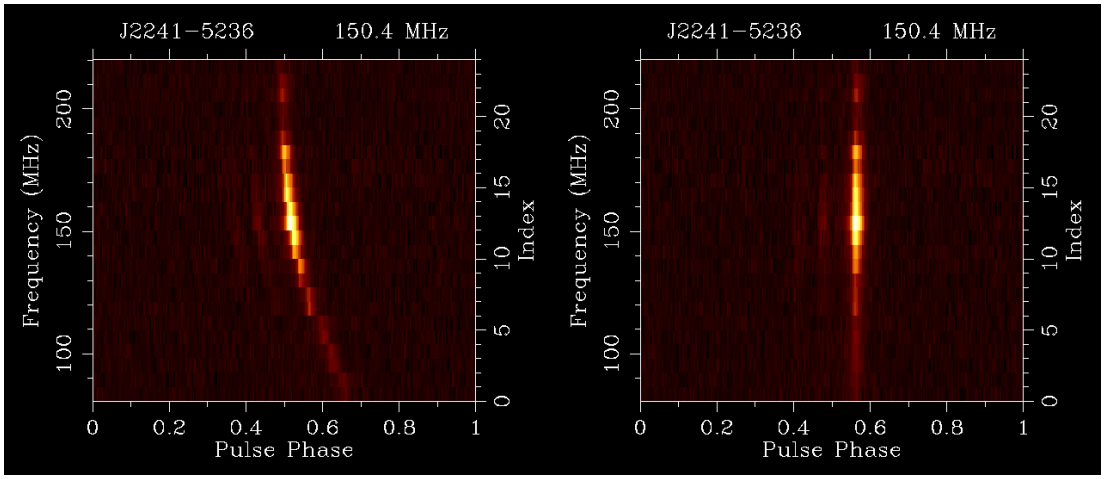

Figure 3.3: Detection of PSR J2241−5236 across the 80-220 MHz frequency range of the MWA from observations made at MJD = 57979. Plots showing pulse intensity as a function of frequency vs. pulse phase, where 12 sub-bands, each 2.56 MHz wide, at separations ∼ 8-16 MHz, are joined together. Left: data processed with the catalog DM of 11.41085 pc cm^{-3} and the quadratic sweep of 0.4 ms implies an excess DM of 0.000667 pc cm^{-3}. Right: data reprocessed with the refined DM of 11.41151 pc cm^{-3}, demonstrating the MWA's sensitivity to subtle DM variations.

profile. Observations at intermediate frequencies (∼ 300-700 MHz), as presented in chapter 4, would be useful to further investigate this.

3.6.1 DM measurements and precision

We initially de-dispersed the data using the catalogue DM of 11.41085 pc cm^{-3}. This revealed a clear quadratic sweep of approximately 0.4 ms as seen in Figure 3.3. We subsequently reprocessed the data using our refined DM measurements, as summarized in Table 3.2. Our measured DMs are consistently larger than the catalogue value. The average DM from all three observations is 11.411505 pc cm^{-3}, which may suggest an "excess" DM of 0.000655 pc cm^{-3}, compared to the catalogue value as reported in Keith et al. (2011)[‡].

Such subtle changes can in principle arise due to effects such as chromatic (frequency-dependent) DMs, as recently theorised by Cordes et al. (2016). The chromatic DM being a consequence of multi-path scattering, in general, one may

[‡]Based on timing data (∼ **1**-2 GHz) taken over a ∼ 15-month time span in 2009-2010.

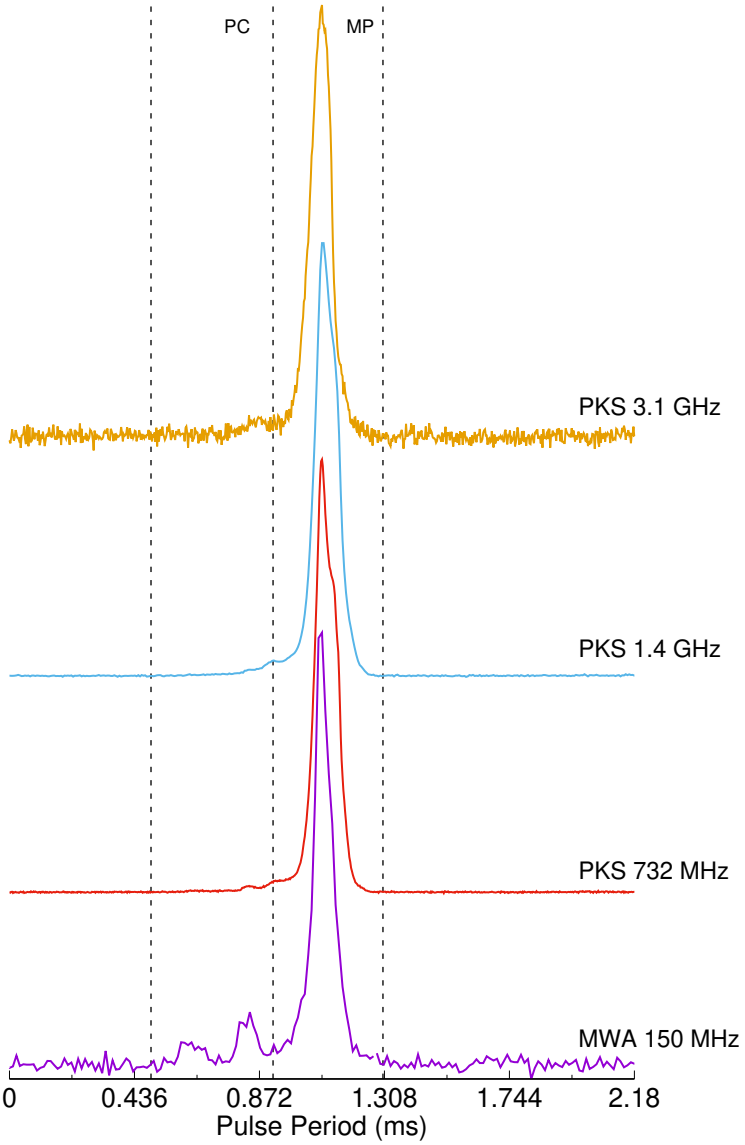

Figure 3.4: Integrated pulse profiles of PSR J2241−5236 at frequencies from 150 MHz to 3.1 GHz. The MWA profile has a time resolution of $\sim 8.5\,\mu$s, whereas Parkes profiles (from Dai et al., 2015) have a time resolution of $\sim 2\,\mu$s.

expect a dependence on the degree of scattering. However, our current observations (where we distribute the recording bandwidth to sample multiple spot frequencies across a large frequency range) are not ideal for a meaningful scintillation analysis. In any case, there has been some observational evidence in support of excess DM at low frequencies, e.g. in the case of PSR J2145−0750, for which MWA and LWA measurements by Bhat et al. (2018) and Dowell et al. (2013) report a δDM of $0.006\pm0.003\,\mathrm{pc\,cm^{-3}}$. More recently, DM variations have been reported for PSR J2219+4754 by Donner et al. (2019) and Lam et al. (2019) from LOFAR observations, and have been attributed to chromatic DMs, although their interpretations differ. With only limited observational efforts to date to investigate this important effect, routine observations with low-frequency instruments such as the MWA and LWA will be especially useful.

PSR J2241−5236 is a high-priority target for PTA applications (i.e. along the class of pulsars like J1909−3744 and J1744−1134). However, to date, there are no published measurements of temporal DM variations (on time scales of $\sim$ months to years) for this pulsar. As can be seen from Table 3.2, our observations suggest DM variations, $\delta\mathrm{DM} \sim 10^{-4}\,\mathrm{pc\,cm^{-3}}$, on timescales of $\sim$1-2 years. Since the observed DM variation is subtle, multiple different sources of origin can be considered. For example, the Solar wind is known to produce DM variations up to $\sim 10^{-5}\,\mathrm{pc\,cm^{-3}}$ (e.g., Kumar et al., 2013; Lam et al., 2016), when observations are made very close to the Sun. However, this seems unlikely, as our observations were made at large Solar elongations ($\gtrsim 80^{\circ}$), and as such the pulsar is far from the ecliptic plane. There has been some recent evidence that the companion winds can modulate the DM for binary pulsars. PSR J2241−5236 is in a 3.5-hr, almost circular orbit with a low-mass ($\sim 0.01\,\mathrm{M_{\odot}}$) black widow type companion. We may therefore expect subtle variations in DM as a function of the orbital phase, especially in light of the recent work by An et al. (2018), who report orbital modulation in gamma-ray due to intra-binary shock emission. There has been observational evidence for such black-widow like system with an ablating

Table 3.2: DM measurements from the five observed epochs.

Date of Obs MJD	DM $\mathrm{pc\,cm^{-3}}$	σ_{DM} † $\mathrm{pc\,cm^{-3}}$	Post-fit* residual (μs)
57287.58	11.41165	(3-9)$\times10^{-5}$	1.54
57707.45	11.411626	(6-9)$\times10^{-6}$	1.4
57978.70	11.411512	(2-7)$\times10^{-6}$	0.8
58795.53	11.411327	(4)$\times10^{-6}$	1.25
58816.55	11.411301	(2)$\times10^{-6}$	1.91

The catalogue DM value for PSR J2241−5236 is 11.41085 $\mathrm{pc\,cm^{-3}}$, with uncertainties of $3 \times 10^{-5}\,\mathrm{pc\,cm^{-3}}$
†The achievable DM precision (σ_{DM}) varies depending on the frequency lever arm, which ranges from ∼140 MHz to ∼10 MHz in our analysis (see Table 3.1 and Figure 3.2)
*Observation made on MJD 57978.70 was used to generate a template because of which the data presents inflated timing precision as the measured profile will self correlate with the template.

companion producing DM variations, e.g., PSR B1957+20 (Fruchter et al., 1990). However, in the case of J2241−5236, no eclipses have been seen as the inclination angle is likely large (Keith et al., 2011), making this less probable. Moreover, our limited data and a sparse coverage of the orbit refrain us from making definitive comments on this.

The DM precision depends on the frequency lever arm, with the best precision achieved for the longest, which, in our case, is 80-220 MHz. As can be seen in Table 3.2, this is in the range $(2-6) \times 10^{-6}\,\mathrm{pc\,cm^{-3}}$, depending on the quality of detection. This is already an order of magnitude better than what is currently achievable at timing frequencies ($3 \times 10^{-5}\,\mathrm{pc\,cm^{-3}}$; Jones et al., 2017), and even the most recent work of Donner et al. (2019), who reach a similar level of precision. Our reduced χ^2 values ranges from 1-0.99. Since our analysis relied on the use of a single template (and not frequency-dependent templates that are ideal for wide-band timing), there is indeed scope for considerable improvement as we accrue more data with the MWA. Furthermore, the measured DM variation (δDM), is about ∼3-10 times larger than our measurement uncertainties (see Table 3.2), highlighting the MWA's high sensitivity to measuring such subtle changes in DMs.

3.6.2 Temporal variation in DM

Ideally, one would be able to measure the DM as a function of time for this pulsar. However, this effort is impeded by the MWA-VCS's high data rate ($\sim$ 30 TB per hour of observation). Therefore, only a small number of MWA measurements are currently available. Although, J2241−5236 is a PPTA target and its DM variations are being studied very regularly with the Parkes, this information has not been published at the time of this writing. As very high precision DM measurements are possible with the MWA, compared to higher frequency observations, it is worth reporting the variations with the available MWA data. With the available observations, here we present the temporal variation over the time scale of $\sim$ 5 years. Figure 3.5 represents the change in DM from 2015 to 2019. The base DM of 11.41151 pc cm^{-3} was removed from the measured DM values, yielding δDM = 0.0002 pc cm^{-3}.

PTA pulsars are regularly monitored for temporal variations in DM. These variations can show different trends (e.g., linear, annual or random), which results from electron density irregularities in the ISM, changing distance between Earth and the pulsar, and solar wind contributing to the measured DM when line of sight passes closer to the Sun. As discussed in previous Section 3.6.1, the Solar wind is unlikely to affect the MWA measurements, and cannot be the cause of the observed variations. The variations seen in our data could be due to electron density fluctuations in the ISM. However, it is difficult to further comment these variations due to sparse sampling of the data over many years.

The measured δDM of 2×10^{-4} pc cm^{-3} can cause a timing delay of $\sim 7\,\mu$s at MWA's frequencies (80-220 MHz), which translates to $\sim$ 170 ns in the Parkes UWL band (700-4000 MHz). This is an order of magnitude smaller compared to other PTA pulsars such as PSR J1909−3744, where the temporal variations are of the order of $\sim 2.3 \times 10^{-3}$ pc cm^{-3} over a period of $\sim$ 8 years (Jones et al., 2017). Accounting for such DM variations in the timing model removes the majority of the DM noise and thus can be used to improve timing precision (Reardon et al.,

2016). For example, Shannon et al. (2015) made use of DM-corrected, 10 cm (3-4 GHz) PPTA data of PSR J1909−3744, which led to the most stringent limit on the stochastic GW background to date.

Temporal variations seem to be not a significant issue for PSR J2241−5236. Its narrow pulse profile and a low DM make it a suitable target for PTAs, with the potential to emerge as one of the best-timed pulsars. On the other hand, the line of sight may have frequency dependence, which is studied and described in Chapter 4.

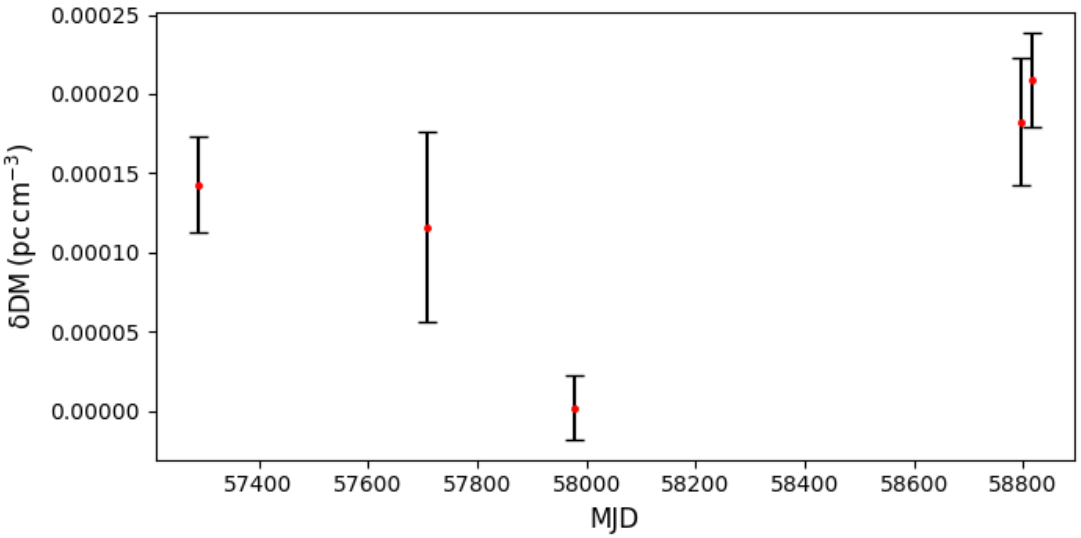

Figure 3.5: Plot of DM measurements obtained from the MWA observations over the period from 2015 to 2019. The delta DM is relative to the baseline DM value of 11.41151 pc cm^{-3}.

3.6.3 Spectral behavior at low frequencies

The pulsar spectra generally follow a single power-law $S_\nu \propto \nu^\alpha$, where S_ν is the flux density at the observing frequency ν and α is the spectral index. However, there are exceptions, where the spectral form tends to either steepen, or flatten, or even turns over (e.g., Kramer et al., 1998; Maron et al., 2000; Jankowski et al., 2018). MSP spectra were initially reported to be steeper, compared to those of long-period pulsars (Toscano et al., 1998). However, the later work by Kuzmin

& Losovsky (2001) claimed a lack of low-frequency spectral turnover for MSPs. More recent work by Dai et al. (2015) suggests a possible turnover for at least a few pulsars, and the work by Kondratiev et al. (2016), at frequencies below 300 MHz, suggests that for many MSPs their measured flux densities are lower than the predicted ones, again hinting at a possible spectral turnover.

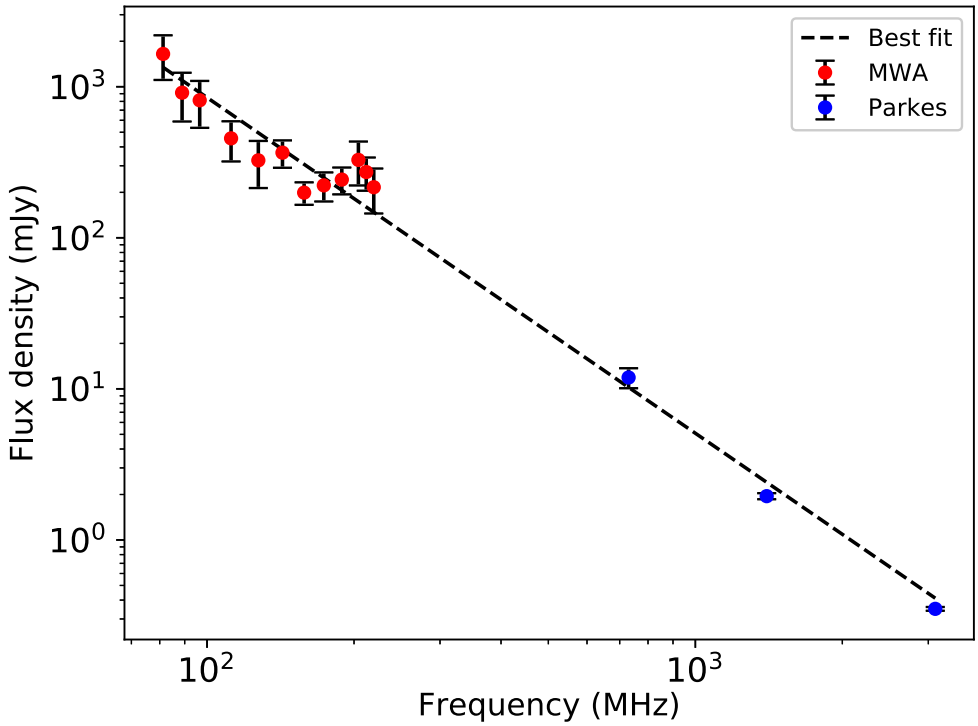

Figure 3.6: Flux density measurements of PSR J2241−5236 from 80 MHz to 3 GHz. For the MWA range (80-220 MHz), measurements are averaged over all three observations. The best-fit spectral index is $\alpha_{\rm MP} = -2.25 \pm 0.10$, compared to $\alpha_1 = -2.12 \pm 0.04$ from Parkes measurements.

Using the procedure explained in Section 3.5.2, we estimated the flux densities from our integrated pulse profiles. By combining the Parkes and MWA data, we estimated a spectral index for the main pulse (MP) $\alpha_{\rm MP} = -2.25 \pm 0.10$. Since the precursor components (PC) are not prominent in the Parkes band, they were excluded from our analysis. Figure 3.6 presents the mean flux densities measured from multiple MWA observations (see Table 3.2) along with Parkes data from

Dai et al. (2015). Parkes measurements are from regularly sampled, six-year data set, whereas MWA measurements are from just three observations over a ~ 3 year time span. Variability in measured flux densities between different observations at the MWA's frequencies is generally within a factor of two, across the entire frequency range, and this is consistent with expectations from refractive scintillation at these low frequencies.[§] The time scale for refractive interstellar scintillation (RISS), $\tau_{\rm riss} = (\nu/\nu_{\rm diss})\,\tau_{\rm diss}$, where $\nu_{\rm diss}$ and $\tau_{\rm diss}$ are the frequency and time scales for diffractive interstellar scintillation, respectively (Rickett, 1990). For our observations at 158 MHz (MJD = 57979), preliminary estimates are ~ 200 kHz[¶] for decorrelation bandwidth ($\nu_{\rm diss}$) and ~ 1000 s for time scale ($\tau_{\rm diss}$). Thus, we estimate a refractive time scale, $\tau_{\rm riss} \sim 9$ days. The small number of observations and a sparse sampling of refractive scintillation cycles can therefore somewhat bias our flux density measurements, and this is reflected by the scatter in Figure 3.6. Nonetheless, since our observations were made in a distributed sub-band setup (i.e. 12×2.56 MHz spread over the 80-220 MHz range), our measurements at any given epoch are essentially independent (i.e. 3×12 independent measurements that constrain the low-frequency part of the spectrum in Figure 3.6). The combination of multiple independent measurements, and multiple observations with a time separation much longer than the RISS time scale, effectively works to decrease any possible bias. Indeed, more observational data will help further refine these measurements and thus yield more robust estimates of the spectrum.

Our measured spectral index is consistent with one of the two estimates ($\alpha_1 = -2.12 \pm 0.04$) from Dai et al. (2015), which is the best fit to their observations made at three Parkes bands. Dai et al. (2015) also quote a much larger value for the spectral index, $\alpha_2 = -2.93 \pm 0.07$, when suitable weights are applied to longer observations. Incidentally, all these estimates are discrepant with the estimate from Murphy et al. (2017), who report $\alpha = -1.3 \pm 0.1$. This discrepancy

[§]The modulations due to diffractive scintillation is $\sim 30\%$, based on our estimated scintillation parameters. For the method i.e., correlation analysis of dynamic spectra and determining the scintillation bandwidth cf. Bhat et al. (2018).

[¶]This can scale to 1 MHz scintles at higher end of the MWA observed band (220 MHz).

is likely due to their use of comparatively less reliable measurements (at ~ 1 GHz) and the measurements from continuum imaging data (at lower frequencies).

A closer examination of Parkes data suggests that the spectrum is steeper for most of the main pulse ($-3.0 < \alpha < -2.5$), and shallower towards the trailing side of the main pulse (> -2.5; see Figure A24, Dai et al., 2015). Given the prominence of precursor emission ($\sim 10-15\%$ of the pulse peak, which corresponds to ~ 380 mJy at 158 MHz) in the MWA band, we can place an upper limit on its spectral index ($\alpha_{\rm PC} < -3.7$), which may indicate a likely spectral steepening at low frequencies. The other plausible cause is possible frequency evolution of the pulse profile, which would require further detailed investigations using the wideband instrumentation now available at the Parkes and Giant Metrewave Radio Telescopes, preferably from observations conducted simultaneously with the MWA.

The recent discoveries of MSPs at low frequencies (Bassa et al., 2017; Lynch et al., 2018) re-affirms the general trend of MSPs exhibiting steeper spectra, which is also consistent with our recent work (e.g., Bhat et al., 2018). This is encouraging from the perspective of finding new pulsars using current and next-generation low-frequency telescopes such as the low-frequency SKA.

3.7 Polarimetric profile of PSR J2241−5236

Pulsar radiation is known to be highly polarized. The polarization profile of this pulsar has not been studied below 700 MHz (Dai et al., 2015). The MWA data thus enables low frequency polarimetry studies of this pulsar for the first time.

The polarimetric profiles with the MWA and Parkes are shown in Figures 3.7 and 3.8. The data were first corrected for the effect of Faraday rotation. The catalog rotation measure (RM) towards this pulsar is 13.3 ± 0.1 rad m^{-2}. The true RM at the MWA's frequencies is obtained using the process of RM synthesis (Burn, 1966). In short, the Stokes I, Q, U and V parameters (as a function of frequency) are extracted from the full intensity profile using the `rmfit` quadratic

fitting function within the PSRCHIVE package (Noutsos et al., 2008), which are then subjected to the RM synthesis technique as described in Xue et al. (2019).

The Earth's ionosphere also contributes to the measured RM. The true RM from the ISM (RM_{ISM}) can be obtained by accounting for the RM contribution from the ionosphere (RM_{ion}). For the MWA observations, RM_{ion} is estimated by using ionFR [‖] (Sotomayor-Beltran et al., 2013) which takes input from the International Geomagnetic Reference Field (IGRF-12; Thébault et al., 2015), and the International Global Navigation Satellite Systems Service (IGS) vertical total electron content (TEC) maps (e.g. Hernández-Pajares et al., 2009). However, ionFR can be inaccurate in certain contexts as noted by Porayko et al., 2019.

Most of the MWA observations are typically made during nightly hours when the RM_{ion} ranges from ~ -0.8 to $-2.0\,\mathrm{rad\,m^{-2}}$ (Xue et al., 2019). Subtracting the measured value of $RM_{ion} = -1.834 \pm 0.004\,\mathrm{rad\,m^{-2}}$ from the measured value ($RM_{obs} = 12.24 \pm 0.43\,\mathrm{rad\,m^{-2}}$), the RM_{ISM} for PSR J2241−5236 is estimated to be $14.074 \pm 0.434\,\mathrm{rad\,m^{-2}}$. This is measured from the 30.72 MHz contiguous data taken on MJD 57288. We also attempted RM synthesis on picket-fence observations; however, application of the same technique did not yield high quality measurements, primarily due to the limited signal to noise of the pulsar detections. The measured RM is consistent with the published RM within the errors.

The MWA data were then updated with true RM value. Figure 3.7 presents the low frequency polarimetric profile from the MWA data. Figure 3.8 shows the Parkes polarization profile from UWL data taken in November 2019. The Parkes polarimetric profile was generated using the catalog RM. There is a notable increase in the degree of linear polarization between UWL to MWA frequencies. This is in line with the generally observed trend for many pulsars, where the degree of linear polarization increases towards lower observing frequencies (Manchester, 1971). Dai et al. (2015) measured the polarization profiles of 24 PPTA MSPs using the Parkes 10, 20, and 50cm data (i.e. 3.1 GHz, 1.4 GHz and

[‖] https://sourceforge.net/projects/ionfarrot/

732 MHz). They also noticed a similar trend of increase in the fractional linear polarization for J2241−5236 along with nine other millisecond pulsars over the Parkes frequency band; i.e., a higher degree of linear polarization at 50 cm compared to the 10 cm band, and the PAs follows the λ^2 relation. In contrast, the millisecond pulsars PSRs J1045−4509, J1603−7202, J1730−2304 and J1824−2452A show the opposite behaviour, i.e. the mean fractional linear polarization significantly increases with frequency. Different profile components of a pulsar can also show different frequency evolution in the fractional linear polarization. For J2241−5236, Dai et al. (2015) noticed that the main component has a lower fractional linear polarization than leading components.

For the MWA polarization analysis, we also acknowledge the possibility of polarization leakage. Although aspects of the MWA's polarimetric response have been explored to a certain extent (e.g., Lenc et al., 2017; Line et al., 2018), a full understanding of the degree of polarisation leakage, especially with regards to the VCS observing mode, is still under active investigation (McSweeney et al. in prep.).

3.8 Conclusions

The development of a new software beamformer for MWA pulsar processing has enabled high-quality, low-frequency detections of the short-period MSP J2241−5236, a top-priority target for PTA applications. By inverting the polyphase filter-bank operation that was performed prior to the VCS recording, the new beamformer produces high-time resolution ($\sim 1\,\mu$s) voltage time series data that are amenable for phase-coherent de-dispersion. With the resultant high-fidelity detections, we were able to achieve a timing precision of the order $\sim 1\,\mu$s at the low frequencies of the MWA, which allowed us to measure the pulsar DM with a very high precision of the order of (2-6) $\times 10^{-6}\,\mathrm{pc\,cm^{-3}}$. This provides an excellent demonstration of the MWA's capability to monitor subtle DM variations ($\sim 10^{-4}\,\mathrm{pc\,cm^{-3}}$) reliably for southern pulsars. The DM precision, and the sensitivity to DM changes,

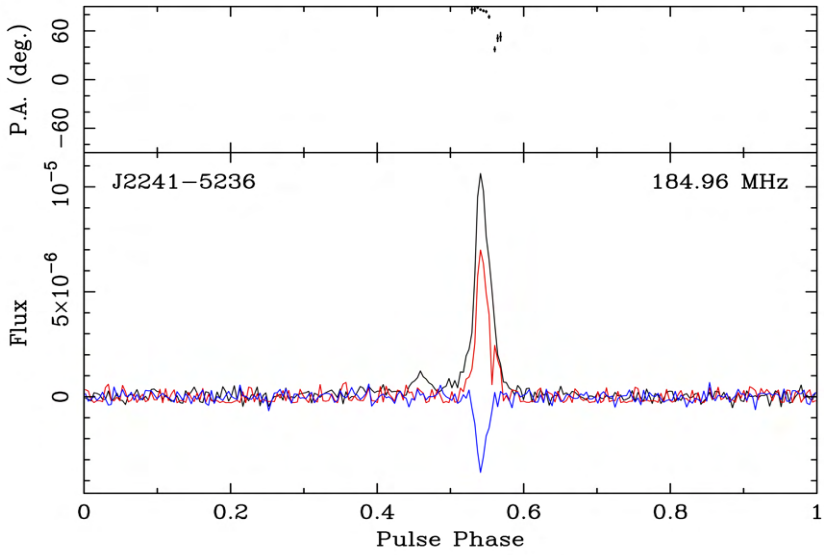

Figure 3.7: Polarimetric profile (lower panel) and PA curve (upper panel) for pulsar PSR J2241−5236 in the MWA's band centred at 185 MHz. The black solid line represents the total intensity whereas red and blue lines represent the linear and circular polarization, respectively. The profile is generated from the data taken on MJD 57288 with contiguous (1×30.72 MHz) mode of observation.

can be further improved in future as more observations accrue and the use of frequency-dependent templates becomes possible. Given PSR J2241−5236 is likely to be one of the high-priority targets for current and future PTAs, DM excess or variation at the level of $\sim 10^{-4}\,\mathrm{pc\,cm^{-3}}$ can be particularly important, as any residual uncorrected DM variations may impact the achievable timing precision.

Our observations also reveal a dual-precursor type feature in the pulse profile, which appears to be far less prominent at higher frequencies from Parkes. The precursor emission appears to have a steeper spectrum than that of the main pulse. The estimated spectral index for pulsar's main pulse emission, $\alpha_{\mathrm{MP}} = -2.25 \pm 0.10$, and there is no sign of any turnover within the observed

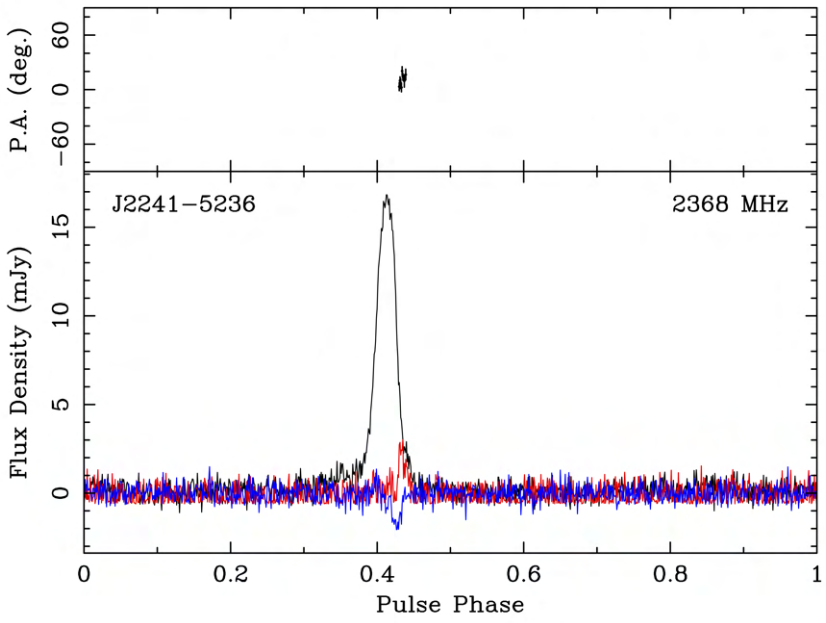

Figure 3.8: Polarimetric profile (lower panel) and PA curve (upper panel) for pulsar PSR J2241−5236 at the Parkes UWL band centred at ~ 2368 MHz. The black solid line represents the total intensity whereas red and blue lines represents the linear and circular polarization respectively.

MWA band. This is consistent with the general trend as reported in other recent studies of MSPs, and is promising for their low-frequency studies in general, particularly for finding new ones at low frequencies.

We measured temporal DM variations of the order of $\delta\mathrm{DM} = 0.0002\,\mathrm{pc\,cm^{-3}}$, with the available data for this pulsar, which can induce ~ 170 ns of timing delay in the 700-4000 MHz band. With the current limitations of the MWA (i.e., possible polarization leakage), we also attempted to study the low frequency polarimetric profile for the first time. With measured RM of $14.074 \pm 0.434\,\mathrm{rad\,m^{-2}}$ in the MWA's band, a noteworthy increase in the degree of linear polarization is observed from high (4 GHz) to low (100 MHz) frequencies.

Chapter 4

Frequency-dependent dispersion measures toward the millisecond pulsar J2241−5236

4.1 Summary

A more detailed analysis of the work presented in this chapter is now published in ApJ letters (Kaur et al., 2022). This includes additional analysis using the wideband timing technique, which takes into account the profile evolution in frequency. The revised analysis essentially confirmed the analysis and results presented in this chapter, thereby reinforcing the significance and reliability of the results presented in this chapter.

4.2 Introduction

Pulsar-timing array (PTA) experiments require sub-microsecond accuracies in the measured arrival times for the eventual detection of low-frequency (nanohertz) gravitational waves (GWs; e.g., Foster & Backer, 1990; Manchester et al., 2013; Demorest et al., 2013; Bailes et al., 2018; van Haasteren et al., 2011; Janssen

et al., 2015). With PTAs around the world striving to achieve timing precisions of $\sim$100-200 ns in pulse times of arrival (TOAs), it has become imperative to carefully assess various astrophysical and instrumental effects contributing to the timing noise budget, and to develop strategies to either mitigate or correct for them in the timing data, in order to reach the required sensitivity to detect nanohertz GWs (Cordes & Shannon, 2010; Lentati et al., 2013; Levin et al., 2016; Lam et al., 2016; Shannon et al., 2014; Foster et al., 2015).

The advent of wide-band receivers, such as the Ultra-Wideband Low-frequency Receiver (UWL; Hobbs et al., 2020) at the Parkes telescope, the wide-band receiver at the MeerKAT (580-1670 MHz) telescope (Bailes et al., 2020), and the ultra-broadband receiver at the Effelsberg 100 m radio telescope (Freire, 2012), is highly promising for improved timing precision in PTA observations. However, these large bandwidths also necessitate additional considerations, for example, correcting for the interstellar medium effects on pulsar signals such as dispersion, scintillation and multi-path scattering, which scale strongly with the inverse of the observing frequency.

As described in Chapter 1, the dispersive delay is proportional to the column density of free electrons along the line of sight of the pulsar. The dispersion measure (DM) is the integral of the electron density along the line of sight (LOS). For PTAs it is a time-varying quantity, largely due to the pulsar's proper motion (typically $\sim$ 50-100 $\mathrm{km\,s^{-1}}$), as a result of which different parts of the ISM are sampled by the observations. Since spatial variations in electron density are present on a wide range of scales, ($\sim 10^6$ to 10^{13} m or even larger; Lam et al., 2015; Cordes & Rickett, 1998), PTA observations require measuring and correcting for DM at every observing epoch. Measuring DMs accurately and applying suitable corrections for their temporal variability has been an integral part of pulsar timing array experiments (Jones et al., 2017; Lam et al., 2016; Keith et al., 2013; Lee et al., 2014; You et al., 2007).

Aside from the time variability in DM, there may also be a frequency de-

pendence; sometimes referred to as 'chromaticity' in DM. This effect was first investigated by Cordes et al. (2016), who provide a detailed theoretical account of the underlying physics. It arises as a result of multi-path scattering by the electron density fluctuations present in the ISM. Since the radiation received at a given frequency depends on the size of the scattering disk, which scales as the square of the observing wavelength ($\theta_s \propto \lambda^2$), the volume of the ISM (or path lengths) sampled at lower frequencies can be significantly larger than those at higher frequencies, especially when observations are made over very large bandwidths (hundreds of MHz to a few GHz). Cordes et al. (2016) formulated this effect theoretically, and demonstrated it through simulations.

Such a frequency dependence in DM can give rise to subtle differences in DMs as measured in observations, depending on the observing frequency and the bandwidths over which such measurements are made. For example, a DM difference of $\sim 10^{-5}\,\mathrm{pc\,cm^{-3}}$ can induce 110 ns of timing noise at the PTA timing frequency bands $\sim$1-2 GHz (Cordes et al., 2016). Recent work by Donner et al. (2019) reported the detection of a frequency dependence in DM in their observations of PSR J2219+4754 made using the low-frequency ($\sim$50-225 MHz) data.

As is well known, the pulse profile evolution also has a strong frequency dependence, and therefore accounting for this in the DM determination is very important. Disentangling the profile evolution from the DM was earlier investigated using wide-band observations by Hassall et al. (2012). The development of wide-band receivers has led to the development of wide-band timing techniques, which attempt to model timing data by jointly modeling the spectral evolution of the pulse profiles as well as the potential dependence of the DM (Pennucci, 2019; Lentati et al., 2017; Liu et al., 2014). Recently, Alam et al. (2020) tried to examine wideband timing technique on the NANOGrav 12.5 year data. Their analysis produce consistency with the narrow-band timing (with the use of single frequency analytic templates) for the measured DMs and presented that wide-band timing is beneficial for high-DM pulsars with profile broadening, or sources

that are weak and scintillating. However, wide-band timing is beneficial even for low DM pulsars as shown by Krishnakumar et al. (2021) and in this thesis Chapter 5.

Another important source of noise is additional DM contribution that may arise in the case of binary systems with black widow type companions. There are studies that show a DM modulation as a function of the orbital phase. These modulations arise when the companion winds interact with the pulsar signal. Such variations are reported towards many eclipsing millisecond pulsars; (Fruchter et al., 1990; Kudale et al., 2020; Polzin et al., 2019, 2018; Parent et al., 2019; Guillemot et al., 2019; Nice et al., 2005). Therefore, understanding the pulsar's binary system is very important for pulsar timing to check for any residual DM noise contribution for such systems.

This Chapter presents the measurements of frequency-dependent DMs toward the millisecond pulsar PSR J2241−5236. Its low DM ($11.41151\,\mathrm{pc\,cm^{-3}}$) and short pulse period (2.18 ms) makes it an important target for PTAs. As described in Chapter 3, the pulsar is in a 3.5 hour, almost circular orbit with a low-mass ($\sim 0.012\,\mathrm{M_\odot}$), black widow (BW) type companion (Keith et al., 2011). For this work, observations were carried out *contemporaneously* using the Murchison Widefield Array (MWA), the upgraded Giant Metrewave Radio Telescope (uGMRT), and the new ultra-wide band low-frequency receiver (UWL) at the Parkes radio telescope, thus providing a frequency coverage from 80 MHz to 4 GHz.

4.3 Observations

PSR J2241−5236 was observed contemporaneously, (i.e. within a 24 hour duration) using the MWA, Parkes and uGMRT in November 2019. This pulsar is ideal for our analysis since it has a narrow pulse profile and almost negligible profile evolution across the observed frequency range. The pulsar was observed at multiple (three) epochs with all three telescopes. At two of the epochs, it was

observed within a 24 hour block using all three telescopes, while at one of the epochs only two telescopes (uGMRT and Parkes) were available. Observational details are summarised in Table 4.1, and are further elaborated below.

Date of observation	Telescope (length of observation)(No. of scans)		
07 July 2019	–	–	MWA (full orbit)
16 July 2019	–	–	MWA (full orbit)
07 November 2019	–	uGMRT BAND3 (90 min)(3)	–
08 November 2019	Parkes (65 min)(3)	–	MWA (45 min)(1)
09 November 2019	Parkes (65 min)(3)	–	–
12 November 2019	–	uGMRT BAND3 (105 min)(4)	–
13 November 2019	Parkes (65 min)(3)	–	–
29 November 2019	Parkes (65 min)(3)	uGMRT BAND4 (65 min)(2)	MWA (45 min)(1)
30 November 2019	Parkes (65 min)(2)	–	–

Table 4.1: Observation details of the multi-telescope campaign for pulsar PSR J2241−5236. The MWA full orbit data were taken in multiple 10 minute observations, each separated by 15 minutes to cover the maximum 3.5 hour binary orbit. See Section 4.3.3.1 for further details.

4.3.1 Parkes

Pulsar J2241−5236 is regularly monitored at Parkes under the ongoing Parkes pulsar timing array (PPTA; Manchester et al., 2013) project. The use of the Ultra-Wideband Low receiver (UWL) provides simultaneous frequency coverage from 704 to 4032 MHz. It records signals at three adjacent radio frequency bands; 704-1344 MHz, 1344-2368 MHz and 2368-4032 MHz. The entire band is sampled by digitisers for both polarisations. Digitised data from the telescope's focus cabin are transported to the signal pre-processing units where the entire band is channelised into 26 contiguous sub-bands, each 128 MHz wide, and for each

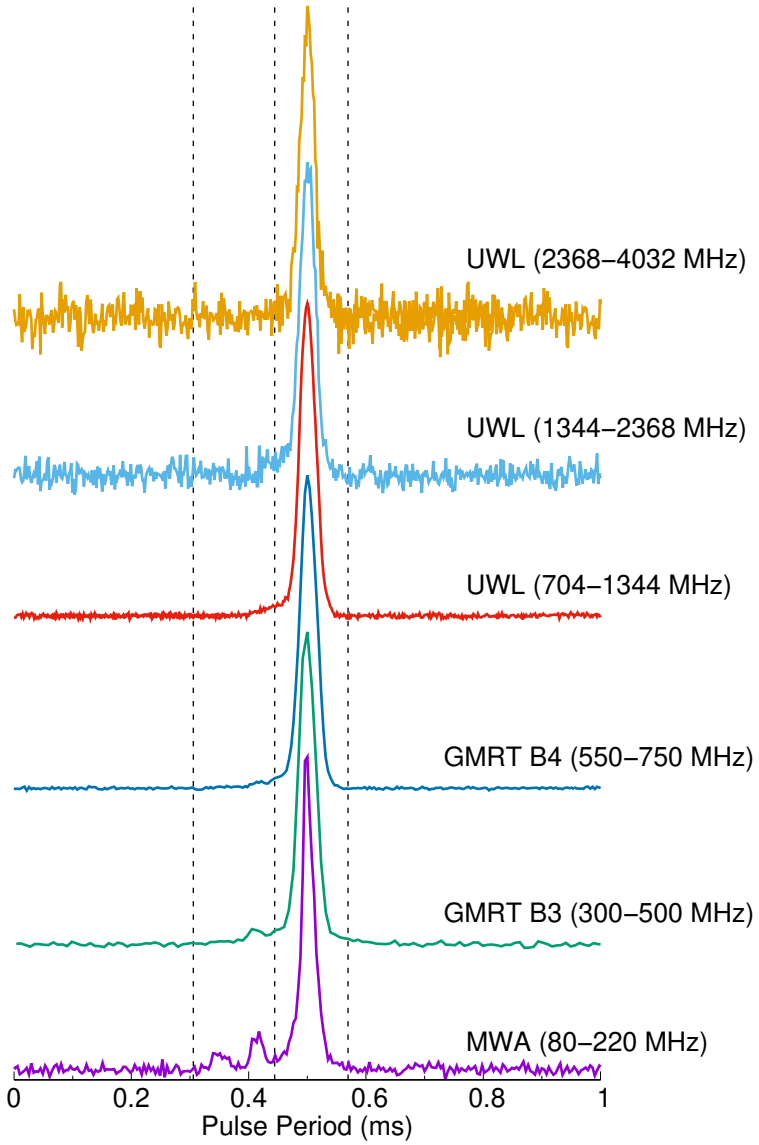

Figure 4.1: Integrated pulse profiles of PSR J2241−5236 at frequencies from 150 MHz to 4.0 GHz. The Parkes profiles were obtained by dividing the entire UWL band into 3 sub-bands to showcase the negligible profile evolution.

polarisation.

Parkes observations used the pulsar fold mode where data are synchronously folded modulo the pulse period, with 1024 phase bins in each of the 1 MHz channels, and integrated for 30 s before written out to disk. Data were coherently dedispersed at a DM of 11.41151 pc cm^{-3}, and the full Stokes information was recorded.

4.3.2 The uGMRT

We conducted observations using the upgraded GMRT (uGMRT; Gupta et al., 2017). Two observations were made in BAND3, which covers from 300 to 500 MHz, and one observation in BAND4, which covers 550 to 750 MHz. Observations were made using the phased array total intensity mode with an average 28 antennas, the data from which were coherently combined to generate spectral (channelised) voltages time series data. These spectral voltages were processed in real-time for coherent dedispersion using the coherent de-dispersion processing pipeline of the uGMRT wideband backend (GWB, Reddy et al., 2017). For all observations, data were recorded in 512×0.390 MHz coherently-dedispersed filter-bank format, and at 10.24 μs time resolution, in order to avoid residual dispersion smearing using the catalog DM of 11.41085 pc cm^{-3}(at the time of observations). In order to avoid de-phasing of an array due to ionospheric effects or antenna gain changes, we performed re-phasing of the array periodically, at an average interval of $\sim$ 30 minutes, using a nearby phase calibrator $2225-049$, which has a flux density of 15 Jy at P-band (400 MHz). The incoming data are then processed by the GWB, and data were recorded with 256 phase bins across the pulse period, for both the uGMRT BAND3 and BAND4 observations.

4.3.2.1 Orbital coverage

Given the far southern declination of the pulsar, and the geographic location of the uGMRT, PSR J2241−5236 is visible for a maximum of 2.1 hours on any

particular day. This covers approximately 60% of the orbit. In order to span the full 3.5 hour orbit, two successive observations were carried out, 5 days apart. As shown in Figure 4.3, the first observation on 7$^{\rm th}$ November 2019 covered the orbital phase range from $\sim$0.6 to 0.8 and 0.0 to $\sim$0.1, while the second observation on 12$^{\rm th}$ November 2019 covered from $\sim$0.8 to 1.0 and 0.0 to $\sim$0.3 phase ranges. The two observations thus partially covered the orbit, with no coverage for $\sim$0.3 to $\sim$0.6 in the orbital phase range (see Figure 4.3). Data recording was interrupted for a short duration ($\sim$5 minutes) to accommodate the phase calibrators and re-phasing of the array.

4.3.3 The MWA

The ability for reconstructing higher time resolution data (at $\sim 1\,\mu$s resolution) via an inversion of a polyphase filterbank (PFB) operation is described in detail by McSweeney et al. (2020). Observations were made at two epochs, separated by three weeks, with the MWA's voltage capture system (VCS; Tremblay et al., 2015). The VCS records 24 (1.28 MHz wide) coarse channels, each of which has been finely channelized to 10 kHz. These data were recorded in both polarizations, from all 128 tiles. The 30.72 MHz observing bandwidth of the MWA can be flexibly placed (e.g., 12×2.56 MHz coarse channels) anywhere across the nominal operating frequency range (80-300 MHz). For the observations presented in this Chapter, a frequency set-up similar to that described in 3 was employed, i.e., a distributed 24×1.28 MHz channel mode, covering a frequency range from 80 MHz to 220 MHz. The VCS data were then transported to the Pawsey super-computing facility, where all further processing, including calibration and beamforming, was carried out.

4.3.3.1 Orbital coverage

An ability to sample the full orbit of the pulsar in a single day can help minimise any temporal variations in DM with the orbital phase, particularly for a black

Date of obs (MJD)	MWA (80-220)	uGMRT B3 (300-500)	uGMRT B4 (550-750)	Parkes UWL (704-1344)	Parkes UWL (1344-2368)	Parkes UWL (2368-4032)
07-11-2019 (58794)		11.41134(2)				
08-11-2019 (58795)	11.411327(4)			11.410(2)	11.4075(8)	11.397(4)
09-11-2019 (58796)				11.4099(4)	11.411(1)	11.397(4)
12-11-2019 (58799)		11.41131(2)				
13-11-2019 (58800)				11.41119(2)	11.4084(8)	11.397(3)
29-11-2019 (58816)	11.411301(3)		11.41112(2)	11.4111(4)	11.408(1)	11.393(3)
30-11-2019 (58817)				11.41132(9)	11.4086(9)	11.389(5)

Table 4.2: Observation details and measured DM values from the contemporaneous data. The top parenthesis represents the frequency range covered from each telescope. The DM uncertainties are also presented in parenthesis along with the measured DM values. For the MWA data, the DM precision is quite high of the order of $10^{-6}\,\mathrm{pc\,cm^{-3}}$. The precision is $10^{-5}\,\mathrm{pc\,cm^{-3}}$ for the uGMRT bands and ranges between 10^{-3} to $10^{-5}\,\mathrm{pc\,cm^{-3}}$ for the UWL band.

widow type of binary system. With the VCS, the maximum recording time is however limited to $\sim$ 90 minutes, which will result in a data volume of $\sim$ 50 TB (data rate = $7.78\,\mathrm{GB\,s^{-1}}$). As demonstrated in diagram 4.2, the data were recorded in multiple 10 minute recordings at $\sim$15 minute intervals between the recordings. This allowed us to optimally use the available 90 minutes of recording time to sample the full binary orbital period of 3.5 hours. A "picket-fence" mode of observation was adopted in order to achieve a large frequency leverage, but with a lightly modified frequency-channel selection, as shown in Figure 4.2. This was done to increase the sub-bandwidth in order to compensate for the reduced S/N associated with breaking up the recording time into 10 minute chunks. The main purpose was to ensure sufficiently high S/N to detect the pulsar in each of the sub-bands in 10 minute recordings (as compared to typical observing time of $\sim$1 hour for this pulsar that was used for the work presented in Chapter 3). In summary, by making an optimal use of available resources in bandwidth and time, the full 3.5 hour orbit was sampled in a total of eight 10 minute recording runs.

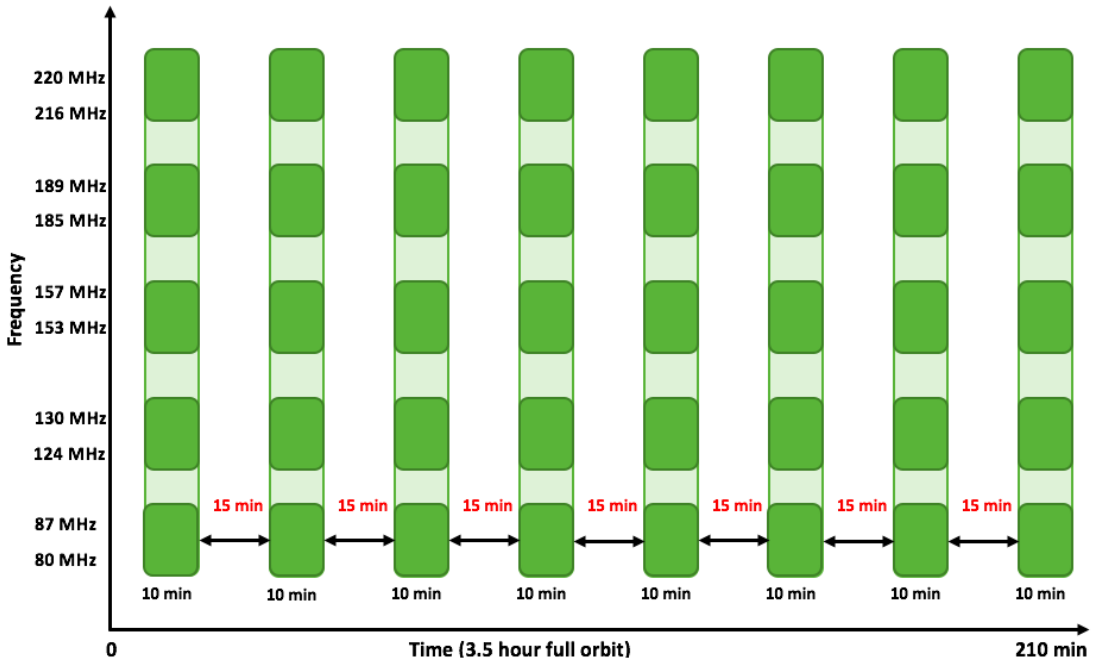

Figure 4.2: Observation strategy used for recording 3.5 hour orbit within 90 minute recording limit of the MWA-VCS system. Data was recorded every 15 minute for 10 minutes, hence, covering the orbit in total 8×10 minute recordings. The y-axis represents the frequency sub-bands used to cover maximum possible frequency lever arm i.e. 80-220 MHz.

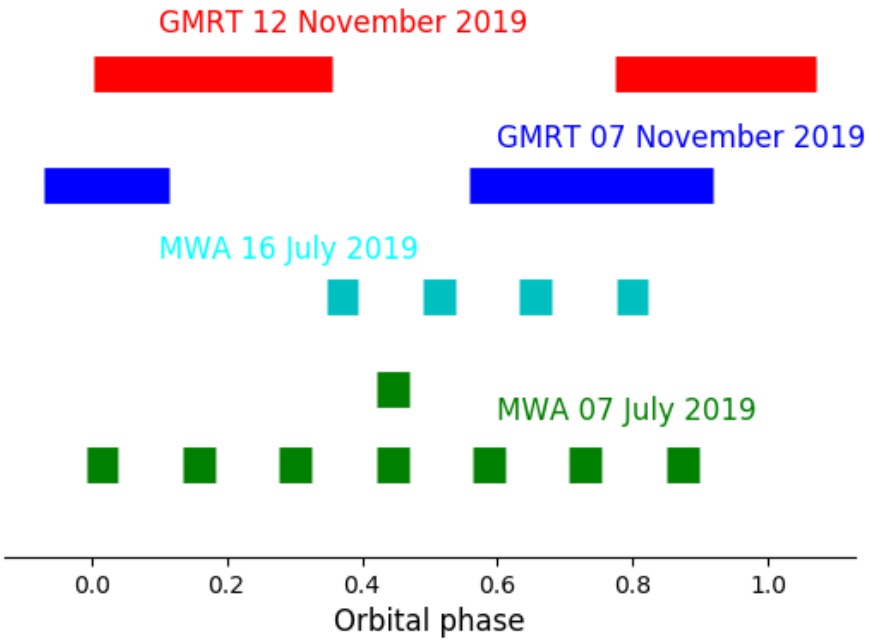

Figure 4.3: Representation of the orbital phase covered in a single day in different observations by the MWA and uGMRT BAND3.

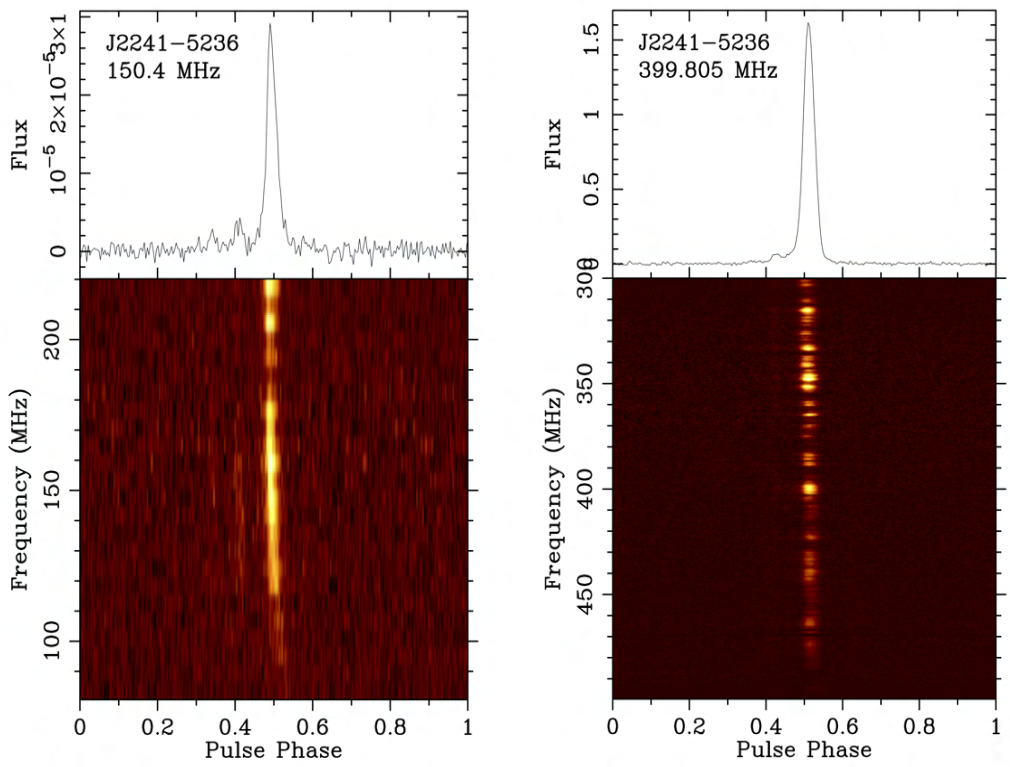

Figure 4.4: Coherently de-dispersed pulsar detections shown as frequency and time averaged pulse profiles in the top panels and frequency vs. pulse phase (bottom panels). Left: detection across the MWA's band (80-220 MHz, centred at 150.4 MHz), and right: detection across uGMRT BAND3 (300-500 MHz, centred at 399.805 MHz). The MWA data are at time resolution of $\sim 1\,\mu$s and uGMRT data are at $\sim 10\,\mu$s time resolutions.

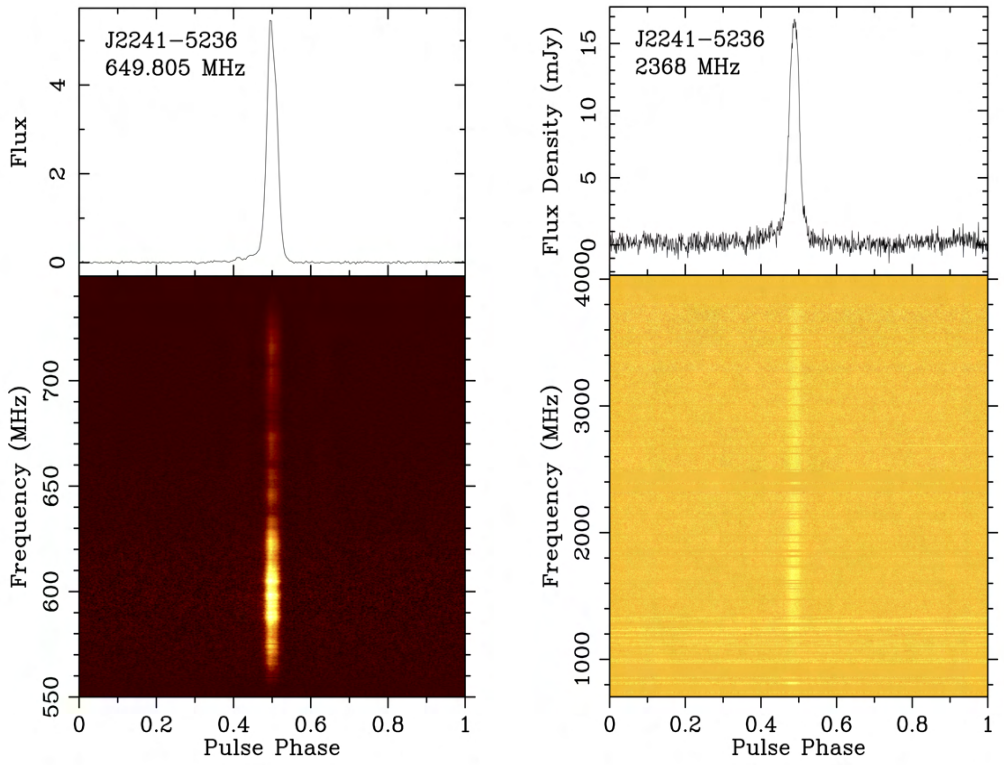

Figure 4.5: Coherently de-dispersed pulsar detections shown as frequency and time averaged pulse profiles in the top panels and frequency vs. pulse phase (bottom panels). Left: detection across the uGMRT BAND4 (550-750 MHz, centred at 649.805 MHz), and right: detection across the entire UWL band (704-4032 MHz, centred at 2368 MHz). The uGMRT data are at time resolution of $\sim 10\,\mu$s and UWL data are at $\sim 1\,\mu$s time resolutions.

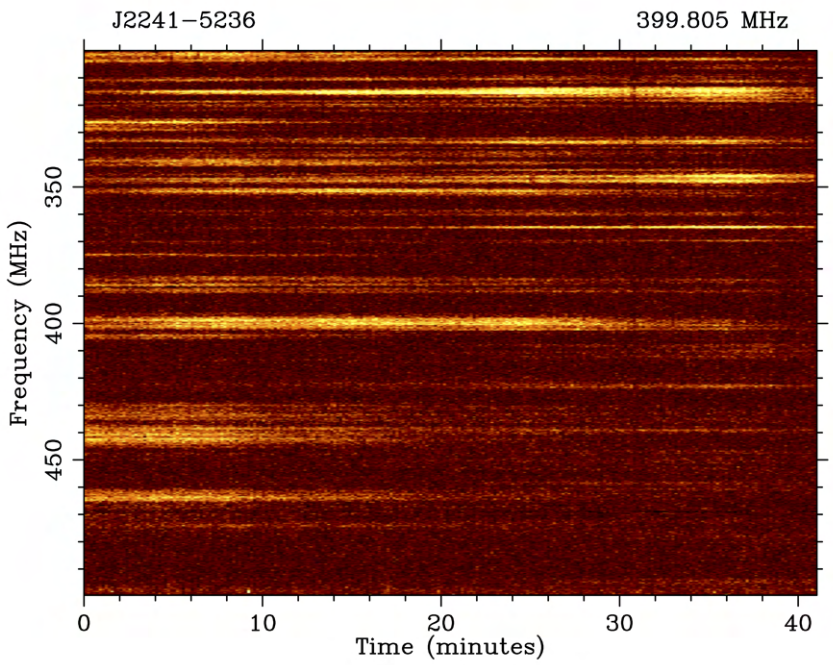

Figure 4.6: Dynamic scintillation spectra of PSR J2241−5236 from uGMRT BAND3 observations over a 200 MHz bandwidth.

4.4 Data processing and calibration

4.4.1 Parkes

Parkes data reduction closely followed the procedures as described in Hobbs et al. (2020) and Dai et al. (2019). In short, we removed the 5 MHz of the bandpass at each edge of the 26 sub-bands to mitigate aliasing. The "CoastGuard" package (Lazarus et al., 2016) was used to carry out the automatic RFI cleaning. Pulsed noise signal recorded before each observation, together with observations of the radio galaxy 3C 218 and PSR J0437−4715, were used to calibrate the differential and absolute gains and polarimetric responses of the receiver (cf. van Straten, 2004). After the calibration, data were further RFI cleaned using the `paz` routine of `PSRCHIVE` by carefully (manually) flagging the problematic channels. The calibrated and RFI cleaned data were then polarization and time averaged for further timing and DM analysis.

4.4.2 The uGMRT

The uGMRT is located in a RFI hostile environment, because of which data are typically RFI contaminated. Although online RFI mitigation is possible with the uGMRT system, that was not used for our observations. All the RFI excision analysis was performed offline using the `paz` routine of `PSRCHIVE` by identifying and flagging the problematic channels. uGMRT BAND3 data are typically more prone to RFI, resulting in $\sim 20\%$ excised data, whereas only $\sim 10\%$ data were excised in BAND4.

4.4.3 The MWA

The MWA make use of the VCS and the post-processing chain (Bhat et al., 2016; McSweeney et al., 2017). All the calibration and processing were performed on the Galaxy cluster at the Pawsey Supercomputing Centre. The MWA-VCS data can be combined for beamforming either coherently or incoherently. For our

analysis we used coherent beamforming to generate a phased-array beam, which involves considering the polarimetric response from each of the tiles along with the cable and geometric delays, as well as complex gains of the tiles (Ord et al., 2019).

Data were then calibrated using one of the standard calibrators 3C444, recorded in pointed observations prior to pulsar observations. Amplitude and phase calibration solutions were generated for each frequency sub-band using the real time system (RTS; Mitchell et al., 2008). A coherent tied-array beam is produced by phasing up of the signals from all tiles with good calibration solutions. The high time resolution, (coarse channelised) data were recovered using an enhanced capability of the beamforming pipeline (McSweeney et al., 2020). Coherently de-dispersed data were then generated using the DSPSR pulsar package (van Straten & Bailes, 2011) and were written in the form of archives with $\sim 0.78\,\mu$s time resolution.

4.5 DM Measurements

As evident from Figure 4.7, 4.9 and 4.11, there is no significant profile evolution within any of the 3 bands as well as throughout the entire observed band $\sim$100 MHz to 4 GHz (Figure 4.1). Ordinarily, such large bandwidth observations would be subbanded into smaller frequency chunks, and TOAs would be generated from each subband in order to properly account for the profile evolution (e.g., Pennucci, 2019). For PSR J2241$-$5236, even though there is some measurable profile variation from the MWA to UWL band due to precursor emission, the degree of variation of the main pulse is very small. In fact, the measured pulse width (W_{10}) changes from the MWA to UWL band by about $\sim$10% (150 μs to 130 μs). The degree of profile evolution within any single frequency band (as shown in Figure 4.7 and Figure 4.11) is also very small ($\sim$ 2%). The degree of profile evolution within any single frequency band (as shown in Figure 4.13) is generally small; in terms of measured pulse width (e.g., quantified using W50, at

50% of the peak), we measure a change of ∼2% across the two uGMRT bands, ∼5% across the MWA band, whereas it is ∼10% across the large frequency range of Parkes UWL (0.7 to 4 GHz). Given all this, we have chosen a single template for each observing band; specifically, four different templates were used each for the MWA, uGMRT BAND3, uGMRT BAND4, and Parkes-UWL, to incorporate the small degree of profile evolution.

Since we have not used any frequency-dependent templates for this pulsar, as a further cross check, we used the `pat` routine from `PSRCHIVE` to examine the difference. Figure 4.14 shows an example screenshot from this analysis, in the MWA's band, where the three panel output shows (from bottom up): (1) the profile, (2) the template, and (3) the difference between the two. The goodness of fit for our templates, can be justified considering the lack of any prominent profile-like feature appearing in the residuals.

Observing Band (frequency range MHz)	Post-fit residuals (μs)	No. of TOAs (per observation)	Template used (frequency MHz)
MWA (80-220)	1.5	24	150
uGMRT BAND3 (300-500)	1-2	32	400
uGMRT BAND4 (550-750)	0.1-0.6	32	650
UWL (704-4032)	0.9-3.5	26	1300

Table 4.3: A summary of observing bands and timing analysis.

For the UWL data, we chose the Parkes 20 cm template. UWL data were frequency averaged to 26 channels and then cross-correlated with the template to obtain the TOAs. For the uGMRT data (i.e., BAND3 and BAND4), we chose one of the brightest scans to generate a noise free analytic templates by modeling a sum of von Mises using the `paas` utility of `PSRCHIVE`. The uGMRT data were then frequency averaged to 32 frequency channels and then cross-correlated with respective analytic templates to obtain the TOAs. For the MWA data, we used an analytic template from one of our bright observations taken in 2017 (also

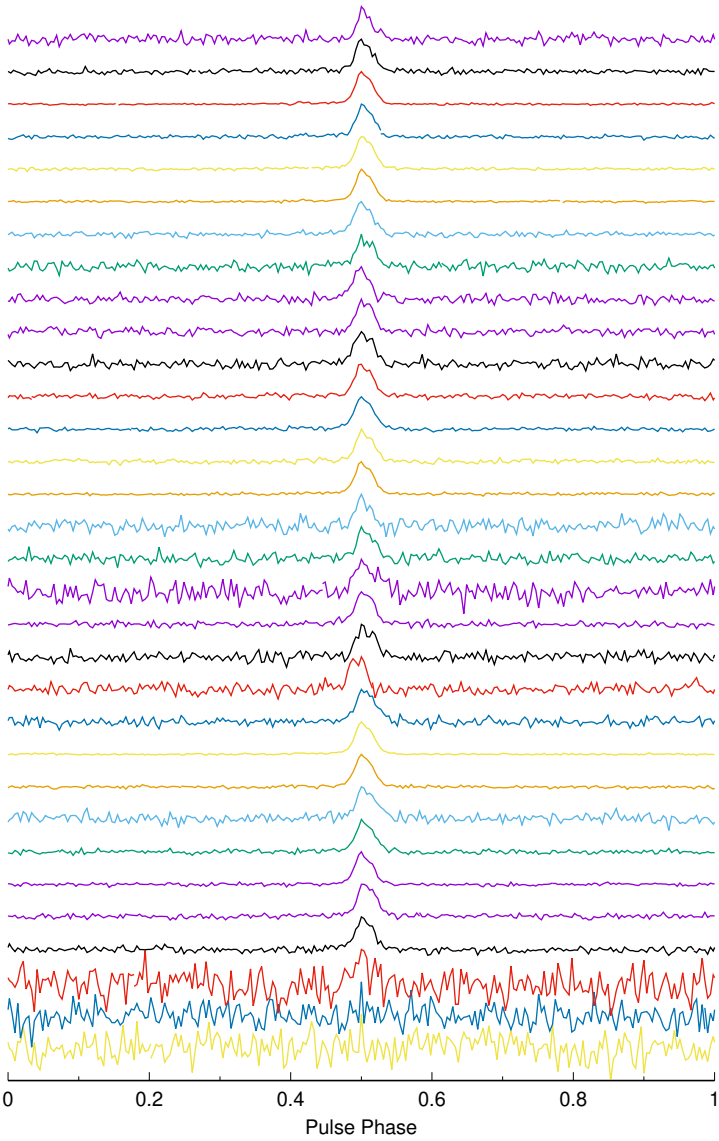

Figure 4.7: Profile stack of uGMRT BAND3. Frequency averaged to 32 channels therefore, 32 profiles stacked. Plot shows that there is negligible profile evolution of the pulsar over the entire bandwidth. The noisy profiles are due to RFI and were flagged while measuring the TOAs.

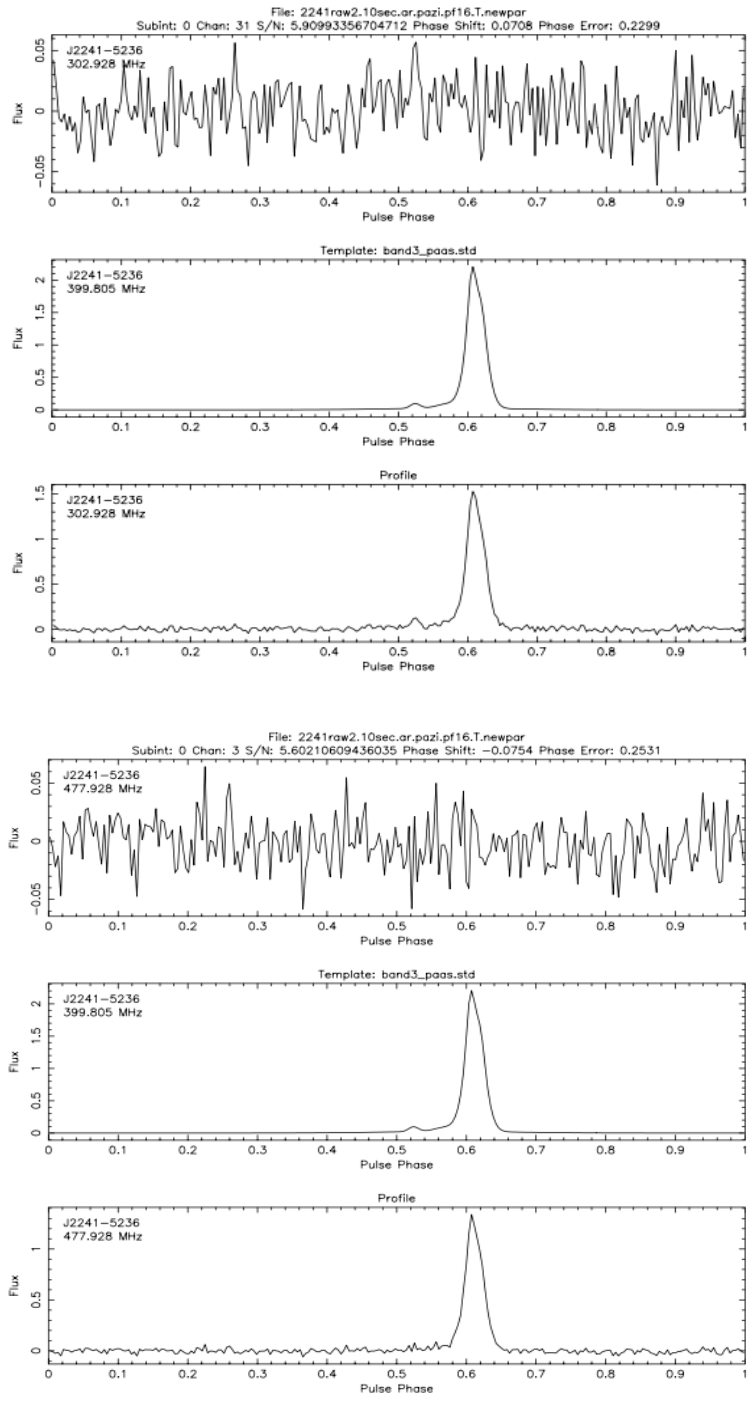

Figure 4.8: Pulse profile residuals when the top and bottom frequency profiles are cross correlated with the template. Top plot for the lowest frequency profile and bottom plot for highest frequency profile of uGMRT BAND3. Each plot has three panels representing pulse profile in the lowest panel, the middle one is the template, and the top panel shows the difference between the profile and template.

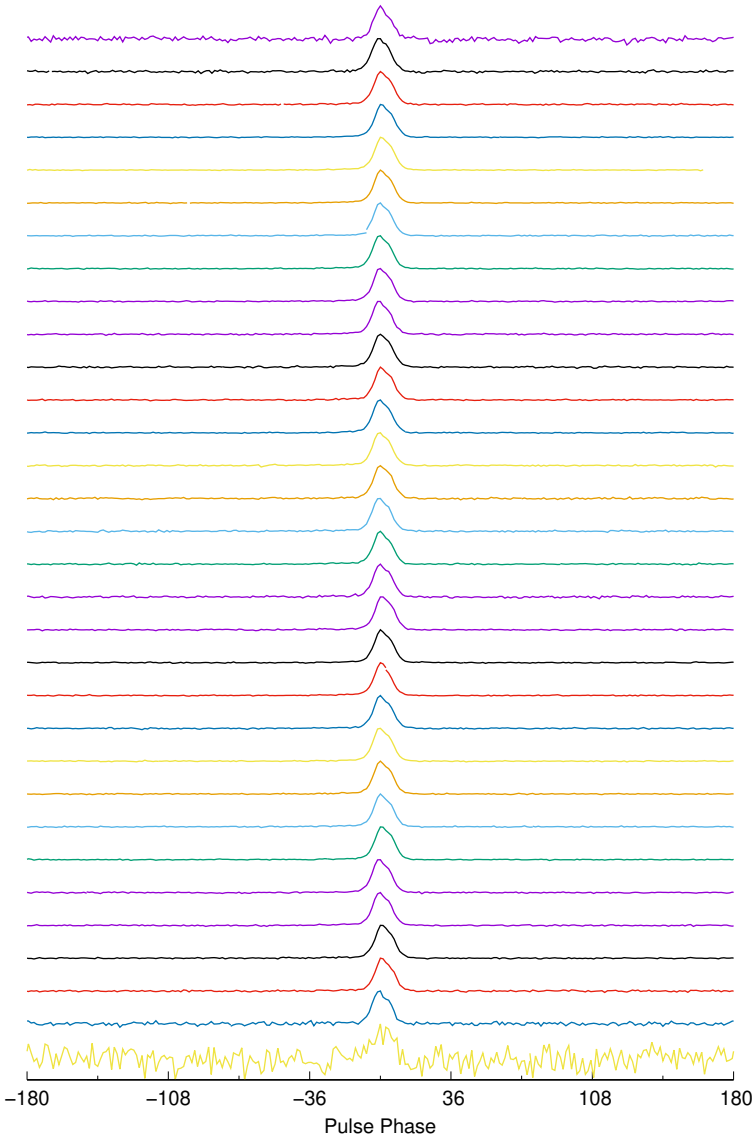

Figure 4.9: Profile stack of uGMRT BAND4. Frequency averaged to 32 channels therefore, 32 profiles stacked. Plot shows that there is negligible profile evolution of the pulsar over the entire bandwidth.

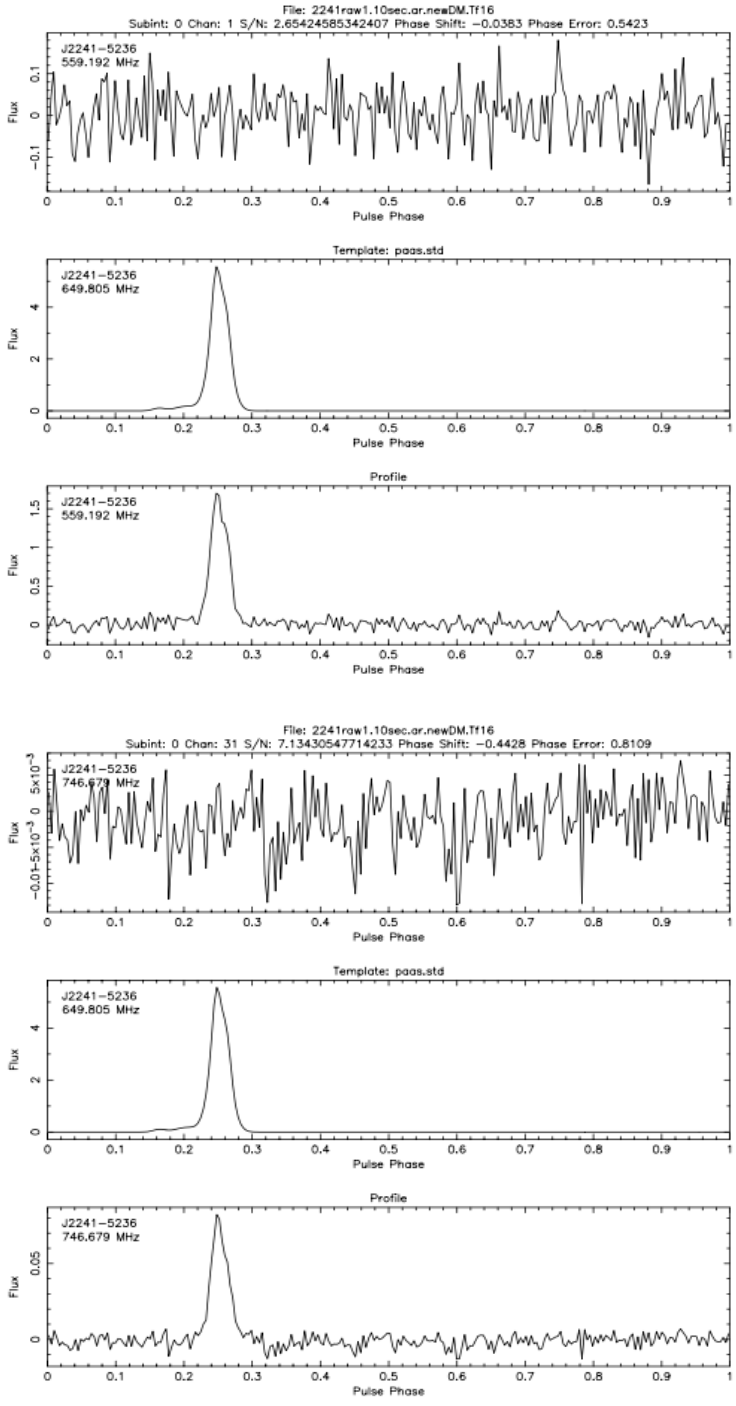

Figure 4.10: The top plot for the lowest frequency profile and bottom plot for highest frequency profile of uGMRT BAND4. Description same as figure 4.8.

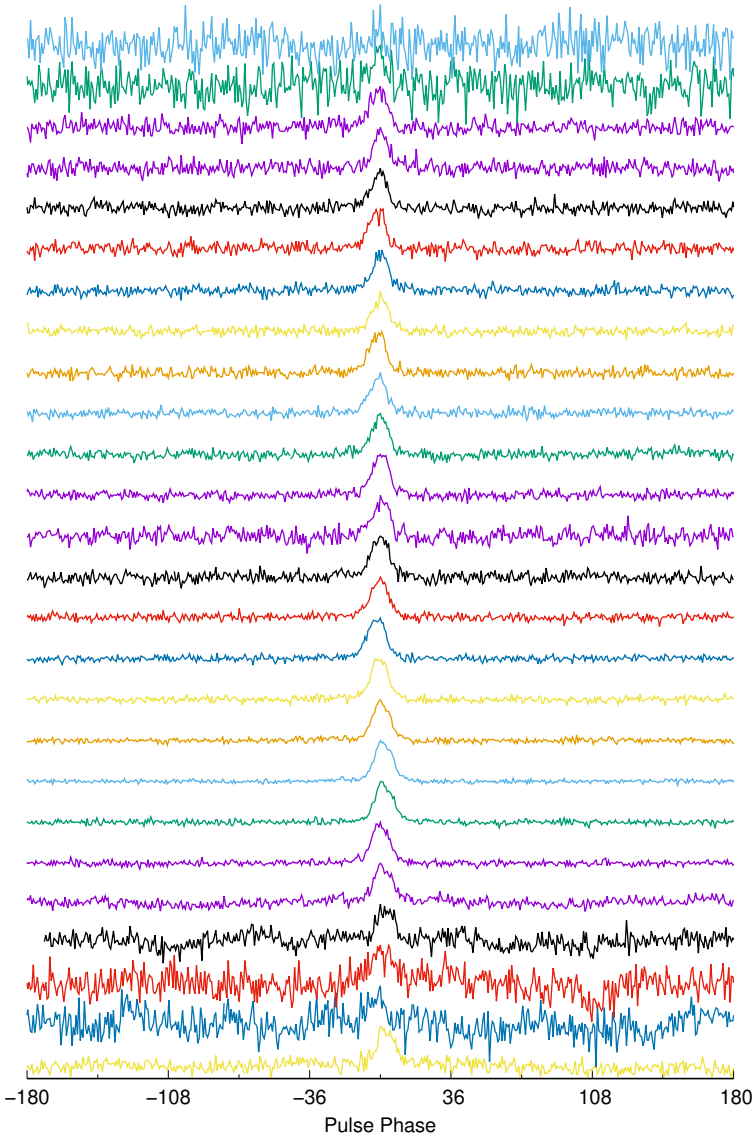

Figure 4.11: Profile stack of Parkes UWL band covering 700 MHz to 4 GHz. Frequency averaged to 26 channels therefore, 26 profiles stacked. Plot shows that there is negligible profile evolution of the pulsar over the entire UWL band. The noisy profiles are due to RFI and were flagged while measuring the TOAs.

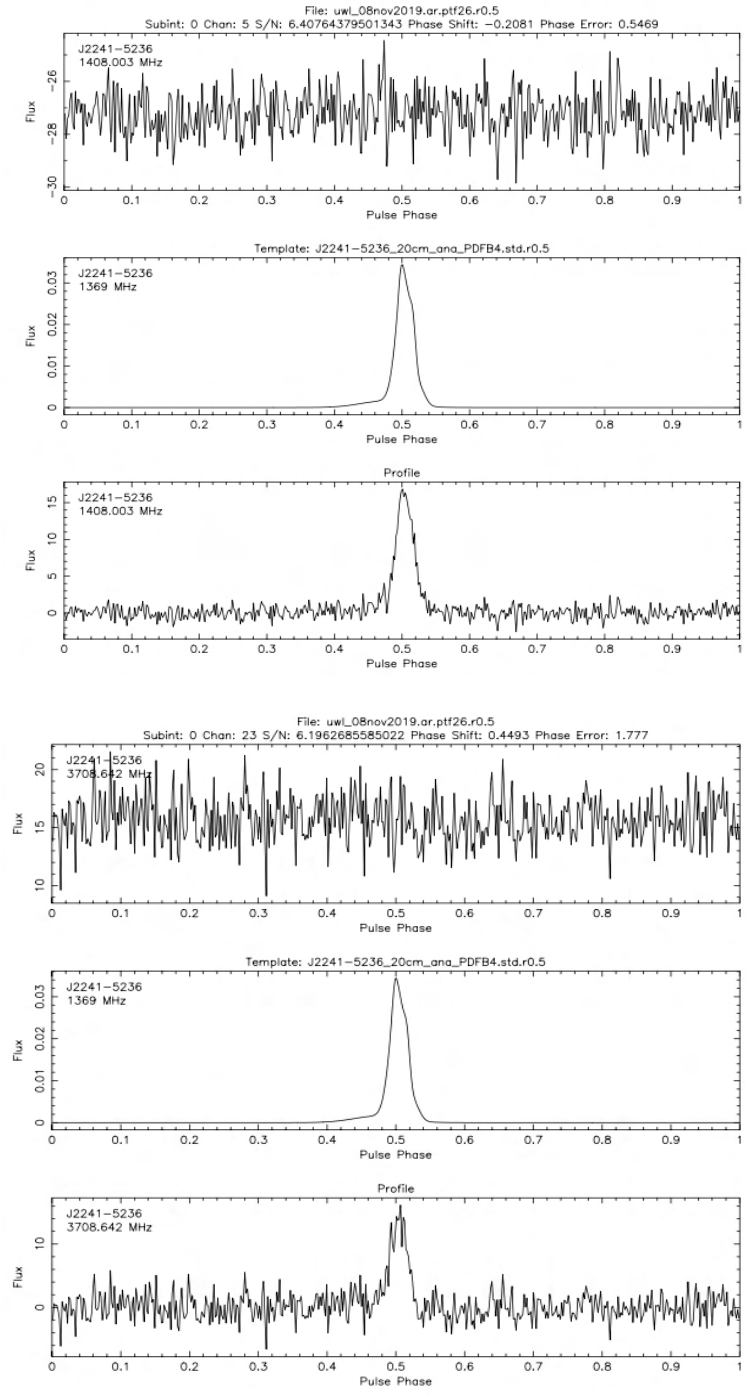

Figure 4.12: The top plot for the lowest frequency profile and bottom plot for highest frequency profile of the UWL band. Description same as figure 4.8.

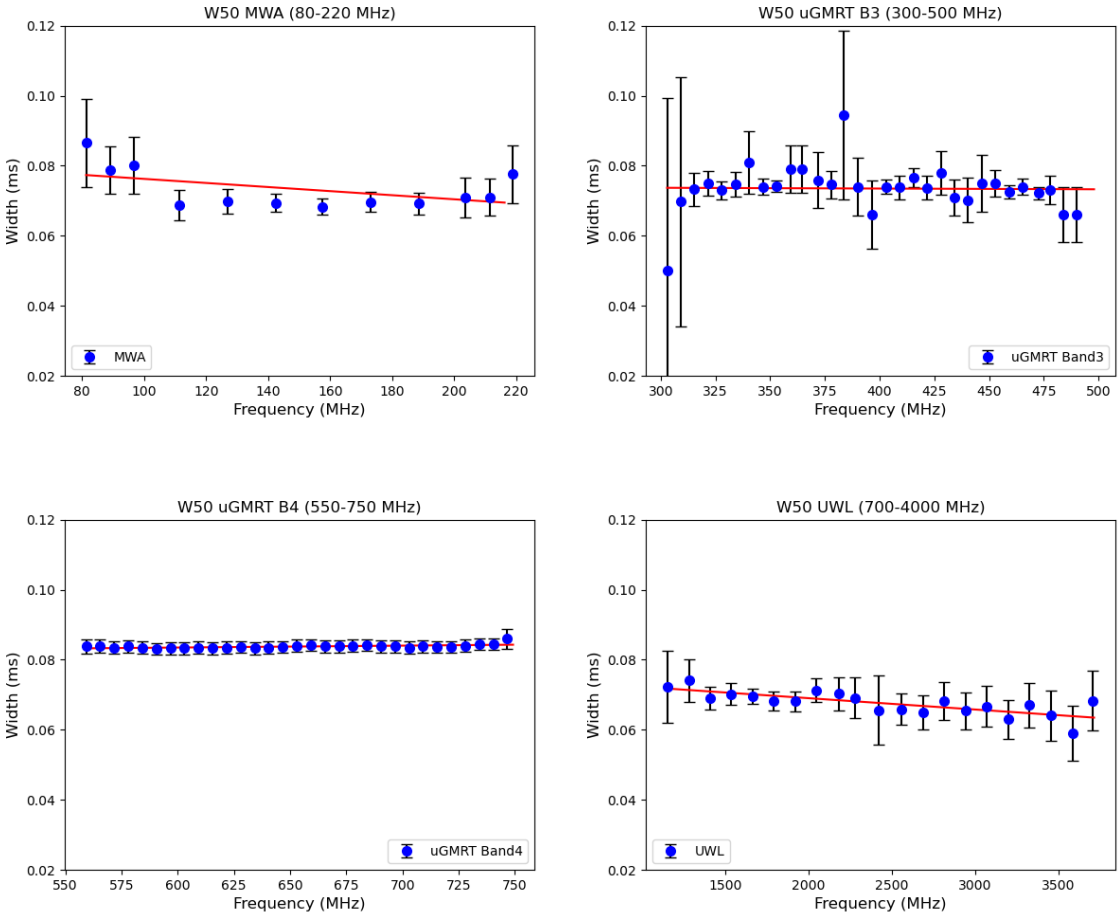

Figure 4.13: These figures represent the degree of profile evolution, quantified in terms of the change in W50, which is $\sim$ 2% across the two uGMRT bands (with fractional bandwidths of 50% and 30% respectively for uGMRT BAND3 and 4) and $\sim$5% for the MWA band (from $\sim$80 to 220 MHz), whereas the degree of profile evolution across the UWL range is $\sim$10% in terms of measured changes in W50.

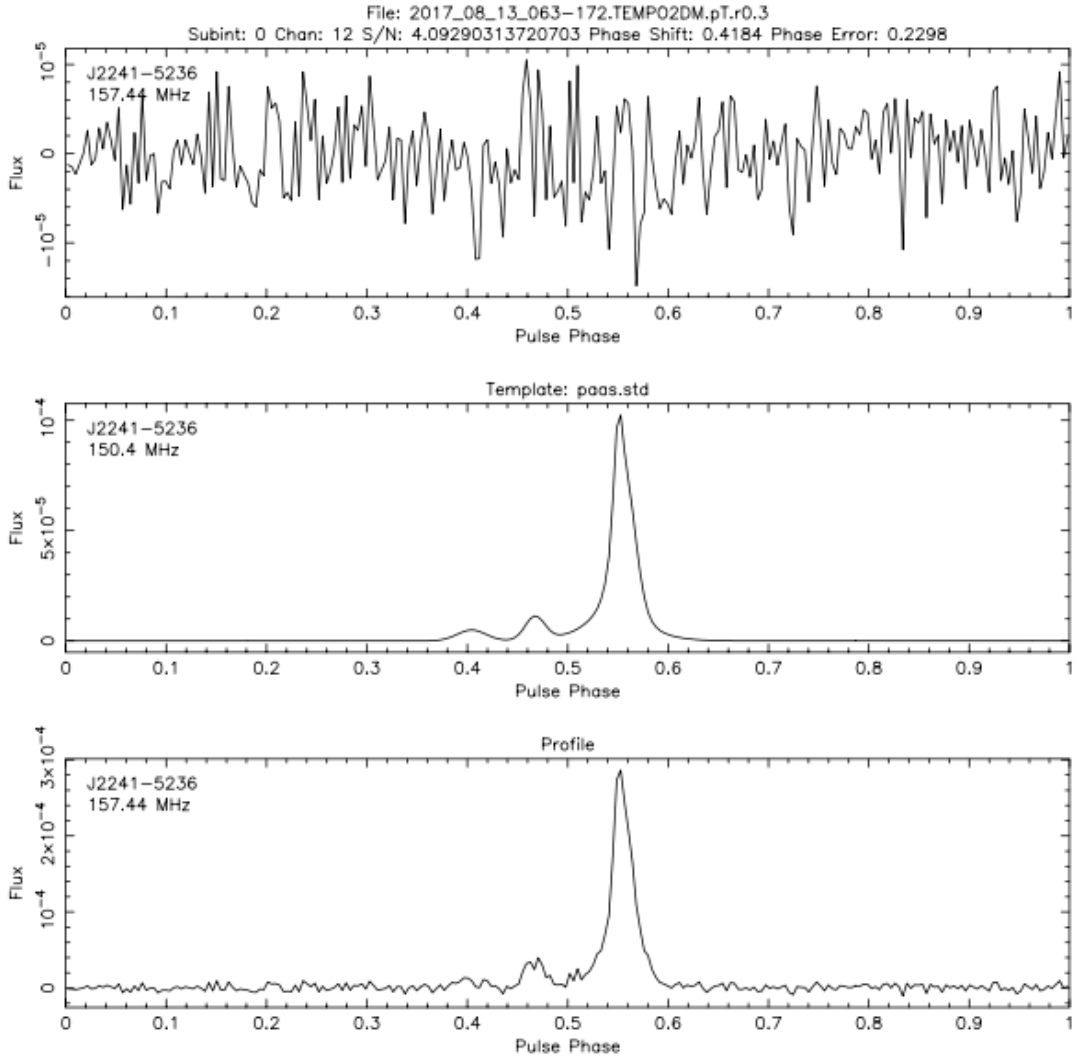

Figure 4.14: A screenshot of output from the `pat` command. The lowest panel is the pulse profile, the middle one is the template, and the top panel shows the difference between the profile and template.

published in Kaur et al., 2019) to generate an analytic template. The analytic template is then cross-correlated with the observed profiles to obtain the TOAs using the `PSRCHIVE` package.

The TOAs are then analysed using the pulsar timing package TEMPO2 (Hobbs et al., 2006) to determine the DM. We adopted the latest available timing solution of the pulsar and only fit for the DM in this analysis. As described in 3, for most of our observations, with the MWA, we typically achieve a timing precision of the order of $\sim 1\,\mu$s. Timing precision of the order of $\sim$2 μs was achieved with uGMRT BAND3 and a better timing precision of $\sim$0.5 μs with BAND4. For our Parkes analysis, timing precision range from 0.9 μs to 3.5 μs across the three sub-bands of the UWL. Details are described in Table 4.3. This timing precision is reasonable considering the use of the multi-frequency arrival times to determine the DM. The DM measurements from our analysis are summarised in Table 4.2.

The DM precision highly depends on the observing frequency band. The low frequencies of the MWA allows the most precise DMs, typically of the order of $(2-4) \times 10^{-6}\,\mathrm{pc\,cm^{-3}}$, which is comparable to our previously published results (Kaur et al., 2019). However, at uGMRT BAND3, DM precision achieved is $\sim 10^{-5}\,\mathrm{pc\,cm^{-3}}$, an order of magnitude lower than that compared to the MWA, whereas due to the lower levels of RFI in BAND4, (and due to a fortuitous scintillation brightening), we were able to achieve a better precision of the order of $2 \times 10^{-5}\,\mathrm{pc\,cm^{-3}}$. In the Parkes UWL band, the achieved DM precision varies from 10^{-3} to $10^{-5}\,\mathrm{pc\,cm^{-3}}$.

4.6 Results and discussion

4.6.1 Precursor emission at low frequencies

Millisecond pulsars are known for their remarkable pulse profile evolution (Dai et al., 2015). Unlike other bright southern MSPs (such as PSRs J0437−4715 and J2145−0750), PSR J2241−5236 has a narrow pulse profile and shows very

little profile evolution from 100 MHz to 4 GHz, as discussed earlier. As seen from Figure 4.1, overall, the main profile shows very minimal profile evolution above 500 MHz. At frequencies below 500 MHz, there is a clear evidence of the presence of additional precursor components, which were first seen at the MWA frequencies below 300 MHz (Kaur et al., 2019). The uGMRT BAND3 data has now unambiguously confirmed the presence of this evolving precursor emission.

Based on our previous results and a non-detection of precursor emission at Parkes frequencies, we had earlier suggested that the precursor emission may have a steeper spectrum (spectral index ($\alpha_{\rm PC}$) < -3.7) compared to that of the main pulse. Even though our uGMRT data are not flux calibrated, the precursor detection in uGMRT BAND3 has an amplitude $\sim 5\%$ of the main pulse, which is consistent with expectations, considering the number of antennas (26) used in that observation (see Figure 4.1).

In general, understanding and modeling MSP profiles tends to be rather challenging due to their complexity in terms of a large number of evolving and emerging components. For example, some of the recent studies with the MWA, suggest that the profile evolution can be quite dramatic for MSPs from timing frequencies ($\sim 1-2$ GHz) to very low frequencies (upto 100s of MHz Bhat et al., 2018). This means in general, pulsar timing will necessitate accurate modeling of the profile evolution. This has motivated the development of wide-band timing techniques.

4.6.2 Orbital DM dependence

The high DM precision achievable with the MWA, offers the prospects of investigating DM variations as a function of orbital phase. Figure 4.15 shows DM measurements for PSR J2241−5236 across the full 3.5 hour orbital period of the pulsar, obtained from our MWA measurements. The DM and the orbital phase is measured using the pulsar timing software TEMPO2. The top panel shows the DM measurements over the full orbit using the MWA and the bottom panel shows a similar plot for a separate MWA observation, taken nine days later. As

is evident from these, there is no significant DM variation seen as a function of the orbital phase, except a statistically significant excess near an orbital phase of 0.4 to 0.5, where a DM change of the order of $(1.4 \pm 0.6) \times 10^{-5}\,\mathrm{pc\,cm^{-3}}$ is measured.

Pulsar Name	Pulse Period (ms)	DM ($\mathrm{pc\,cm^{-3}}$)	Excess DM ($\mathrm{pc\,cm^{-3}}$)	Full orbit (hours)	Eclipse Duration (%)	Reference
J1227−4853	1.686	43.4235	0.079(607)	6.9	37	Kudale et al. (2020)
J1807−2459	3.06	134.00401	0.003	1.7	–	Nice et al. (2005)
J1810+1744	1.66	39.7	0.015(325)	3.6	13	Polzin et al. (2019)
J1906+0454	2.08	142.9	–	169	–	Parent et al. (2019)
B1957+20	1.607	29.1168	0.01(149)	9.2	10	Polzin et al. (2020)
B1980+00	3.618	202.678	0.03	3.4	–	Nice et al. (2005)
J2051−0827	4.5	20.729	0.13	2.4	10	Polzin et al. (2019, 2020)
J2055+3829	2.089	91.8295	0.032	3.1	10	Guillemot et al. (2019)
J2241−5236	2.18	11.41151	0.0000137(6)	3.5	No	Current work

Table 4.4: Parameters of millisecond pulsars with eclipsing binaries.

Figure 4.16 shows similar measurements for the uGMRT data, which were taken at two different epochs, separated by five days. Even though the DM measurements with the uGMRT data is an order of magnitude less precise than those from the MWA measurements, and do not sample the exact same orbital phase, there is a marginal trend for a slightly higher DM around ~ 0.3 to 0.6 in the orbital phase. The uGMRT measurements also show larger DM variations on the order of $\sim 9.2 \times 10^{-5}\,\mathrm{pc\,cm^{-3}}$. However, unlike the case with MWA observations, these observations were not made on the same day, and therefore these orbital DM variations could be difficult to disentangle from the DM variations occurring over longer timescales (i.e., temporal) DM variations. However, the fact that the MWA observations were taken on the same day gives us confidence that the variations are loosely correlated with the binary orbital phase, and are not due to other (temporal) DM variations.

A summary of related work is presented in Table 4.4. As well known, PSR

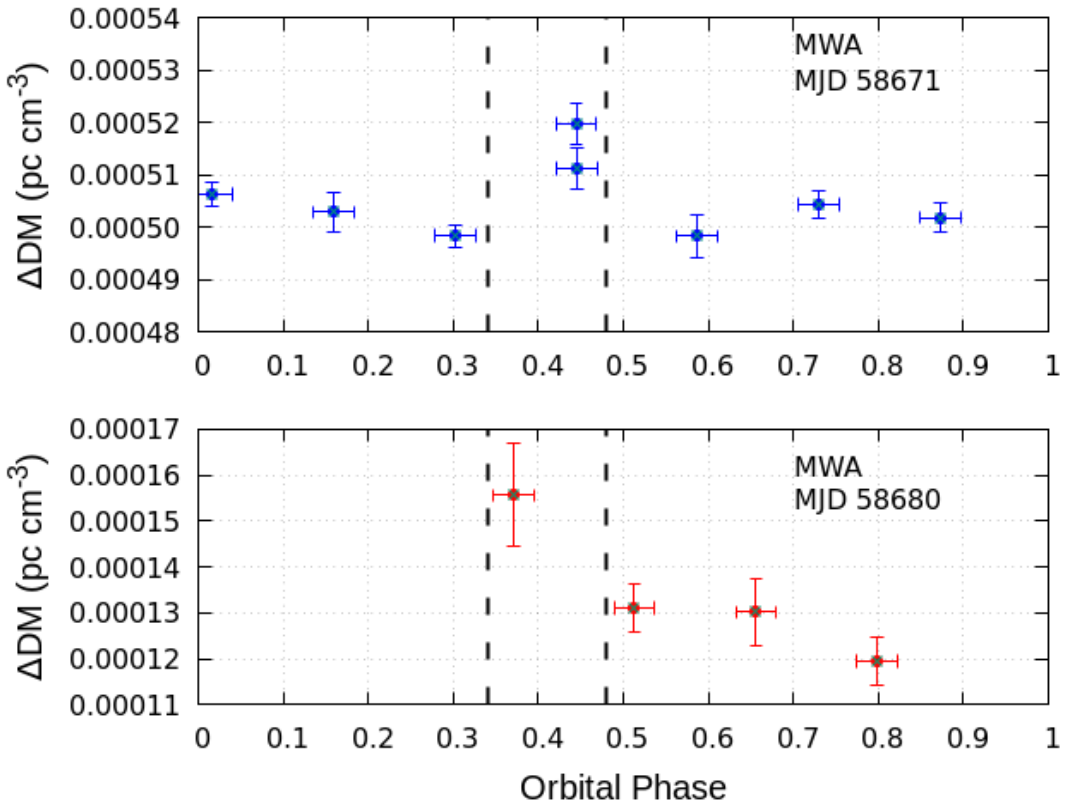

Figure 4.15: The plots showing ΔDM vs orbital phase from the MWA data. *T*op: DM measurements are obtained on a single day with almost full coverage of the orbit; *B*ottom: partial orbital coverage with another observation. The y-bars represents the measured DM uncertainties and x-bars represents the duration of observations.

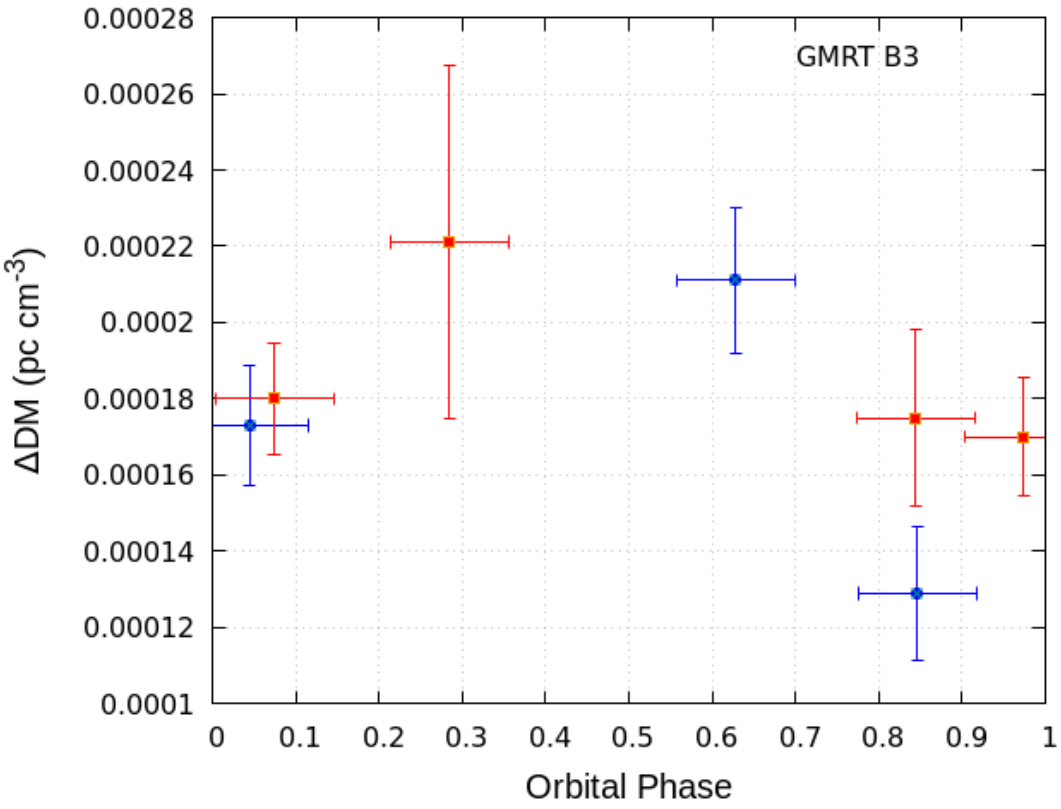

Figure 4.16: ΔDM vs orbital phase from the uGMRT BAND3 data. The plot is a combination of DM values measured at two different epochs (07^{th}and12^{th} November), represented by different colours. Half of the orbit covered on 07^{th} and another half on 12^{th}. The y-bars represents the DM uncertainties and x-bars represents the duration of observations. The result is a combination of orbital and temporal DM variations.

J2241−5236 does not show any evidence of eclipsing (Keith et al., 2011). Therefore, the chances of large DM modulations across the binary orbital phase are rather low for this pulsar. However, eclipses (and their associated delays) are also highly frequency dependent, as shown by Stappers et al. (1996). On the other hand, orbital modulations have been reported in the high-energy gamma-ray observations of PSR J2241−5236 due to intra-binary shock emission (An et al., 2018). This emission is centred around an orbital phase of ϕ =0.25, i.e. at superior conjunction. Our data show a DM excess in the 0.35-0.45 orbital phase range.

4.6.2.1 Definition of the orbital phase

As described in Chapter 1, the orbital phase is defined from the line of nodes. TEMPO2 package reads the orbital phases from the TASC parameter, which refers to the epoch of the ascending node. As the orbit of PSR J2241−5236 is almost circular, the mean orbital anomaly (M) at any time t, can be given as

$$\mathrm{M} = 2(\pi/\mathrm{P_b})(\mathrm{t} - \mathrm{T_0}) \tag{4.1}$$

where $\mathrm{P_b}$ is the binary period and $\mathrm{T_0}$ is the epoch of periastron. There is also the eccentric anomaly (E) and the true anomaly (U), which for circular orbits are related and therefore, will be equal to the mean anomaly (i.e., E = M = U). The orbital phase is defined as $\phi = U + \omega$, where ω is same as described in Chapter 1, Figure 1.10. So the orbital phase measured using $\mathrm{T_0}$ would differ from the TASC orbital phase by a factor of $\omega/360$ (ω in degrees). However, for this pulsar, ω is unknown. In this case $\mathrm{T_0}$ = TASC. However, given the available parameters for this pulsar, it is difficult to interpret the physical orbital geometry which can give rise to an excess DM at a pulse phase of ~ 0.45. The observed excess DM in our data could be possibly caused by the low density tailing plasma wind, coming from the companion.

In any case, the measured DM excess (δDM) from the MWA measurements is

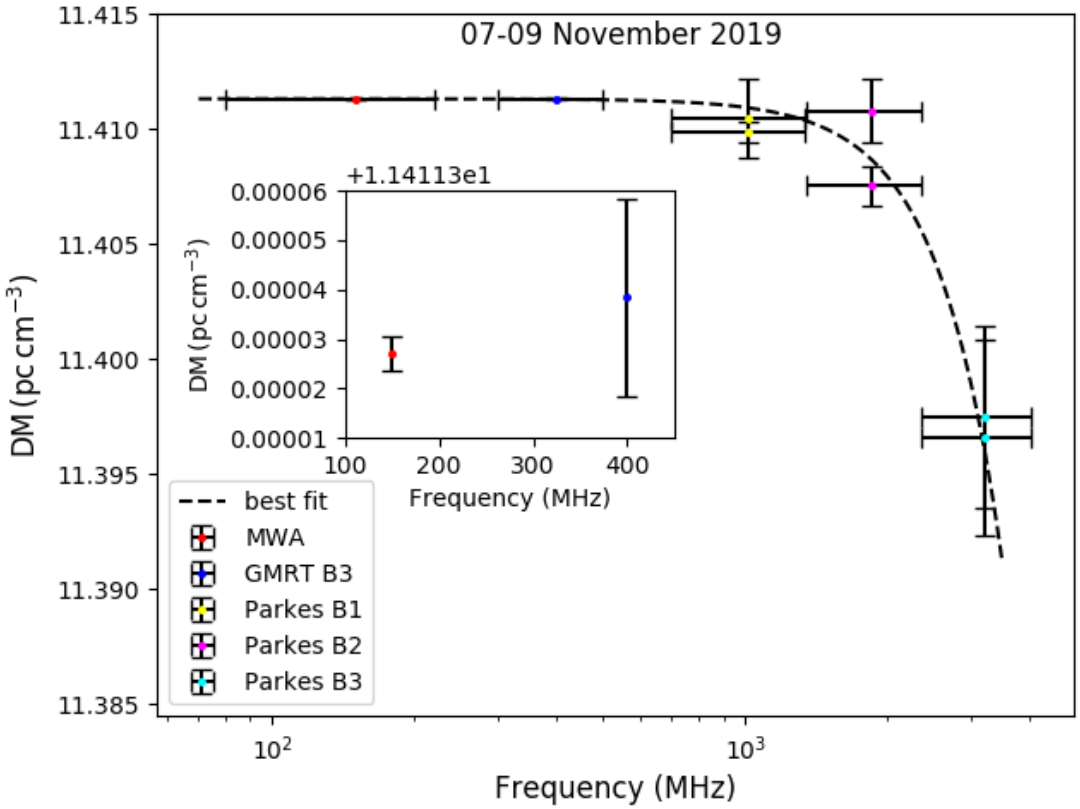

Figure 4.17: The dispersion measure measurements of PSR J2241−5236 from 80 MHz to 4.0 GHz range. The dashed line represents the best-fit power law. The inset plots represent the zoomed scale of low frequency measurements to highlight the quality of DM precision (of the order of 10^{-6} pc cm^{-3}) obtained at the MWA's frequencies. The data show measurements from the MWA, uGMRT BAND3, and the Parkes UWL giving a scaling index of 3.19 ± 0.6.

significantly lower than that seen in any other such binary systems (Table 4.4). The measured δDM of 1.4×10^{-5} pc cm^{-3} could cause a timing delay of $\sim 3\,\mu$s at the MWA's observing band (120-220 MHz), which can translate to a delay of ~ 110 ns in the Parkes UWL band (700-4000 MHz). Future MWA observations can help further investigate this.

4.6.3 Frequency dependent DM

Figure 4.17 to 4.19 present DM variations over the large frequency range from 80 MHz to 4 GHz. The x-axis represents the logarithmic scale of the observed

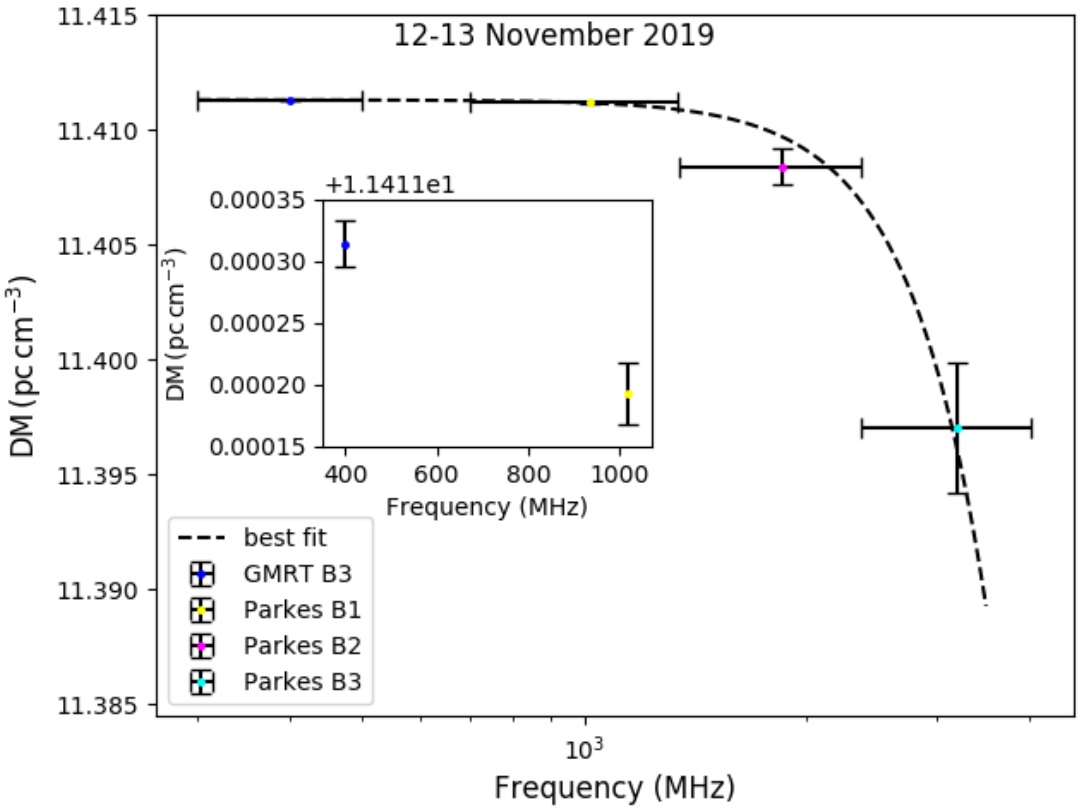

Figure 4.18: The dispersion measure measurements of PSR J2241−5236 from 300 MHz to 4.0 GHz range. The dashed line represents the best-fit power law. The inset plot represent the zoomed in scale to highlight y-error bars. The data show measurements from the uGMRT BAND3, and Parkes UWL, giving a scaling index of 4.1 ± 0.4.

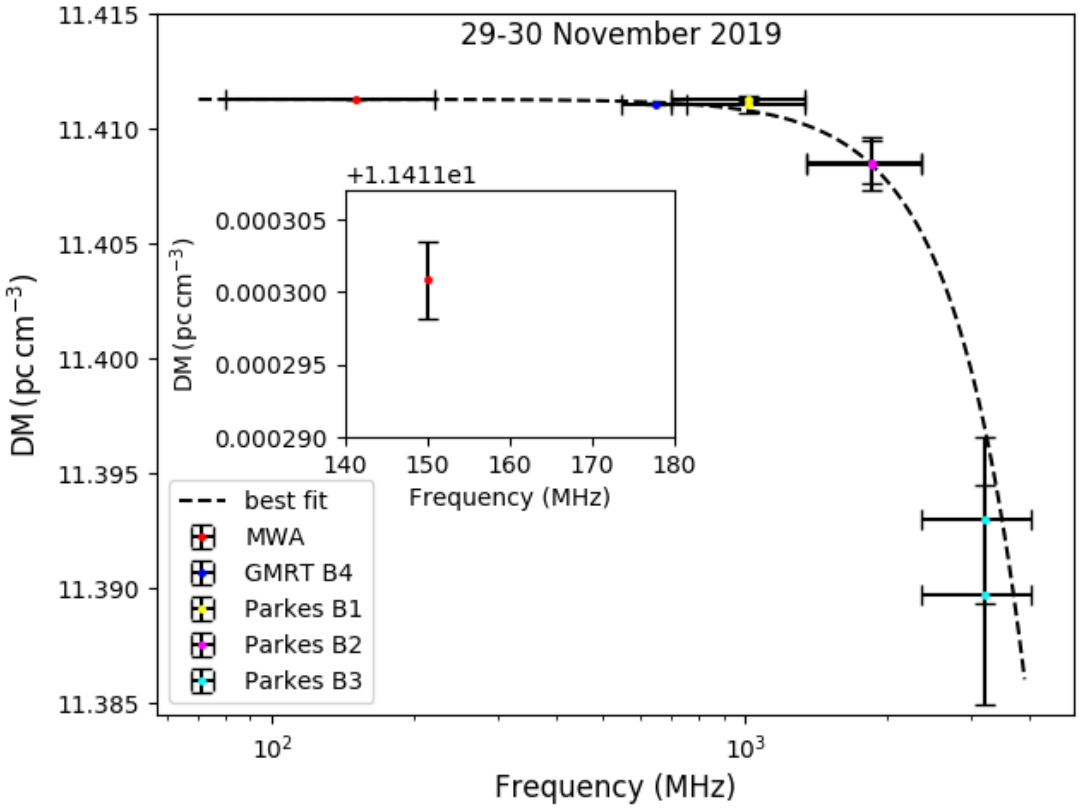

Figure 4.19: The dispersion measure measurements of PSR J2241−5236 from 80 MHz to 4.0 GHz range. The dashed line represents the best-fit power law. The inset plots represent the zoomed in scale to highlight the quality of DM precision (of the order of 10^{-6} pc cm^{-3}) obtained at the MWA's frequencies. The data show measurements from the MWA, uGMRT BAND4 and Parkes UWL, giving a scaling index of 2.9 ± 0.4.

frequencies and y-axis represents the measured DM value. Three different plots are for different data sets taken at different epochs. Measurements in each plot are from observations over ∼24-hour windows, in order to reduce the impact of temporal variations in DM, caused by the motion of pulsar, ISM and the observer. For example, the MWA, uGMRT BAND3 and UWL were available for observations made on 7-8 November; whereas uGMRT BAND3 and UWL were used for observations on 12-13 November. For observations made on 29-30 November 2019, the MWA, BAND4 and UWL were used.

Our data sets clearly indicate that the DM changes measurably across the frequency band. This frequency dependent behavior is seen consistently at all three epochs. We attempted to model this empirically using a power-law of the functional form $\delta\mathrm{DM} \propto \nu^{\alpha}$, where α is the scaling index. We measured scaling indices of 3.2 ± 0.6, 4.1 ± 0.5, 2.9 ± 0.4 at three epochs respectively. Our data suggested an average DM value of $11.411318\,\mathrm{pc\,cm^{-3}}$ with the precision of $5 \times 10^{-6}\,\mathrm{pc\,cm^{-3}}$ as the best fitted DM for this pulsar, whereas the catalog value is $11.41151\,\mathrm{pc\,cm^{-3}}$*.

Evidently the DM measured at low frequencies ($\lesssim 1\,\mathrm{GHz}$) is significantly different to those measured at higher frequencies ($\gtrsim 1\,\mathrm{GHz}$). However, it may be possible to measure a predictive scaling, which can be applied to make meaningful DM corrections in PTA observations. This can be verified using further observations. Whether this scaling is pulsar dependent or epoch dependent, may need further investigation.

4.7 Discussion

Cordes et al. (2016) theoretically described the nature of frequency-dependent (chromatic) DM. To date, there have been limited studies that investigated this effect observationally. Donner et al. (2019) studied observations taken with

*The catalog DM value is based on the low frequency DM measurements made at 150 MHz, and are presented in Kaur et al. (2019)

three German LOng-Wavelength (GLOW) stations, which are part of the LOw-Frequency ARray (LOFAR). They presented 3.5 years of weekly observations of PSR J2219+4754. The frequency-dependent DM trends seen towards this pulsar (at frequencies above and below 149 MHz) were attributed to extreme scattering events (ESEs). The ESE was estimated to be due to a cloud roughly halfway to the pulsar, with a size of about 20 AU and a density $\sim$ 10s of electrons per cm^{-3}. However, later these results were revisited by Lam et al. (2020), who concluded that the DM variations were solely due to the turbulent ISM and no ESE occurred along PSR J2219+4754's LOS. Lam et al. (2020) also comment on the suitability of long-period pulsars for the investigation of frequency-dependent DMs, given these are a separate population from the millisecond pulsars that are used in timing-array experiments.

Our analysis suggests a clear evidence of frequency-dependent DM towards the line of sight of PSR J2241−5236, seen consistently at three independent observing epochs. The observations were conducted contemporaneously using three different telescopes, covering a large frequency range from 80 MHz to 4 GHz. The reduced chi-squared values for our MWA analysis range between 0.99-1.3; for uGMRT, it ranges from 1.4-1.7; for the UWL band, the range is 0.6-2. Furthermore, the measured changes in DM values are significantly higher than the uncertainties in our estimated DM values, as evident from Figure 4.17 to 4.19. We measure an excess of δDM $\sim (1.2 \pm 0.2) \times 10^{-4}$ pc cm^{-3} across 0.1-0.5 GHz, and δDM $\sim (1.5 \pm 0.3) \times 10^{-2}$ pc cm^{-3} across 0.1-3 GHz. Empirically, the excess in DM scales with the observing frequency (ν) as δDM $\sim \nu^{-3.8\pm0.5}$, where the quoted scaling index is the mean value of the indices estimated for three different observations.

In order to further investigate this, we considered several possibilities that may produce a variable DM measurement as a function of frequency:

- DM variation as a function of the binary orbital phase; however, this was negligible compared with the observed frequency dependence.

- We were able to rule out other temporal variations by having sets of observations that cover the entire frequency range (∼100 MHz to 4 GHz) within a span of one day.

- We minimised the possibility of DM measurement errors due to profile evolution by choosing a suitable pulsar, where the observed profile evolution is very small across the observing band.

On this last point, we also tested our data with single frequency (20 cm) template in order to check if the frequency-dependent DM trend still persists. The analysis produced similar results, which further strengthen the fact that our analysis is not biased by any un-modeled profile evolution (which is almost negligible for this pulsar). The frequency-dependent DM variations are significantly higher than the measured DM uncertainties and the orbital DM variations.

4.7.1 Scintillation bandwidth

As well known, the scintillation phenomenon can produce a scatter broadening of the observed pulse. For PSR J2241−5236, our observations do not reveal any visible scatter broadening even at the lowest frequencies of our observations (at 80 MHz). A closer examination of data presented in Figure 4.4, and **??** suggests a scintillation bandwidth ∼5 MHz at 400 MHz (i.e., uGMRT BAND3), which translates to a pulse broadening time of ∼30 ns at this frequency, and ∼20 μs at the MWA's 80 MHz (assuming a scaling of $\nu^{-3.9}$ as per Bhat et al., 2004), which is in agreement with the expected measurements at 200 MHz presented in chapter 3. This is still smaller compared to the dispersive delay ∼75 μs due to the measured excess in DM. Therefore, the frequency dependent DM seen in our data is less likely due to the variable scatter broadening across this frequency range.

4.7.2 Aberration and retardation

Aberration and retardation effects, both of which advance a pulse in time in a frequency-dependent way, might masquerade as a frequency-dependent DM. A detailed description is given in Appendix B. Briefly, expressing the DM in $\mathrm{pc\,cm^{-3}}$, ν in MHz, and pulsar period (P) in ms, the ΔDM can be

$$\begin{aligned}\Delta\mathrm{DM} &\equiv \mathrm{DM} - \mathrm{DM_{meas}} \\ &\simeq 2.41 \times 10^{-7}\,\mathrm{pc\,cm^{-3}} \left(\frac{P}{\mathrm{ms}}\right) \left(\frac{\nu}{\mathrm{MHz}}\right)^{2} \alpha r' \end{aligned} \tag{4.2}$$

where $\mathrm{DM_{meas}}$ is the measured DM. For J2241−5236, the light cylinder radius ($r_L = cP/2\pi$) is $\approx 100\,\mathrm{km}$. Therefore the quantities α and r' can be assumed as 0.33 and 0.01, respectively. With our data, assuming a "true" DM value of $11.41151\,\mathrm{pc\,cm^{-3}}$, this effect is negligible for this pulsar ($0.000039\,\mathrm{pc\,cm^{-3}}$ at 150 MHz). However, the AR-DM effect will be stronger for more slowly rotating pulsars.

4.8 Conclusion

In this chapter we have presented the results from our contemporaneous observations of PSR J2241−5236 made with the MWA, uGMRT and Parkes at three epochs, spanning about a month. Our observing and analysis strategies have been devised such that the effects such as temporal variations and orbital contribution of DM can be either measured, or minimised before frequency dependence in DM can be investigated. This is for the first time this pulsar been observed over such a wide-frequency range. In fact, low frequencies of the MWA allow us to obtain DMs with precision of the order of $10^{-6}\,\mathrm{pc\,cm^{-3}}$, which is better than that typically obtained from timing-array observations.

We have reported the first convincing evidence of frequency-dependent ("chromatic") DM along the line of sight of PSR J2241−5236, seen consistently at three different observing epochs. Effects of this kind, if confirmed for other PTA pul-

sars, will have important implications for timing-array experiments. Our observations can not be readily attributed to any of the above mentioned effects such as temporal variations or orbital contribution, and suggests a real frequency dependence in DM. The fact that the low-frequency observations measure a DM that is different from that measured at high frequencies, suggest that low-frequency observations cannot be straightforwardly used to apply DM corrections in PTA observations.

However, the achievable DM precision in the UWL band is only of the order of $2.4 \times 10^{-5}\,\mathrm{pc\,cm^{-3}}$ which translates to $\sim$200 ns of timing noise within the 700-4000 MHz frequency range. This is very significant, especially considering that pulsar J2241−5236 is a promising target for PTA experiments. Recent reports of this pulsar exhibiting astonishingly low levels of "jitter noise" (~ 4 ns Parthasarathy et al., 2021) further strengthen such prospects.

Our analysis suggests that it may be possible to empirically estimate the scaling of frequency-dependent DM (just like the case for other frequency-dependent effects such as scintillation bandwidth or pulse broadening). For a given pulsar, if such a scaling can be verified, e.g., via suitable monitoring campaigns, low-frequency pulsar observations may still have a role to play in applying effective DM corrections for pulsar timing. Whether the scaling is constant for a given pulsar, or it is epoch dependent, needs further investigation.

Chapter 5

Wideband timing and precision dispersion measures of the millisecond pulsar J2145−0750

5.1 Introduction

The imprint of low-frequency gravitational waves of pulsar timing data is expected to be of the order of several tens of nanoseconds, whereas the current timing studies are only able to reach several hundreds of nanosecond of timing precision for most PTA pulsars. In order to increase the detection sensitivity of PTAs to gravitational waves, several different approaches need to be considered. For example, increasing the cadence of observations, or increasing the number of pulsars in the pulsar timing array, or using larger (more sensitive) telescopes to increase the accuracy of the time of arrival (TOA) measurements (e.g., Siemens et al., 2013). It also necessitates developing a better understanding of different noise processes, including pulsar's emission related processes, interstellar medium effects and instrumental effects. Another important factor is the observing bandwidth. Based on the radiometer equation as given in equation (1.23), the TOA uncertainties are inversely proportional to square root of the bandwidth of the

receivers.

$$\sigma_{\rm rad} \propto \frac{\rm T_{sys}}{\rm A_e\sqrt{t_{int}\Delta\,\nu}} \tag{5.1}$$

In equation (5.1), $\sigma_{\rm rad}$ is the radiometer noise typically expressed in Jy, $\rm T_{sys}$ is the system temperature, $\rm A_e$ represents effective area of the telescope and $\rm t_{int}$ and $\Delta\,\nu$ are the integration time of the observation and the bandwidth respectively. The increase in fractional bandwidth of the receivers has gained significant attention by virtue of recent developments and commissioning of wide band receivers; e.g., the Ultra-Wideband Receiver (UWL; Hobbs et al. (2020)) at Parkes telescope, wide band UHF and L-band receivers at the MeerKAT (580-1670 MHz) telescope (Bailes et al., 2020), the ultra-broadband receiver at the Effelsberg 100 m radio telescope (Freire 2012) and the ultra-wideband (UWB; 0.7 to 4.2 GHz) receiver for the Green Bank Telescope (GBT) (Bulatek & White, 2020). This necessitates the consideration of profile evolution over such large bandwidths.

Millisecond pulsars are known to show a variety of pulse profile shapes, with typically many more components when compared to those observed for normal pulsars (Dai et al. 2015), with the exception of a few MSPs with a single narrow pulse profile; e.g., PSR J2241−5236, J1909−3744. The profiles of most MSPs are generally quite complex and show a rapid profile evolution with the observing frequency (e.g., Kaur et al., 2019; Bhat et al., 2018). The pulsar timing relies on the stability of the average pulse profile. A noise-free model of the averaged profile is cross-correlated with the observed data to estimate the TOAs and their uncertainties. With large bandwidths, any un-modeled profile shape variations that arise due to scintillation can result in degraded precision and sensitivity, due to imperfect template matching (Liu et al. 2014; Pennucci et al. 2014; Lentati et al. 2017).

One way to deal with this issue is to generate sub-banded TOAs, where the observed bandwidth is divided into a suitable number of sub-bands, instead of averaging in frequency across the entire band. Moreover, there may be still some

residual profile evolution which can produce a substantial bias in the TOAs. As PTAs starting to observe more pulsars with more telescopes and over broader bandwidths, this would produce a large number of TOAs, which can be unmanageable for already computationally-intense algorithms that are considered (or being explored) for the prospective detection of nHz GWs.

However, another way to deal with this is to make use of two-dimentional templates for timing, which can incorporate the profile evolution and produce a single, unbiased TOA for each observation. Pennucci et al. (2014) and Liu et al. (2014) have already described how the frequency evolution of a pulse profile can be accounted for by generalising the standard cross-correlation method. Their procedure produces pulse TOAs and a measure of the instantaneous DM simultaneously. They do not directly account for the Earth's motion, and measure the topocentric DMs, which can be corrected for the Doppler shifts to obtain the actual DMs. Pennucci's software package, which is known as "pulse portraiture", is the only published and publicly available 2D timing software. However, this method has not yet been applied to a large sample of actual observations. Recently, Alam et al. (2020) attempted to apply pulse portraiture on the NANOGrav's 12.5 year data set but no significant difference was found in the measured DM. The improvement in DM measurements is only seen very marginally for very high DM pulsars.

Independently from Pennucci et al. (2014) and Liu et al. (2014), members of the Parkes PTA team have also been developing a 2D timing software package, which is a direct extension of the original template matching algorithm (Taylor, 1992). The development of this software, called PTIME, is led by Dai et al. Since the software description is not readily available in the form of a publication, we present an overview and a short description of its usage in this Chapter. PTIME offers an interactive interface for generating 2D templates, and in that sense conceptually different from the principal component analysis that is employed by Pennucci et al. (2014).

In this chapter, we demonstrate the application of PTIME software package and try to derive unbiased TOAs for each observation, in an attempt to account for the effects of interstellar scintillation, the pulse frequency evolution and DM variations. The main aim of this chapter is to present this new software package for pulsar timing, and demonstrate (via tests conducted on data spanning large frequency ranges), its reliability to make precise DM measurements and compare the results with those obtained with the use of single-frequency templates.

The PTIME software package is described in Section 5.2, and the usage of PTIME is presented in Section 5.3. Observational details are described in Section 5.4. Data processing in Section 5.5. The application on PSR J2145−0750 and results are described in Section 5.6.

5.2 PTIME

PTIME is a software package that is still under active development. While the idea of 2D timing is quite similar to that described in Pennucci et al. (2014), many of the implementations are different. Therefore, it will be worthwhile to compare the results extracted using different software packages. PTIME can be used to generate analytic 2D templates from pulsar observations and use those templates to determine pulse times of arrival. The software package comes with individual routines that can be used to develop the templates, to plot and analyse the templates, and to generate TOAs.

As described earlier, frequency-dependent timing has been studied before (Pennucci et al., 2014; Liu et al., 2014). The algorithm implemented in PTIME is similar to these and is also based on Taylor (1992). Assuming that we have a frequency-dependent template with N_{chn} subbands, to apply the frequency dependent timing, we first frequency collapsed the data files into N_{chn} subbands and de-disperse them with a nominal DM. If the template well represents the

profile closely, they can be related by an equation of the form

$$\mathrm{p_h(t) = a_h + b_h s(t - \tau_h) + g_h(t)} \tag{5.2}$$

where h represents different subbands; $\mathrm{a_h}$ and $\mathrm{b_h}$ are constants; $\mathrm{g_h(t)}$ represents radiometer and background noise. τ_h is the phase shift in each subband, and is defined as

$$\tau_\mathrm{h} = \tau_0 + \mathrm{A_h} \times \mathrm{DM} \tag{5.3}$$

$$\mathrm{A_h} = \frac{2\pi \times \mathrm{K}}{\mathrm{P}} \times \nu_\mathrm{h}^{-2} \tag{5.4}$$

where τ_0 is the common phase shift, ν_h is the subband central frequency, P is the pulse period and $\mathrm{K} = 4.149 \times 10^3\,\mathrm{MHz^2\,cm^3\,pc^{-1}}$ is the dispersion constant. To derive the pulse time of arrival τ_h and the gain factor $\mathrm{b_h}$, we transform both the template and the profile into the frequency-domain and globally minimise the goodness-of-fit statistic over the band. Details of the goodness-of-fit statistic and uncertainty estimation are presented in a series of steps: first the profile and template are transformed into frequency domain as

$$P_{h,k}\exp(i\theta_{h,k}) = \sum_{j=0}^{N-1} p_{h,j} e^{i2\pi jk/N}, \tag{5.5}$$

$$S_{h,k}\exp(i\phi_{h,k}) = \sum_{j=0}^{N-1} s_{h,j} e^{i2\pi jk/N} \tag{5.6}$$

where the frequency index, $k = 0, ..., (\mathrm{N} - 1)$

$$P_{h,k}\exp(i\theta_{h,k}) = a_h N + b_h S_{h,k}\exp[i(\phi_{h,k} + k\tau_h)] + G_{h,k} \tag{5.7}$$

where $G_{h,k}$ represents the frequency domain representation of the sampled noise in the time-domain profile, $g_h(t_j)$. The above algorithm has been implemented in the PTIME software package. The Nelder-Mead Simplex algorithm in the GNU

Scientific Library* is used for multidimensional minimization. To derive the pulse time of arrival τ_h and the gain factor b_h, we minimise the goodness-of-fit statistic

$$\chi^2(\tau_0, DM, b_0, ..., b_{N_{chan}}) = \sum_{h=1}^{N_{chan}} \sum_{k=1}^{N/2} \left| \frac{P_{h,k} - b_h S_{h,k} \exp[i(\phi_{h,k} - \theta_{h,k} + k\tau_h)]}{\sigma_{h,k}} \right|^2 \tag{5.8}$$

In this Equation 5.8, $\sigma_{h,k}$ is the root-to-mean-square amplitude of the noise at frequency k. An anti-aliasing low-pass filter is designed to make $\sigma_{h,k}$ fall off somewhat at larger values of k. In practice, however, this subtlety is usually not important since the amplitudes $P_{h,k}$, and $S_{h,k}$ decrease even faster than $\sigma_{h,k}$. Owing to inherent symmetries in the transforms, the limits of summation in the above equation can be taken as 1 to N/2, rather than 0 to N − 1. For convenience of notation, in the remaining equations the summation limits have been omitted and the $\sigma_{h,k}$ treated as constant. This algorithm has been implemented into the PTIME software package. A detailed description will be presented in a future publication (Dai et al.).

5.3 Usage of PTIME software

To model the frequency evolution of pulse profile, we use `ptime_create` routine, which can be used to create a frequency-dependent template for the determination of the times of arrival. It requires input data in the PSRFITS format with desired number of channels. For example, running the initial command,

```
> ptime_create -f file_name.fits -g 2/xs
```

will display a two-panel plot (cf. Figure 5.1), the top panel of which contains the selected channel profile (white) along with a fitted template (red). In the absence of any fitting information, the fit is initialised to a flat baseline. The bottom panel shows the residuals between the profile and the fit. The channel

*http://www.gnu.org/software/gsl/

number and polarization (Stokes I, Q, U, V are represented by the numbers 0-3) are displayed in the plot header. In our case, data are polarization averaged, and therefore, the panel shows polarization value equal to zero.

A fitted template is then created by interactively (and iteratively) fitting individual components in the profile (key press 'f'). The procedure is similar to that of `paas`, in which the width and height of each fitted component are manually adjusted until the residuals resemble noise. Fine adjustments can be made to small components via the zoom functionality (key press 'z'). Once the fit is good enough such that the residuals are noise-like, the fit for that channel can be saved (key press 'c'). The next channel will then be displayed and the fitting procedure can be repeated. For each successive channel, the fit is initialised to that of the previous channel, so that if the profile evolution is negligible across successive channels, the existing template can be immediately saved. On the other hand, if the profile evolution is significant, the fit can be reset to the baseline (key press 'r') and the process repeated from scratch. Once all the channels have been fitted, the set of individual channel templates (collectively called the 'template') can be saved to a file (key press 's'). The saved file is in a human-readable text format, such as shown in Figure 5.3 for MSP J2145−0750. In this case, the template consists of distinct fits for three frequency ranges, each of which contains two Von Mises components. The six numbers for each component represent the three fitting parameters of the Von Mises (height, centre, width) and their respective errors.

The file saved with the `ptime_create` routine can be directly used with the another routine `ptimeT` to generate TOAs. Arrival times can be produced in the form of one per observation, or one per frequency channel. In our case, we generated TOAs for each channel. The command to generate TOAs per frequency channel is,

```
> ptimeT -f file_name.fits -pt ptime_template.pt -multi -I
    -o output.tim
```

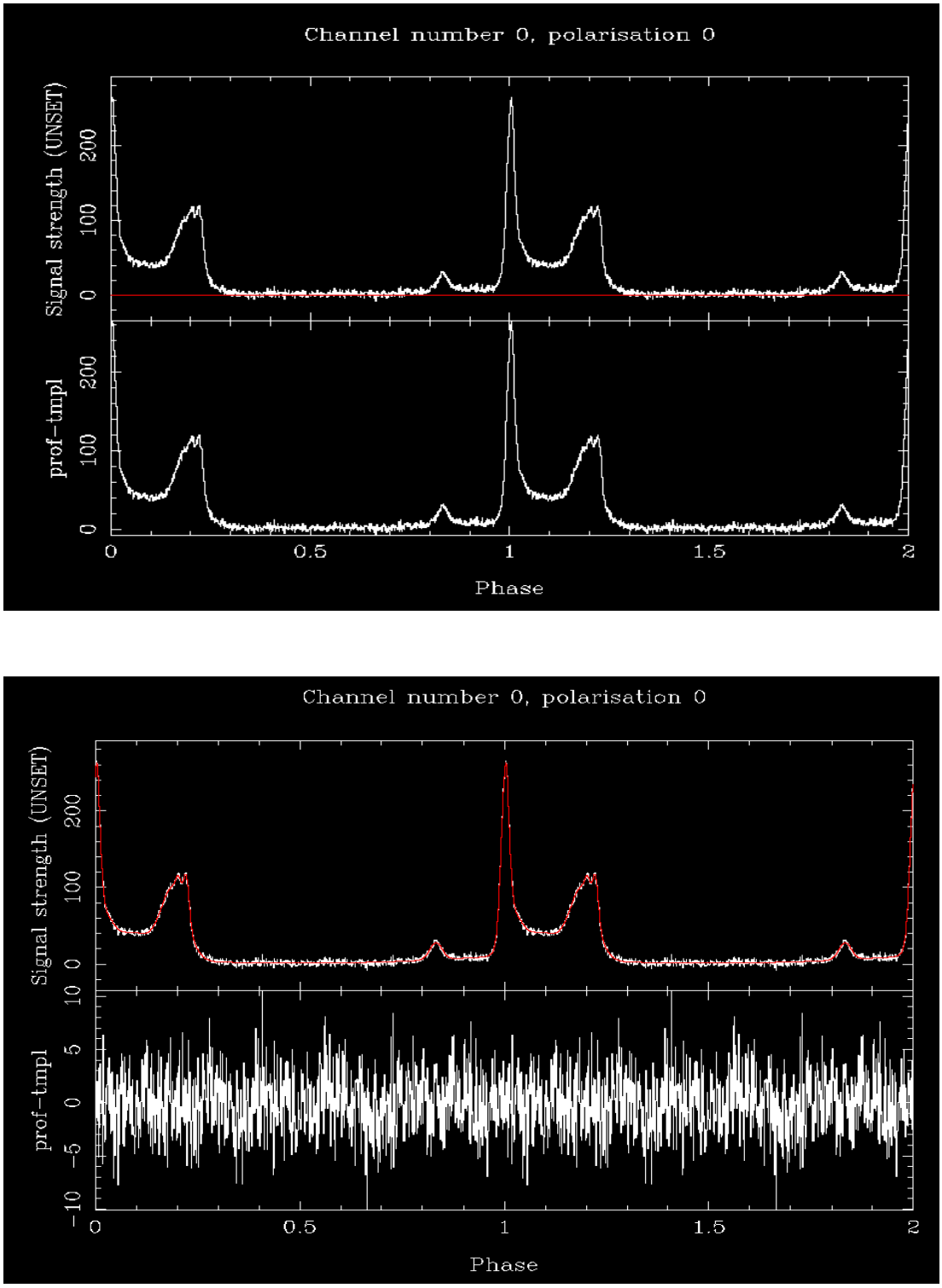

Figure 5.1: `ptime_create` example

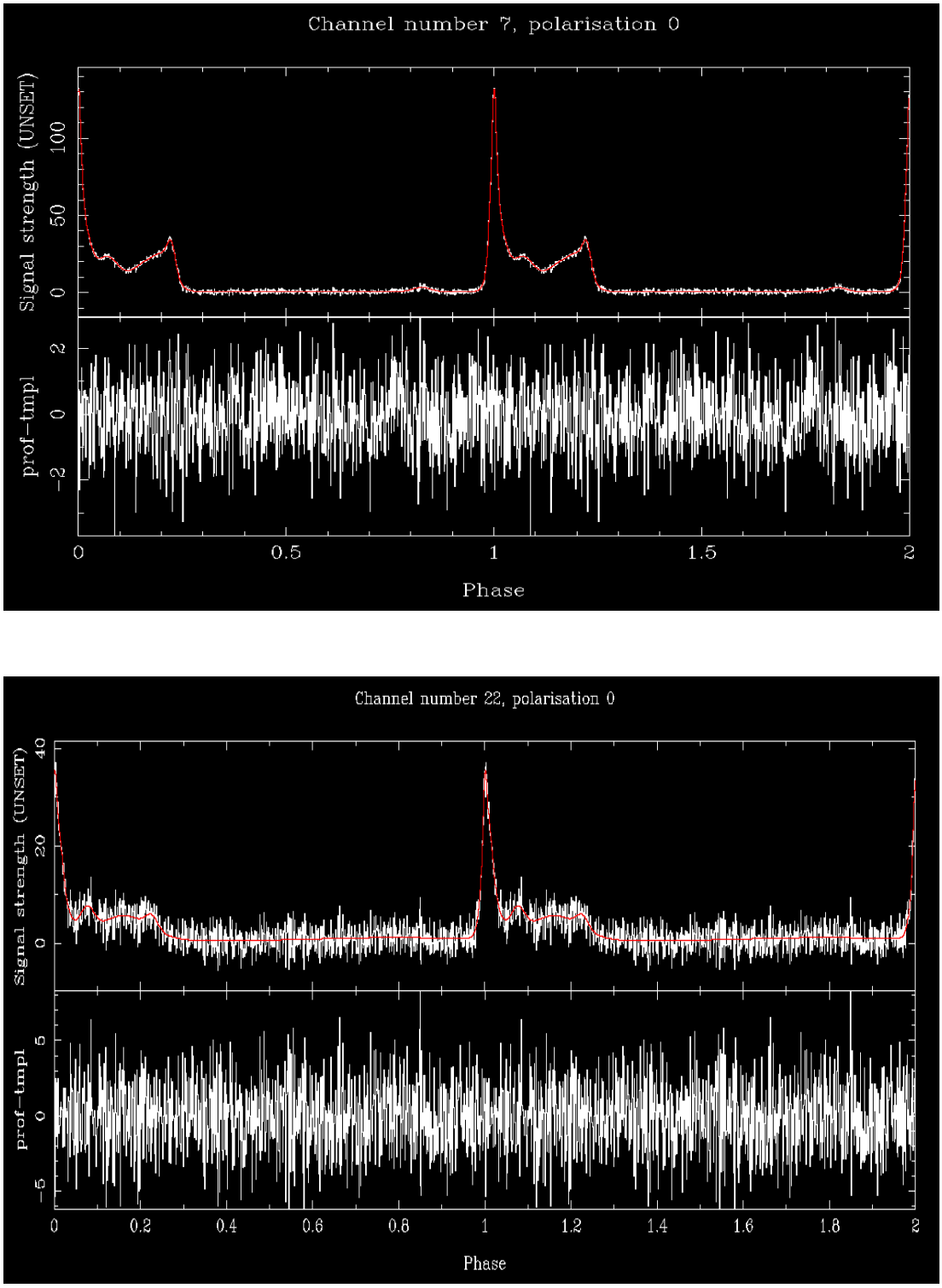

Figure 5.2: `ptime_create` example

```
TEMPLATE_VERSION: 1.0
PROFILE_FILE: 2017_07_26_063-172.fdDM.D
SOURCE: J2145-0750
DATE: UNSET
ID: UNSET
UNITS: UNSET
NCHAN: 24
#
#
STOKES: I
FREQUENCY_RANGE: 134.399994 135.679994
NCOMP: 2
COMP1: 0.00001072 1.00000000 43.0615 0.00000000 0.05415293 0.00000000
COMP2: 0.00000243 0.00000000 1.6674 0.00000000 0.95477386 0.00000000
#
#
STOKES: I
FREQUENCY_RANGE: 135.679994 136.959994
NCOMP: 2
COMP1: 0.00001190 0.00000000 44.2067 0.00000000 0.05144969 0.00000000
COMP2: 0.00000215 0.00000000 0.8980 0.00000000 0.95347508 0.00000000
#
#
STOKES: I
FREQUENCY_RANGE: 136.959994 138.239994
NCOMP: 2
COMP1: 0.00001373 0.00000000 41.5969 0.000000 0.04877905 0.00000000
COMP2: 0.00000319 0.00000000 6.3721 0.000000 0.97143610 0.00000000
```

Figure 5.3: An example of final template file, a portion of output from PTIME.

The command to generate single TOAs per observation is

```
> ptimeT -f file_name.fits -pt ptime_template.pt -single -I
    -o output.tim
```

The timing file containing the TOAs can be then fed to TEMPO2 for the further analysis via the command

```
> tempo2 -gr plk -f ephemeris.par file.tim -nofit
```

Argument	Description
f	Fit components
c	Create template
r	Restart template from current frequency channel
R	Restart from beginning
z	Zoom
s	Save template
p	Select polarization
q	Quit
mouse	Select profile components

Table 5.1: Options for creating the frequency dependent template

5.4 Observations

PSR J2145−0750 was observed at multiple different epochs with the MWA between 2016 and 2018, and was observed contemporaneously with three different telescopes— the MWA, Parkes and the uGMRT— as part of the multi-telescope campaign that we undertook in November 2019. For the MWA observations, the pulsar was observed using both the compact and long-baseline configurations of the array (cf. Wayth et al., 2018). The MWA-VCS data were recorded in two different observing modes: (1) a distributed channel setup, as explained in Chapter 2, i.e. 30.72 MHz bandwidth split into smaller (24×1.28 MHz) sub-bands, spread across the 80-220 MHz frequency range; (2) a single contiguous band 30.72 MHz, centred at 155 MHz.

The multi-frequency observations of PSR J2145−0750 were conducted in an identical mode that was used for PSR J2241−5236, as described in Section 4.3 of Chapter 4. PSR J2145−0750 is in a long 6.8 day binary orbit with a low-mass white-dwarf companion (Bailes et al. 1994). Our observations were limited to a maximum of ∼2 hours and therefore, covering only a tiny fraction of the orbit. Details of observations are summarised in Tables 5.2 and 5.3.

MJD	Frequency range (MHz)	Channel setup	Observing duration (s)	N^{c}_{tile}
57701.451089	80-220	12×2.56[a]	2384	108
57704.416736	140-170	1×30.72[b]	3600	110
57960.715336	80-220	12×2.56	3600	116
57976.675058	80-220	12×2.56	3600	122
58271.863948	80-220	12×2.56	3600	116
58291.809143	80-220	12×2.56	3600	114
58305.760532	80-220	12×2.56	5040	106
58795.482871	80-220	12×2.56	2691	125
58816.496112	80-220	12×2.56	2691	122

Table 5.2: Observational details of PSR J2145−0750 with the MWA
[a] Two consecutive 1.28 MHz channels joined together
[b] Single contiguous band
[c] No. of tiles used while producing calibration solutions.

Date of observation	Telescope (length of observation) (No. of scans)		
07 November 2019	–	uGMRT BAND3 (60 min)(4)	–
08 November 2019	Parkes (86 min)(4)	–	MWA (45 min)(1)
12 November 2019	–	uGMRT BAND3 (50 min)(3)	–
29 November 2019	Parkes (124 min)(2)	uGMRT BAND4 (145 min)(8)	MWA (45 min)(1)

Table 5.3: Observational details of the multi-telescope campaign that was carried out for pulsar PSR J2145−0750

Date of obs (MJD)	MWA (80-220)	uGMRT B3 (300-500)	uGMRT B4 (550-750)	Parkes UWL (704-1344)	Parkes UWL (1344-2368)	Parkes UWL (2368-4032)
09-11-2016 (57701.45)	9.00292(2)	–	–	–	–	–
26-07-2017 (57960.71)	9.00316417(3)	–	–	–	–	–
02-06-2018 (58271.86)	9.00384(6)	–	–	–	–	–
22-06-2018 (58291.80)	9.00377(2)	–	–	–	–	–
06-07-2018 (58305.76)	9.00351(3)	–	–	–	–	–
07-11-2019 (58794.52)	–	8.99653(1)	–	–	–	–
08-11-2019 (58795.48)	9.00284(2)	–	–	8.998(1)	8.9961(7)	8.98(1)
12-11-2019 (58799.50)	–	8.99725(1)	–	–	–	–
29-11-2019 (58816.49)	9.00283(2)	–	9.00811(3)	–	–	–

Table 5.4: Details of measured DM values (in units of $\mathrm{pc\,cm^{-3}}$) from the MWA and contemporaneous data. The top parenthesis represents the frequency range covered from each telescope. The DM uncertainties , in the last significant number in the measured DM values, are presented in parenthesis. For the MWA data, the DM precision is of the order of $10^{-5}\,\mathrm{pc\,cm^{-3}}$. The highest precision presented on MJD 57960.71 is the result of the template being generated from the same data, hence obtained very low TOA residuals. The uGMRT BAND3 and BAND4 precision is also very competitive $10^{-5}\,\mathrm{pc\,cm^{-3}}$. For the UWL band it ranges between 10^{-2} to $10^{-4}\,\mathrm{pc\,cm^{-3}}$.

5.5 Data processing

The data from all three telescopes were processed (i.e., calibrated, and/or beam-formed, as relevant) using similar procedures as described in Section 4.4 of Chapter 4. The final archives were then prepared for the PTIME software, in order to create frequency-dependent templates. The software requires the input data to be in the `PSRFITS` format. Therefore, the MWA and uGMRT data were first converted into the `PSRFITS` format using the `psrconv` utility of `PSRCHIVE`. The standard MWA data are usually written in the `VDIF` file format and the uGMRT data file has its own bespoke format. The MWA and uGMRT observations were taken in the "search mode"; however, the data needs to be in the "pulsar fold mode" for PTIME. To achieve this, the header information of both the MWA and uGMRT data were updated using a python script.

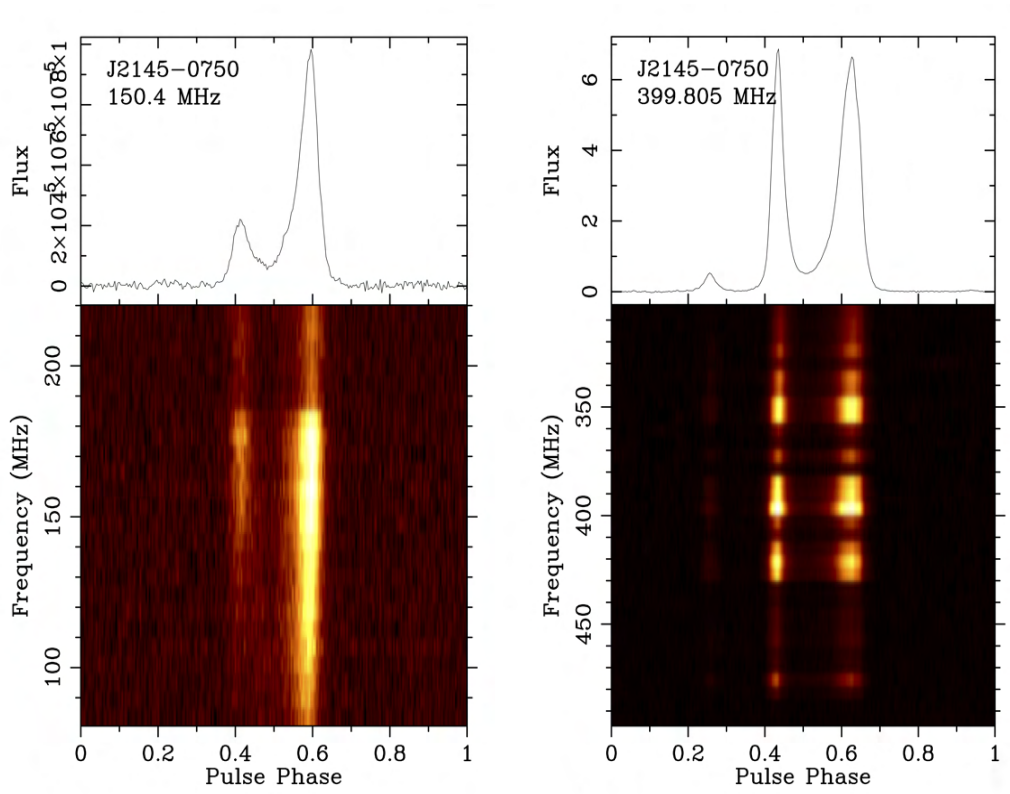

Figure 5.4: Coherently de-dispersed pulsar detections shown as frequency and time averaged pulse profiles in the top panels and frequency vs. pulse phase (bottom panels). Left: detection across the MWA's 80-220 MHz band centred at 150.4 MHz, and right: detection across uGMRT BAND3, 300-500 MHz centred at 399.805 MHz. The MWA data are at time resolution of $\sim 1\,\mu$s and uGMRT data are at $\sim 10\,\mu$s time resolutions.

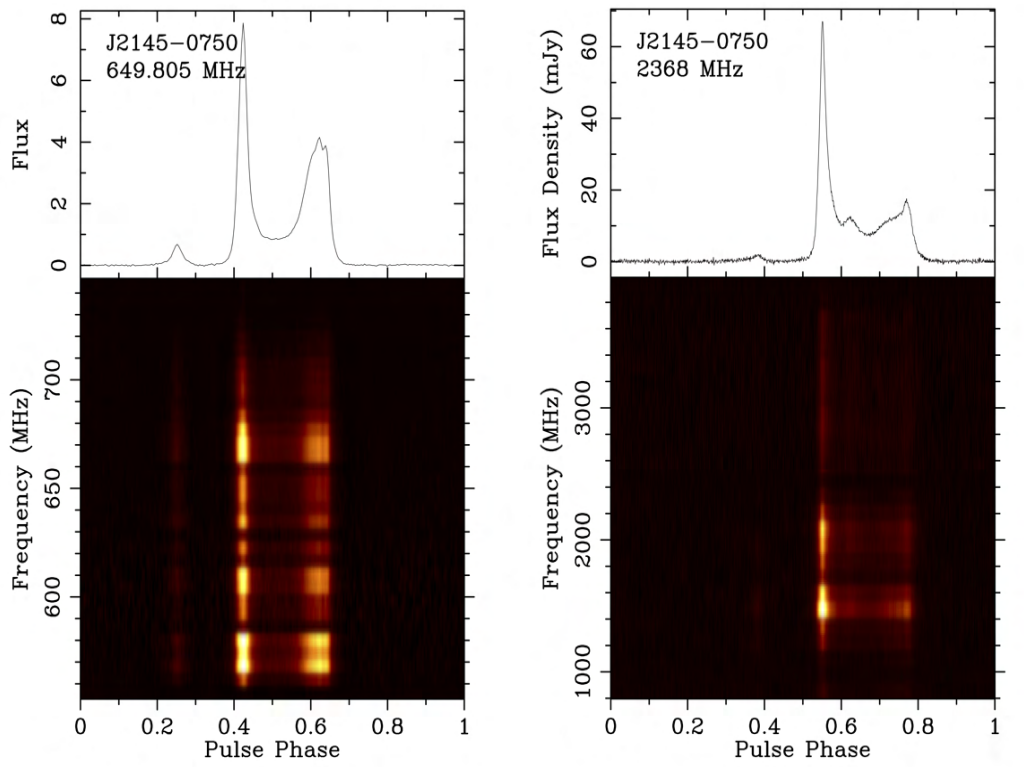

Figure 5.5: Coherently de-dispersed pulsar detections shown as frequency and time averaged pulse profiles in the top panels and frequency vs. pulse phase (bottom panels). Left: detection across the uGMRT BAND4 550-750 MHz band centred at 649.805 MHz, and right: detection across the entire UWL band 704-4032 MHz centred at 2368 MHz. The uGMRT data are at time resolution of $\sim 10\,\mu$s and UWL data are at $\sim 1\,\mu$s time resolutions.

5.5.1 DM analysis

The main focus in the analysis of PSR J2145−0750 is to assess the efficacy of the frequency-dependent template technique to measure DMs. As is evident from the data presented in Figures 5.4 to 5.10, this pulsar shows a significant profile evolution. In order to demonstrate the applicability of frequency-dependent template technique on this pulsar, we therefore adopted two different methods to generate templates. In `Method 1`, we generated an analytic template from time and frequency averaged bright observation by fitting von Mises function using the `paas` facility of PSRCHIVE. This is performed for every observing band. The analytic template profile is then cross-correlated with the data using the `pat` utility to determine the TOAs, which were then used to determine the DM using the TEMPO2 package.

In `Method 2`, we first divided each observing band into suitable sub-bands depending upon the profile evolution. The PTIME software is then used to create frequency-dependent templates. The UWL band was frequency averaged into 26 frequency channels from a total of 3328 frequency channels, yielding 26 template profiles created using PTIME to determine the DM. The uGMRT BAND3 and BAND4 data were frequency averaged to 32 channels from a total of 512 frequency channels, and PTIME was then used to generate 32 profiles for the uGMRT data. The 30.72 MHz bandwidth of the MWA is already in 24×1.28 MHz frequency channels, and so no further frequency averaging was performed, yielding 24 template profiles generated from the time and polarization scrunched MWA data.

Figures 5.6, 5.7, 5.8, and 5.9 present the profile stacks in each of the observed bands, overlaid with the single-frequency template profile. As seen from these figures, using a single-frequency template profile is highly sub-optimal as the profile evolution is quite significant for this pulsar, even within the individual bands. The frequency-dependent template profiles generated using PTIME are then cross-correlated with the data using PTIME to generate TOAs which were

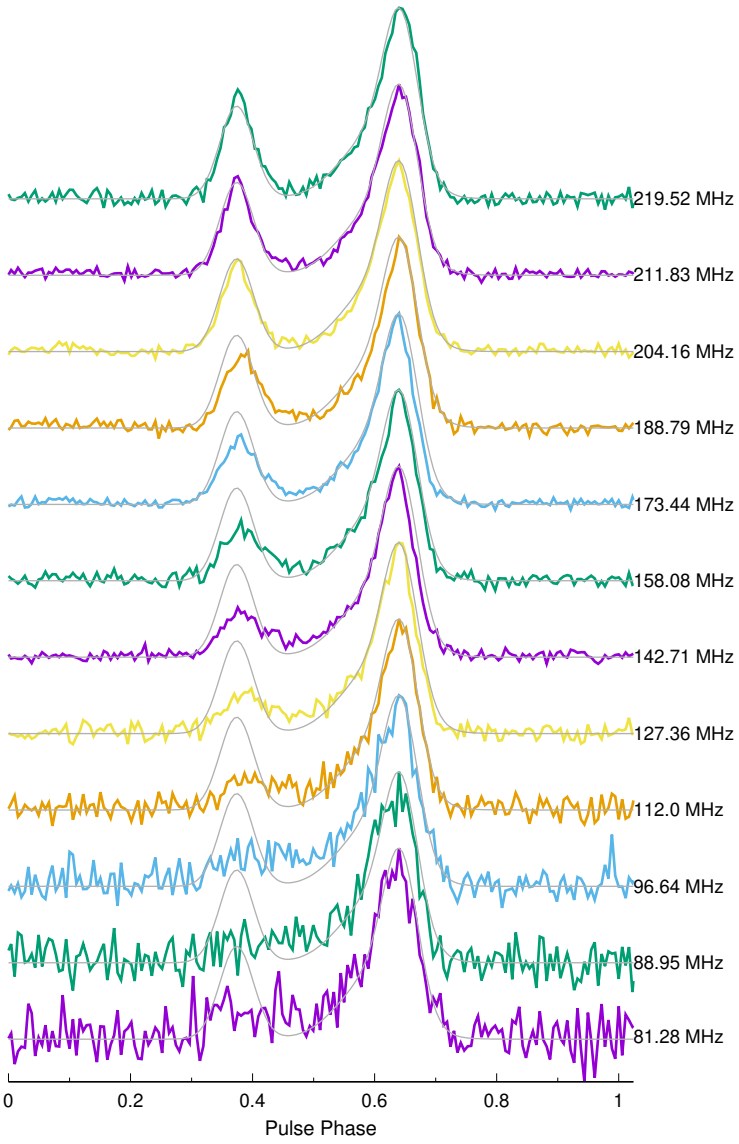

Figure 5.6: Profile stack of PSR J2145−0750 in the MWA band (80-220 MHz). The different colors represent profiles at different frequencies within the band. The overlaid gray profile is a single-frequency analytic template created by averaging the whole MWA band, centered at 150 MHz, presented to showcase the mismatch between the template and profile evolution, mainly because the template is effectively weighted by the high intensity in the upper part of the band as compared to the lower side of the band.

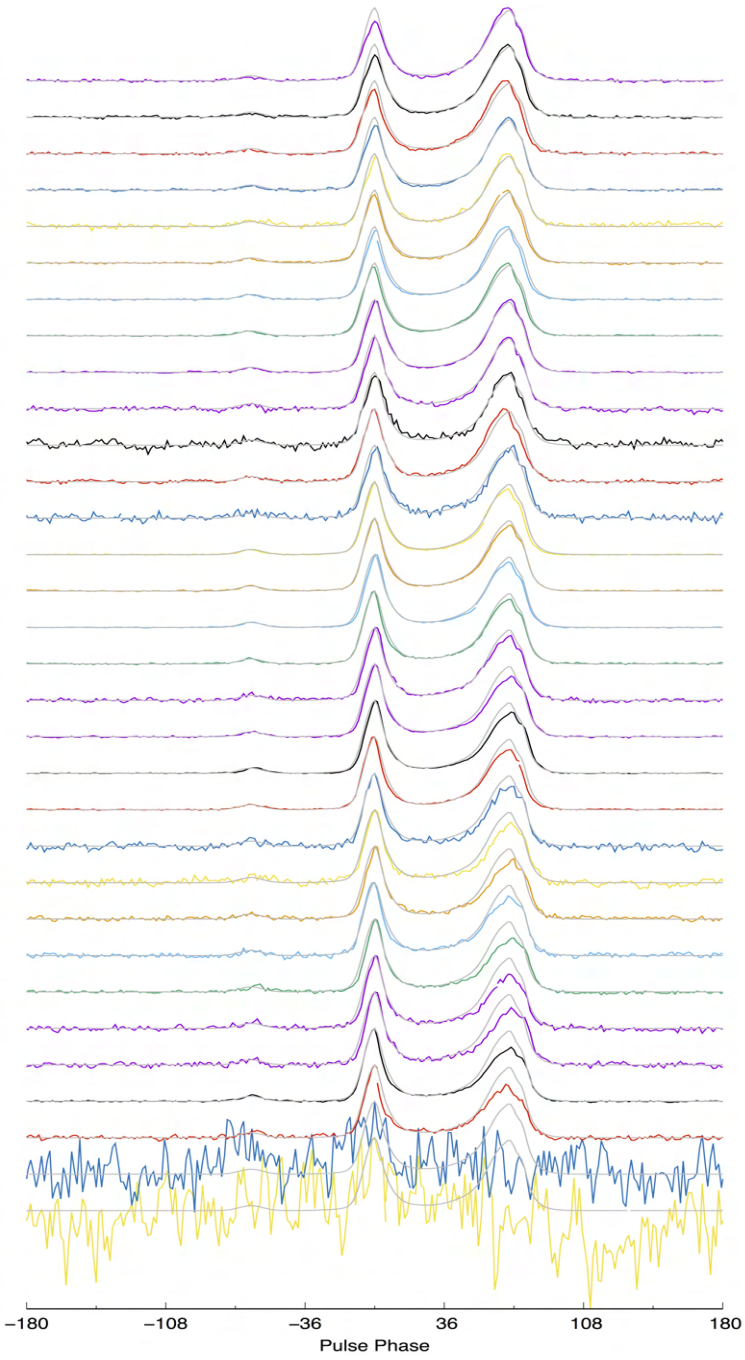

Figure 5.7: Profile stack of PSR J2145−0750 in the uGMRT BAND3 (300-500 MHz). The 200 MHz band is divided into 32 subbands. The different colors represent profiles at different frequencies within the band starting from lower to higher frequencies from top to bottom. The overlaid gray profile is a single-frequency analytic template centered at 400 MHz, presented to showcase the mismatch between the template and profile evolution.

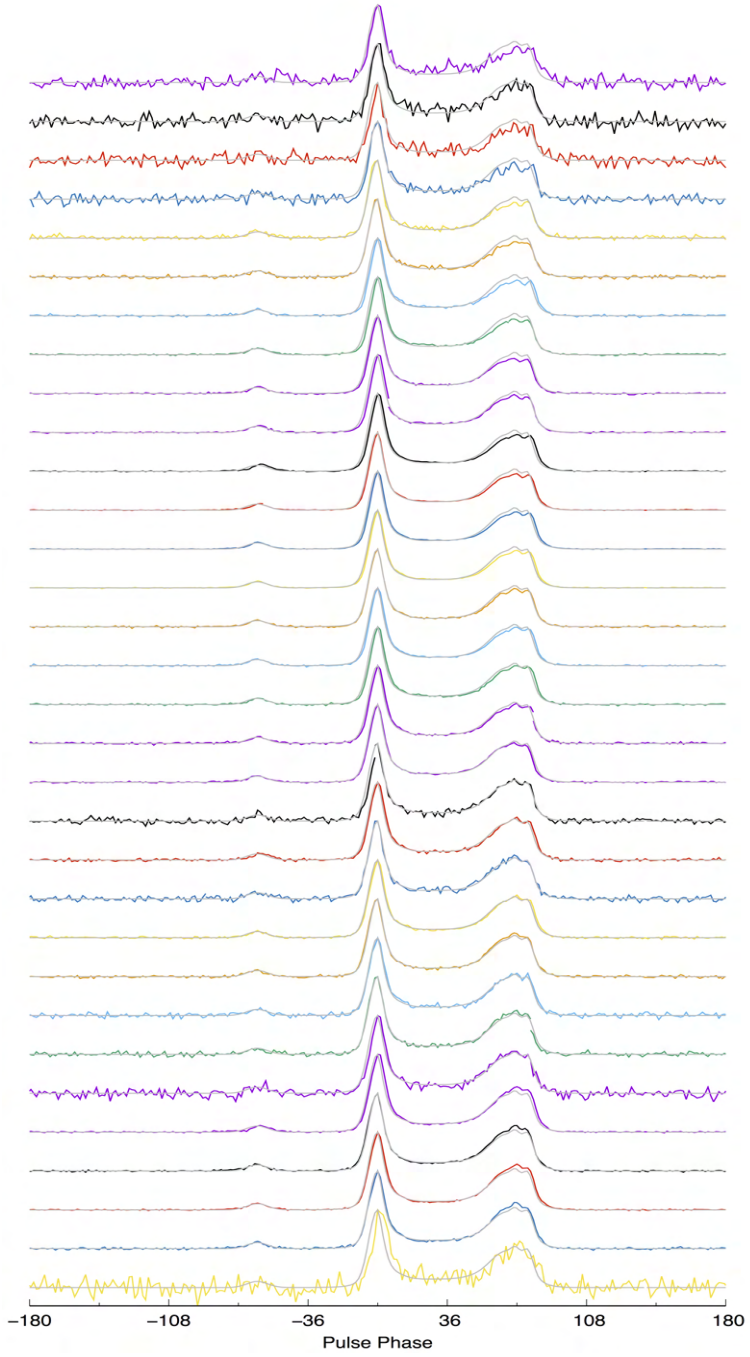

Figure 5.8: Profile stack of PSR J2145−0750 in the uGMRT BAND4 (550-750 MHz). The 200 MHz band is divided into 32 subbands. The different colors represent profiles at different frequencies within the band starting from lower to higher frequencies from top to bottom. The overlaid gray profile is a single-frequency analytic template centered at 650 MHz, presented to showcase the mismatch between the template and profile evolution.

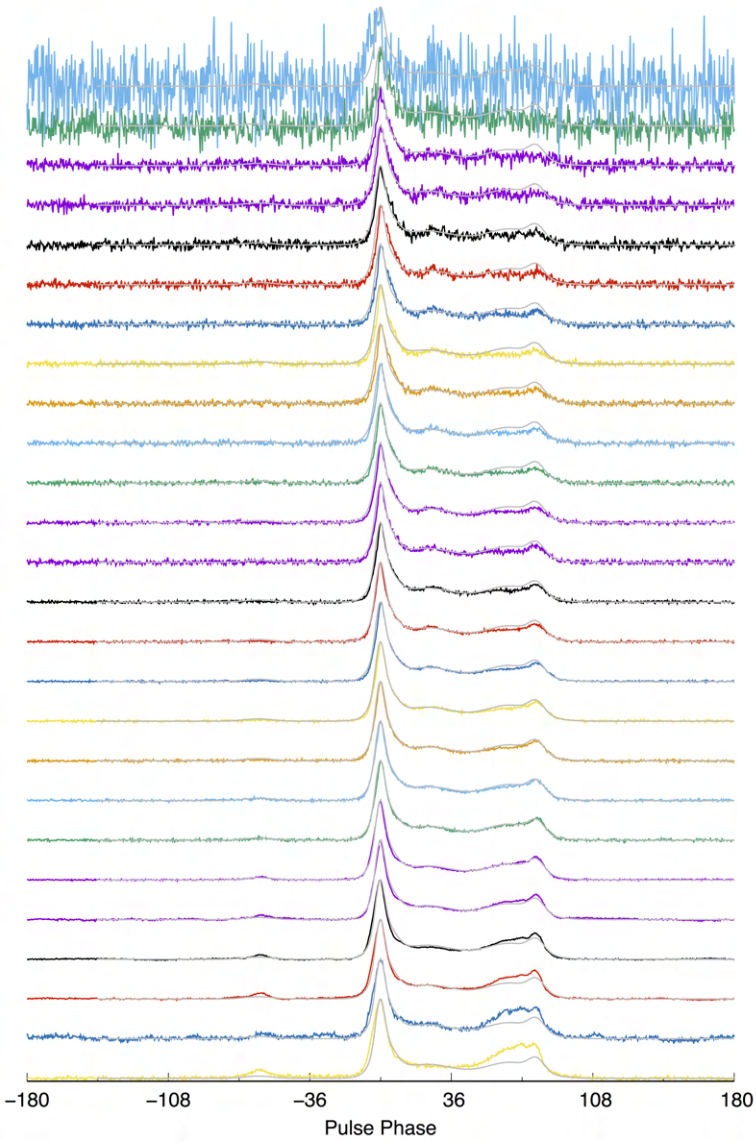

Figure 5.9: Profile stack of PSR J2145−0750 in the UWL band (704-4032 MHz). The entire UWL band is divided into 26 subbands. The different colors represent profiles at different frequencies within the band. The overlaid gray profile is a single-frequency analytic template centred at 2678 MHz, created by frequency and time averaging the entire UWL band, presented to showcase the mismatch between the template and profile evolution.

then processed with TEMPO2 to determine the DM.

5.6 Results and Discussion

Pulsar J2145−0750 is a well-studied millisecond pulsar, and has been part of PTA monitoring for the past decade. It is also one of the pulsars common for all major PTAs: the Parkes Pulsar Timing Array (PPTA; Manchester et al., 2013; Reardon et al., 2016; Kerr et al., 2020), the European Pulsar Timing Array (EPTA; van Haasteren et al., 2011; Desvignes et al., 2016), the North American Nanohertz Observatory for Gravitational Waves (NANOGrav; Demorest et al., 2013; Arzoumanian et al., 2018, 2020), as well as some of the emerging PTAs e.g., Indian PTA (InPTA; Joshi et al., 2018), MeerTime Pulsar Timing Array program (MPTA; Bailes et al., 2020), and Chinese PTA (CPTA; Lee, 2016). Pulsar J2145−0750 is known for being one of the brightest MSPs in the 20 cm band (1-2 GHz) and its pulse profile is dominated by two main components. Figure 5.10 presents the integrated pulse profiles centered at six different frequencies, covering the frequency range from 100 MHz all the way up to 4 GHz, to illustrate the frequency evolution of the mean pulse profile. The data are coherently dedispersed using the DM measured from our own observations using TEMPO2. The DM values are summarised in Table 5.4.

As seen from Figure 5.10, the strength of the leading and trailing components are reversed as we progress from higher to lower frequencies. Studies by Bhat et al. (2018) and Dai et al. (2015) show that there is a significant evolution in its pulse profile from high to low frequencies (3 GHz to 100 MHz). Bhat et al. (2018) also published the pulse profiles but the information at the intermediate frequencies between the Parkes and the MWA was lacking in their work. Dai et al. (2015) focused at high frequencies ($\gtrsim$700 MHz). Our uGMRT observations are thus useful to develop a more comprehensive picture and are well suited to explore the frequency evolution, where remarkable changes in profile shape are seen in. Such a reversal of profile components was also seen in the LOFAR data

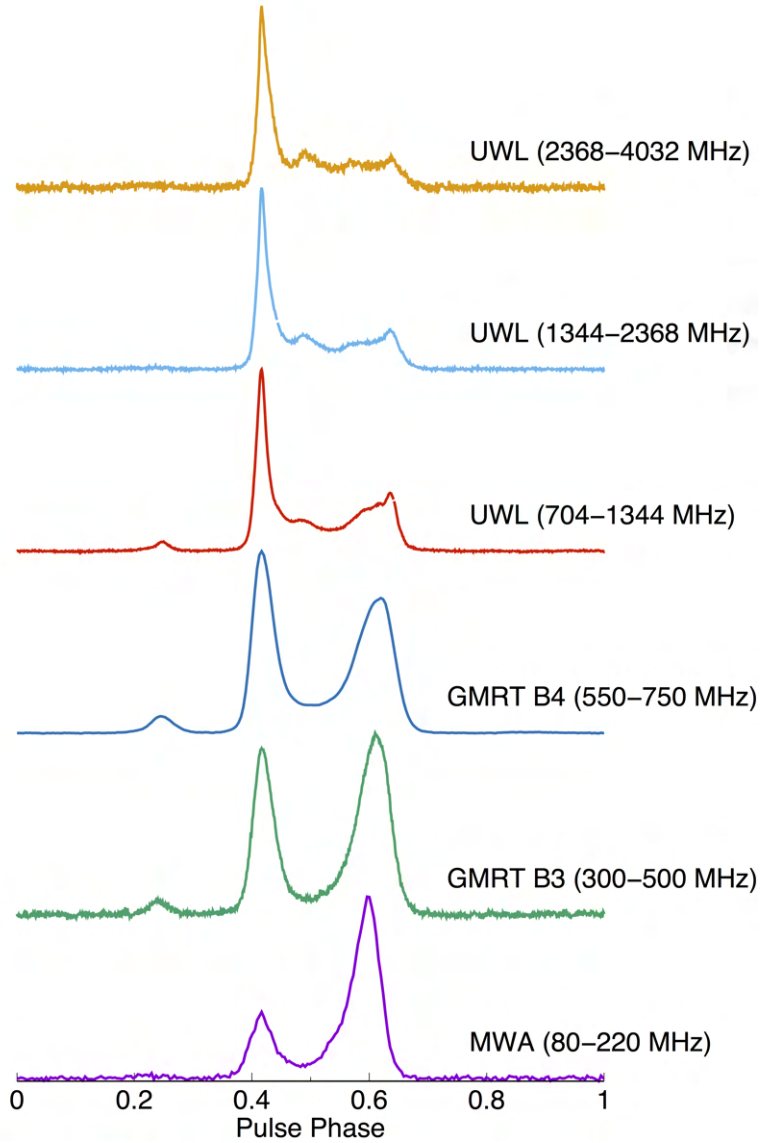

Figure 5.10: Integrated pulse profile stack of PSR J2145−0750 from 150 MHz to 4.0 GHz. The profiles at higher frequencies are by dividing the UWL band into three sub bands to showcase the pulse profile evolution. The strength of leading and tailing profile components reverses from Parkes to the MWA band.

(Kondratiev et al., 2016).

The changes in the strengths of the leading and trailing profile components can be characterised in terms of phase-resolved spectral index studies. Dai et al. (2015) studied the pulse profiles at ~ 700 MHz to ~ 3 GHz, and suggest different spectral indices for the leading and trailing components. The estimated spectral index (α) ranges from $-1.5 > \alpha > -2$ for the leading component to $-2 > \alpha > -2.5$ for the trailing one. They also inferred a steep spectrum ($\alpha \sim -2$) for the precursor component that appears prior to the leading peak (at a pulse phase of 0.2 in Figure 5.10) at 700 MHz. The uGMRT (BAND3 and BAND4) detections reveal this precursor component clearly but its disappearance at lower frequencies ($\lesssim 300$ MHz) of the MWA remains unexplained. This may be due to a possible turnover of the precursor, or its intermittent nature, as suggested by Bhat et al. (2018) or may simply be a beam geometric effect.

The DM measurements obtained using two different methods (as described in Section 5.5.1) are represented in Figure 5.11. The different colours represent the DM measurements made using two different techniques of template creation. The average DM value of 8.99761 pc cm^{-3} is represented by the solid black line. DM measurements using `Method 1` show a significant deviation from the standard DM value. However, the DM values derived using frequency-dependent templates are closer to the average DM value as can be seen from the blue data points in Figure 5.11. The revised DM values are in a closer agreement with the average DM value, although there is a slight deviation which may be due to the actual frequency dependence of the DM, or may be due to a residual profile evolution that was not taken care of by the PTIME software (see Section 5.6.3 for further details).

Another striking observation in Figure 5.11 is a DM offset at low frequencies even with the use of frequency-dependent templates. This is most likely due to a genuine excess in DM for PSR J2145−0750 at low frequencies. The average DM measured in the MWA's band is 9.00284 ± 0.00002 pc cm^{-3}, which is significantly

Observing Band	Single-frequency template `Method 1`	Frequency-dependent template `Method 2`
MWA	3.2×10^{-5}	1.7×10^{-5}
uGMRT BAND3	2.9×10^{-4}	1×10^{-5}
uGMRT BAND4	2×10^{-3}	5.4×10^{-4}
Parkes UWL	1.9×10^{-3}	2×10^{-4}

Table 5.5: The table shows the DM precision (in $\mathrm{pc\,cm^{-3}}$) achievable for PSR J2145−0750 with `Method 1` (i.e., using single frequency template), and with `Method 2` (i.e., using frequency-dependent templates generated by using PTIME software).

larger than the catalog value of $8.99761\,\mathrm{pc\,cm^{-3}}$. The implied DM excess of δDM $= 0.0052\,\mathrm{pc\,cm^{-3}}$ is in close agreement with that was previously reported from the low-frequency studies with the MWA and LWA (Bhat et al., 2018; Dowell et al., 2013; Kondratiev et al., 2016).

The precision in DM measurements is greatly improved with the application of `Method 2`. A summary of DM precisions obtained using the two methods is given in Table 5.5. An improvement in DM precision can be clearly seen with the use frequency dependent templates. This means the cause of a lower DM precision with `Method 1` that relies on a single-frequency template is manifestly the profile evolution. As the profile changes across frequency, the template used in the cross-correlation becomes more and more inaccurate and will induce systematic drifts in the residuals towards earlier or later TOAs. Until recently, pulsar timing was generally performed at higher frequencies ($\gtrsim 1\,\mathrm{GHz}$) where the profile evolves to a lesser degree across the available narrow bandwidths. However, with the advent of wideband receivers, and their increasing adoption in timing experiments, not taking into account profile evolution across the large bandwidths can easily introduce errors that masquerade as incorrect DM in timing residuals.

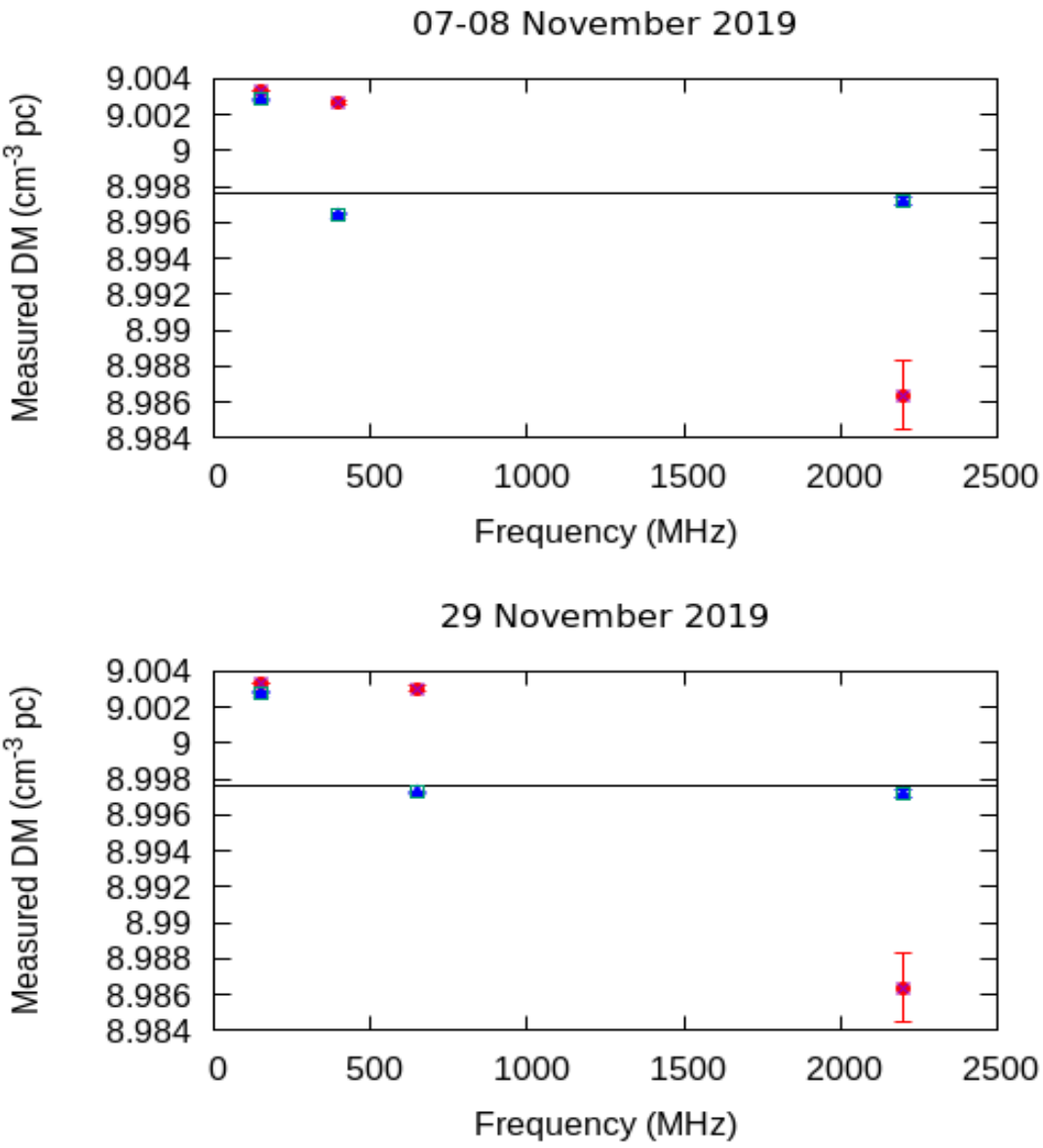

Figure 5.11: A plot showing measured DM vs frequency in each of the observed band i.e. the MWA, uGMRT and UWL. The red points represents the DM measured using a single frequency template and the blue points represents the DM measured using a frequency dependent DM. PTIME is used to create the frequency dependent template to account for the profile evolution. In both the observed epochs, where larger range in frequency was covered using all three telescopes, the DM values obtained using a frequency dependent template are consistent across the fixed DM value of $8.99761\,\mathrm{pc\,cm^{-3}}$, whereas the single frequency template results in significant scatter in the DM values.

5.6.1 Temporal variability in DM

Temporal variability in DM is a well-known in pulsar timing array data. It was first detected in the Crab Pulsar (Roberts & Richards 1971). PSR J2145−0750 is a PPTA target and its DM variations are studied regularly by all major PTAs. The reported temporal variations for this pulsar is of the order of $\sim 0.001\,\mathrm{pc\,cm^{-3}\,yr^{-1}}$ (Keith et al., 2013; Alam et al., 2020; Demorest et al., 2013). Although the temporal variations published are from larger time spans (e.g., 12 years of monitoring by the NanoGrav; Alam et al., 2020), high-precision DM measurements are only possible with telescopes such as the MWA due to its low frequencies and a large fractional bandwidth achievable via the "picket fence" mode of MWA-VCS observations. Therefore, to help compare with higher-frequency observations, here we report the temporal variations over a time span of ∼4 years.

The blue data points in Figure 5.12 presents the measured changes in DM over the period 2016 to 2019. The base DM of $8.99761\,\mathrm{pc\,cm^{-3}}$ was subtracted from the measured DM values, yielding DM variations of $\sim 0.001\,\mathrm{pc\,cm^{-3}}$. It is also important to note that these temporal variations are smaller than the reported excess in DM of $\sim 0.0052\,\mathrm{pc\,cm^{-3}}$ that was measured at low frequencies. The measured temporal DM variations can introduce $\sim 56\,\mu$s of delay in the MWA's band (80-220 MHz), whereas only ~ 800 ns of timing delay in the timing data at the Parkes UWL band (700-4000 MHz). Accounting for such DM variations in the timing model is therefore important in order to minimise the DM noise, in an effort to reach the required timing precision to detect the signatures of ultra-low frequency GWs in PTA measurements.

* Both of these data sets have publicly available DM time series which can be accessed from the links provided in the respective publications.

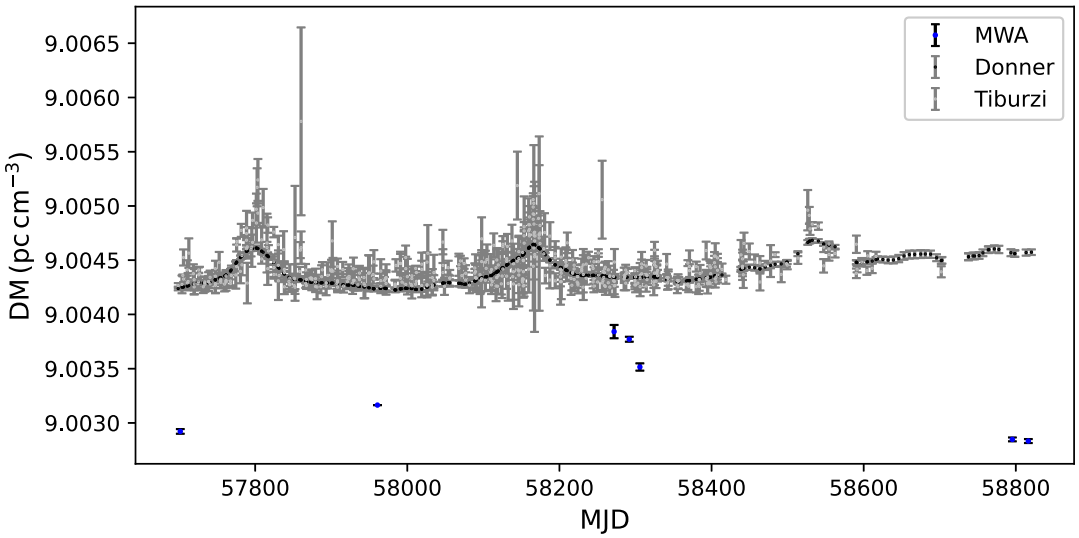

Figure 5.12: Measured DM variations in PSR J2145−0750 over a period of four years. Data presented are from the MWA observations from 2016 to 2019 (blue data points), from Donner et al. (2020)* (black) and Tiburzi et al. (2020)* (light grey). The later two data sets show strong modulations in the measured DM values due to the effect of Solar wind.

5.6.2 Solar wind

DM variations due to the Solar wind may be expected when the angular distance of the pulsar is in the range of a few degrees to $\sim 50°$, relative to the ecliptic plane. Pulsar J2145−0750 has been regularly observed with the LOFAR and uGMRT as part of their pulsar monitoring programs. It has been reported that the line of sight (LOS) to this pulsar passes very close to the Sun at a solar elongation of ∼5 to 10 degrees. Due to these close passes, the DM variations can be heavily dominated by the Solar wind as shown in Figure 5.12 where Donner et al. (2020) and Tiburzi et al. (2020) DM values have contribution from the Solar activity. As discussed above, because these data sets are different to those obtained from MWA observations, a further investigation may be needed for understanding the discrepancies. The DM tends to show variations due to a changing LOS with respect to the Sun and will be observed as an annual activity (Kumar et al., 2013; Donner et al., 2019; Alam et al., 2020; Tiburzi et al., 2020; Krishnakumar et al., 2021). There is no indication of such events in our data because of the very

sparse nature of measurements, and moreover, observations were generally made during nightly hours (i.e., $\gtrsim 70^{\circ}$ away from the Sun). Therefore it is unlikely that our DM measurements are contaminated by the Solar wind. Observations of pulsars with their LOS close to the Sun can be used to understand the impact of enhanced density structures of the Solar wind on the DM variations.

5.6.3 Frequency dependent DM

We have examined our measurements for frequency dependence (Figure 5.13). Our current DM measurements show a strikingly different trend, compared to what has been seen in the case of PSR J2241−5236 (see Chapter 4). The most important observation is that at very low frequencies, the measured DM is significantly offset (i.e., DM excess), but is in agreement with previous work. Figure 5.13 show measurements from observations taken on 8^{th} November. Given the trend, it is perhaps not meaningful to fit for frequency dependence and finding out the scaling. A more detailed analysis is required to further investigate the frequency dependence for this pulsar.

5.7 Summary and Conclusions

Pulse profile evolution can cause systematic errors in pulse arrival times, and therefore an important effect to be accounted for in wideband timing observations. In reality there are very few pulsars that have a truly symmetric pulse profile evolution, so in order to obtain high timing precision (on the order of nanoseconds for millisecond pulsars), it is crucial to account for the evolution of the pulse shape across the observing band. Although the degree of frequency evolution across the relatively small bandwidths that were available up until recently will likely be small, it may still manifest when we attempt to combine data from more than two frequencies, and can be absorbed into a fit for a dispersion delay. The problem becomes more acute as we strive for greater sensitivity by using wider

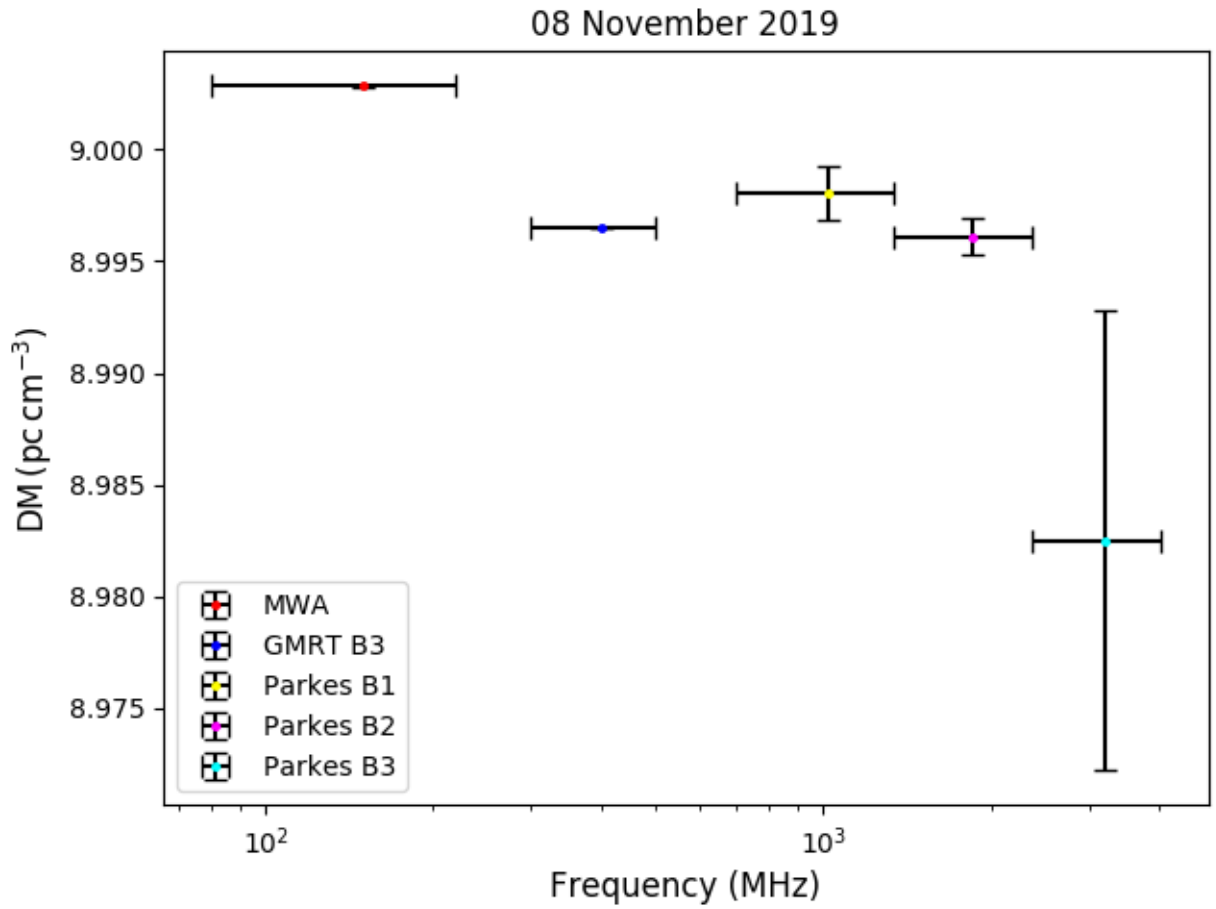

Figure 5.13: Dispersion measure measurements of PSR J2145−0750 in the 80 MHz to 4.0 GHz range. The data show measurements from the MWA, uGMRT BAND3 and UWL.

instantaneous bandwidths. As demonstrated in this Chapter, the profile evolution can impact the measured TOAs and hence the DM measurements. The `Method 2` presented here provides a way in which wideband data can be meaningfully used to model the profile evolution sufficiently accurately, and to build a template which incorporates all these effects. It can be compared with other techniques of creating frequency-dependent templates.

In this chapter, we compared two possible strategies for aligning the frequency-resolved pulsar profile templates and investigated their impact on subsequent DM estimations. We used PSR J2145−0750 observations made using the MWA for a period of four years. Contemporaneous observations were made at two different epochs with the Parkes, uGMRT (BAND3 and BAND4), and the MWA covering a large frequency coverage from 100 MHz to 4 GHz. We conclude that it is possible to achieve a higher precision in DM measurements with `Method 2`. Our analysis hints at the presence of frequency-dependent DM for this pulsar; however, a more detailed analysis is required to investigate this further.

Chapter 6

Conclusions and future prospects

The MWA is a relatively new instrument in the field of pulsar astronomy. The original capability was limited to 100 μs in time resolution and 10 kHz in frequency resolution. The complexity of working with the voltage capture system (VCS), which produces large data rates (30 TB/hour), and hence demands substantial processing resources, was one of the major limitations to be overcome in order to gear up the MWA for productive pulsar science. For this thesis work, observations were taken in the "picket-fence" mode of VCS, where the maximum 30.72 MHz bandwidth currently achievable with the MWA is distributed into multiple sub-bands across the 80-300 MHz range, which further increases the complexity of calibration. Despite all these limitations, this thesis undertook some of the first millisecond pulsar studies with the MWA with the goal of making high-precision DM measurements, and examining its relevance in the context of PTA efforts. The implementation of data reconstruction, via the inversion of polyphase filter bank (PFB) operation in the signal path, enabled us to study pulsars with $\sim 1\,\mu$s time resolution. In this chapter, we summarise the main scientific results that have emerged from this thesis work, and comment on some possible directions that can be pursued in the future.

6.1 Summary of the main results

Due to strong frequency dependencies of interstellar propagation effects, low-frequency observations provide significant advantages for characterising the ISM in the lines of sight to pulsars, which was the the main theme of this thesis. The high time resolution data obtained with the advancements made in the software beamforming (McSweeney et al., 2020) are also amenable for performing phase-coherent de-dispersion. With these enhancements, it became possible to undertake useful studies of even short-period millisecond pulsars, down to frequencies $\sim$ 80 MHz. This was demonstrated using the observations of the millisecond pulsar PSR J2241−5236, which resulted in high-precision DM measurements towards its line of sight. The DM precision attained is (2-6)$\times 10^{-6}$ pc cm^{-3}, almost an order of magnitude better than that currently achieved at higher frequencies by telescopes around the world. This formed the main theme of Chapter 3.

The relevance of frequency-dependent or "chromatic" dispersion measure (DM) gained significant attention within the past few years. A detailed theoretical treatment was provided by Cordes et al. (2016). This subtle effect arises as a consequence of multipath scattering, as the volume or path lengths sampled by the pulsar radiation is a strong function of the observing frequency. If proven to be relevant, it may have potential implications for timing array experiments, particularly for informing suitable observing strategies for future PTAs. To date, very limited observational studies have been made to investigate this potentially important effect. The only reported work in the literature is by Donner et al. (2019), who claimed the detection of this effect in their low-frequency observations (made with the German LOFAR stations) of the long-period pulsar PSR J2219+4754. Their analysis and results were revisited by Lam et al. (2020), who also called into question some of the adopted strategies for their analysis.

Furthermore, some of the recent studies with the MWA and LWA suggested that MSP J2145−0750 tends to show significantly measurable "excess" DM when observations are made at frequencies below 300 MHz (Bhat et al., 2018; Dowell

et al., 2013). This could possibly be due to a similar effect (i.e., frequency dependent DMs). The MWA observations presented in Chapter 3 hint at a similar trend (i.e., excess DM at low frequencies) for MSP J2241−5236.

If there exists a frequency-dependence for DM, one way to further investigate it, and unambiguously confirm it, is via making contemporaneous observations covering a very large range in frequency. This motivated my second PhD project, which involved multi-telescope observations of the pulsar J2241−5236. This was realised through a combination of targeted telescope proposals and the ongoing MSP monitoring projects at the MWA and Parkes telescopes. The main result from these observations is a clear detection of a frequency dependence in DM across the 80 MHz to 4 GHz range. This formed the subject of Chapter 4.

As well known, most MSPs display rather complex evolution of their pulse profiles as a function of the observing frequency. Observations of PSR J2145−0750, which has a significant profile evolution, proved particularly useful for the application of frequency-dependent timing templates in an effort to obtain improved DM measurements. The related techniques are being developed by members of the PPTA group, who are developing a software called "PTIME", which is being tested for high precision timing using data obtained with the ultra-wide band receiver that has been in operation at the Parkes radio telescope since 2019.

The PTIME software was used for the analysis of PSR J2145−0750 observations. It was tried systematically, and consistently, on data from multiple contemporaneous observations of this pulsar obtained using the MWA, uGMRT and Parkes telescopes. Our analysis shows that, for the uGMRT and Parkes data (>300 MHz), where the profile evolution is relatively less complex (compared to those seen at the MWA's frequencies), such an analysis leads to almost an order of magnitude improvement in DM precision, when compared to what is achievable with the use of a single frequency template. Whereas in the case of MWA data, the application of PTIME leads to an improvement by only a factor of $\sim$ 2-3 in DM precision. This lower than expected improvement could be due to sys-

tematics in the data, or because of a more complex profile evolution seen at low frequencies, and the possibility that it is not adequately modeled by the current techniques implemented in PTIME. This formed the subject of Chapter 5.

6.2 High time resolution detection of MSPs

Over the past years, a series of developments has made the MWA a pulsar-capable telescope. The most significant addition has been the implementation of a new beamforming software, which generates high time resolution pulsar data at $\sim 1\,\mu s$ time resolution. This facilitated high-quality detections of millisecond pulsars and we are able to resolve temporal structures in the pulsar's profiles. This thesis undertook the very first application and demonstration of this new functionality. This was done using early science observations of MSP J2241−5236, one of the high priority targets for pulsar timing array experiments.

The important outcome is that even with the MWA's modest sensitivity, and notwithstanding the complexity of observing pulsars with the MWA, we have been able to make high-precision DM measurements for this pulsar. Even though it was demonstrated using a small number of observations, the precision achieved is highly competitive, down to $\sim 10^{-6}\,\mathrm{pc\,cm^{-3}}$, which is better than those currently achieved at other frequencies, or with most currently operational telescopes. This is primarily resulting from the micro second level timing precision that is currently achieved for this pulsar with the MWA. It essentially showcases the prospects of instruments like the MWA to make high-precision DM measurements. Even though the focus of this thesis was limited to two specific objects (PSRs J2241−5236 and J2145−0750), with the capability demonstrated using these two pulsars, similar studies can be readily extended to other millisecond pulsars, including those that display a complex and significant evolution in their pulse profiles. For example, PSR J0437−4715 is an another important target for PTAs. It has also been the subject of active studies with the MWA (Bhat et al., 2014, 2016, 2018). It is known for a highly complex variation in the profile shape

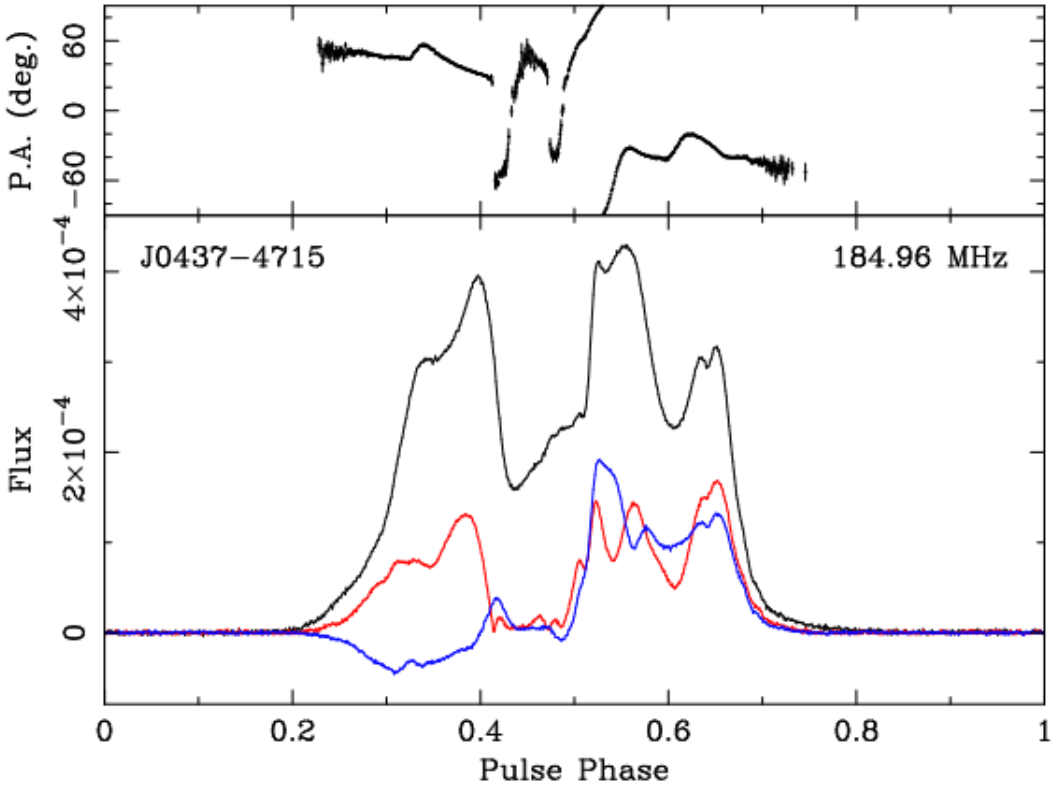

Figure 6.1: Coherently de-dispersed, high time resolution profile of PSR J0437−4715. Observations were taken over a 30 MHz bandwidth centered at 185 MHz frequency with the upgraded MWA (Phase 2). The original observations were published in Bhat et al. (2018), and were reprocessed using the high time resolution capability presented in this thesis (McSweeney et al., 2020). The top panel represents the polarisation position angle. The bottom panel represents the total intensity profile (black curve) revealing some notch-like features, which can be clearly seen at pulse phases of ∼0.5 and ∼0.7. Different colours represent the linear (red) and circular (blue) polarisations.

with frequency. As seen from Figure 6.1, the pulse profile shows multiple notch-like features in the observations made with the MWA. The timing analysis of this particular pulsar is as such intended to be the subject of a Honours research project in the coming year. With instruments like Parkes and MeerKAT operating primarily at high frequencies (above 500 MHz), the MWA can now fill in the low-frequency gap, and can thus help develop a more comprehensive picture of the profile evolution for a large sample of southern MSPs, as well as for normal pulsars.

Most of the MSPs in the southern sky have been discovered using Parkes or other instruments using high frequency surveys. The fact that MSPs generally tend to have steeper spectra, also strengthens the case of considering low frequency surveys. Pulsar search efforts are just beginning to ramp up with the MWA (e.g., Swainston et al., 2021) and there is potential for low frequency telescopes such as the MWA to contribute in this area by finding MSPs in the southern sky. Furthermore, the planned major upgrade in the coming year (i.e., MWA Phase 3) is expected to result in significantly enhanced sensitivity with the addition of a new correlator and beamformer, which will help to characterize a large sample of MSPs at low frequencies. This will eventually help the MWA to emerge as a prominent facility for a more effective integration into global PTA efforts.

6.3 Frequency-dependent DMs

The high quality MWA pulsar data can also be used to investigate the recently advanced frequency-dependent dispersion measures. As such there have been very few studies on this front. In this thesis, I undertook the very first study to look at two specific millisecond pulsars over a very large frequency range ($\sim$100 MHz to 4 GHz) using data obtained from contemporaneous observations. The most significant result of this multi-frequency campaign is a clear evidence of frequency-dependent DM in the line of sight toward MSP J2241$-$5236, which

is seen consistently at multiple different epochs. A hint of this effect was also seen in the sight line toward PSR J2145−0750.

Having seen this effect for two pulsars, it seems worthwhile to perform such observations for a larger sample of PTA pulsars. This was however beyond the scope of this thesis work. Nonetheless, the feasibility of such studies has been demonstrated through coordinated observing programs. This will help determine how many pulsars exhibit such a frequency dependence and the magnitude of this effect. Some related points are summarised below:

- Observing more MSPs with such contemporaneous wide-band coverage will help confirm (and further investigate) the scaling in frequency that is seen in the frequency dependent DM measured towards MSPs J2241−5236 and J2145−0750.

- The nature of the ISM tends to be different for every pulsar, and therefore monitoring a large sample of pulsars may help better understand the ISM and frequency dependence.

- Profile evolution varies substantially between pulsars. Therefore, the application of 2-D template technique may help distinguish between the DM variations resulting from profile evolution and that caused by chromatic DM effects.

- Estimates of DM may be contaminated by other chromatic effects in timing data that result from refraction and multi-path propagation. For example, multipath propagation causes temporal broadening of the pulse shapes that is more prominent at lower frequencies. Pulse broadening may couple with intrinsic profile shape changes, adding additional time-dependent time-of-arrival (TOA) errors, and thus producing apparent DM changes.

- Frequency-dependent effects also need to be measured simultaneously, or at least contemporaneously, or else they can be potentially confused with temporal variations in the ISM.

6.4 Temporal variations in DM

Low frequency pulsar observations can also be used to track small variations in dispersion measure. In Chapters 3 and 5, we have presented temporal DM variations for PTA pulsars J2241−5236 and J2145−0750 deduced from observations made with the MWA. We have reported δDM of $\sim 2 \times 10^{-4}\,\mathrm{pc\,cm^{-3}}$ for PSR J2241−5236 over a time span of 5 years, and δDM of $\sim 1 \times 10^{-3}\,\mathrm{pc\,cm^{-3}}$ for PSR J2145−0750 over a time span of 4 years. The number of observations are currently limited with the MWA, and this is because the MWA is a complex instrument and every single observation produces a large amount of data (∼30 TB per hour) and therefore requires substantial offline processing. Regardless of this, low frequency observations are inherently more sensitive to the variations in DM. For PSR J2145−0750, the measured DM variations are also comparable to those seen in 12 years of NanoGrav monitoring ($\sim 0.001\,\mathrm{pc\,cm^{-3}}$; Alam et al. 2020), despite the fact that NanoGrav observations are made at a much higher cadence, and over much longer time spans.

6.5 Low frequency studies of binary pulsars

In addition to frequency-dependent DMs and temporal variations in DM, it is also important to look for any orbital DM dependence of measured DMs. In order to investigate this, we need to sample the binary orbit in a single observation, if at all possible, so it can be disentangled from temporal DM variations (due to the ISM), or ionospheric variations. With the limitations of the MWA (i.e., a maximum recording capacity for ∼90 minutes and a 30.72 MHz bandwidth of the voltage capture mode), an attempt was made to sample the 3.5-hour orbit of PSR J2241−5236 using multiple short (10 minute) observations. The observations were performed such that the 90 minute VCS recording time was divided into shorter (10 minute) observations. The analysis of these data revealed an excess DM of the order of $(1.4 \pm 0.6) \times 10^{-5}\,\mathrm{pc\,cm^{-3}}$ near the orbital phase of ∼0.4-0.5

for this pulsar. This is much smaller than those reported for all other binary systems currently known. This could be due to the fact that the companion of J2241−5236 is not eclipsing the pulsar signal. The variations may be attributed to tailing companion winds, which interact with the pulsar radiation. In any case, these observations and analysis showcase the MWA's sensitivity to measure small DM variations with a high precision. With the improved capabilities of the MWA in the future, it will be possible to carry out longer (and continuous) recording in time, and over a larger bandwidth, which will enable the investigation of orbital dependence of DM for more PTA pulsars.

6.6 Timing data from wide-band observations

As is well known, pulsar profiles evolve significantly as a function of the observation frequency. This can result in inaccurate estimates of TOA uncertainties, if not adequately modeled into the timing analysis. In the modern era of wide-band radio receivers with larger fractional bandwidths, this is an important consideration. As discussed in Chapter 5, we have tested a software package PTIME, which offers an interactive interface for generating 2-dimensional timing templates by accounting for the effects of interstellar scintillation, the frequency evolution of pulse profiles, and DM variations. Through the application of this software, we have attempted to minimise the bias in TOAs for each of our observation.

The software was used for the analysis of observations of MSP J2145−0750, a well-studied pulsar by multiple different PTAs. The pulsar shows a significant profile evolution with frequency. Contemporaneous data from the MWA, uGMRT and Parkes were used in order to minimise any temporal variations due to the ISM and to cover a wide range in frequency ($\sim 100\,\mathrm{MHz}$ to $4\,\mathrm{GHz}$). The degree of profile evolution at low observing frequencies is particularly complex for this pulsar. Therefore, the focus of this work was to investigate the effectiveness of the PTIME technique in the determination of DMs from low frequency data. The results were compared against those obtained using a single frequency analytic

template which does not account for the profile evolution with frequency.

The application of frequency-dependent templates resulted in a DM precision improvement from $2.9 \times 10^{-4}\,\mathrm{pc\,cm^{-3}}$ to $1 \times 10^{-5}\,\mathrm{pc\,cm^{-3}}$ for uGMRT BAND3 (300-500 MHz); $2 \times 10^{-3}\,\mathrm{pc\,cm^{-3}}$ to $5.4 \times 10^{-4}\,\mathrm{pc\,cm^{-3}}$ for uGMRT BAND4 (550-750 MHz); and $1.9 \times 10^{-3}\,\mathrm{pc\,cm^{-3}}$ to $2 \times 10^{-4}\,\mathrm{pc\,cm^{-3}}$ for the Parkes UWL band (700-4000 MHz). Whereas, only a marginal improvement from $3.2 \times 10^{-5}\,\mathrm{pc\,cm^{-3}}$ to $1.7 \times 10^{-5}\,\mathrm{pc\,cm^{-3}}$ was seen in the MWA band (80-220 MHz). This is possibly due to a more complex nature of the profile evolution at low frequencies. However, the MWA observations yield a precision $\sim 10^{-5}\,\mathrm{pc\,cm^{-3}}$ for this pulsar, which is quite comparable to that is currently achieved at other timing frequencies, and also comparable to that measured for PSR J2241−5236.

Following the generally encouraging results from the work presented here, the PTIME technique of generating frequency-dependent templates can be considered for applying to a wider variety of pulsars, in order to develop a detailed understanding of the impact of profile evolution in achievable timing and DM precisions. Additionally, other techniques can also be explored; for example, the method that employs PulsePortraiture (Pennucci, 2019). However, an exploration of this method on our data was outside the scope of this thesis work. A detailed comparison of multiple different techniques may help converge on most effective (and optimal) techniques which can be routinely used for the analysis of PTA data from wide-band observations as well as data from contemporaneous wideband frequency coverage.

Appendices

Appendix A

Statement of Originality

This section is to comply with the requirement that all co-authors of work included in this thesis outline their contributions. In communicating this statement to the co-authors, they were also informed that the lack of a response would be taken as unconditional tacit approval. Otherwise, all co-authors have read and agreed to the following statement, and their responses can be found afterward.

A.1 Statement of contribution for Chapter 3

The MWA-VCS observations (obtained through the G0021 project; PI Bhat) were scheduled and undertaken by Dr Steven Tremblay, and processed using the beamformer software that was developed by Dr Steve Ord and Dr McSweeney. Data processing was carried by myself under the supervision of Dr Ramesh Bhat and Dr Steven Tremblay. All MWA data used for this project were reduced and calibrated by myself. The analysis and interpretation were carried out under the supervision of R. Bhat, S. Tremblay and R. Shannon. I wrote all the sections of the article. R. Bhat, S. Tremblay and R. Shannon aided in the preparation of the article writing process by providing guidance with the structure and contextual discussion, both before and after referee comments were received. Rest of the co-authors are the MWA's builder's list at the time and so were included as a

part of the MWA's publication policy.

Below are the co-author responses to this statement of contribution:

Ramesh Bhat <ramesh.bhat@curtin.edu.au>

All good, Dilpreet. Good luck this week.

Regards,

Ramesh

Steven Tremblay <quantumswordsman@gmail.com>

Yes, I approve.

Good luck with submission :-)

Steve Tremblay

Samuel McSweeney <sammy.mcsweeney@gmail.com>

I agree!

Cathryn Trott <Cathryn.Trott@curtin.edu.au>

Dear Dilpreet,

Congratulations!!!!!

I agree with the statement provided about co-authorship.

Cheers,

Cath

Steven Tingay <s.tingay@curtin.edu.au>

Dear Dilpret,

Thanks. I agree.

Good luck with the submission.

Regards,

Steven

Randall Wayth <R.Wayth@curtin.edu.au>

Great to hear this Dilpreet. I'm happy to agree/approve.

Cheers,

Randall

Miguel F Morales <miguelfm@uw.edu>

I agree

-Miguel

Adam Beardsley <adam.p.beardsley@gmail.com>

Hi Dilpreet,

I agree with your statement of originality. Congrats on this great milestone, and good luck!

-Adam

David Kaplan <kaplan@uwm.edu>

Hi, Dilpreet

I agree. Congratulations!

-David Kaplan

David Kenney <david.kenney@curtin.edu.au>

Hi Dilpreet,

You have my unconditional approval.

Regards

DaveK

Mia Walker <Mia.Walker@curtin.edu.au>

Hi Dilpreet,

I agree with the statement below and wholeheartedly support your submission.

Kind regards,

Mia Walker

David Emrich <D.Emrich@curtin.edu.au>

Hi Dilpreet,

I have no objection to your statement, so “I agree”.

Hope your thesis submission goes really well!

Cheers, Dave E.

Appendix B

Aberration, retardation, and radius-to-frequency mapping

Apart from the average shape of the intrinsic pulse (before it travels through the ISM), the location of its centroid in time, t, may also be a non-constant function of frequency. If this function happens to also go as ν^{-2}, where ν is the frequency, then the observer will not be able to disentangle the effect of the ISM from the intrinsic pulse evolution, and will measure a single value of dispersion measure (DM). Any other functional form will show up as a deviation from the inverse-square dependence.

Aberration and retardation (AR) effects can shift a pulse component forward in phase (Dyks et al., 2004). The amount of shift depends upon the emission height ($r_{\rm em}$).

$$\Delta\phi_{\rm AR} \simeq -2r' \equiv -\frac{2r_{\rm em}}{r_{\rm LC}} \tag{B.1}$$

where $r_{\rm LC}$ is the radius of the light cylinder. The dependence of emission height with observing frequency can be expressed via relation

$$r_{\rm em} = K\,\nu^{-\alpha} \tag{B.2}$$

where K is the constant of proportionality, and with α ranging from roughly 0.25

to 0.5, with a typical value of 0.33 for normal pulsars (Cordes, 1978; Kijak & Gil, 1998). If an average profile is subjected to both ISM dispersion and AR effects, the DM over an arbitrarily small band can be measured by measuring the slope of the pulse as it appears in a dynamic spectrum. At each frequency, they would expect to find the measured slope to be

$$\frac{dt}{d\nu} = -2\mathcal{D}\nu^{-3} \times \mathrm{DM_{meas}} \tag{B.3}$$

where $\mathrm{DM_{meas}}$ is the measured DM. However, this measured slope will in reality be made up of the slope due to the true DM and that due to the combined effects of AR and radio-to-frequency mapping (RFM),

$$\frac{dt_{\mathrm{AR}}}{d\nu} \simeq \frac{-2P}{r_{\mathrm{LC}}}\frac{dr_{\mathrm{em}}}{d\nu}$$

$$\simeq \frac{2P}{r_{\mathrm{LC}}} K\alpha\nu^{-\alpha-1}$$

$$\simeq \frac{2P\alpha r^{'}}{\nu}$$

Thus,

$$\frac{dt}{d\nu} = \frac{dt_{\mathrm{DM}}}{d\nu} + \frac{dt_{\mathrm{AR}}}{d\nu}$$

$$-2\mathcal{D}\nu^{-3}\mathrm{DM_{meas}} \simeq -2\mathcal{D}\nu^{-3}\mathrm{DM} + \frac{2P\alpha r^{'}}{\nu}$$

$$\mathrm{DM_{meas}}(\nu) \simeq \mathrm{DM} - \frac{P\alpha r^{'}\nu^2}{\mathcal{D}}$$

Expressing the DM in $\mathrm{pc\,cm^{-3}}$, ν in MHz, and pulsar period (P) in ms,

$$\Delta\mathrm{DM} \equiv \mathrm{DM} - \mathrm{DM_{meas}}$$

$$\simeq 2.41 \times 10^{-7}\,\mathrm{pc\,cm^{-3}}\Big(\frac{P}{\mathrm{ms}}\Big)\Big(\frac{\nu}{\mathrm{MHz}}\Big)^2 \alpha r' \tag{B.4}$$

where $\mathrm{DM_{meas}}$ is the measured DM.

Appendix C

Copyright information

Chapters 3 was published in Astrophysical Journal (ApJ) and below is the permissions email from the publisher, approving me to include this journal articles in my PhD thesis.

Re: Request to re-publish article as a thesis chapter

Permissions <permissions@ioppublishing.org>
Fri 7/9/2021 6:13 PM
To: Dilpreet Kaur <dilpreetkaur2@postgrad.curtin.edu.au>

DearÀDilpreet Kaur,
À
Thank you for your email.
À
AAS authors may reuse their own work in a thesis without needing permission, providing it is not then being published commercially. You are also allowed to use flgures from the article. Therefore, please go ahead with the inclusion of this material in your new work —no permission is required from AAS. À
À
Please include the following alongside the material: À
À

- oÀÀÀÀthe source of the material, including author, article title, title of journal, volume number, issue number (if relevant), page range (or flrst page if this is the only information available) and date of flrst publication. This material can be contained in a footnote or reference.À
- oÀÀÀÀfor material being published electronically, a link back to the article (via DOI)À
- oÀÀÀÀif practical and IN ALL CASES for works published under any of the Creative Commons licences the words "© AAS. Reproduced with permission".ÀÀ

This permission does not apply to any material/flgure which is credited to another source in the AAS publication or has been obtained from a third party.ÀExpress permission for such materials/flgures must be obtained from the copyright owner.

Kind regards,
À

Sophie
Copyright & Permissions Team
Sophie Brittain - Rights & Permissions AssistantÀ
Cameron Wood - Legal & Rights Adviser
Contact Details
E-mail: permissions@ioppublishing.org

For further information about copyright and how to request permission:
https://publishingsupport.iopscience.iop.org/copyright-journals/
See also:Àhttps://publishingsupport.iopscience.iop.org/
Please see our Author Rights Policy https://publishingsupport.iopscience.iop.org/author-rights-policies/
Please note: We do not provide signed permission forms as a separate attachment. Please print this email and provide it to your publisher as proof of permission. **Please note**: Any statements made by IOP Publishing to the effect that authors do not need to get permission to use any content where IOP Publishing is not the publisher is not intended to constitute any sort of legal advice. Authors must make their own decisions as to the suitability of the content they are using and whether they require permission for it to be published within their article.

À

From: Dilpreet Kaur <dilpreetkaur2@postgrad.curtin.edu.au>
Sent: 08 July 2021 06:26
To: permissions@iop.org <permissions@iop.org>
Subject: Request to re-publish article as a thesis chapter

Hello,

I'm writing to request the re-publication of my article "A high time resolution study of the millisecond pulsar J2241-5236 at frequencies below 300 MHz" (doi: 10.3847/1538-4357/ab338f) as a chapter in my Doctoral thesis. My ORCID is **0000-0003-4879-1019**

From reading the AAS Copyright information, I understand that as first author I retain the right to reproduce the material how I see fit, however my University requires that I retrieve formal permission from the journal. Is it possible to get a letter or other official document allowing me to publish the material unchanged as part of my thesis?

Kind regards,
Dilpreet Kaur
PhD Candidate Curtin University | Curtin Institute of Radio Astronomy
International Centre for Radio Astronomy Research

Bibliography

B. P. Abbott, et al. (2016). 'GW151226: Observation of Gravitational Waves from a 22-Solar-Mass Binary Black Hole Coalescence'. **116**(24):241103.

B. P. Abbott, et al. (2017). 'GW170817: Observation of Gravitational Waves from a Binary Neutron Star Inspiral'. **119**(16):161101.

A. L. Ahuja, et al. (2007). 'The effect of pulse profile evolution on pulsar dispersion measure'. *Monthly Notices of the Royal Astronomical Society* **377**(2):677–686.

M. F. Alam, et al. (2020). 'The NANOGrav 12.5-year Data Set: Wideband Timing of 47 Millisecond Pulsars'. *arXiv e-prints* p. arXiv:2005.06495.

H. An, et al. (2018). 'Signatures of Intra-binary Shock Emission in the Black Widow Pulsar Binary PSR J22415236'. *The Astrophysical Journal Letters* **868**:L8.

J. Antoniadis, et al. (2013). 'A Massive Pulsar in a Compact Relativistic Binary'. *Science* **340**(6131):448.

A. M. Archibald, et al. (2014). 'Millisecond Pulsar Scintillation Studies with LOFAR: Initial Results'. *The Astrophysical Journal Letters* **790**(2):L22.

Z. Arzoumanian, et al. (2020). 'The NANOGrav 12.5 yr Data Set: Search for an Isotropic Stochastic Gravitational-wave Background'. *The Astrophysical Journal Letters* **905**(2):L34.

Z. Arzoumanian, et al. (2018). 'The NANOGrav 11-year Data Set: High-precision Timing of 45 Millisecond Pulsars'. *The Astrophysical Journal Supplement Series* **235**(2):37.

Z. Arzoumanian, et al. (2015). 'NANOGrav Constraints on Gravitational Wave Bursts with Memory'. *The Astrophysical Journal* **810**(2):150.

W. Baade & F. Zwicky (1934). 'Cosmic Rays from Super-novae'. *Contributions from the Mount Wilson Observatory* **3**:79–83.

D. C. Backer, et al. (1982). 'A millisecond pulsar'. *Nature* **300**(5893):615–618.

M. Bailes, et al. (2018). 'MeerTime - the MeerKAT Key Science Program on Pulsar Timing'. *arXiv e-prints* p. arXiv:1803.07424.

M. Bailes, et al. (1994). 'Discovery of Three Binary Millisecond Pulsars'. *The Astrophysical Journal Letters* **425**:L41.

M. Bailes, et al. (2020). 'The MeerKAT telescope as a pulsar facility: System verification and early science results from MeerTime'. *Publications of the Astronomical Society of Australia* **37**:e028.

C. G. Bassa, et al. (2017). 'LOFAR Discovery of the Fastest-spinning Millisecond Pulsar in the Galactic Field'. *The Astrophysical Journal Letters* **846**:L20.

S. D. Bates, et al. (2013). 'The pulsar spectral index distribution'. *Monthly Notices of the Royal Astronomical Society* **431**:1352–1358.

N. D. R. Bhat, et al. (2004). 'Multifrequency Observations of Radio Pulse Broadening and Constraints on Interstellar Electron Density Microstructure'. *The Astrophysical Journal* **605**:759–783.

N. D. R. Bhat, et al. (2016). 'Scintillation Arcs in Low-frequency Observations of the Timing-array Millisecond Pulsar PSR J0437-4715'. *The Astrophysical Journal* **818**:86.

N. D. R. Bhat, et al. (2014). 'The Low-frequency Characteristics of PSR J0437-4715 Observed with the Murchison Wide-field Array'. *The Astrophysical Journal Letters* **791**:L32.

N. D. R. Bhat, et al. (2018). 'Observations of Low-frequency Radio Emission from Millisecond Pulsars and Multipath Propagation in the Interstellar Medium'. *The Astrophysical Journal Supplement Series* **238**(1):1.

H. Bignall, et al. (2015). 'Microarcsecond structure of an AGN Jet via Interstellar Scintillation'. In F. Massaro, C. C. Cheung, E. Lopez, & A. Siemiginowska (eds.), *Extragalactic Jets from Every Angle*, vol. 313, pp. 143–144.

A. Bulatek & S. White (2020). 'Designing and testing an ultra-wideband receiver for the Green Bank Telescope'. In *American Astronomical Society Meeting Abstracts #235*, vol. 235 of *American Astronomical Society Meeting Abstracts*, p. 175.17.

B. J. Burn (1966). 'On the depolarization of discrete radio sources by Faraday dispersion'. *Monthly Notices of the Royal Astronomical Society* **133**:67.

S. Chamberlin & X. Siemens (2012). 'Overlap Reduction Functions for Pulsar Timing Arrays in Alternative Theories of Gravity'. In *American Astronomical Society Meeting Abstracts #219*, vol. 219 of *American Astronomical Society Meeting Abstracts*, p. 146.13.

I. Cognard, et al. (1993). 'An extreme scattering event in the direction of the millisecond pulsar 1937 + 21'. *Nature* **366**(6453):320–322.

W. A. Coles, et al. (2015). 'Pulsar Observations of Extreme Scattering Events'. *The Astrophysical Journal* **808**(2):113.

J. M. Cordes (1978). 'Observational limits on the location of pulsar emission regions'. *The Astrophysical Journal* **222**:1006–1011.

J. M. Cordes & T. J. W. Lazio (2002). 'NE2001.I. A New Model for the Galactic Distribution of Free Electrons and its Fluctuations'. *arXiv e-prints* pp. astro–ph/0207156.

J. M. Cordes & B. J. Rickett (1998). 'Diffractive Interstellar Scintillation Timescales and Velocities'. *The Astrophysical Journal* **507**(2):846–860.

J. M. Cordes & R. M. Shannon (2010). 'A Measurement Model for Precision Pulsar Timing'. *arXiv e-prints* p. arXiv:1010.3785.

J. M. Cordes, et al. (2016). 'Frequency-dependent Dispersion Measures and Implications for Pulsar Timing'. *The Astrophysical Journal* **817**:16.

J. M. Cordes, et al. (1985). 'Small-scale electron density turbulence in the interstellar medium.'. *The Astrophysical Journal* **288**:221–247.

R. E. Crochiere & . Rabiner, Lawrence R. (1983). *Multirate digital signal processing*. Englewood Cliffs, N.J. : Prentice-Hall. Includes bibliographical references and index.

S. Dai, et al. (2015). 'A study of multifrequency polarization pulse profiles of millisecond pulsars'. *Monthly Notices of the Royal Astronomical Society* **449**:3223–3262.

S. Dai, et al. (2019). 'Wideband Polarized Radio Emission from the Newly Revived Magnetar XTE J1810-197'. *The Astrophysical Journal Letters* **874**(2):L14.

A. de Oliveira-Costa, et al. (2008). 'A model of diffuse Galactic radio emission from 10 MHz to 100 GHz'. *Monthly Notices of the Royal Astronomical Society* **388**:247–260.

P. B. Demorest (2011). 'Cyclic spectral analysis of radio pulsars'. *Monthly Notices of the Royal Astronomical Society* **416**:2821–2826.

P. B. Demorest, et al. (2013). 'Limits on the Stochastic Gravitational Wave Background from the North American Nanohertz Observatory for Gravitational Waves'. *The Astrophysical Journal* **762**(2):94.

P. B. Demorest, et al. (2010). 'A two-solar-mass neutron star measured using Shapiro delay'. *Nature* **467**:1081–1083.

G. Desvignes, et al. (2016). 'High-precision timing of 42 millisecond pulsars with the European Pulsar Timing Array'. *Monthly Notices of the Royal Astronomical Society* **458**(3):3341–3380.

J. Y. Donner, et al. (2020). 'Dispersion measure variability for 36 millisecond pulsars at 150 MHz with LOFAR'. *Astronomy and Astrophysics* **644**:A153.

J. Y. Donner, et al. (2019). 'First detection of frequency-dependent, time-variable dispersion measures'. *Astronomy and Astrophysics* **624**:A22.

J. Dowell, et al. (2013). 'Detection and Flux Density Measurements of the Millisecond Pulsar J2145-0750 below 100 MHz'. *The Astrophysical Journal Letters* **775**:L28.

G. S. Downs & P. E. Reichley (1983). 'JPL pulsar timing observations. II. Geocentric arrival times.'. *The Astrophysical Journal Supplement Series* **53**:169–240.

J. Dyks, et al. (2004). 'On the Methods of Determining the Radio Emission Geometry in Pulsar Magnetospheres'. *The Astrophysical Journal* **607**(2):939–948.

R. L. Fiedler, et al. (1987). 'Extreme scattering events caused by compact structures in the interstellar medium'. *Nature* **326**(6114):675–678.

E. Fonseca, et al. (2021). 'Refined Mass and Geometric Measurements of the High-mass PSR J0740+6620'. *The Astrophysical Journal Letters* **915**(1):L12.

G. Foster, et al. (2015). 'Intrinsic instrumental polarization and high-precision pulsar timing'. *Monthly Notices of the Royal Astronomical Society* **453**(2):1489–1502.

R. S. Foster & D. C. Backer (1990). 'Constructing a Pulsar Timing Array'. *The Astrophysical Journal* **361**:300.

P. Freire (2012). 'weblink'. https://www3.mpifr-bonn.mpg.de/staff/pfreire/BEACON.html.

A. S. Fruchter, et al. (1990). 'The Eclipsing Millisecond Pulsar PSR 1957+20'. *The Astrophysical Journal* **351**:642.

J. R. Gair, et al. (2015). 'Mapping gravitational-wave backgrounds of arbitrary polarisation using pulsar timing arrays'. **92**(10):102003.

M. Geyer, et al. (2017). 'Scattering analysis of LOFAR pulsar observations'. *Monthly Notices of the Royal Astronomical Society* **470**(3):2659–2679.

J. Gil & A. Krawczyk (1997). 'PSR J0437-4715: a challenge for pulsar modelling'. *Monthly Notices of the Royal Astronomical Society* **285**:561–566.

T. Gold (1968). 'Rotating Neutron Stars as the Origin of the Pulsating Radio Sources'. *Nature* **218**:731–732.

J. A. Green, et al. (2009). 'The 6-GHz multibeam maser survey - I. Techniques'. *Monthly Notices of the Royal Astronomical Society* **392**(2):783–794.

L. P. Grishchuk (2005). 'REVIEWS OF TOPICAL PROBLEMS: Relic gravitational waves and cosmology'. *Physics Uspekhi* **48**(12):1235–1247.

L. Guillemot, et al. (2019). 'Timing of PSR J2055+3829, an eclipsing black widow pulsar discovered with the Nançay Radio Telescope'. *Astronomy and Astrophysics* **629**:A92.

Y. Gupta (1995). 'On the Correlation between Proper Motion Velocities and Scintillation Velocities of Radio Pulsars'. *The Astrophysical Journal* **451**:717.

Y. Gupta, et al. (2017). 'The upgraded GMRT: opening new windows on the radio Universe'. *Current Science* **113**(4):707–714.

Y. Gupta, et al. (2000). 'Pulsar Research with the GMRT: A Status Report'. In M. Kramer, N. Wex, & R. Wielebinski (eds.), *IAU Colloq. 177: Pulsar Astronomy - 2000 and Beyond*, vol. 202 of *Astronomical Society of the Pacific Conference Series*, p. 277.

P. A. Hamilton, et al. (1985). 'Changing parameters along the path to the VELA pulsar.'. *Monthly Notices of the Royal Astronomical Society* **214**:5P–8.

J. L. Han, et al. (2006). 'Pulsar Rotation Measures and the Large-Scale Structure of the Galactic Magnetic Field'. *The Astrophysical Journal* **642**(2):868–881.

T. H. Hankins & B. J. Rickett (1975). 'Pulsar signal processing.'. *Methods in Computational Physics* **14**:55–129.

T. E. Hassall, et al. (2012). 'Wide-band simultaneous observations of pulsars: disentangling dispersion measure and profile variations'. *Astronomy and Astrophysics* **543**:A66.

D. J. Helfand, et al. (1977). 'Pulsar flux observations: long-term intensity and spectral variations.'. *The Astronomical Journal* **82**:701–705.

R. W. Hellings & G. S. Downs (1983). 'Upper limits on the isotropic gravitational radiation background from pulsar timing analysis.'. *The Astrophysical Journal Letters* **265**:L39–L42.

M. Hernández-Pajares, et al. (2009). 'The IGS VTEC maps: a reliable source of ionospheric information since 1998'. *Journal of Geodesy* **83**(3-4):263–275.

J. W. T. Hessels, et al. (2006). 'A Radio Pulsar Spinning at 716 Hz'. In *American Astronomical Society Meeting Abstracts #207*, vol. 207 of *American Astronomical Society Meeting Abstracts*, p. 209.07.

A. Hewish, et al. (1968). 'Observation of a Rapidly Pulsating Radio Source'. *Nature* **217**:709–713.

G. Hobbs, et al. (2012). 'Development of a pulsar-based time-scale'. *Monthly Notices of the Royal Astronomical Society* **427**:2780–2787.

G. Hobbs, et al. (2006). 'TEMPO2: a New Pulsar Timing Package'. *Chinese Journal of Astronomy and Astrophysics Supplement* **6**(2):189–192.

G. Hobbs, et al. (2005). 'A statistical study of 233 pulsar proper motions'. *Monthly Notices of the Royal Astronomical Society* **360**(3):974–992.

G. Hobbs, et al. (2020). 'An ultra-wide bandwidth (704 to 4 032 MHz) receiver for the Parkes radio telescope'. *Publications of the Astronomical Society of Australia* **37**:e012.

A. W. Hotan, et al. (2004). 'PSRCHIVE and PSRFITS: An Open Approach to Radio Pulsar Data Storage and Analysis'. *Publications of the Astronomical Society of Australia* **21**(3):302–309.

A. H. Jaffe & D. Backer (2003). 'Gravitational Radiation from Massive Black Hole Binaries'. In *IAU Joint Discussion*, vol. 25 of *IAU Joint Discussion*, p. 27.

F. Jankowski, et al. (2017). 'Spectral properties of 441 radio pulsars'. *ArXiv e-prints* .

F. Jankowski, et al. (2018). 'Spectral properties of 441 radio pulsars'. *Monthly Notices of the Royal Astronomical Society* **473**:4436–4458.

G. Janssen, et al. (2015). 'Gravitational Wave Astronomy with the SKA'. In *Advancing Astrophysics with the Square Kilometre Array (AASKA14)*, p. 37.

F. A. Jenet, et al. (2004). 'Constraining the Properties of Supermassive Black Hole Systems Using Pulsar Timing: Application to 3C 66B'. *The Astrophysical Journal* **606**(2):799–803.

M. L. Jones, et al. (2017). 'The NANOGrav Nine-year Data Set: Measurement and Analysis of Variations in Dispersion Measures'. *The Astrophysical Journal* **841**:125.

B. C. Joshi, et al. (2018). 'Precision pulsar timing with the ORT and the GMRT and its applications in pulsar astrophysics'. *Journal of Astrophysics and Astronomy* **39**(4):51.

A. Karastergiou & S. Johnston (2007). 'An empirical model for the beams of radio pulsars'. *Monthly Notices of the Royal Astronomical Society* **380**:1678–1684.

V. M. Kaspi (2010). 'Grand unification of neutron stars'. *Proceedings of the National Academy of Science* **107**(16):7147–7152.

D. Kaur, et al. (2019). 'A High Time-resolution Study of the Millisecond Pulsar J2241-5236 at Frequencies Below 300 MHz'. *The Astrophysical Journal* **882**(2):133.

D. Kaur, et al. (2022). 'Detection of Frequency-dependent Dispersion Measure toward the Millisecond Pulsar J2241-5236 from Contemporaneous Wideband Observations'. *The Astrophysical Journal Letters* **930**(2):L27.

E. Keane, et al. (2015). 'A Cosmic Census of Radio Pulsars with the SKA'. In *Advancing Astrophysics with the Square Kilometre Array (AASKA14)*, p. 40.

M. J. Keith, et al. (2013). 'Measurement and correction of variations in interstellar dispersion in high-precision pulsar timing'. *Monthly Notices of the Royal Astronomical Society* **429**(3):2161–2174.

M. J. Keith, et al. (2011). 'Discovery of millisecond pulsars in radio searches of southern Fermi Large Area Telescope sources'. *Monthly Notices of the Royal Astronomical Society* **414**:1292–1300.

M. Kerr, et al. (2018). 'Extreme scattering events towards two young pulsars'. *Monthly Notices of the Royal Astronomical Society* **474**(4):4637–4647.

M. Kerr, et al. (2020). 'The Parkes Pulsar Timing Array project: second data release'. *Publications of the Astronomical Society of Australia* **37**:e020.

J. Kijak & J. Gil (1998). 'Radio emission regions in pulsars'. *Monthly Notices of the Royal Astronomical Society* **299**(3):855–861.

F. Kirsten, et al. (2019). 'Probing Pulsar Scattering between 120 and 280 MHz with the MWA'. *The Astrophysical Journal* **874**(2):179.

V. I. Kondratiev, et al. (2016). 'A LOFAR census of millisecond pulsars'. *Astronomy and Astrophysics* **585**:A128.

M. Kramer, et al. (1999). 'The Characteristics of Millisecond Pulsar Emission. III. From Low to High Frequencies'. *The Astrophysical Journal* **526**:957–975.

M. Kramer, et al. (2006). 'Tests of General Relativity from Timing the Double Pulsar'. *Science* **314**(5796):97–102.

M. Kramer, et al. (1998). 'The Characteristics of Millisecond Pulsar Emission. I. Spectra, Pulse Shapes, and the Beaming Fraction'. *The Astrophysical Journal* **501**:270–285.

M. A. Krishnakumar, et al. (2017). 'Multi-frequency Scatter Broadening Evolution of Pulsars. I'. *The Astrophysical Journal* **846**(2):104.

M. A. Krishnakumar, et al. (2021). 'High Precision Measurements of Interstellar Dispersion Measure with the upgraded GMRT'. *arXiv e-prints* p. arXiv:2101.05334.

S. Kudale, et al. (2020). 'Study of eclipses for Redback pulsar J1227−4853'. *arXiv e-prints* p. arXiv:2007.10005.

U. Kumar, et al. (2013). 'Tracking dispersion measure variations of timing array pulsars with the GMRT'. In J. van Leeuwen (ed.), *Neutron Stars and Pulsars: Challenges and Opportunities after 80 years*, vol. 291, pp. 432–434.

A. D. Kuzmin & B. Y. Losovsky (2001). 'No low-frequency turn-over in the spectra of millisecond pulsars'. *Astronomy and Astrophysics* **368**:230–238.

M. T. Lam, et al. (2015). 'Pulsar Timing Errors from Asynchronous Multi-frequency Sampling of Dispersion Measure Variations'. *The Astrophysical Journal* **801**(2):130.

M. T. Lam, et al. (2016). 'Systematic and Stochastic Variations in Pulsar Dispersion Measures'. *The Astrophysical Journal* **821**(1):66.

M. T. Lam, et al. (2019). 'On Frequency-Dependent Dispersion Measures and the Extreme Scattering Events Toward PSR J2219+4754'. *arXiv e-prints* p. arXiv:1903.00426.

M. T. Lam, et al. (2020). 'On Frequency-dependent Dispersion Measures and Extreme Scattering Events'. *The Astrophysical Journal* **892**(2):89.

H. C. Lambert & B. J. Rickett (1999). 'On the Theory of Pulse Propagation and Two-Frequency Field Statistics in Irregular Interstellar Plasmas'. *The Astrophysical Journal* **517**(1):299–317.

P. Lazarus, et al. (2016). 'Prospects for high-precision pulsar timing with the new Effelsberg PSRIX backend'. *Monthly Notices of the Royal Astronomical Society* **458**(1):868–880.

K. J. Lee (2016). 'Prospects of Gravitational Wave Detection Using Pulsar Timing Array for Chinese Future Telescopes'. In L. Qain & D. Li (eds.), *Frontiers*

in Radio Astronomy and FAST Early Sciences Symposium 2015, vol. 502 of *Astronomical Society of the Pacific Conference Series*, p. 19.

K. J. Lee, et al. (2014). 'Model-based asymptotically optimal dispersion measure correction for pulsar timing'. *Monthly Notices of the Royal Astronomical Society* **441**(4):2831–2844.

K. J. Lee, et al. (2008). 'Pulsar Timing as a Probe of Non-Einsteinian Polarizations of Gravitational Waves'. *The Astrophysical Journal* **685**(2):1304–1319.

E. Lenc, et al. (2017). 'The Challenges of Low-Frequency Radio Polarimetry: Lessons from the Murchison Widefield Array'. *Publications of the Astronomical Society of Australia* **34**:e040.

L. Lentati, et al. (2013). 'How to take the interstellar weather with you in pulsar timing analysis'. *arXiv e-prints* p. arXiv:1312.2403.

L. Lentati, et al. (2017). 'Wide-band profile domain pulsar timing analysis'. *Monthly Notices of the Royal Astronomical Society* **466**(3):3706–3727.

L. Lentati, et al. (2016). 'From spin noise to systematics: stochastic processes in the first International Pulsar Timing Array data release'. *Monthly Notices of the Royal Astronomical Society* **458**(2):2161–2187.

L. Levin, et al. (2016). 'The NANOGrav Nine-year Data Set: Monitoring Interstellar Scattering Delays'. *The Astrophysical Journal* **818**:166.

W. Lewandowski, et al. (2015). 'The study of multi-frequency scattering of 10 radio pulsars'. *Monthly Notices of the Royal Astronomical Society* **454**(3):2517–2528.

J. L. B. Line, et al. (2018). 'In situ measurement of MWA primary beam variation using ORBCOMM'. *Publications of the Astronomical Society of Australia* **35**:45.

K. Liu, et al. (2014). 'Measuring pulse times of arrival from broad-band pulsar observations'. *Monthly Notices of the Royal Astronomical Society* **443**(4):3752–3760.

D. R. Lorimer & M. Kramer (2004). *Handbook of Pulsar Astronomy.*

D. R. Lorimer & M. Kramer (2005). *Handbook of Pulsar Astronomy.*

R. S. Lynch, et al. (2018). 'The Green Bank North Celestial Cap Pulsar Survey. III. 45 New Pulsar Timing Solutions'. *The Astrophysical Journal* **859**:93.

A. G. Lyne & R. N. Manchester (1988). 'The shape of pulsar radio beams'. *Monthly Notices of the Royal Astronomical Society* **234**:477–508.

A. G. Lyne, et al. (1985). 'The galactic population of pulsars.'. *Monthly Notices of the Royal Astronomical Society* **213**:613–639.

A. G. Lyne, et al. (1988). 'Crab pulsar timing 1982-87.'. *Monthly Notices of the Royal Astronomical Society* **233**:667–676.

A. G. Lyne & B. J. Rickett (1968). 'Radio Observations of Five Pulsars'. *Nature* **219**:1339–1342.

D. R. Madison, et al. (2019). 'The NANOGrav 11 yr Data Set: Solar Wind Sounding through Pulsar Timing'. *The Astrophysical Journal* **872**(2):150.

R. A. Main, et al. (2020). 'Measuring interstellar delays of PSR J0613-0200 over 7 yr, using the Large European Array for Pulsars'. *Monthly Notices of the Royal Astronomical Society* **499**(1):1468–1479.

V. Maitia, et al. (2003). 'A 3 Year Long Extreme Scattering Event in the Direction of the Millisecond Pulsar J1643-1224'. *The Astrophysical Journal* **582**(2):972–977.

R. N. Manchester (1971). 'Observations of Pulsar Polarization at 410 and 1665 MHz'. *The Astrophysical Journal Supplement Series* **23**:283.

R. N. Manchester (2017). 'Pulsar timing and its applications'. In *Journal of Physics Conference Series*, vol. 932 of *Journal of Physics Conference Series*, p. 012002.

R. N. Manchester, et al. (2013). 'The Parkes Pulsar Timing Array Project'. *Publications of the Astronomical Society of Australia* **30**:e017.

R. N. Manchester, et al. (2005). 'The Australia Telescope National Facility Pulsar Catalogue'. *The Astronomical Journal* **129**:1993–2006.

R. N. Manchester & J. H. Taylor (1981). 'Observed and derived parameters for 330 pulsars.'. *The Astronomical Journal* **86**:1953–1973.

O. Maron, et al. (2000). 'Pulsar spectra of radio emission'. *Astronomy and Astrophysics Supplement Series* **147**:195–203.

S. J. McSweeney, et al. (2017). 'Low-frequency Observations of the Subpulse Drifter PSR J0034-0721 with the Murchison Widefield Array'. *The Astrophysical Journal* **836**(2):224.

S. J. McSweeney, et al. (2020). 'MWA tied-array processing III: Microsecond time resolution via a polyphase synthesis filter'. *arXiv e-prints* p. arXiv:2007.03171.

B. W. Meyers, et al. (2017). 'Spectral Flattening at Low Frequencies in Crab Giant Pulses'. *The Astrophysical Journal* **851**:20.

D. Michilli, et al. (2018). 'Low-frequency pulse profile variation in PSR B2217+47: evidence for echoes from the interstellar medium'. *Monthly Notices of the Royal Astronomical Society* **476**(2):2704–2716.

D. A. Mitchell, et al. (2008). 'Real-Time Calibration of the Murchison Widefield Array'. *IEEE Journal of Selected Topics in Signal Processing* **2**(5):707–717.

D. Mitra & J. M. Rankin (2002). 'Toward an Empirical Theory of Pulsar Emission. VII. On the Spectral Behavior of Conal Beam Radii and Emission Heights'. *The Astrophysical Journal* **577**:322–336.

T. Murphy, et al. (2017). 'Low-Frequency Spectral Energy Distributions of Radio Pulsars Detected with the Murchison Widefield Array'. *Publications of the Astronomical Society of Australia* **34**:e020.

D. J. Nice, et al. (2005). 'GBT Observations of Very Low-Mass Binary Millisecond Pulsars: A Search for Eclipses'. In F. A. Rasio & I. H. Stairs (eds.), *Binary Radio Pulsars*, vol. 328 of *Astronomical Society of the Pacific Conference Series*, p. 419.

A. Noutsos, et al. (2008). 'New pulsar rotation measures and the Galactic magnetic field'. *Monthly Notices of the Royal Astronomical Society* **386**:1881–1896.

L. O'Beirne, et al. (2019). 'Constraining alternative polarization states of gravitational waves from individual black hole binaries using pulsar timing arrays'. **99**(12):124039.

A. V. Oppenheim, et al. (1999). *Discrete-time signal processing*. Upper Saddler River, N.J. : Prentice Hall, 2nd ed edn. "International edition"–Cover.

S. M. Ord, et al. (2015). 'The Murchison Widefield Array Correlator'. *Publications of the Astronomical Society of Australia* **32**:e006.

S. M. Ord, et al. (2019). 'MWA tied-array processing I: Calibration and beamformation'. *Publications of the Astronomical Society of Australia* **36**:e030.

E. Parent, et al. (2019). 'Eight Millisecond Pulsars Discovered in the Arecibo PALFA Survey'. *The Astrophysical Journal* **886**(2):148.

A. Parthasarathy, et al. (2021). 'Measurements of pulse jitter and single-pulse variability in millisecond pulsars using MeerKAT'. *Monthly Notices of the Royal Astronomical Society* **502**(1):407–422.

T. T. Pennucci (2019). 'Frequency-dependent Template Profiles for High-precision Pulsar Timing'. *The Astrophysical Journal* **871**(1):34.

T. T. Pennucci, et al. (2014). 'Elementary Wideband Timing of Radio Pulsars'. *The Astrophysical Journal* **790**(2):93.

B. B. P. Perera, et al. (2019). 'The International Pulsar Timing Array: second data release'. *Monthly Notices of the Royal Astronomical Society* **490**(4):4666–4687.

E. J. Polzin, et al. (2020). 'Study of spider pulsar binary eclipses and discovery of an eclipse mechanism transition'. *Monthly Notices of the Royal Astronomical Society* **494**(2):2948–2968.

E. J. Polzin, et al. (2019). 'Long-term variability of a black widow's eclipses - A decade of PSR J2051-0827'. *Monthly Notices of the Royal Astronomical Society* **490**(1):889–908.

E. J. Polzin, et al. (2018). 'The eclipses of the black widow pulsar J1810+1744 at low radio frequencies'. In P. Weltevrede, B. B. P. Perera, L. L. Preston, & S. Sanidas (eds.), *Pulsar Astrophysics the Next Fifty Years*, vol. 337 of *IAU Symposium*, pp. 396–397.

N. K. Porayko, et al. (2019). 'Testing the accuracy of the ionospheric Faraday rotation corrections through LOFAR observations of bright northern pulsars'. *Monthly Notices of the Royal Astronomical Society* **483**(3):4100–4113.

T. Prabu, et al. (2015). 'A digital-receiver for the MurchisonWidefield Array'. *Experimental Astronomy* **39**(1):73–93.

G.-J. Qiao, et al. (2002). 'More Emission Cones: Multi-frequency Simulation of the Pulse Profiles of PSR J0437-4715'. **2**:361–368.

M. Rajagopal & R. W. Romani (1995). 'Ultra–Low-Frequency Gravitational Radiation from Massive Black Hole Binaries'. *The Astrophysical Journal* **446**:543.

D. J. Reardon, et al. (2016). 'Timing analysis for 20 millisecond pulsars in the Parkes Pulsar Timing Array'. *Monthly Notices of the Royal Astronomical Society* **455**(2):1751–1769.

S. H. Reddy, et al. (2017). 'A Wideband Digital Back-End for the Upgraded GMRT'. *Journal of Astronomical Instrumentation* **6**(1):1641011–336.

B. J. Rickett (1990). 'Radio propagation through the turbulent interstellar plasma.'. *Annual Review of Astronomy and Astrophysics* **28**:561–605.

B. J. Rickett, et al. (1984). 'Slow scintillation in the interstellar medium.'. *Astronomy and Astrophysics* **134**:390–395.

T. E. Riley, et al. (2021). 'A NICER View of the Massive Pulsar PSR J0740+6620 Informed by Radio Timing and XMM-Newton Spectroscopy'. *The Astrophysical Journal Letters* **918**(2):L27.

J. A. Roberts & D. W. Richards (1971). 'Timing Observations of the Crab Nebula Pulsar at the Arecibo Observatory'. *Nature Physical Science* **231**(19):25–28.

J. Roy, et al. (2010). 'A real-time software backend for the GMRT'. *Experimental Astronomy* **28**(1):25–60.

S. A. Sanidas, et al. (2013). 'Projected Constraints on the Cosmic (Super)string Tension with Future Gravitational Wave Detection Experiments'. *The Astrophysical Journal* **764**(1):108.

M. V. Sazhin (1978). 'Opportunities for detecting ultralong gravitational waves'. *Soviet Astronomy* **22**:36–38.

P. A. G. Scheuer (1968). 'Amplitude Variations in Pulsed Radio Sources'. *Nature* **218**(5145):920–922.

R. M. Shannon & J. M. Cordes (2017). 'Modelling and mitigating refractive propagation effects in precision pulsar timing observations'. *Monthly Notices of the Royal Astronomical Society* **464**(2):2075–2089.

R. M. Shannon, et al. (2014). 'Limitations in timing precision due to single-pulse shape variability in millisecond pulsars'. *Monthly Notices of the Royal Astronomical Society* **443**(2):1463–1481.

R. M. Shannon, et al. (2015). 'Gravitational waves from binary supermassive black holes missing in pulsar observations'. *Science* **349**:1522–1525.

W. Sieber (1973). 'Pulsar Spectra'. *Astronomy and Astrophysics* **28**:237.

W. Sieber (1982). 'Causal relationship between pulsar long-term intensity variations andthe interstellar medium.'. *Astronomy and Astrophysics* **113**:311–313.

X. Siemens, et al. (2013). 'The stochastic background: scaling laws and time to detection for pulsar timing arrays'. *Classical and Quantum Gravity* **30**(22):224015.

A. Sillanpaa, et al. (1988). 'OJ 287: Binary Pair of Supermassive Black Holes'. *The Astrophysical Journal* **325**:628.

J. Simon & S. Burke-Spolaor (2016). 'Constraints on Black Hole/Host Galaxy Coevolution and Binary Stalling Using Pulsar Timing Arrays'. *The Astrophysical Journal* **826**(1):11.

C. Sobey, et al. (2019). 'Low-frequency Faraday rotation measures towards pulsars using LOFAR: probing the 3D Galactic halo magnetic field'. *Monthly Notices of the Royal Astronomical Society* **484**(3):3646–3664.

M. Sokolowski, et al. (2017). 'Calibration and Stokes Imaging with Full Embedded Element Primary Beam Model for the Murchison Widefield Array'. *Publications of the Astronomical Society of Australia* **34**:e062.

C. Sotomayor-Beltran, et al. (2013). 'ionFR: Ionospheric Faraday rotation'.

G. Srinivasan, et al. (1990). 'A novel mechanism for the decay of neutron star magnetic fields'. *Current Science* **59**:31–38.

B. W. Stappers, et al. (1996). 'Probing the Eclipse Region of a Binary Millisecond Pulsar'. *The Astrophysical Journal Letters* **465**:L119.

L. Staveley-Smith, et al. (1996). 'The Parkes 21 CM multibeam receiver'. *Publications of the Astronomical Society of Australia* **13**(3):243–248.

D. R. Stinebring, et al. (1996). 'Refractive and Diffractive Scintillation of the Pulsar PSR B0329+54'. *The Astrophysical Journal* **460**:460.

D. R. Stinebring, et al. (2001). 'Faint Scattering Around Pulsars: Probing the Interstellar Medium on Solar System Size Scales'. *The Astrophysical Journal Letters* **549**(1):L97–L100.

A. T. Sutinjo, et al. (2015). 'Characterization of a Low-Frequency Radio Astronomy Prototype Array in Western Australia'. *IEEE Transactions on Antennas and Propagation* **63**(12):5433–5442.

N. A. Swainston, et al. (2021). 'Discovery of a Steep-spectrum Low-luminosity Pulsar with the Murchison Widefield Array'. *The Astrophysical Journal Letters* **911**(2):L26.

G. Swarup (1991). 'Giant metrewave radio telescope (GMRT)'. In T. J. Cornwell & R. A. Perley (eds.), *IAU Colloq. 131: Radio Interferometry. Theory, Techniques, and Applications*, vol. 19 of *Astronomical Society of the Pacific Conference Series*, pp. 376–380.

G. B. Taylor, et al. (2012). 'First Light for the First Station of the Long Wavelength Array'. *Journal of Astronomical Instrumentation* **1**:1250004–284.

J. H. Taylor (1992). 'Pulsar Timing and Relativistic Gravity'. *Philosophical Transactions of the Royal Society of London Series A* **341**(1660):117–134.

J. H. Taylor & J. M. Cordes (1993). 'Pulsar Distances and the Galactic Distribution of Free Electrons'. *The Astrophysical Journal* **411**:674.

J. H. Taylor & J. M. Weisberg (1989). 'Further Experimental Tests of Relativistic Gravity Using the Binary Pulsar PSR 1913+16'. *The Astrophysical Journal* **345**:434.

S. R. Taylor, et al. (2017). 'Constraints on the Dynamical Environments of Supermassive Black-Hole Binaries Using Pulsar-Timing Arrays'. **118**(18):181102.

E. Thébault, et al. (2015). 'International Geomagnetic Reference Field: the 12th generation'. *Earth, Planets, and Space* **67**:79.

C. Tiburzi, et al. (2020). 'The impact of Solar wind variability on pulsar timing'. *arXiv e-prints* p. arXiv:2012.11726.

S. J. Tingay, et al. (2013). 'The Murchison Widefield Array: The Square Kilometre Array Precursor at Low Radio Frequencies'. *Publications of the Astronomical Society of Australia* **30**:e007.

M. Toscano, et al. (1998). 'Spectra of Southern Pulsars'. *The Astrophysical Journal* **506**:863–867.

S. E. Tremblay, et al. (2015). 'The High Time and Frequency Resolution Capabilities of the Murchison Widefield Array'. *Publications of the Astronomical Society of Australia* **32**:e005.

M. J. Valtonen, et al. (2016). 'Primary Black Hole Spin in OJ 287 as Determined by the General Relativity Centenary Flare'. *The Astrophysical Journal Letters* **819**(2):L37.

C. L. Van Eck, et al. (2011). 'Modeling the Magnetic Field in the Galactic Disk Using New Rotation Measure Observations from the Very Large Array'. *The Astrophysical Journal* **728**:97.

M. P. van Haarlem, et al. (2013). 'LOFAR: The LOw-Frequency ARray'. *Astronomy and Astrophysics* **556**:A2.

R. van Haasteren, et al. (2011). 'Placing limits on the stochastic gravitational-wave background using European Pulsar Timing Array data'. *Monthly Notices of the Royal Astronomical Society* **414**:3117–3128.

W. van Straten (2004). 'Radio Astronomical Polarimetry and Point-Source Calibration'. *The Astrophysical Journal Supplement Series* **152**(1):129–135.

W. van Straten & M. Bailes (2011). 'DSPSR: Digital Signal Processing Software for Pulsar Astronomy'. *Publications of the Astronomical Society of Australia* **28**:1–14.

W. van Straten, et al. (2012). 'Pulsar Data Analysis with PSRCHIVE'. *Astronomical Research and Technology* **9**(3):237–256.

J. P. W. Verbiest, et al. (2016). 'The International Pulsar Timing Array: First data release'. *Monthly Notices of the Royal Astronomical Society* **458**(2):1267–1288.

M. A. Walker (2007). 'Extreme Scattering Events: Insights into the Interstellar Medium on AU-Scales'. In M. Haverkorn & W. M. Goss (eds.), *SINS - Small Ionized and Neutral Structures in the Diffuse Interstellar Medium*, vol. 365 of *Astronomical Society of the Pacific Conference Series*, p. 299.

R. B. Wayth, et al. (2018). 'The Phase II Murchison Widefield Array: Design overview'. *Publications of the Astronomical Society of Australia* **35**:33.

M. Xue, et al. (2017). 'A Census of Southern Pulsars at 185 MHz'. *Publications of the Astronomical Society of Australia* **34**:e070.

M. Xue, et al. (2019). 'MWA tied-array processing II: Polarimetric verification and analysis of two bright southern pulsars'. *Publications of the Astronomical Society of Australia* **36**:e025.

J. M. Yao, et al. (2017). 'A New Electron-density Model for Estimation of Pulsar and FRB Distances'. *The Astrophysical Journal* **835**(1):29.

X. P. You, et al. (2007). 'Dispersion measure variations and their effect on precision pulsar timing'. *Monthly Notices of the Royal Astronomical Society* **378**(2):493–506.